Visualizing Influenza Virus Membrane Fusion: Inhibition and Kinetics

Visualizing Influenza Virus Membrane Fusion: Inhibition and Kinetics

A dissertation presented
by
Jason John Otterstrom
to
The Harvard Biophysics Program

in partial fulfillment of the requirements
for the degree of
Doctor of Philosophy
in the subject of
Biophysics

Harvard University
Cambridge, Massachusetts

December 2013

Dissertation Advisor: Professor Antoine M. van Oijen Author: Jason John Otterstrom

Visualizing Influenza Virus Membrane Fusion:
Inhibition and Kinetics

Abstract

The influenza virus hemagglutinin (HA) surface protein is a primary antigenic target for neutralization of viral infection. HA also mediates membrane fusion between the virus and a cell, which is the first critical step during infection. Traditional techniques to study infection neutralization by antibodies or the membrane fusion process rely on ensemble measurements, confounding the precise mechanism of infection neutralization and obscuring transient conformational intermediates. This dissertation describes advances made in a fluorescence microscopy-based single-particle fusion assay to overcome the limitations of ensemble measurements in these types of studies. Virus particles are labeled to visualize lipid mixing between a virus and a target membrane formed upon a glass or polymer support. Optionally, the viral lumen can be labeled to visualize the subsequent release of viral contents.

Recently isolated antibodies recognizing highly conserved epitopes on the HA protein that are critical for the protein's fusogenic capacity are able to neutralize infection from a broad range of influenza subtypes. Binding of these antibodies to a virus prior to inducing fusion with a target membrane resulted in inhibition of the fusion process, directly confirming one mechanism of infection neutralization. Fluorescently labeling the antibodies allowed for functional stoichiometric measurements that indicate a virion can be rendered non-fusogenic without the need for antibodies to bind and inactivate every HA present on the viral surface. A molecular model of fusion inhibition is proposed wherein coordination between neighboring HA is disrupted that leads to neutralization of the entire particle.

Though polyunsaturated lipids are critical components of biological membranes that frequently undergo membrane fusion, their precise effects on the fusion process are poorly characterized. A fully automated data extraction program was designed and implemented to enhance the reproducibility of selecting fusing and non-fusing virions. Analysis of the resulting fusion kinetics revealed that the rate of fusion pore expansion is enhanced by high degrees of lipid unsaturation. During fusion at low pH, lower degrees of saturation resulted in the onset of a restricted hemifusion state. It is postulated that cholesterol and the HA fusion peptide create a molecular fence that confines lipid diffusion between the virus and target membranes.

Table of Contents

Chapters

Appendices

List of Figures

List of Tables

List of Abbreviations

bnAbs ..... broadly neutralizing antibodies
diC18:1 ..... 1,2-dioleoyl-*sn*-glycero-3-phosphocholine
diC18:3 ..... 1,2-dilinolenoyl-sn-glycero-3-phosphocholine
diC22:1 ..... 1,2-dierucoyl-*sn*-glycero-3-phosphocholine
diC22:6 ..... 1,2-didocosahexaenoyl-*sn*-glycero-3-phosphocholine
Fab ..... fragment of antibody / IgG
FFT ..... fast Fourier transform
Gd1a ..... disialoganglioside GD1a
GYPA ..... glycophorin A
HA ..... influenza A hemagglutinin
IgG ..... immunoglobulin G
MUFA / mono-UFA ..... monounsaturated fatty acid
PC ..... phosphatidylcholine
PDMS ..... polydimethylsiloxane
PUFA / poly-UFA ..... polyunsaturated fatty acid
R18 ..... octadecyl rhodamine B
Rh110 ..... octadecyl rhodamine 110
SG ..... Savitzky-Golay filter
SLB ..... supported lipid bilayer
SRB ..... sulforhodamine B
TIRF / TIRFM ..... total internal reflection fluorescence microscopy

Acknowledgements

Just as no man is an island, no dissertation is completed in solitude. And while my thesis may be scarcely read, I am still happy to have this singular opportunity to express my gratitude to everyone who helped and supported me in my journey through graduate school.

I would first like to thank my advisor, Antoine van Oijen, for his patient guidance over the past six years and on two continents. I feel fortunate to have found an advisor who is both a great scientist and a wonderful mentor. Many were the times I begrudgingly dragged him through tedious detail, which he would concisely put into a bigger picture. Our (semi) weekly meetings taught me pragmatism and fomented my ability to discern the essential elements of a project or experiment from the detail and minutia that my initial reactions tend to focus on. Through example, he trained me to present my research in an energetic yet focused fashion. From him I learned that presenting one's science well is as important as doing it well in the first place. Beyond work, he truly cares for all of the people who work for him both in and out of the lab. Antoine was a great help for me and my wife in our big move across the Atlantic and in adapting to Groningen. He puts great effort, too, in encouraging a lab atmosphere where people are not only colleagues, but also friends. The trip to the La Chouffe brewery in Belgium he allowed us to plan was truly awesome and unforgettable! So, thank you, Antoine, for all that you've taught me and for making the lab such a wonderful place to work.

I am very grateful to my loving and lovely wife, Noelia, for all of her patients and encouragement. She has supported me 100% from my first inklings of going to graduate school in 2005, when our relationship was a mere six months old, through the move to Groningen and up until the end of my dissertation. I thank her for always standing by me, both on the good days when we celebrated steps that moved things forward and on the bad days when she motivated me to smile and keep pushing. I thank her, too, for the sacrifice of putting her professional career on hold by giving up a permanent teaching position in Murcia to be with me while I worked to advance my studies. I am happy that I had her with me to pull me out of the lab and away from work, from time to time; she makes sure that I take full advantage of all that life has to offer. I am lucky to have such a wonderful, joyful and supportive wife to share all of it with!

I am fortunate to have two remarkable parents, Jim and Kathy Potter, who have formed the foundation of all the achievements I have earned. None of it would have been possible without their love, encouragement and support. They've taught me to always strive for excellence and surpass the limitations I place upon myself, all without being demanding. Together, they have opened my eyes to the world and showed me to appreciate it in all of its complexity. Thank you for sacrificing so much of yourselves to make my life so spectacular!

I would like to wholeheartedly thank Dr. Dan Floyd for his dedication in devising and establishing the viral fusion assay that is the basis for my doctoral work and dissertation. Moreover, he undertook the task of teaching a physicist how to work and function in a wet lab for the first time – my first step in becoming a biophysicist. I enjoyed the time we shared at HMS making beer-hour posters and finding entertaining uses for liquid nitrogen and dry ice.

Many thanks to Dr. Boerries Brandenburg who initiated the collaboration between my project and Crucell, I consider myself very fortunate to have been part of such innovative work. More than a collaborator, I consider Boerries also as a mentor as he provided me with advice both on how to approach scientific projects and on developing a professional career. He greatly fomented my training in visualizing a nascent manuscript and developing the story around the

data it contains. Also at Crucell, thanks to Dr. Martin Koldijk who helped me learn a great deal of statistics and statistical analysis.

I am very grateful for the hard work and dedication of Prof. Jim Hogle and Michele Jakoulov, they are the heart and soul of the Harvard Biophysics program. Together, they have made it an excellent experience that I'm thrilled and honored to have been a part of. I thank them for the extra effort on their part to keep me going through my graduate studies while I was living on a separate continent six time zones away. I very much enjoyed participating in all of the events that they, especially Michele, organize throughout the year to unite the motley group of students who are spread throughout Boston. Retreats, BBQ's, clambakes and outings to Northern beaches, I had a lot of fun at all of them!

There have been many people in the two van Oijen labs who have helped me throughout the years, a few of which are of particular note and whose help and support I want to acknowledge. Dr. Karl Duderstadt, my fellow compatriot in Groningen, taught me both the concept and application of maximum likelihood estimators, which form the calculational basis of the automated analysis program described in chapter 4. Also, I often sought his advice when looking at my next career step and I want to thank him for his encouragement; as well Karl is an excellent editor and helped me with many abstracts and letters. Similarly, thanks to Dr. Andrew Robinson for his thoughts on career planning and help with editing many, many items. It was also great to have Andrew around to share Simpson's quotes. With both of them, I always enjoyed sharing English-based culture, phrases and the humor with our international colleagues there in Groningen.

Thanks to Dr. Mark Elenko for making many late nights at HMS fun and for introducing me to MATLAB programming (along with Dan). In Groningen, Michiel Punter was also a great resource for programming advice and fun, with his ability to generate hilarious and crazy conversations at any instant. Joris Goudsmits was a great resource for math and adobe illustrator/photoshop, and regularly helped me to overcome problems. Thanks to Dr. Victor Krasnikov who taught me volumes about optics and microscopy, and who always had an open door to help out with troubleshooting issues. I also have greatly enjoyed hearing his stories about life in the USSR before he moved to the Netherlands. Thanks to Dr. Irene Kim and Dr. Tijana Ivanovic for their help and support in advancing the microfluidics aspects of the fusion setup while at HMS, and for being generally great colleagues.

Life is most enjoyable when we are surrounded by good people and those who comprised the two instances of the van Oijen lab made my graduate school experience an entertaining and wonderful experience. It was a pleasure and a privilege to have spent so much time with them. Dr. Jan Peter Birkner's mischievous, child-like sense of humor made the office in Groningen a jovial one. Dr. Evelyn Plötz and Dr. Giorgos Gouridis were also fun, energetic officemates and our conversations have helped to prepare me to begin my own upcoming postdoc experience. Hylkje Geertsema's infectious laughter makes any group gathering fun and lively; thanks to her along with Lisanne Spenkelink, Victor Caldas and Jasper van der Velde for consistently volunteering to organize fun group activities and outings. Lastly, many thanks to Jelle Blijleven, whom I am honored to have mentored, for being a great student and for giving me new motivation for my projects in the last months of my dissertation work. I drew many insightful conclusions and interpretations of my data thanks to our many conversations. I wish you the best in your own graduate studies pursuing the elusive details of viral membrane fusion.

This dissertation is dedicated to:

My wife, Noelia Fernández Carmona, for all of her love, support and patience over the past eight years;

And my parents, Kathy & James Potter, who form the foundation of all I have achieved and will accomplish.

Chapter 1

Visualization of Membrane Fusion, One Particle at a Time

Abstract

Protein-mediated fusion between phospholipid bilayers is a fundamental and necessary mechanism for many cellular processes. The short-lived nature of the intermediate states visited during fusion makes it challenging to capture precise kinetic information using classical, ensemble-averaging biophysical techniques. Recently, a number of single-particle fluorescence microscopy-based assays have been developed that allow researchers to obtain highly quantitative data on the fusion process by observing individual fusion events in real time. These assays depend upon changes in acquired fluorescence signal to provide a direct read out for transitions between the various fusion intermediates. The resulting data yields meaningful and detailed kinetic information on the transitory states en route to productive membrane fusion. In this review, we highlight recent *in vitro* and *in vivo* studies of membrane fusion at the single-particle level in the contexts of viral membrane fusion and SNARE-mediated synaptic vesicle fusion. These studies afford insight into mechanisms of coordination between fusion-mediating proteins as well as coordination of the overall fusion process with other cellular processes. The development of single-particle approaches to investigate membrane fusion and their successful application to a number of model systems has resulted in a new experimental paradigm and opens up considerable opportunities to extend these methods to other biological processes that involve membrane fusion.

Material in this chapter was originally published in the journal *Biochemistry*:

Otterstrom, J. & van Oijen, A.M. (2013) Visualization of Membrane Fusion, One Particle at a Time. *Biochemistry* **52**: 1654-1668.

1.1 Introduction

Membranes comprised of phospholipid bilayers are essential for all cellular life. They encapsulate cytoplasmic components, allow for enrichment of metabolites and restrict the entry of foreign pathogens and damaging chemicals. Further, eukaryotes have developed inner membranes to form organelles that allow for compartmentalization of metabolic and replicative processes. At times, though, this resolute barrier must be perturbed, broken and subsequently reformed – namely, membranes must fuse. While the final state of fully merged membranes from two initially separate bilayers is an energetically favorable one, there are many energetic barriers that must be overcome to achieve this final fused state.

Membrane fusion generally occurs through a series of steps including close bilayer apposition, fusion of the proximal leaflets– termed hemifusion – and finally merger of the distal leaflets – termed pore formation [1,2]. These metastable intermediates along the fusion pathway are depicted in Figure 1-1 and can be experimentally probed, as will be discussed in this review. Significant energetic barriers separating these intermediates make the energetic landscape a rough terrain to traverse. Dehydration of a limited area between two closely apposed bilayers, formed by a fusion dimple or point-like protrusion, poses the first sizeable energy barrier [2,3]. Formation of a hemifusion stalk (Figure 1-1B) is also energetically expensive, with an energy barrier to formation that can be on the order of ~20-40 k_BT (12-24 kcal/mol, where 1 $k_BT \approx 0.6$ kcal/mol) [1,2,4]. The hemifused state can progress in two directions: it can develop into a full fusion pore that allows mixing of the contents initially separated by the two bilayers (Figure 1-1C); or it can become an extended hemifusion diaphragm that is a kinetic dead end and prevents content mixing [6]. In addition, alternative pathways could supplant the lipidic hemifusion stalk with a nascent proteinaceous pore that subsequently develops into a full lipidic fusion pore [5,7]. Moreover, the initial fusion pore is not necessarily a stable structure and work is required to drive it open [5]. If a nascent fusion pore

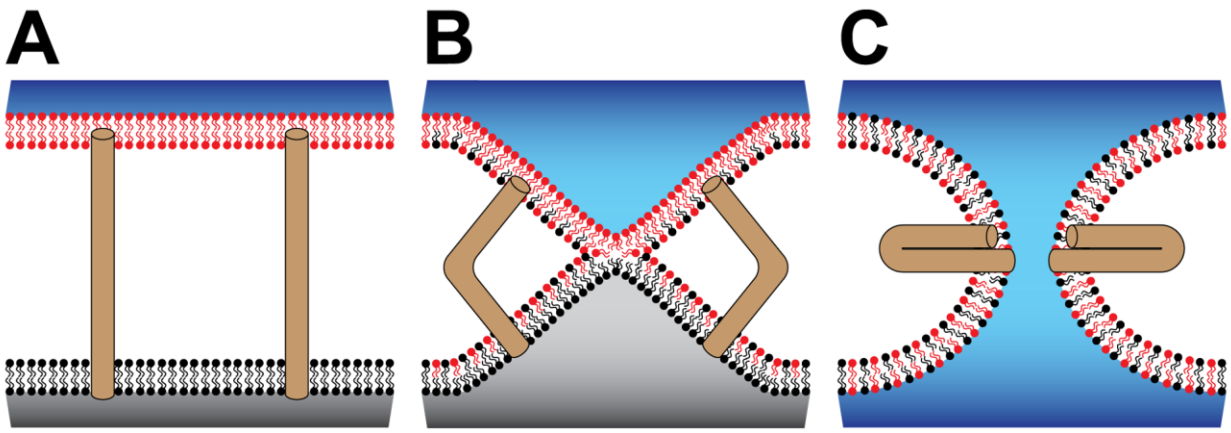

Figure 1-1 – *States of protein-mediated membrane fusion that are accessible by fluorescence microscopy.* ***A****) Two bilayers (red and black) are in close apposition and separate two luminal compartments (blue and grey, respectively). Fusion proteins (brown cylinders) in their extended conformation couple the two bilayers and are formed following unfolding of a viral surface fusion protein or v-SNARE–to–t-SNARE interaction during docking of a synaptic vesicle.* ***B****) The initial refolding of fusion proteins back upon themselves brings sections of the two membranes into yet closer apposition and facilitates the onset of hemifusion, which is an intermediate state characterized by merger of the proximal leaflets from each of the two bilayers. In this state, lipid molecules are able to exchange between the two proximal leaflets, as indicated by mixing of the red and black lipids.* ***C****) Additional fusion protein rearrangements cause full fusion, a state characterized by merger of the distal leaflets and the formation of a pore connecting the two previously separated compartments to allow content mixing. In the case of viral fusion, pore formation creates a corridor the viral genome can pass through, while in SNARE-mediated fusion the fusion pore may be closed before all contents have been released.*

is prone to collapse, what is the lifetime of a pore and what pore size can be obtained before collapse occurs? If a hemifusion intermediate is formed, what factors determine if it will productively develop into a full fusion pore and what is the lifetime of such a hemifused state? These aspects of fusion kinetics are of key importance for the proper functioning of a fusogenic system and any biological situation driving membrane fusion must evolve to form a stable fusion pore of appropriate size.

Two biological solutions to overcome these energy barriers and traverse the intermediate fusion states have been well characterized structurally and functionally: fusion proteins on the surface of several enveloped viruses and eukaryotic soluble NSF attachment protein receptor (SNARE) proteins. These transmembrane proteins confer fusogenic capacity to the viruses or synaptic vesicles, respectively, that house them. Recent technological advances in fluorescence microscopy have facilitated sensitive and detailed studies of protein-mediated fusion events at the single-particle level – a single particle in this context being a macromolecular object comprised of phospholipids and fusion-mediating proteins, *e.g.* enveloped viruses or vesicles incorporating SNARE proteins, which is appropriately labeled for visualization on a fluorescence microscope. Observing individual fusion events is essential for gaining access to the intermediate states visited during membrane fusion and transitions between them. These states are often short-lived and inaccessible to bulk membrane fusion studies, where only average kinetic characterization is possible and individual or rare events are obfuscated. Furthermore, the single-particle based experimental designs can (partially) overcome technical problems such as vesicle aggregation, bursting or leakiness that are often obstacles in bulk phase fusion experiments. This review aims to highlight a number of recent experimental methods used to investigate membrane fusion at the single-particle level. These new approaches are allowing direct visualization of fusion intermediates, and a probing of stimuli and conditions governing their behavior.

1.2 Fluorescence as a reporter for fusion

Fluorescence microscopy has proven a revolutionary tool for study of biological systems by simultaneously allowing real-time observation, low invasiveness and high specificity. Systems to study membrane fusion can be based on individual live cells or on purified, individual fusogenic particles (*i.e.*, liposomes or viruses) re-constituted into a controlled fusion scenario. Fluorescent probes used in single-particle fusion studies are typically either small-molecule organic dyes or fluorescent proteins. Organic dyes are frequently used in membrane fusion studies because these can be used to label the lipid-membrane substrates in a straightforward manner. Lipids coupled to bright fluorophores can be mixed with reconstituted lipids when used *in vitro* and can spontaneously insert into biological membranes, such as those of intact viruses, and achieve high local concentrations. Commonly used fluorescent lipophilic probes (Table 1) include long-chain dialkylcarbocyanine dyes such as DiD and DiI, and dyes having phosphoethanolamine (PE) head groups such as tetramethylrhodamine (TMR-PE or TRITCH-PE), octadecyl-rhodamine B (R18), lissamine rhodamine B (Rh-PE), or Texas-red-PE (Rh-PE). These lipophilic dyes provide a direct read-out for lipid mixing between two bilayers, either through dequenching or FRET (Förster or Fluorescence Resonance Energy Transfer) (Figure 1-2). It is of critical importance, however, to realize that lipid mixing is not necessarily a direct read-out for full fusion. Full fusion, characterized by a lipidic fusion pore, requires separate fluorescent measurement to detect transfer of content after the formation of a pore.

Various steps in the fusion pathway can be visualized using fluorescence reporters of lipid and content mixing; three such visualization strategies are depicted in Figure 1-2. When the lipophilic dyes are incorporated into a bilayer at a sufficiently high concentration, their tight molecular packing can cause quenching of fluorescence by relaxation of an excited dye through a non-photon emitting process. When labeled and unlabeled membranes fuse, the lipids rapidly re-distribute from the labeled into the unlabeled membrane, decreasing the local concentration of the dye molecules in the labeled membrane. This dilution alleviates the neighbor-neighbor

Table 1-1 – Fluorescent Dyes for Visualizing Membrane Fusion

Fusion Event	Type	Fluorescent Label	Detection Signal [a]
Lipid mixing (hemifusion)	*in vitro*	R18	Dequenching [48]
		Rh110 [b]	Dequenching [38]
		TMR-PE or TRITCH-PE [e]	Dequenching [57, 58]
		Rh-PE	Dequenching [80] Dissipation [55]
		DiD	Dequenching [11,12]
		DiD + DiI	FRET increase [84]
	in vivo	DiD	Dequenching [61] Dissipation [64]
Content mixing or release (pore formation)	*in vitro*	SRB	Dissipation [38,48] Dequenching [11,12]
		Fluorescein [c]	Dissipation [48]
		Calcein	Dequenching [10]
		DNA hairpin	FRET decrease [91,93]
	in vivo	Palmitylated YFP [c, d]	Dissipation and Recovery [65]
		Cleaved GFP fusion [c]	Dissipation [64]
		FM1-43	Dissipation [106]
		FM4-64	Dissipation [20]
		Quantum Dots [c, d]	Fluorescence increase or loss [108]

[a] Selected references only; not a complete listing. [b] Not commercially available. [c] pH-sensitive, which might be observed when it is used. [d] Not released upon partial pore opening. [e] Reported to visualize both inner and outer leaflet fusion.

quenching and results in a rapid fluorescence increase known as dequenching (Figure 1-2A). Detection of this signal is a common indicator for the creation of the hemifusion intermediate and has been described as a 'flash' [8]. R18, in particular, is a commonly used dye to detect lipid mixing because it does not rapidly redistribute between closely apposed membranes in the absence of (hemi)fusion and unincorporated dye can easily be removed [9]. The formation of a fusion pore can be directly read out through dequenching of a content label contained within vesicles or liposomes. Calcein [10] and Sulforhodamine B [11,12] (Table 1) exhibit a strong degree of quenching at high concentration and when the labeled vesicle or liposome contents mix with unlabeled buffer a dequenching spike similar to that observed for hemifusion can be visualized. Both dyes are charged compounds and can leak from labeled liposomes, so care should be taken to ensure that leakage does not affect experimental outcomes.

The dyes DiD and DiI can be used as a FRET pair (Table 1), wherein the green-emitting DiI is excited by appropriate illumination and its emission is transferred through non-radiative resonance to DiD neighbors, which then emit a photon. This process is highly distance dependent and can be observed as an increase in red emission with a concomitant decrease in green emission once lipid mixing between two apposed membranes has occurred (Figure 1-2C). This technique is commonly used in bulk lipid mixing studies, but has also been applied to single-particle fluorescence microscopy studies.

The advantage of small, organic dyes is their superior photostability and brightness in comparison to fluorescent proteins. These benefits generally come with the difficulty of applying them to specifically label a protein or structure of interest *in vivo*. Techniques for applying this type of labeling are nicely reviewed elsewhere [13-15] as is the applicability fluorescent proteins for the labeling of lipid membranes [16-18]. Synaptic and secretory vesicles are exceptions to this generality, however, and the exogenous addition of styryl pyridinium dyes can label these structures *in vivo* with good specificity and selectivity. These types of dyes rapidly insert into the outer leaflet of bilayers in a reversible fashion and concomitantly exhibit an increase in fluor-

Figure 1-2 – *Visualizing membrane fusion through fluorescence signals. Labeled and surface-immobilized fusogenic particles are depicted on the left of each panel. Grayscale images, as captured on a CCD camera, and 3D fluorescence profiles above those images show how the recorded and peak intensity, respectively, of a particle's fluorescence signal change through the time-course of fusion at a fusion site. Quantifying the fluorescence intensity present in the CCD images provides "intensity vs. time" diagrams.* ***A****) Dequenching upon hemifusion to a large, planar bilayer (black) with outward diffusion of lipophilic dyes (red) from the fusion site. When the dequenching signal arises from content mixing of two vesicles, as done by Kyoung et al. [11], diffusion away from the site of fusion is not possible.* ***B****) Dissipative fluorescence loss upon escape of an aqueous fluorescence signal (purple) from the lumen of a fusogenic particle through the fusion pore. A similar fluorescence signal is obtained for lipid mixing when dequenching does not occur.* ***C****) FRET-based detection of hemifusion between two immobilized and labeled fusogenic vesicles (red and cyan). Independent excitation of acceptor and donor dyes allows for visualization of each of the overlapping vesicles. Only after fusion is the acceptor vesicle visualized via donor dye excitation, producing a high FRET efficiency signal.*

*(**Figure 1-2 Continued**)*

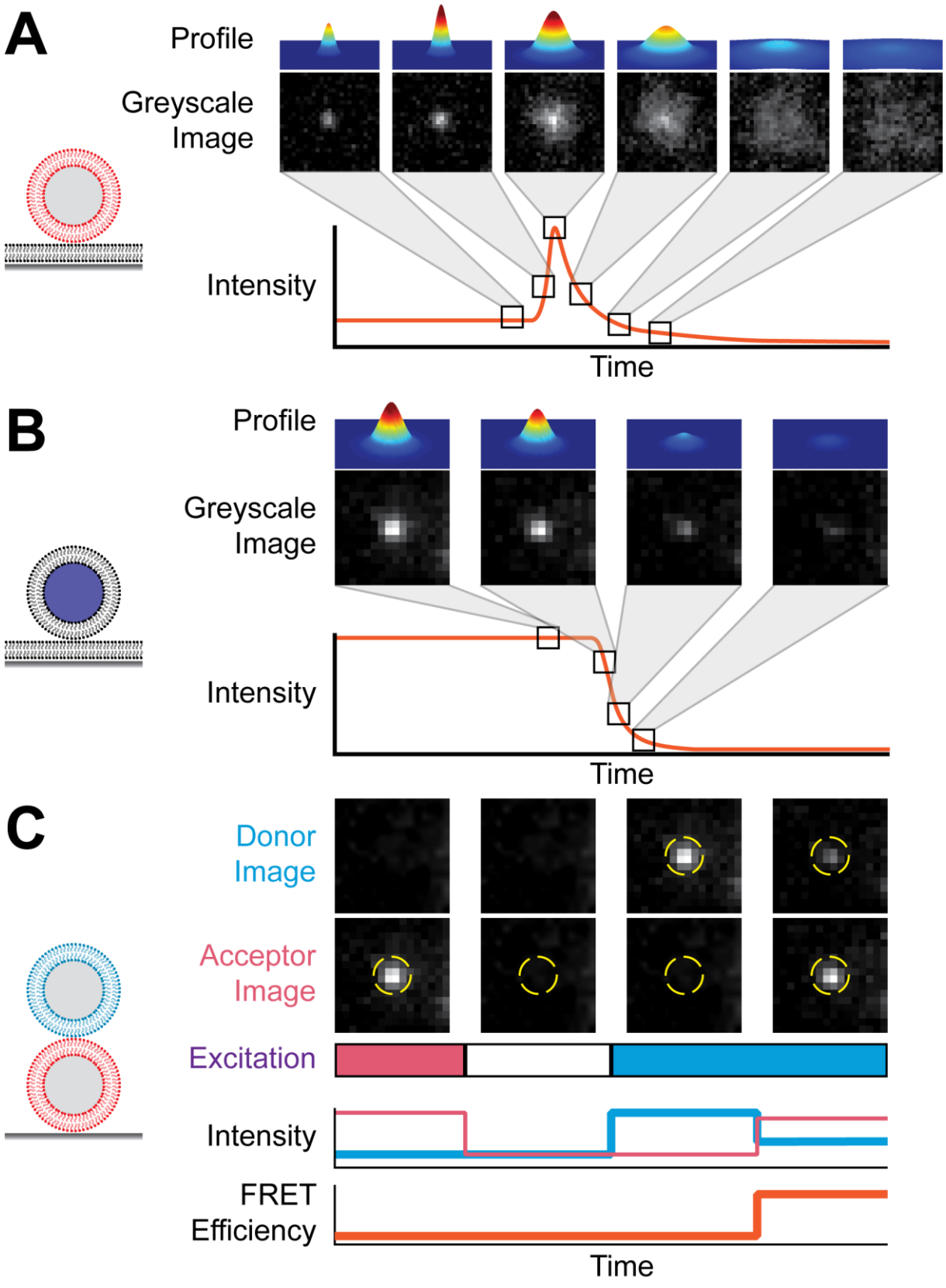

escent brightness within a bilayer's hydrophobic interstice. Dyes such as FM1-43 and FM4-64 are commonly used to visualize these types of vesicles, which then appear as punctate structures within neuronal or secretory cells. Fusion events are detected as a loss of signal from a fluorescent punctate as the dye molecules departition from the membrane and both escape through small fusion pores [19] and become dispersed into the plasma membrane [20]. Since the entire plasma membrane is labeled in this technique, there are fluorescent background and potential phototoxic effects that must be taken into account.

Fluorescent proteins (FP) make up for their comparatively poor photostability and brightness with their *in vivo* specificity. A majority of the common fluorescent proteins are monomeric and can be genetically encoded as in-frame fusions with a protein of interest at either the N- or C-terminal or even within a flexible loop. Recent reviews [21-24] provide detailed overviews of fluorescent proteins, their properties, uses and pitfalls. One particular characteristic of fluorescent proteins that has been exploited in the study of membrane fusion is their pH sensitivity (Table 1). Generally, fluorescent proteins lose fluorescence brightness gradually as the pH decreases to acidic conditions, but maintain ~50% of their brightness down to ~pH 5.0. To leverage this effect for the study of secretory and synaptic vesicle dynamics, Miesenböch *et al.* [25] engineered green fluorescent proteins to have increased pH sensitivity. Their 'pHluorin' mutants displayed a marked change in either the excitation spectrum or fluorescent brightness upon neutralization of an acidic synaptic vesicle following fusion with the plasma membrane.

1.3 Fluorescence microscopy

Common fluorescence microscope designs for the study of membrane fusion kinetics are the epifluorescent and total internal reflection fluorescent (TIRF) microscopes. Both are wide-field microscopy techniques since they illuminate a large field of view (FOV) continuously.

Modern electron-multiplying charge coupled device (EM-CCD) cameras are able to image the fluorescence from large FOVs at high frame rates and with single-molecule sensitivity.

In epifluorescence microscopy, the excitation light propagates through the entire sample, causing fluorescence in any of the vast number of molecules it may come across. This illumination strategy gives great penetration depth for imaging, but produces a high background that can quickly degrade the signal-to-background ratio in an image. TIRF microscopy, in contrast, selectively illuminates only a very thin region, with a thickness of approximately 100 nm, immediately above the glass substrate surface. The exclusion of background fluorescence from elsewhere in the sample results in a high signal-to-background ratio for fluorescent molecules within the excitation volume at the expense of low penetration depth. The physical explanation for this effect and guidelines for construction of a TIRF microscope are nicely described elsewhere [26-28]. TIRF microscopy is particularly useful for the study of membrane fusion events because the plasma membrane of many cell types can be brought within the TIR illumination volume. Confocal microscopes can also be used, where the light is focused into a diffraction-limited volume or "spot" rather than illuminating a large volume of the sample. Images are obtained by raster-scanning the confocal volume throughout a defined FOV and the fluorescence information collected with a photomultiplier tube or photo diode. Fluorescence emanating from outside the focal volume of interest is eliminated to provide images with a high signal-to-noise ratio and low background. Even though full images are acquired at a much lower time resolution, the signal from one particular spot can be followed with sampling rates orders of magnitude higher than with wide-field imaging techniques.

These microscopy techniques allow for a range of temporal resolutions (Table 2), but the spatial resolution is generally dictated by the diffraction limit of ~300 nm. If sufficient photons are collected and the fluorescent particle is a point source with dimensions smaller than the diffraction limit, then the particle's position can be determined to ~1-2 nm accuracy [29], which is useful for particle tracking. Super resolution imaging (*i.e.* STORM, PALM, *etc.*, reviewed in [30])

Table 1-2 – Novel and Notable Single-Particle Experimental Setups for Visualizing Membrane Fusion

Type	Experimental design		Microscope Setup [a]	Time Resolution	Advantages	Limitations
in vitro	SLB-based membrane fusion	Docking under fusogenic conditions	TIRFM [10,47,55]	1− 100 ms	Simultaneous lipid and content mixing observation.	SLB formation, stability, reproducibility.
		Pre-docking with fusion trigger	TIRFM [38,48]	100 − 1000 ms	Simultaneous lipid and content mixing observation; trigger to fusion event time extraction.	SLB formation, stability, reproducibility.
	Tethered vesicle−vesicle fusion	Pre-docking with fusion trigger	TIRFM [11,12,84]	100 − 900 ms	Simultaneous lipid and content mixing observation; trigger to fusion event time extraction.	Small number of observations per experiment because of two-body binding.
			Confocal [92]	200 − 1000 ms	Simultaneous lipid and content mixing observation; potentially larger FOV.	Time resolution depends on the size of the FOV.
in vivo	Viral tracking within a target cell	Temperature- or pH-synchronized fusion	Confocal [64,68]	6 − 8 s	Trigger to fusion event time extraction [b]; simultaneous lipid and content mixing observation; amenable to labeling of other cellular proteins; three dimensional tracking; potentially larger FOV.	Time resolution depends on the size of the FOV; small number of observations per experiment.
			Epifluorescence or TIRFM [69,71,72]	0.5 − 10 s	Simultaneous lipid and content mixing observation; obtain waiting time between trigger and fusion events [b]; amenable to labeling of other cellular proteins.	Small number of observations per experiment.
	Synaptic vesicle fusion in live neurons	Styryl dye labeling	Epifluorescence [106,110]	15 − 36 ms	Fluorescent dye can undergo endocytotic recycling; potentially amenable to labeling of other cellular proteins.	Whole cell, nonspecific labeling; potential for high fluorescence background and phototoxicity.
		Quantum dot labeling	Epifluorescence [108]	33 − 300 ms	Direct observation of multiple kiss-and-run fusion events; extended observation with minimal photobleaching.	Broad quantum dot emission spectra limit labeling of other cellular proteins; quantum dots exhibit higher cellular toxicity than dyes or FP; high phototoxicity at long observation times.
		pHluorin fusion-protein labeling	Epifluorescence [111]	9.6 ms	Specific labeling of synaptic vesicles by SNARE protein; amenable to labeling of other cellular proteins.	High fluorescence background; rapid photobleaching.

[a] Selected references only; not a complete listing. [b] Trigger refers either to a synchronizing event or to a change in pH when pH-sensitive FP are attached to virions. [68,69]

could be used in conjunction with single-particle tracking to precisely localize fusion events within a cell, though this has yet to be demonstrated.

1.4 Supported lipid bilayers

Many *in vitro* studies of membrane fusion make use of artificial lipid bilayers supported by a solid substrate. Several techniques exist to construct these supported lipid bilayers (SLB) and have recently been reviewed for a wide range of applications by Czolkos *et al.* [31] and Richter *et al.* [32]. For microscopy purposes, they are formed upon the surface of a cleaned, hydrophilic glass or quartz substrate and, in many cases, can allow for the incorporation of functional transmembrane proteins. The most common techniques to form SLBs are through vesicle rupture and self-spreading [33] and through successive transfer of two phospholipid monolayers using a Langmuir-Blodgett approach [34]. In its simplest implementation, the former technique requires incubation of a lipid solution with a solid, hydrophilic support, while the latter is more involved and involves sequential transfer of the two phospholipid monolayers. SLBs can also be formed upon a polymer cushion (such as polyethylene glycol, PEG [35,36]) or tethered to the solid substrate (such as with DNA, [35,37]) with the goal of creating a (mostly) aqueous volume that entirely separates the bilayer from the substrate's surface. High-molecular weight dextran has also been used as a cushion suitable for conducting single-particle viral fusion experiments [38], expanding on a technique that had been previously reported [39]. The practical difficulty in reproducibly creating fluid and continuous SLBs using these methods necessitates further work in optimizing surface chemistry.

1.5 Viral membrane fusion

Influenza hemagglutinin (HA) is the most intensively investigated of all the viral fusion proteins. The structural and functional aspects of HA have been thoroughly discussed in

several publications [40-43]. Briefly, HA is a class I trimeric fusion protein, with each monomer containing the two disulfide-linked HA1 and HA2 domains. HA thereby combines the domains responsible for receptor binding (HA1) and fusion (HA2) into a single protein machine. During clathrin-mediated endocytosis, the HA2 domain responds to acidification of the endosomal lumen by undergoing a conformational unfolding into an extended rod-shaped protein consisting of a 3-helix bundle of coiled alpha helices. The critical pH for this unfolding step is ~pH 5.5 for most influenza strains. Unfolding exposes the hydrophobic N-terminus of HA2, termed the fusion peptide, which inserts into the proximal leaflet of the target bilayer. When the HA2 refolds back upon itself, the fusion peptide serves as an anchor to bring the target membrane into close proximity of the viral envelope. This action facilitates fusion of the proximal leaflets of the two bilayers (Figure 1-1) into a hemifusion structure. The distal leaflets are merged by subsequent re-arrangements of the HA2 transmembrane domain, thereby creating a fusion pore for escape of viral contents into cellular cytosol. The three major classes of viral fusion proteins are all trimeric in their fusion-active state and are thought to follow the overarching scheme described here for HA [42]. The unfolding event is not necessarily pH-dependent, though, and can occur at neutral pH for some virus types. While these structural rearrangements required of HA2 and other fusion proteins to mediate fusion are widely accepted, there is much debate regarding the number of activated trimers on the viral surface required to act in concert for the fusion process to occur.

1.5.1 Single-particle viral fusion kinetics studied *in vitro*

Several decades of fluorescence-microscopy studies of HA-mediated fusion have contributed significantly to our understanding of the intermediate states and molecular processes that occur en route to viral membrane fusion. These studies have principally implemented two strategies: cell-cell fusion using HA-expressing cells, and single-particle virus-target or virosome-target fusion. In the single-particle context of this review, we will focus on the

latter of these techniques, though this is not to downplay the many insights into HA-fusion and membrane fusion in general provided by studies of cell-cell fusion with fluorescence microscopy.

Target membranes used to study HA-mediated fusion (Figure 1-3A and 3B) at the single-particle level are formed by different techniques. The earliest single-particle studies used intact erythrocytes [44,45] or black lipid membranes (BLM) [8,46] as targets for fusion. A BLM is a small circular patch of lipid bilayer painted onto a small hole in a Teflon sheet that serves as an aperture to support the bilayer at its edges. More recent studies were based on the formation of glass- or quartz-supported lipid bilayers through incubation with vesicles [38,47,48], as described above, or on the immobilization of erythrocytes to a glass surface and rupturing them to leave an adhered cellular SLB [49].

Intact and infectious influenza virions can be readily labeled with high concentrations of the self-quenching red-emitting dye R18 [50] without compromising infectivity. A similar octadecyl-rhodamine 110 (Rh110), a green-emitting lipophilic dye, has also been used to monitor hemifusion [38], though it is not commercially available. Viral contents can be exogenously labeled with sulforhodamine B (SRB) [38] or with pH-sensitive fluorescein [48] by overnight incubation of the virus particles with high concentrations of the dyes. Loss of these content signals during the fusion process (Figure 1-3B) indicates the opening of a fusion pore large enough for the dye molecules to pass through (SRB or fluorescein) or the acidification of the viral lumen (fluorescein). HA-mediated fusion events are visualized by first immobilizing the intact and labeled virus onto the target membrane, followed by synchronously inducing fusion through a rapid pH drop (Figure 1-3B). Kinetics are extracted as the elapsed time between acidification and the dequenching event for hemifusion, or the time passed between pH drop and loss of content fluorescence for pore formation or acidification.

Floyd *et al.* [38] found that upon decreasing the pH from neutral to a range of pH 4.5-5.3 the rate of hemifusion rapidly becomes faster with lower target pH. When the pH is lowered

Figure 1-3 – *Observing membrane fusion in vitro utilizing fluorescence. Fusogenic proteins are drawn as light brown half-cylinders and docking elements, such as t-SNARE proteins or receptor molecules, are drawn as complementary half-cylinders. Lipophilic dye labeling is shown in red and content labeling is shown in purple.* ***A****) Observation of the transitions from particle docking to hemifusion as implemented by Wessels et al. [47] and others [10,55-58]. Kinetics obtained are: the residency time between docking and the dequenching fusion signal,* t_{Res}*, the 2-dimensional diffusion constant of the lipophilic dye away from the site of fusion, and, in some instances, the time between fusion and the onset of outward dye diffusion,* t_{Delay}*.* ***B****) Transitions from triggering fusion to full fusion with a polymer cushion-supported (black mesh below lipids) planar bilayer as implemented by Floyd et al. [38]. Kinetics obtained are: time between fusion trigger and hemifusion,* t_H*; the time between trigger and full fusion,* t_F*; and the time between hemifusion and full fusion,* t_{HL}*, which is the lifetime of the hemifused state.* ***C****) Transitions from triggering fusion to full fusion to an immobilized target vesicle as implemented by Kyoung et al. [11]. In contrast to (A) and (B), immobilization is achieved through avidin-biotin (brown rectangles and green cones, respectively) interaction rather than through a fusion-related interaction. Accessible kinetics are similar to those in (B).*

*(**Figure 1-3 Continued**)*

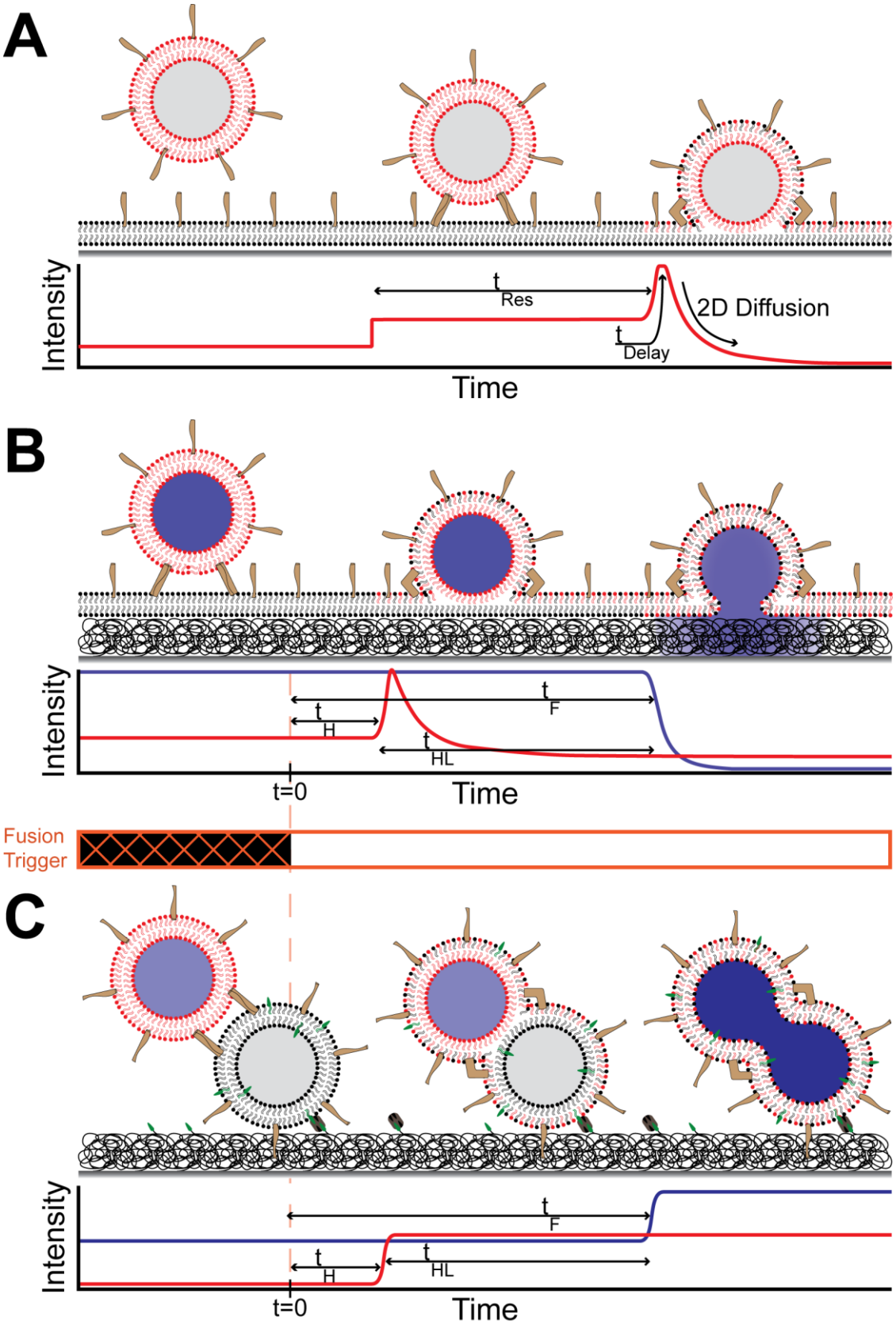

below 4.5, the rate of hemifusion plateaus and is no longer pH dependent. These results confirm a trend initially described by Niles & Cohen [46], but do so with greater sensitivity, greater delineation of receptor binding and fusion, and more robust statistics. In the experiments by Floyd *et al.*, the onset of acidification was directly read out as a loss of fluorescence signal from a buffer-exposed pH-sensitive fluorescein dye that was bound to the target membrane. The waiting-time distributions between the pH drop and the onset of hemifusion showed a clear rise and decay, indicative of multiple biochemical intermediate steps [51,52]. Modeling the waiting times with a gamma distribution allowed for an estimation of both the velocity of the rate-limiting step in the process and the number of rate-limiting steps that are required for hemifusion to occur. While the rate of fusion in the pH-dependent regime varied from 0.03-0.3 s^{-1}, the number of rate-limiting steps remained constant at approximately three. This result was interpreted to be that three HA trimer molecules are required to undergo conformational unfolding and re-folding to mediate hemifusion.

A requirement for three HA trimers to undergo a conformational change and coordinate their actions for fusion to occur was in agreement with theoretical estimates [53], which were based on electrical admittance measurements for fusion of HA-expressing cells with a SLB [54]. A previous study by Imai *et al.* [49] followed the hemifusion kinetics in a similar fashion while varying the concentration of fusion-active HA present on the surface of reconstituted virosomes. With the assumption that assembly of a number, n, of fusogenic HA trimers would be the rate-limiting step in the kinetics, they fit their data to a function of $V = k[HA_{1,2}]^n$, where V is the fusion rate and 'k' is a constant, to obtain $n = 0.9 \pm 0.4$. They interpreted this to indicate that a single HA trimer was necessary and sufficient to mediate fusion, though the waiting-time distributions between acidification and hemifusion showed clear rise-and-decay characteristics. A subsequent re-analysis of their waiting time distributions [59] found that their kinetic data was identical to that of Floyd *et al.* [38] and corroborated the need for three HA trimers to undergo conformational refolding. Unfolding of the HA trimer (*i.e.,* the loop-to-helix transition) has been

calculated to liberate ~125 k_BT (75 kcal/mol) of free energy [60]. If three trimers unfold, only a fraction of the total free energy liberated would need to be recaptured to overcome the initial energetic barrier to hemifusion [42].

Wessels *et al.* [47] observed hemifusion of influenza and Sindbis (an alphavirus with a pH-sensitive Class II fusion protein) viruses by first mixing them with acidic solution, then exposing them to a target bilayer lacking receptor molecules (Figure 1-3A). In this experimental configuration, the fusion proteins unfold in the absence of a bilayer. Exposure of their hydrophobic fusion peptide/loop causes them to briefly immobilize upon the bilayer just prior to fold back and fusion. The viruses were found to differ in residency time between bilayer interaction and fusion. For influenza, the residency time was constant regardless of conditions. For the Sindbis virus, on the other hand, the residency time varied as cholesterol and sphingomyelin were added to the phosphatidylcholine/phosphatidylethanolamine target bilayers. Separately, the Sindbis residency time also varied with pH, increasing five- to ten-fold as conditions were progressively made more acidic. Hence, viruses can exhibit varied kinetic behavior and dependencies starting from a situation in which the fusion proteins have already unfolded and only fold-back is necessary.

Fusion completion by the opening of a full fusion pore, allowing viral content release, was also studied by Floyd *et al.* [38] who employed a dual-labeled virus (rhodamine-110 lipid dye in combination with SRB content dye). The aforementioned hemifusion kinetics were used in conjunction with the waiting time between acidification and content signal dissipation to probe the lifetime of the hemifused state that exists prior to the opening of a full fusion pore (Figures 1B, 1C and 3B). They found that lipid mixing preceded content release and the elapsed time between the two events as measured for individual particles provided a direct measure of the hemifusion lifetime. The dwell-time distributions for these lifetimes were well described by a single-exponential distribution for the full range of pH 3.5 – 5.3, indicating that only a single rate-limiting step gave rise to full membrane merger after hemifusion was established. Importantly,

the transition from the hemifusion intermediate to pore opening is difficult to access by bulk fusion techniques.

A recent study using viral content labeling by Ivanovic *et al.* [48] compared the rate of SRB signal loss to that of signal loss from the pH-sensitive dye fluorescein. The latter allowed for a measurement of the kinetics for acidification of the viral lumen, mediated by the influenza integral membrane proton pump, M2. Acidification of the viral interior is a critical step for release of the viral genome from the structural matrix protein, and internal acidification was hypothesized to take place prior to fusion. Two time points were identified in the single-particle acidification study: the time to onset of internal virus acidification following the external pH drop; and the time from the onset of internal acidification to loss of half the fluorescent signal, termed the dissipation time. The time to onset and to dissipation were compared for the fluorescein and SRB content label and showed that internal viral acidification precedes fusion pore opening, occurring on average about 100 seconds earlier at a target pH of pH 4.5. Using the dissipation time of the fluorescence signal, the authors estimated that the M2 channel transferred between 100 – 400 protons/second into the viral lumen prior to pore opening. Adding the M2 channel-blocking molecule Rimantadine caused the fluorescein loss to become kinetically indistinguishable from SRB loss, suggesting that with inhibited M2, internal acidification took place only after pore formation. Further, the kinetics of SRB loss were indistinguishable from those measured in the presence of fully active M2 proton channels. This observation established that there was no effect of acidification of the matrix on the kinetics of pore formation.

1.5.2 Single-particle viral fusion kinetics in living cells (*in vivo)*

Visualization of the fusion between a virus and a cellular target in living cells (*in vivo*) provides insight into how viral fusion proteins mediate fusion during the initiation of infection in their intended environment. Of great interest and importance is the cellular location where and

the conditions under which membrane fusion occurs for the infection process to functionally begin. These initial steps are well characterized for some viruses, such as influenza, while they are contested for others, such as HIV-1. It is advantageous that in these studies the virus is necessarily added exogenously and so can be labeled and manipulated independent of the target cellular system. The bright lipophilic dye DiD is often used to label the envelope of a number of viruses types, such as influenza, HIV, murine leukemia virus (MLV), and avian sarcoma leucosis virus (ASLV). In some cases, it incorporates to a degree sufficient for dequenching upon membrane fusion [61-63], or can report fusion through disappearance of the fluorescent signal upon near infinite dilution into large cellular membranes [64-66,66].

Measuring fusion kinetics requires a synchronization time point from which the time until lipid mixing (hemifusion) can be measured (Figure 1-4A). A sudden temperature jump starting in a range of 4ºC to 18ºC and rising rapidly to 37ºC has served as synchronization in numerous experiments [61,64,67,68]. Acidification of the extracellular buffer can force pH-dependent viral fusion at the plasma membrane [65]. Alternatively, incubation with ammonium chloride can be used to neutralize all cellular compartments followed by its removal to allow endosomal acidification, thus synchronizing the fusion of internalized virions [69]. Acidification of individual endosomes harboring and transporting viruses can be directly measured by incorporating transmembrane domain-associated GFP proteins to the viral envelope [68,69]. Detection of a pH-drop and subsequent fusion allows for direct kinetic measurements to be made en route to infection, akin to *in vitro* measurements for extraction of pH dependencies.

Tracking the location of a labeled virus particles has provided valuable information regarding entry, subsequent trafficking and egress of new virus particles. These results have been reviewed by Brandenburg & Zhuang [70], along with a discussion of additional labeling techniques and pitfalls. The relevance of trafficking behavior to viral membrane fusion was first described by Lakadamyali *et al.* [61] who followed the movement of intact influenza virus following endosomal internalization. The authors describe a three-stage transport process in

which the virus is first bound to the cell periphery with a low degree of mobility, and then suddenly undergoes a unidirectional, rapid movement toward the cell nucleus (Figure 1-4A). This transport behavior is most often tightly coupled with clathrin-coated pit formation [62]. Finally, the virus experiences intermittent back-and-forth movement finally terminating in membrane fusion with the endosome in the perinuclear region of the cell.

Trafficking of intact dengue virus [63] and ASLV-Env pseudoviruses [66,68] also gave rise to such a three-stage transport behavior, indicating it may be a general pathway followed by viruses during endocytosis. Pseudoviruses are particles having surface proteins from one virus type and a core from a second virus type, for instance HIV-1 Env fusion proteins with a MLV core of matrix proteins with associated genome [67]. Concomitant labeling of the early and late endosomal markers Rab5 and Rab7, respectively, provides information regarding the particular stage of endosomal maturation during which membrane fusion is most likely to occur [69,71]. Single-particle tracking has also shown that the surface receptor to which a virus first binds a target cell can directly affect subcellular transport, the rate of fusion and the compartment where the viral core is released [66,68,69].

To assess infection with single-particle fluorescence assays, it is necessary to separately and simultaneously measure the release of viral contents. Such observations allow for detection of intermediates along the fusion pathway, such as hemifusion and small, nascent fusion pores. Melikyan and colleagues have developed several strategies for detecting content release by incorporating pH-sensitive fluorescent proteins into the lumen of a number of pseudoviruses. One such pseudovirus was constructed to have a palmitylated YFP coating the luminal leaflet of the viral membrane [65]. Small, transient fusion pores were observed to allow mixing between viral contents and the cytosol, but without release of the lipid-bound protein from within the virus. Half of these small and non-expanding fusion pores had surprisingly long lifetimes, lasting for tens of seconds and some as long as several minutes. The size of the fusion pore can also be dependent upon the receptor used by the virus and the compartment in

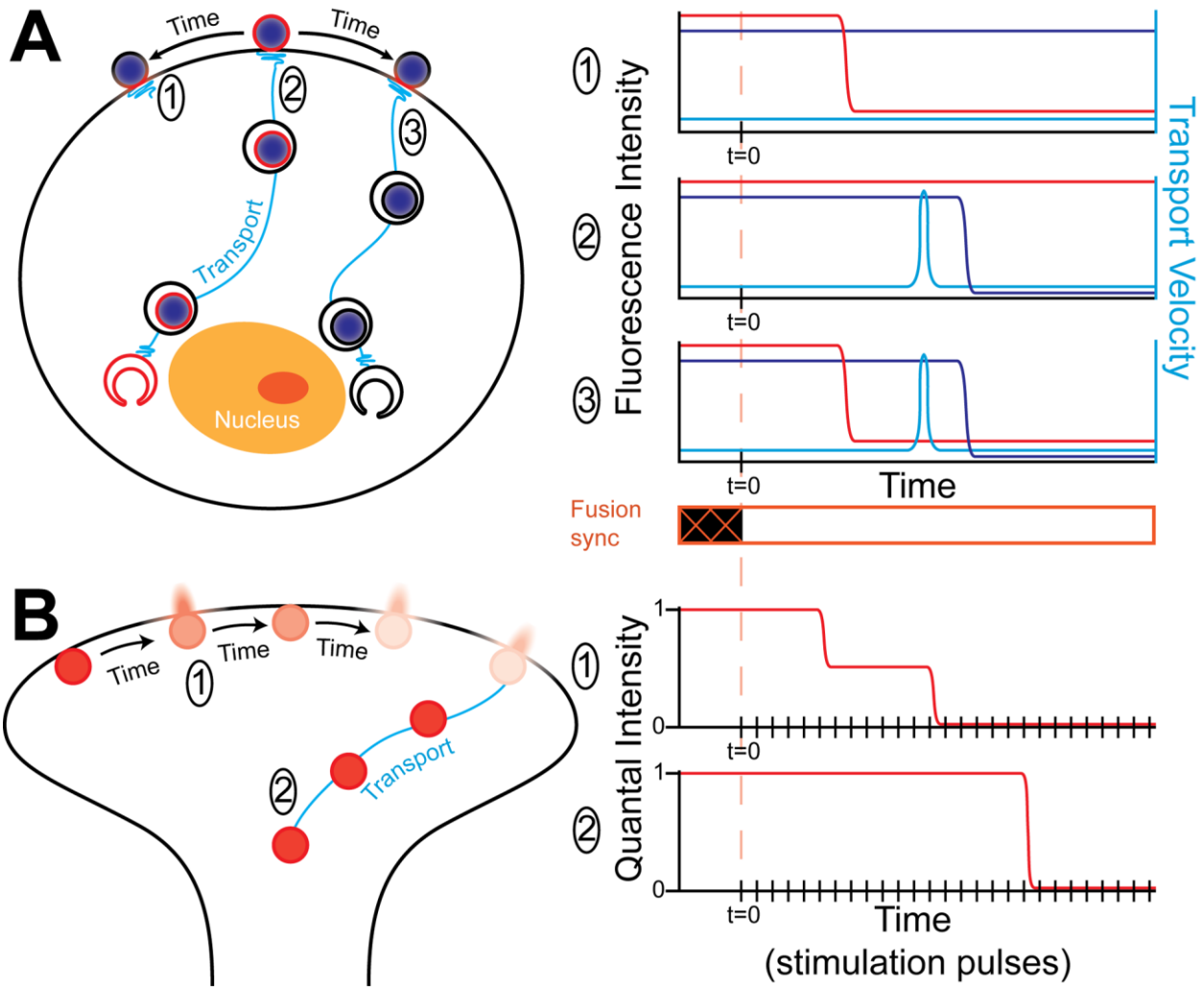

Figure 1-4 – *In vivo visualization of membrane fusion during viral infection and synaptic firing.* ***A****) Lipid mixing and content release during viral infection as utilized by Miyauchi et al. [64] and described in the text. Lipophilic dye to monitor membrane mixing is indicated in red, content labeling in purple and the velocity of viral movement in light blue. Dual-labeled viruses first bind to the target cell at the start of path 2. Once fusion is synchronized the virus may undergo hemifusion with the plasma membrane via paths 1 or 3, or with the endosome via paths 2 or 3 that releases viral contents into the target cell.* ***B****) Subquantal and full quantal content release during synaptic vesicle fusion based upon the experimental design of Aravanis et al. [106,107]. Fluorescence from FM1-43 is shown in red and stimulatory pulses are indicated as vertical hashes in the intensity diagrams. Path 1 depicts kiss-and-run fusion with multiple events and path 2 depicts full fusion event without prior kiss-and-run. Synaptic vesicle transport was not directly followed by particle tracking; rather it was inferred from the fusion kinetics. Quantum dots report kiss-and-run fusion events through a small fluorescence increase [108] rather than signal loss.*

which fusion occurs [66,68]. These observations indicated that pore expansion could be a significant energetic barrier to infection following hemifusion.

Another method used with several pseudoviruses involves use of the MLV Gag protein fused to a GFP in such a way that when the Gag is cleaved during viral maturation, it becomes a freely diffusing fluorescent viral-content marker [64,66-69,72]. A recent study using this type of pseudovirus [64] provided strong support that the pH-independent HIV-1 Env proteins mediate an endosomal route for viral entry and fusion, similar to pH-dependent viral surface proteins like HA. Miyauchi *et al.* [64] followed the fusion pathway through the disappearance of either the DiD envelope dye, which indicated hemifusion with the cellular plasma membrane, or the GFP content marker, which indicated content release (Figure 1-4A); fusion with an endosome resulted in a persistent DiD signal and loss of the content signal. Using a number of HIV-1 pseudoviruses and one fully infectious strain, they observed many viruses fusing with the plasma membrane, but not losing their contents (Figure 1-4A.1), while others had a persistent lipid signal and a rapid content loss (Figure 1-4A.2). Importantly, the viruses exhibiting plasma-membrane hemifusion often showed limited movement, while those losing their contents showed transport towards the cell nucleus before content loss and a continued movement of the lipid dye afterward, observations consistent with endosomal trafficking and perinuclear viral-genome release. A very few number of viruses showed loss of both signals (Figure 1-4A.3), with a considerable delay separating content release from lipid mixing. The delay time between lipid mixing and content release was consistent with the time measured as being necessary for endocytosis (10-15 minutes). These observations were supported with experiments providing a cellular read out to indicate successful viral-core transfer. Moreover, a long-lived intermediate state following HIV-1 Env mediated lipid mixing and preceding content loss had been reported previously [67], consistent with the observations of Miyauchi *et al.*

As further evidence of HIV-1 endosomal uptake and fusion, Miayuchi *et al.* [64] and a follow-up study by de la Vega *et al.* [72] showed that inhibition of the dynamin GTPase (the protein responsible for scission of clathrin-coated pits from the plasma membrane during endocytosis) abolished viral content release, but did not inhibit lipid mixing with the plasma membrane. Together, these studies indicated that the HIV-1 Env fusion protein can mediate the transition into a long-lived hemifusion state with the plasma membrane before the virus is internalized, but that a functional fusion pore is not created at the plasma membrane, rather within the endosome.

Taken together, these studies demonstrate that the intermediates in viral fusion as derived from biophysical, biochemical and structural data are experimentally resolvable at a single-particle level. The kinetic insight obtained with these studies has contributed significantly to our understanding of the molecular mechanisms by which fusion proteins catalyze fusion. Moreover, additional processes, such as acidification of the viral lumen, can occur in parallel with traversing of the intermediate physical states leading to membrane fusion. Results also indicate that there is a coordination between viral surface proteins that must occur for membrane fusion to occur and that the kinetics for coordination vary with pH regimes. Within a cellular context, endosomal trafficking and maturation appear to provide receptor-dependent pathways for productive viral fusion. Such deep understanding of the molecular nature of fusion intermediates may prove crucial to relate *in vivo* and *in vitro* observations as well as to develop novel antiviral therapeutics that neutralize specific intermediates along the fusion pathway .

1.6 SNARE-mediated membrane fusion

Recently, fluorescence microscopy has also been applied extensively to the study of fusion of membranes driven by the SNARE machinery in eukaryotes. SNARE proteins are responsible for the fusion of synaptic vesicles with the neuronal plasma membrane, supporting rapid action potential-triggered exocytosis of neurotransmitters into the synaptic cleft. Function

of these proteins has been the subject of thorough and recent reviews by Brunger and colleagues [73,74], only a brief outline of how they mediate fusion is given here.

The SNARE proteins are divided into two groups: 'target' t-SNARE proteins anchored to the luminal side of the plasma membrane and 'vesicle' v-SNARE proteins anchored to the synaptic vesicles, which contain neurotransmitters. The principal t-SNARE proteins are syntaxin-1 (Syx) and SNAP25, while synptobrevin-2 (Syb, also known as VAMP, Vesicle Associated Membrane Protein) is the principal v-SNARE. Together, these three proteins are considered the functional core responsible for mediating membrane fusion. Synaptotagmin-1 (Syt) and complexin are two important protein factors that interact with the SNARE proteins and have been incorporated into single-particle SNARE fusion studies; the factors Munc13 and Munc18, though critical for vesicle priming [75], have not yet been included in such studies. Syt is the calcium (Ca^{2+}) sensor required for fast synchronous release of neurotransmitters and complexin is a modulator regulating SNARE-driven exocytosis. For fusion to occur, SNARE proteins first associate with each other to form a tetra-alpha-helical complex comprised of two SNAP25 proteins, one Syx and one Syb that, together, link the v- and t-membranes in close proximity. In response to a rapid influx of Ca^{2+} ions into a neuron following the arrival of an action potential, the SNARE proteins re-fold upon each other in a fashion enhanced by the concerted action of additional protein factors. These interactions bring the apposed membranes into close proximity and facilitate their fusion, releasing neurotransmitters into the synaptic junction for action potential propagation.

Neurotransmitter release has been demonstrated to occur in as little as 0.2 milliseconds following an action potential [76]. Additionally, neurons can be required to transmit high-frequency signals rapidly and continuously. There are two principal modes by which a vesicle can fuse during exocytosis. One is complete fusion, where the vesicle fully collapses to become continuous with the plasma membrane and simultaneously releases its entire contents [77]. These vesicles are replenished by *de novo* synthesis coupled with endocytotic recycling.

Alternatively there is “kiss-and-run” fusion where the exocytotic vesicle does not undergo complete fusion, but rather releases a portion of its contents followed by fusion pore closure [78]. The kinetics and intermediates involved in both modes of fusion are amenable to fluorescence microscopy and their study paints a picture of the bilayer rearrangements and vesicle cycling that occur during action potential propagation.

1.6.1 Single-particle SNARE fusion kinetics studied *in vitro*

In vitro studies attempting to reconstitute the SNARE fusion process have traditionally been performed using bulk lipid-mixing assays. Recent investigations are moving these studies onto the microscope to observe the vesicles fusing individually. Single-vesicle fusion studies have the advantage over ensemble-averaging experiments in their ability to directly differentiate full fusion and content mixing from hemifusion and lipid mixing. This differentiation avoids the misinterpretation of implying content mixing by only monitoring lipid mixing, a potential pitfall discussed elsewhere [12,79]. As well, these studies can clearly distinguish docking of a v-SNARE vesicle to a t-SNARE membrane from the subsequent fusion event. Docking is observed as the rapid increase of fluorescence from the background at a localized spot as the vesicle becomes immobilized upon the target surface. Lipophilic dyes used *in vitro* for labeling the vesicle bilayer are often PE-modified lipids such as, TMR-PE/TRITCH-PE [57,58], R18 [10], and Rh-PE [55,56,80-83]. These dyes can indicate lipid mixing through fluorescence dequenching (Figure 1-2A). Alternatively, DiD and DiI can be used to follow lipid mixing measured as an increase in FRET [84-87] (Figure 1-2C) or as a dequenching signal [11,12]. Here, we discuss in detail two experimental geometries developed to observe the fusion reaction as mediated by SNARE’s – one using a planar SLB target and the other using tethered target vesicles.

A planar SLB formed upon an hydrophilic quartz, glass, or polymer substrate allows observation of SNARE-dependent fusion between the SLB and individual fusogenic vesicles

(Figures 3A and 3B). The t-SNARE proteins are typically contained in the target planar SLB, while the v-SNARE protein is present in small unilaminar vesicles (SUV) that bind and subsequently fuse to the SLB. Dequenching signal from lipid dye in the v-SNARE vesicles is a common read out for lipid mixing since dye dilution into the SLB can easily be visualized. The contents of these vesicles have been filled with fluorescent dyes such as calcein [10,88], which reports on the opening of a fusion pore through dequenching followed by fluorescence signal loss. The continuity of the SLB can be monitored within the experimental setup by labeling the SLB using NBD-PE [80,81,83] and performing FRAP measurements immediately prior to fusion experiments. Fusion kinetics are measured as the elapsed time between docking and dequenching and require rapid image acquisition, with frame acquisition times as low as 1-5 milliseconds [10,55] (Figure 1-3A).

A consensus remains to be established for the results produced from planar SLB-based experiments. Fusion was observed in some experimental setups in the absence of the *in vivo* obligate protein SNAP25 [10,58,88] and in the absence of Ca^{2+} [55,58,88]. Bowen *et al.* [88] demonstrated that the fusion they observed was the result of laser-induced heating, though this may not be the case for the other works cited. Their data also indicated that SNAP25 was required to form stable interaction between Syx and Syb prior to fusion. There are, however, a number of key observations were shared between SLB-based studies. Hemifusion to the SLB was measured to occur 5-20 milliseconds after docking to the bilayer [10,55,56]. Release of a content dye to indicate full fusion was measured to occur ~100 ms after lipid mixing, but this observation was convoluted with vesicle rupture that released content dye into the space above a SLB rather than below it [10]. Using polarized laser illumination in a TIRF microscope, Kiessling *et al.* [56] observed the topology changes of the vesicle bilayer as it fused with the planar target. They found that the vesicle becomes flattened along the substrate only 8 ms after fusion begins. While fast, these kinetics are still much slower than the 0.2 ms response observed in living cells [76]. Phospholipid head groups and their ratios appear to have an effect

both on docking and fusion efficiency, but there are still differences reported between different experimental designs and setups (discussed in [82]). Finally, SLB-based single-particle studies have estimated that 5-10 SNARE complexes are needed to induce fusion [55,83], though estimates of as high as 15 complexes exist in the literature [89]. A bulk fusion study measuring only lipid mixing without content mixing found, in contrast, that a single SNARE complex could give rise to lipid mixing [90].

In the tethered-vesicle experimental approach, first developed by Yoon *et al.* [84] (Figure 1-3C) separate populations of v- and t-SNARE containing vesicles are observed while fusing together. Either the v-SNARE [84-86,91] or t-SNARE [11,12] vesicles are immobilized upon a substrate with no preference in terms of effect [87]. Glass or quartz substrates are coated with a PEG/biotinylated-PEG layer to reduce non-specific interactions, wherein the sparse amounts of biotin-PEG enable vesicle immobilization through neutravidin-mediated binding with biotinylated lipids in the vesicles. Lipid mixing is observed via TIRF microscopy as a FRET signal between DiI and DiD (Figure 1-2C), though scanning confocal microscopy has also been used [92]. Fusion pore opening can be followed through dequenching of SRB [11] without outward dissipation. A novel strategy to follow the expansion of a fusion pore utilizes a DNA hairpin encapsulated in the v-SNARE vesicles [91,93,94]. The hairpin is labeled at both ends such that when it folds upon itself, the two FRET-pair dyes are in close proximity and give a high FRET signal. Upon pore expansion a complementary DNA strand present in the t-SNARE vesicles binds to and opens the hairpin, alleviating the donor dye quenching on a time scale much faster than the pore expansion kinetics [91] and indicating that the vesicles are joined by a fusion pore at least 2 nm in diameter [93]. This labeling strategy allows for separation of lipid mixing, nascent pore opening and subsequent pore expansion.

The tethered-vesicle experimental geometry has recapitulated some of the requirements and observations seen in *in vivo* neuronal SNARE fusion. Specifically, the Ca^{2+} induction [11,12,85,93]and SNAP25 [12,85,87] dependency of fusion has been reproduced by several

groups. As well, the hemifusion intermediate has been interpreted from the FRET efficiency data of lipid mixing [84,85,93]. Lipid mixing after docking of one vesicle to another showed heterogeneity with two kinetic populations. When coupled with the SNARE-related factors complexin and Syt, the time constant for lipid mixing of the fast population was typically in the range of 100-950 ms [11,12,85,86,92]. These times are likely upper bounds on the fast population set by the experimental equipment used, since the video acquisition rate was lower than that achieved in the planar SLB experiments [11,12]. The slower kinetic component was on the order of 3-10 seconds and occurred upon Ca^{2+} triggering of the SNARE proteins in the absence of the complexin and Syt factors [11,85]. In agreement with these kinetic measurements, docking was found to be the rate-limiting step in the SNARE fusion process [87,92]. Docking kinetics between complementary SNARE vesicles were found to be enhanced 10- to 100-fold by the SNARE-related factors complexin and Syt [11,85,92].

Of particular note, Kyoung *et al.* [11] enhanced the tethered-vesicle design to include a SRB content label for the v-SNARE vesicles, which allows for direct read out of content mixing, as well as a Cascade Blue fluorescent signal to indicate the arrival of the fusion-inducing Ca^{2+} solution (Figure 1-3C). Within the tethered-vesicle design, they successfully reproduced fast content release kinetics on the millisecond time-scale that was both Ca^{2+} induced and dependent on the presence of both complexin and Syt. Extraction of waiting times between Ca^{2+} arrival and hemifusion or content release allowed for a kinetic analysis of the fusion process. They found that in the presence of the Syt and complexin factors, a “rapid burst” constituting simultaneous lipid and content mixing was prevalent. This phenomenon was characterized by a waiting-time distribution for both fluorescent signals that was well described by a double exponential, indicative of two populations with each displaying different kinetics. The rapidly fusing portion constituted a majority of the vesicle population and displayed a fusion time constant of 250 milliseconds, approximately equal to the frame rate used to capture the fusion movies. Because of this experimental limitation, intermediates between lipid mixing and

content release were not observable. The slower portion of the population displayed a time constant of ~1.5 seconds. Without Syt and complexin, however, the SNARE proteins alone could not efficiently generate these "rapid bursts" or the two kinetic populations. Instead, the waiting-time distributions were described by a single exponential with a rate constant of ~3 seconds. A subsequent study by Diao *et al.* [12] used a similar experimental design with a more physiological 250 mM Ca^{2+} and a shorter frame exposure time of 100 milliseconds, but still did not resolve an intermediate state between lipid and content mixing. Addition of the complexin protein enhanced the rapid bursting behavior and the emergence of two kinetic populations of fusing vesicles. In the presence of SNARE and Syt proteins only, however, a larger number of long-lived hemifusion intermediates were observed that did not evolve into full fusion endpoints.

Enhancement of productive fusion pathways by accessory proteins is supported by recent tethered-vesicle experiments done by Lai *et al.* [93]. Therein the authors report that the Syt protein interacts with SNARE proteins to significantly enhance vesicle docking, hemifusion and the opening of a nascent pore large enough for SRB molecules to pass through. Moreover, using the aforementioned FRET-labeled DNA hairpin, they to found that pore expansion is 13-fold slower than nascent fusion pore opening and that expansion is very inefficient in the absence of Syt or Ca^{2+}. Incorporating complexin into the fusion scheme caused the rate of nascent pore opening to increase 21% and the rate of pore expansion to double. Thus productive fusion pore opening and expansion are modulated, at least, by the accessory proteins Syt and complexin, which can enhance full fusion both in terms of rate and efficiency.

1.6.2 Single exocytotic vesicle fusion in live hippocampal neuronal cells

Fluorescence microscopy-based kinetic measurements have also proven insightful for the *in vivo* study of exocytosis. Methods to fluorescently label exocytotic vesicles in living cells are well reviewed elsewhere by Ge *et al.* [95] and by Keighron *et al.* [96]. These methods have been implemented in monitoring processes closely related to exocytosis, such as endocytosis

[97,98], the role of other key cellular components on exocytosis [99], and non-synaptic exocytosis [100-103]. For continuity with the previous section, the following discussion will focus on synaptic exocytosis in hippocampal neurons and primarily on the kinetic discernment between kiss-and-run fusion and complete fusion wherein the synaptic vesicle fully collapses.

Synaptic vesicles are commonly labeled with organic styryl dyes, such as FM1-43, that have proven powerful tools for studying exocytosis in living cells [95,96]. For instance, FM1-43 was used to determine that 1/3 – 1/4 of the vesicles at the synapse are located in close proximity to the plasma membrane and belong to a readily releasable pool of vesicles, while the remaining vesicles belong to a recruitable reserve pool more distal from the synapse [104,105]. As mentioned previously, these dyes exhibit enhanced fluorescence in hydrophobic environments, but also reversibly departition from membranes into the aqueous vesicular lumen. This behavior allows the dissipation of the dye signal to report on the formation of a fusion pore rather than lipid mixing. Aravanis *et al.* [106,107] used FM1-43 in hippocampal nerve cells, where exocytotic vesicles are clustered into synaptic boutons of approximately 30 vesicles. Using a minimum labeling protocol, they observed individual synaptic vesicles using epifluorescence microscopy. Consistent with other reports of this system [97,109], each vesicle contained a “quantal” amount of dye such that the fluorescent signals from individual vesicles was comparable. Fusion of individual vesicles to the plasma membrane was observed as a loss of fluorescent signal from the vesicle in response to a physiologically relevant 10-Hz train of stimulating electrical pulses (Figure 1-4B).

Aravanis *et al.* [106,107] found that upon stimulation, 85% of the fusing vesicles lost a sub-quantal portion of their fluorescence signal in a single fusion event (Figure 1-4B.1), while a minority of 15% lost their entire fluorescence signal in a single event (Figure 1-4B.2). Analysis of dwell times between initial stimulation and 20% fluorescence loss indicated that the majority of observed fusion events arose from vesicles in the readily releasable pool of vesicles. Further, the times over which fluorescence dropped from 20% to 80% indicated that the vesicles

did not experience complete collapse during fusion. By unambiguously following the behavior of individual particles, they observed single vesicles undergoing multiple kiss-and-run fusion events (Figure 1-4B.1). The latency periods (*i.e.*, number of stimuli) for the first and second fusion events were ~5 and ~7 stimulating electrical pulses, respectively. Thus it appeared that a vesicle could undergo repeated fusion events following a rapid retrieval or "re-priming" event, which retained large amounts of vesicular contents and caused the latency of a second fusion event to be slightly longer than for the first.

Slow, sub-quantal fluorescence loss was confirmed by Richards *et al.* [19] using a similar experimental design, but with elevated potassium concentration as a stimulus. Their calculations estimated that the kiss-and-run fusion pore had a diameter of ~1 nm. While transient, these non-complete fusion events still give rise to lipid-mixing between the vesicle and the plasma membrane [20]. Sub-quantal content loss is stimulation dependent, however, and either disappears or is unresolvable at high-frequency stimulation of 100 Hz, where only full quantal release was observed [110].

Zhang *et al.* [108] incorporated bright quantum dots (Qdot) to label hippocampal synaptic vesicles and directly detected both kiss-and-run and complete fusion. In contrast to loss of FM1-43 fluorescence signal, the Qdot emission intensity increased ~15% upon opening of a kiss-and-run fusion pore, due to neutralization of the acidic intravesicular pH upon pore opening. This persistent fluorescence signal allowed Zhang *et al.* to resolve multiple kiss-and-run fusion events in single vesicles with improved signal-to-noise and extended observation times. Kiss-and-run events were easily distinguished from complete fusion events, which were observed as a full loss of fluorescent signal and subsequent diffusion of the Qdot away from a fusion site. They found that, initially, kiss-and-run fusion was the predominant type of fusion and arose from the readily releasable pool of vesicles, but that complete fusion became dominant after extended stimulation. Kinetically, kiss-and-run fusion events had shorter latencies than complete fusion at stimulation frequencies of 0.1 and 10 Hz, though vesicles exhibiting kiss-and-

run fusion would eventually undergo complete fusion. For the vesicles exhibiting kiss-and-run fusion, those undergoing the largest number of kiss-and-run events prior to complete fusion displayed the shortest latency period between subsequent events. Together, the observations of Zhang *et al*. indicate that the readily releasable pool of vesicles favor kiss-and-run fusion that have shorter latency periods. Once these vesicles are depleted and replenished by vesicles from a reserve pool, the likelihood of a kiss-and-run event diminishes and the full fusion events displaying a longer latency become predominant.

A recent study measured a lower bound on the number of SNARE complexes required for exocytotic fusion *in vivo*. Sinha *et al.* [111] fused the specialized pH-sensitive fluorescent protein pHluorin [25] to the luminal portion of the v-SNARE Syb2 protein. These pHl-Syb2 proteins readily incorporated into hippocampal neuron synaptic vesicles. Initially, fluorescence of the pHluorin was quenched within the acidic synaptic vesicle, but stimulation-induced fusion caused a quantal fluorescence increase upon neutralization of the acidic lumen. Plotting the distributions of fluorescence increases showed several equally spaced peaks and photobleaching analysis indicated that each peak corresponded to a single pHl-Syb2 protein within the synaptic vesicles. Measurements made with neuronal cells containing only pHl-labeled Syb2 proteins resulted in a multi-peaked distribution lacking a peak at a quantum of one, whereas neurons having both labeled and unlabeled Syb2 gave a distribution with a distinct one-quantum peak. Sinha *et al.* thus concluded that a minimal fusion SNARE complex required two Syb2 proteins. Because each assembled SNARE complex is estimated to have ~35 k_BT (21 kcal/mol) [112] of energy available, the coordinated effect of two Syb2 proteins would be more than sufficient to surmount the initial energy barrier separating the initial barriers to fusion (see Introduction).

Taken together, these studies of SNARE-mediated fusion have identified at least two regimes of fusion kinetics that are found *in vivo* and two regimes *in vitro*. The *in vivo* situation appears to be linked to a shift from vesicles initially present at the membrane to the recruitment

of vesicles from the cellular interior, transitioning from shorter latency periods to longer ones. The *in vitro* regimes are likely tied to the dependencies of the SNARE process on accessory proteins. These results hint towards regulatory processes that control these fusion machines to appropriately enhance their fusogenicity or to restrict their catalytic potential, *i.e.* full vesicular membrane merger, and allow only partial content release.

1.7 Outlook

The experimental approaches described here provide a solid foundation for moving forward on a number of fronts. With respect to further investigations into general aspects of membrane fusion, lipid dependencies for the various fusion systems can be probed in a straightforward manner. Target bilayers studied in *in vitro* systems can be readily manipulated to incorporate a range of lipid types and these lipids can be exogenously added and incorporated into *in vivo* systems. Lipids such as lysophosphatidylcholine are considered to inhibit HA-mediated cell-cell fusion through a change in membrane curvature [113]. Demonstration of this effect in single-particle fusion assays of both HA-fusion and SNARE fusion would establish the role of curvature as a general property affecting protein-mediated fusion as catalyzed by the fully intact systems. Cholesterol is another molecular player whose role in fusion has not been fully clarified, being required for some viruses to fuse and irrelevant for others. Single-particle assays could potentially distinguish if an effect of cholesterol arises from requirements regarding lipid arrangements or if the effect arises at the level of interactions between the fusion protein and proximal lipid components. With respect to experimental advances, differentiation of distal leaflet mixing from proximal leaflet mixing at the single-particle level would provide another level of understanding regarding expansion of a lipidic fusion pore.

Concerning fusion-specific scenarios, mutational studies in conjunction with single-particle fusion detection can firmly establish the role of environmental sensitivities and of critical amino-acid residues in governing the fusion behavior . Relatedly, live-cell single-particle fusion

studies can aid in delineating the role that additional cellular factors play in modulating fusion mechanisms. SNARE-related fusion relies on intracellular transport and signaling pathways to shift appropriately between the readily releasable pool and reserve pool of fusion vesicles. Viral fusion, too, can require dynamic cellular components, for instance the molecular trigger causing pH-independent HIV-1 Env mediated content release within an endosome that is not present at the cellular surface.

Technical advances can also play a role, most predominantly in the area of automated data selection. All single-particle studies require, first, experimental optimization to obtain high signal-to-noise ratios in the recorded fusion movies. Once this initial step is achieved, an equally difficult challenge is presented in the extraction and analysis of the fluorescence time trajectories. These challenges can require extensive computer programing, frequently supplemented by manual selection of fusion events, an analysis strategy that can take days to weeks once a successful experimental run is obtained [81,94]. While development of automated analysis algorithms are time consuming, the result can decrease analysis time up to 100-fold [114]. Some steps toward this automatization have been taken with live-cell studies of exocytosis and are reviewed briefly by Burchfield *et al.* [115]. Similarities in the fluorescence signal obtained for both *in vitro* and *in vivo* studies of viral and SNARE fusion (Figure 1-2; and compare Figure 1-3 with Figure 1-4) could allow for unification of analysis strategies among the diverse areas of study and contributing research groups. Progress on this front, in particular, has the potential to drive the field forward by facilitating many more experimental permutations to be performed within a single study, provided by less time-consuming and more consistent data analysis.

1.8 References

1. Chernomordik LV, Kozlov MM. (2003) Protein-lipid interplay in fusion and fission of biological membranes. Annu Rev Biochem 72: 175-207.

2. Markvoort AJ, Marrink SJ. (2011) Lipid acrobatics in the membrane fusion arena. Curr Top Membr 68: 259-294.

3. Efrat A, Chernomordik LV, Kozlov MM. (2007) Point-like protrusion as a prestalk intermediate in membrane fusion pathway. Biophys J 92: L61-L63.

4. Kuzmin PI, Zimmerberg J, Chizmadzhev YA, Cohen FS. (2001) A quantitative model for membrane fusion based on low-energy intermediates. Proc Natl Acad Sci U S A 98: 7235-40.

5. Jackson MB. (2011) Inferring structures of kinetic intermediates in ca(2+)-triggered exocytosis. Curr Top Membr 68: 185-208.

6. Melikyan GB, White JM, Cohen FS. (1995) GPI-anchored influenza hemagglutinin induces hemifusion to both red blood cell and planar bilayer membranes. J Cell Biol 131: 679-691.

7. Chernomordik LV, Kozlov MM. (2005) Membrane hemifusion: Crossing a chasm in two leaps. Cell 123: 375-382.

8. Niles WD, Cohen FS. (1991) Fusion of influenza virions with a planar lipid membrane detected by video fluorescence microscopy. J Gen Physiol 97: 1101-1119.

9. Blumenthal R, Gallo SA, Viard M, Raviv Y, Puri A. (2002) Fluorescent lipid probes in the study of viral membrane fusion. Chem Phys Lipids 116: 39-55.

10. Wang T, Smith EA, Chapman ER, Weisshaar JC. (2009) Lipid mixing and content release in single-vesicle, SNARE-driven fusion assay with 1-5 ms resolution. Biophys J 96: 4122-4131.

11. Kyoung M, Srivastava A, Zhang Y, Diao J, Vrljic M, et al. (2011) In vitro system capable of differentiating fast Ca2+-triggered content mixing from lipid exchange for mechanistic studies of neurotransmitter release. Proc Natl Acad Sci U S A 108: E304-E313.

12. Diao J, Grob P, Cipriano DJ, Kyoung M, Zhang Y, et al. (2012) Synaptic proteins promote calcium-triggered fast transition from point contact to full fusion. elife 1: e00109.

13. Wombacher R, Cornish VW. (2011) Chemical tags: Applications in live cell fluorescence imaging. J Biophotonics 4: 391-402.

14. Dieterich DC. (2010) Chemical reporters for the illumination of protein and cell dynamics. Curr Opin Neurobiol 20: 623-630.

15. Reymond L, Lukinavicius G, Umezawa K, Maurel D, Brun MA, et al. (2011) Visualizing biochemical activities in living cells through chemistry. Chimia (Aarau) 65: 868-871.

16. Cairo CW, Key JA, Sadek CM. (2010) Fluorescent small-molecule probes of biochemistry at the plasma membrane. Curr Opin Chem Biol 14: 57-63.

17. Yano Y, Matsuzaki K. (2009) Tag-probe labeling methods for live-cell imaging of membrane proteins. Biochim Biophys Acta 1788: 2124-2131.

18. Bissig C, Johnson S, Gruenberg J. (2012) Studying lipids involved in the endosomal pathway. Methods Cell Biol 108: 19-46.

19. Richards DA, Bai J, Chapman ER. (2005) Two modes of exocytosis at hippocampal synapses revealed by rate of FM1-43 efflux from individual vesicles. J Cell Biol 168: 929-939.

20. Taraska JW, Almers W. (2004) Bilayers merge even when exocytosis is transient. Proc Natl Acad Sci U S A 101: 8780-8785.

21. Chudakov DM, Matz MV, Lukyanov S, Lukyanov KA. (2010) Fluorescent proteins and their applications in imaging living cells and tissues. Physiol Rev 90: 1103-1163.

22. Day RN, Davidson MW. (2009) The fluorescent protein palette: Tools for cellular imaging. Chem Soc Rev 38: 2887-2921.

23. Wiedenmann J, Oswald F, Nienhaus GU. (2009) Fluorescent proteins for live cell imaging: Opportunities, limitations, and challenges. IUBMB Life 61: 1029-1042.

24. Shaner NC, Steinbach PA, Tsien RY. (2005) A guide to choosing fluorescent proteins. Nat Methods 2: 905-909.

25. Miesenböck G, De Angelis DA, Rothman JE. (1998) Visualizing secretion and synaptic transmission with pH-sensitive green fluorescent proteins. Nature 394: 192-195.

26. Fish KN. (2009) Total internal reflection fluorescence (TIRF) microscopy. Curr Protoc Cytom Chapter 12: Unit12.18.

27. Mattheyses AL, Simon SM, Rappoport JZ. (2010) Imaging with total internal reflection fluorescence microscopy for the cell biologist. J Cell Sci 123: 3621-3628.

28. Millis BA. (2012) Evanescent-wave field imaging: An introduction to total internal reflection fluorescence microscopy. Methods Mol Biol 823: 295-309.

29. Yildiz A, Forkey JN, McKinney SA, Ha T, Goldman YE, et al. (2003) Myosin V walks hand-over-hand: Single fluorophore imaging with 1.5-nm localization. Science 300: 2061-2065.

30. Manley S, Gunzenhauser J, Olivier N. (2011) A starter kit for point-localization super-resolution imaging. Curr Opin Chem Biol 15: 813-821.

31. Czolkos I, Jesorka A, Orwar O. (2011) Molecular phospholipid films on solid supports. Soft Matter 7: 4562-4576.

32. Richter RP, Berat R, Brisson AR. (2006) Formation of solid-supported lipid bilayers: An integrated view. Langmuir 22: 3497-3505.

33. Nollert P, Kiefer H, Jahnig F. (1995) Lipid vesicle adsorption versus formation of planar bilayers on solid surfaces. Biophys J 69: 1447-1455.

34. Brian AA, McConnell HM. (1984) Allogeneic stimulation of cytotoxic T cells by supported planar membranes. Proc Natl Acad Sci U S A 81: 6159-6163.

35. Wagner ML, Tamm LK. (2000) Tethered polymer-supported planar lipid bilayers for reconstitution of integral membrane proteins: Silane-polyethyleneglycol-lipid as a cushion and covalent linker. Biophys J 79: 1400-1414.

36. Roder F, Waichman S, Paterok D, Schubert R, Richter C, et al. (2011) Reconstitution of membrane proteins into polymer-supported membranes for probing diffusion and interactions by single molecule techniques. Anal Chem 83: 6792-6799.

37. Rawle RJ, van Lengerich B, Chung M, Bendix PM, Boxer SG. (2011) Vesicle fusion observed by content transfer across a tethered lipid bilayer. Biophys J 101: L37-L39.

38. Floyd DL, Ragains JR, Skehel JJ, Harrison SC, van Oijen AM. (2008) Single-particle kinetics of influenza virus membrane fusion. Proc Natl Acad Sci U S A 105: 15382-15387.

39. Elender G, Kuhner M, Sackmann E. (1996) Functionalisation of Si/SiO2 and glass surfaces with ultrathin dextran films and deposition of lipid bilayers. Biosens Bioelectron 11: 565-577.

40. Skehel JJ, Cross K, Steinhauer D, Wiley DC. (2001) Influenza fusion peptides. Biochem Soc Trans 29: 623-626.

41. Harrison SC. (2005) Mechanism of membrane fusion by viral envelope proteins. Adv Virus Res 64: 231-261.

42. Harrison SC. (2008) Viral membrane fusion. Nat Struct Mol Biol 15: 690-8.

43. White JM, Delos SE, Brecher M, Schornberg K. (2008) Structures and mechanisms of viral membrane fusion proteins: Multiple variations on a common theme. Crit Rev Biochem Mol Biol 43: 189-219.

44. Georgiou GN, Morrison IE, Cherry RJ. (1989) Digital fluorescence imaging of fusion of influenza virus with erythrocytes. FEBS Lett 250: 487-492.

45. Lowy RJ, Sarkar DP, Chen Y, Blumenthal R. (1990) Observation of single influenza virus-cell fusion and measurement by fluorescence video microscopy. Proc Natl Acad Sci U S A 87: 1850-1854.

46. Niles WD, Cohen FS. (1991) The role of N-acetylneuraminic (sialic) acid in the pH dependence of influenza virion fusion with planar phospholipid membranes. J Gen Physiol 97: 1121-1140.

47. Wessels L, Elting MW, Scimeca D, Weninger K. (2007) Rapid membrane fusion of individual virus particles with supported lipid bilayers. Biophys J 93: 526-538.

48. Ivanovic T, Rozendaal R, Floyd DL, Popovic M, van Oijen AM, et al. (2012) Kinetics of proton transport into influenza virions by the viral M2 channel. PLoS One 7: e31566.

49. Imai M, Mizuno T, Kawasaki K. (2006) Membrane fusion by single influenza hemagglutinin trimers. kinetic evidence from image analysis of hemagglutinin-reconstituted vesicles. J Biol Chem 281: 12729-12735.

50. Hoekstra D, de Boer T, Klappe K, Wilschut J. (1984) Fluorescence method for measuring the kinetics of fusion between biological membranes. Biochemistry 23: 5675-5681.

51. Loparo JJ, van Oijen AM. (2009) Single-molecule enzymology. In: Hinterdorfer P, van Oijen A, editors. Handbook of Single-Molecule Biophysics. New York, NY: Springer New York. pp. 165-182.

52. Floyd DL, Harrison SC, van Oijen AM. (2010) Analysis of kinetic intermediates in single-particle dwell-time distributions. Biophys J 99: 360-366.

53. Bentz J. (2000) Minimal aggregate size and minimal fusion unit for the first fusion pore of influenza hemagglutinin-mediated membrane fusion. Biophys J 78: 227-245.

54. Melikyan GB, Niles WD, Cohen FS. (1995) The fusion kinetics of influenza hemagglutinin expressing cells to planar bilayer membranes is affected by HA density and host cell surface. J Gen Physiol 106: 783-802.

55. Domanska MK, Kiessling V, Stein A, Fasshauer D, Tamm LK. (2009) Single vesicle millisecond fusion kinetics reveals number of SNARE complexes optimal for fast SNARE-mediated membrane fusion. J Biol Chem 284: 32158-32166.

56. Kiessling V, Domanska MK, Tamm LK. (2010) Single SNARE-mediated vesicle fusion observed in vitro by polarized TIRFM. Biophys J 99: 4047-4055.

57. Liu T, Wang T, Chapman ER, Weisshaar JC. (2008) Productive hemifusion intermediates in fast vesicle fusion driven by neuronal SNAREs. Biophys J 94: 1303-1314.

58. Liu T, Tucker WC, Bhalla A, Chapman ER, Weisshaar JC. (2005) SNARE-driven, 25-millisecond vesicle fusion in vitro. Biophys J 89: 2458-2472.

59. Dobay MP, Dobay A, Bantang J, Mendoza E. (2011) How many trimers? modeling influenza virus fusion yields a minimum aggregate size of six trimers, three of which are fusogenic. Mol Biosyst 7: 2741-2749.

60. Huang Q, Sivaramakrishna RP, Ludwig K, Korte T, Bottcher C, et al. (2003) Early steps of the conformational change of influenza virus hemagglutinin to a fusion active state: Stability and energetics of the hemagglutinin. Biochim Biophys Acta 1614: 3-13.

61. Lakadamyali M, Rust MJ, Babcock HP, Zhuang X. (2003) Visualizing infection of individual influenza viruses. Proc Natl Acad Sci U S A 100: 9280-9285.

62. Rust MJ, Lakadamyali M, Zhang F, Zhuang X. (2004) Assembly of endocytic machinery around individual influenza viruses during viral entry. Nat Struct Mol Biol 11: 567-573.

63. van der Schaar HM, Rust MJ, Waarts BL, van der Ende-Metselaar H, Kuhn RJ, et al. (2007) Characterization of the early events in dengue virus cell entry by biochemical assays and single-virus tracking. J Virol 81: 12019-12028.

64. Miyauchi K, Kim Y, Latinovic O, Morozov V, Melikyan GB. (2009) HIV enters cells via endocytosis and dynamin-dependent fusion with endosomes. Cell 137: 433-444.

65. Melikyan GB, Barnard RJO, Abrahamyan LG, Mothes W, Young JAT. (2005) Imaging individual retroviral fusion events: From hemifusion to pore formation and growth. Proc Natl Acad Sci U S A 102: 8728-8733.

66. Jha NK, Latinovic O, Martin E, Novitskiy G, Marin M, et al. (2011) Imaging single retrovirus entry through alternative receptor isoforms and intermediates of virus-endosome fusion. PLoS Pathog 7: e1001260.

67. Markosyan RM, Cohen FS, Melikyan GB. (2005) Time-resolved imaging of HIV-1 env-mediated lipid and content mixing between a single virion and cell membrane. Mol Biol Cell 16: 5502-5513.

68. Padilla-Parra S, Matos PM, Kondo N, Marin M, Santos NC, et al. (2012) Quantitative imaging of endosome acidification and single retrovirus fusion with distinct pools of early endosomes. Proc Natl Acad Sci U S A 109: 17627-17632.

69. Padilla-Parra S, Marin M, Kondo N, Melikyan GB. (2012) Synchronized retrovirus fusion in cells expressing alternative receptor isoforms releases the viral core into distinct sub-cellular compartments. PLoS Pathog 8: e1002694.

70. Brandenburg B, Zhuang X. (2007) Virus trafficking - learning from single-virus tracking. Nat Rev Microbiol 5: 197-208.

71. van der Schaar HM, Rust MJ, Chen C, van der Ende-Metselaar H, Wilschut J, et al. (2008) Dissecting the cell entry pathway of dengue virus by single-particle tracking in living cells. PLoS Pathog 4: e1000244.

72. de la Vega M, Marin M, Kondo N, Miyauchi K, Kim Y, et al. (2011) Inhibition of HIV-1 endocytosis allows lipid mixing at the plasma membrane, but not complete fusion. Retrovirology 8: 99.

73. Brunger AT, Weninger K, Bowen M, Chu S. (2009) Single-molecule studies of the neuronal SNARE fusion machinery. Annu Rev Biochem 78: 903-928.

74. Brunger AT. (2005) Structure and function of SNARE and SNARE-interacting proteins. Q Rev Biophys 38: 1-47.

75. Ma C, Li W, Xu Y, Rizo J. (2011) Munc13 mediates the transition from the closed syntaxin-Munc18 complex to the SNARE complex. Nat Struct Mol Biol 18: 542-549.

76. Llinas R, Steinberg IZ, Walton K. (1981) Relationship between presynaptic calcium current and postsynaptic potential in squid giant synapse. Biophys J 33: 323-351.

77. Heuser J. (1989) The role of coated vesicles in recycling of synaptic vesicle membrane. Cell Biol Int Rep 13: 1063-1076.

78. Ceccarelli B, Hurlbut WP, Mauro A. (1973) Turnover of transmitter and synaptic vesicles at the frog neuromuscular junction. J Cell Biol 57: 499-524.

79. Kyoung M, Zhang Y, Diao J, Chu S, Brunger AT. (2012) Studying calcium-triggered vesicle fusion in a single vesicle-vesicle content and lipid-mixing system. Nat Protoc 8: 1-16.

80. Fix M, Melia TJ, Jaiswal JK, Rappoport JZ, You D, et al. (2004) Imaging single membrane fusion events mediated by SNARE proteins. Proc Natl Acad Sci U S A 101: 7311-7316.

81. Karatekin E, Rothman JE. (2012) Fusion of single proteoliposomes with planar, cushioned bilayers in microfluidic flow cells. Nat Protoc 7: 903-920.

82. Domanska MK, Kiessling V, Tamm LK. (2010) Docking and fast fusion of synaptobrevin vesicles depends on the lipid compositions of the vesicle and the acceptor SNARE complex-containing target membrane. Biophys J 99: 2936-2946.

83. Karatekin E, Di Giovanni J, Iborra C, Coleman J, O'Shaughnessy B, et al. (2010) A fast, single-vesicle fusion assay mimics physiological SNARE requirements. Proc Natl Acad Sci U S A 107: 3517-3521.

84. Yoon TY, Okumus B, Zhang F, Shin YK, Ha T. (2006) Multiple intermediates in SNARE-induced membrane fusion. Proc Natl Acad Sci U S A 103: 19731-19736.

85. Yoon TY, Lu X, Diao J, Lee SM, Ha T, et al. (2008) Complexin and Ca2+ stimulate SNARE-mediated membrane fusion. Nat Struct Mol Biol 15: 707-713.

86. Lee HK, Yang Y, Su Z, Hyeon C, Lee TS, et al. (2010) Dynamic Ca2+-dependent stimulation of vesicle fusion by membrane-anchored synaptotagmin 1. Science 328: 760-763.

87. Smith EA, Weisshaar JC. (2011) Docking, not fusion, as the rate-limiting step in a SNARE-driven vesicle fusion assay. Biophys J 100: 2141-2150.

88. Bowen ME, Weninger K, Brunger AT, Chu S. (2004) Single molecule observation of liposome-bilayer fusion thermally induced by soluble N-ethyl maleimide sensitive-factor attachment protein receptors (SNAREs). Biophys J 87: 3569-3584.

89. Montecucco C, Schiavo G, Pantano S. (2005) SNARE complexes and neuroexocytosis: How many, how close? Trends Biochem Sci 30: 367-372.

90. van den Bogaart G, Holt MG, Bunt G, Riedel D, Wouters FS, et al. (2010) One SNARE complex is sufficient for membrane fusion. Nat Struct Mol Biol 17: 358-364.

91. Diao J, Su Z, Ishitsuka Y, Lu B, Lee KS, et al. (2010) A single-vesicle content mixing assay for SNARE-mediated membrane fusion. Nat Commun 1: 54.

92. Christensen SM, Mortensen MW, Stamou DG. (2011) Single vesicle assaying of SNARE-synaptotagmin-driven fusion reveals fast and slow modes of both docking and fusion and intrasample heterogeneity. Biophys J 100: 957-967.

93. Lai Y, Diao J, Liu Y, Ishitsuka Y, Su Z, et al. (2013) Fusion pore formation and expansion induced by Ca2+ and synaptotagmin 1. Proc Natl Acad Sci U S A 110: 1333-1338.

94. Diao J, Ishitsuka Y, Lee H, Joo C, Su Z, et al. (2012) A single vesicle-vesicle fusion assay for in vitro studies of SNAREs and accessory proteins. Nat Protoc 7: 921-934.

95. Ge S, Koseoglu S, Haynes CL. (2010) Bioanalytical tools for single-cell study of exocytosis. Anal Bioanal Chem 397: 3281-3304.

96. Keighron JD, Ewing AG, Cans AS. (2012) Analytical tools to monitor exocytosis: A focus on new fluorescent probes and methods. Analyst 137: 1755-1763.

97. Gandhi SP, Stevens CF. (2003) Three modes of synaptic vesicular recycling revealed by single-vesicle imaging. Nature 423: 607-613.

98. Balaji J, Ryan TA. (2007) Single-vesicle imaging reveals that synaptic vesicle exocytosis and endocytosis are coupled by a single stochastic mode. Proc Natl Acad Sci U S A 104: 20576-20581.

99. Aoki R, Kitaguchi T, Oya M, Yanagihara Y, Sato M, et al. (2010) Duration of fusion pore opening and the amount of hormone released are regulated by myosin II during kiss-and-run exocytosis. Biochem J 429: 497-504.

100. Bai L, Wang Y, Fan J, Chen Y, Ji W, et al. (2007) Dissecting multiple steps of GLUT4 trafficking and identifying the sites of insulin action. Cell Metab 5: 47-57.

101. Jiang L, Fan J, Bai L, Wang Y, Chen Y, et al. (2008) Direct quantification of fusion rate reveals a distal role for AS160 in insulin-stimulated fusion of GLUT4 storage vesicles. J Biol Chem 283: 8508-8516.

102. Jaiswal JK, Rivera VM, Simon SM. (2009) Exocytosis of post-golgi vesicles is regulated by components of the endocytic machinery. Cell 137: 1308-1319.

103. Allersma MW, Wang L, Axelrod D, Holz RW. (2004) Visualization of regulated exocytosis with a granule-membrane probe using total internal reflection microscopy. Mol Biol Cell 15: 4658-4668.

104. Murthy VN, Stevens CF. (1999) Reversal of synaptic vesicle docking at central synapses. Nat Neurosci 2: 503-507.

105. Pyle JL, Kavalali ET, Piedras-Renteria ES, Tsien RW. (2000) Rapid reuse of readily releasable pool vesicles at hippocampal synapses. Neuron 28: 221-231.

106. Aravanis AM, Pyle JL, Harata NC, Tsien RW. (2003) Imaging single synaptic vesicles undergoing repeated fusion events: Kissing, running, and kissing again. Neuropharmacology 45: 797-813.

107. Aravanis AM, Pyle JL, Tsien RW. (2003) Single synaptic vesicles fusing transiently and successively without loss of identity. Nature 423: 643-647.

108. Zhang Q, Li Y, Tsien RW. (2009) The dynamic control of kiss-and-run and vesicular reuse probed with single nanoparticles. Science 323: 1448-1453.

109. Murthy VN, Stevens CF. (1998) Synaptic vesicles retain their identity through the endocytic cycle. Nature 392: 497-501.

110. Chen X, Barg S, Almers W. (2008) Release of the styryl dyes from single synaptic vesicles in hippocampal neurons. J Neurosci 28: 1894-1903.

111. Sinha R, Ahmed S, Jahn R, Klingauf J. (2011) Two synaptobrevin molecules are sufficient for vesicle fusion in central nervous system synapses. Proc Natl Acad Sci U S A 108: 14318-14323.

112. Li F, Pincet F, Perez E, Eng WS, Melia TJ, et al. (2007) Energetics and dynamics of SNAREpin folding across lipid bilayers. Nat Struct Mol Biol 14: 890-896.

113. Chernomordik LV, Leikina E, Frolov V, Bronk P, Zimmerberg J. (1997) An early stage of membrane fusion mediated by the low pH conformation of influenza hemagglutinin depends upon membrane lipids. J Cell Biol 136: 81-93.

114. Mittal A, Leikina E, Chernomordik LV, Bentz J. (2003) Kinetically differentiating influenza hemagglutinin fusion and hemifusion machines. Biophys J 85: 1713-1724.

115. Burchfield JG, Lopez JA, Mele K, Vallotton P, Hughes WE. (2010) Exocytotic vesicle behaviour assessed by total internal reflection fluorescence microscopy. Traffic 11: 429-439.

Page intentionally left blank.

Chapter 2

Boerries Brandenburg [1], Wouter Koudstaal [1], Jaap Goudsmit [1], Vincent Klaren [1], Chan Tang [1], Miriam V. Bujny [1], Hans J. W. M. Korse [1], Ted Kwaks [1], Jason J. Otterstrom [2,3], Jarek Juraszek [1], Antoine M. van Oijen [2], Ronald Vogels [1] and Robert H. E. Friesen [1]

1) Crucell Vaccine Institute, Janssen Center of Excellence for Immunoprophylaxis, Leiden, The Netherlands

2) Centre for Synthetic Biology, Zernike Institute for Advanced Materials, Groningen, The Netherlands

3) Harvard Biophysics Program, Harvard Medical School, Boston, MA, USA

The experimental design was conceived by Dr. Boerries Brandenburg and Dr. Antoine van Oijen. I designed and constructed the fluorescence microscope used in the single-particle experiments and adapted the fusion assay [24,25] to incorporate the H1N1 and H3N2 strains together with high concentrations of fusion inhibiting antibody. Together with Chan Tang, we established conditions for fluorescent labeling of the virions that did not abrogate viral infectivity. I performed all single-particle experiments, wrote analysis scripts to extract and analyze resulting fusion efficiencies and performed statistical analysis on the data obtained. I wrote the initial version of section 2.2.2 describing and interpreting the single-particle data that was used by Dr. Boerries Brandenburg to write the manuscript. I wrote the methods section A1.1 in Appendix 1, and I used my data to make panels B, C, D and E of Figure 2-2 and also supplemental movies M1-5 and M1-6.

Chapter 2

Mechanisms of Hemagglutinin Targeted Influenza Virus Neutralization

Abstract

Human monoclonal antibodies have been identified which neutralize broad spectra of influenza A or B viruses. Here, we dissect the mechanisms by which such antibodies interfere with infectivity. We distinguish four mechanisms that link the conserved hemagglutinin (HA) epitopes of broadly neutralizing antibodies to critical processes in the viral life cycle. HA-stem binding antibodies can act intracellularly by blocking fusion between the viral and endosomal membranes and extracellularly by preventing the proteolytic activation of HA. HA-head binding antibodies prevent viral attachment and release. These insights into newly identified ways by which the human immune system can interfere with influenza virus infection may aid the development of novel universal vaccines and antivirals.

Material in this chapter has been accepted for publication in the journal *PLoS One*:

Brandenburg, B., Koudstaal, W., Goudsmit, J, Klaren, V., Tang, C., Bujny, M.V., Korse, H. J. W. M., Kwaks, T., Otterstrom, J., Juraszek, J., van Oijen, A.M., Vogels, R. and Friesen, R. H. E. (2013) Mechanisms of hemagglutinin targeted influenza virus neutralization. *PLoS One*.; *Accepted.*

2.1 Introduction

Influenza viruses continue to be a major cause of morbidity and mortality due to shortcomings of currently available vaccines and antivirals. Despite the well-established role of neutralizing antibodies in the defense against influenza virus infection [1,2] there is a lack of evidence on how such antibodies interfere with infection. Further understanding of their mechanisms of action, correlated to the structures involved, may guide the design of better vaccines and antivirals.

Neutralizing antibodies mainly target the hemagglutinin (HA) protein, the major envelope glycoprotein of influenza viruses. The HA protein is synthesized as a single precursor protein (HA0) and requires cleavage by host serine proteases into two disulfide-linked subunits, HA1 and HA2, for the virus to be infectious [3,4]. The HA1 “head” subunit mediates attachment of the virus to target cells through interactions with sialic acid receptors. After endocytosis of the virus, acidification of the endosomes triggers large conformational changes in the HA2 “stem” subunit leading to fusion of the viral and endosomal membranes and release of the viral genome into the cytoplasm, allowing the infection to progress.

The vast majority of neutralizing antibodies in infected or vaccinated individuals interferes with attachment of the virus to cellular receptors by binding to exposed, highly variable loops that surround the receptor binding site. Antibodies binding to these regions are typically strain-specific and immunity following natural exposure or vaccination is mostly restricted to closely related strains. However, in the last five years, several human antibodies with remarkably broad neutralizing activity against influenza virus have been generated and characterized. Most of these broadly neutralizing antibodies (bnAbs), such as CR6261, F10, CR8020, FI6, and CR9114, were shown to bind to epitopes in the HA stem which are highly conserved among various influenza virus subtypes and have heterosubtypic neutralizing activity [5–10]. Others, like CH65, 5J8, CR8033, and C05, bind (close) to the receptor binding site on the HA head and show broad neutralizing activity within one subtype, or neutralize selected

isolates from several subtypes [10–13]. Many of these bnAbs have been shown to have therapeutic efficacy in animal models [5,7–10,12,14,15] and several are being developed as monoclonal antibody therapies. The broad activity of both groups of bnAbs is a result of the high level of conservation of their respective epitopes, which in turn appears to be caused by structural constraints imposed on the HA protein by the necessity to retain its key functions; receptor binding and fusion. To understand the structural basis of the broad activity, much effort has been focused on the molecular characterization of the bnAbs and their epitopes with the ultimate goal of developing a universal vaccine against influenza virus [1,16–18]. Stem binding antibodies as well as head binding antibodies have multiple ways by which they can interfere with the viral life cycle [19–21]. Detailed knowledge on the mechanisms of action of bnAbs, as is presented here, is critical for understanding how the human immune system interferes with processes that are pivotal for influenza virus infection and spread.

2.2 Results

2.2.1 Stem-binding bnAbs are internalized by live cells in complex with viral particles, reach late endosomes, and prevent infection

Stem-binding neutralizing antibodies have been postulated to inhibit the fusion process based on their interaction with the HA2 subunit and lack of activity in hemagglutination-inhibition (HAI) assays, which specifically detect antibodies that interfere with attachment of the virus to sialic acid receptors. Indirect evidence supporting this notion comes from biochemical studies showing that such antibodies can block the conformational changes of recombinant HA required for membrane fusion [6,8,10], or prevent the formation of syncytia in HA-expressing cells [7,22]. Such a mechanism of action implies that these antibodies are internalized together with the virus and reach late endosomes, but this has so far not been shown. By using fluorescence single particle tracking methods we investigated the fate of viral particles and bound antibodies during infection of live cells (Figure 2-1A) [23]. Movies of cells incubated with fluorescently

labeled CR8020 mixed with H3N2 virus, and CR6261 mixed with H1N1 virus (CR8020 and CR6261 specifically bind Group 2 and Group 1 influenza A viruses, respectively. Table A1-1), reveal that stem-binding antibodies are indeed internalized in complex with the virus and transported along the microtubule cytoskeleton (Figure 2-1B,C; Movies M1-1, M1-2). The joint and directed movement of internalized viruses and bound antibodies is evident from their high degree of co-localization over consecutive frames. This behavior was exclusively observed for viruses and bound stem-binding antibodies since head-binding antibodies prevent viral internalization to begin with and no evidence for the internalization of unbound antibody could be found (Figure A1-1A,B; Movies M1-3, M1-4). Furthermore, pulse-labeling with a dye sensitive for low-pH vesicles, combined with single particle tracking in cells, demonstrated that virus-antibody complexes reach acidic late endosomes (Figure 2-1D,E). Prolonged tracking of cells that had internalized virus-antibody complexes allowed us to determine their individual fate. Following a pre-incubation with H3N2 virus, stem-binding bnAb CR8020 was observed co-localizing with viral particles inside cells at early time points (Figure 2-1F, Table A1-2). Cells were imaged every 30 minutes for 15 hours after which they were fixed and probed for the expression of influenza nucleoprotein (NP), which was used as an indicator for infection. In cells that had internalized CR8020 in complex with the virus, no NP expression was detected (Figure 2-1G), indicating that the bound bnAb successfully prevented infection. In contrast, a comparable number of particles led to full infection in the control experiment in which H3N2 virus had been pre-incubated with a non-binding control antibody (Figure 2-1H,I). Similar results were obtained for the inhibition of infection by H1N1 virus following pre-incubation with CR6261 (Figure A1-2).

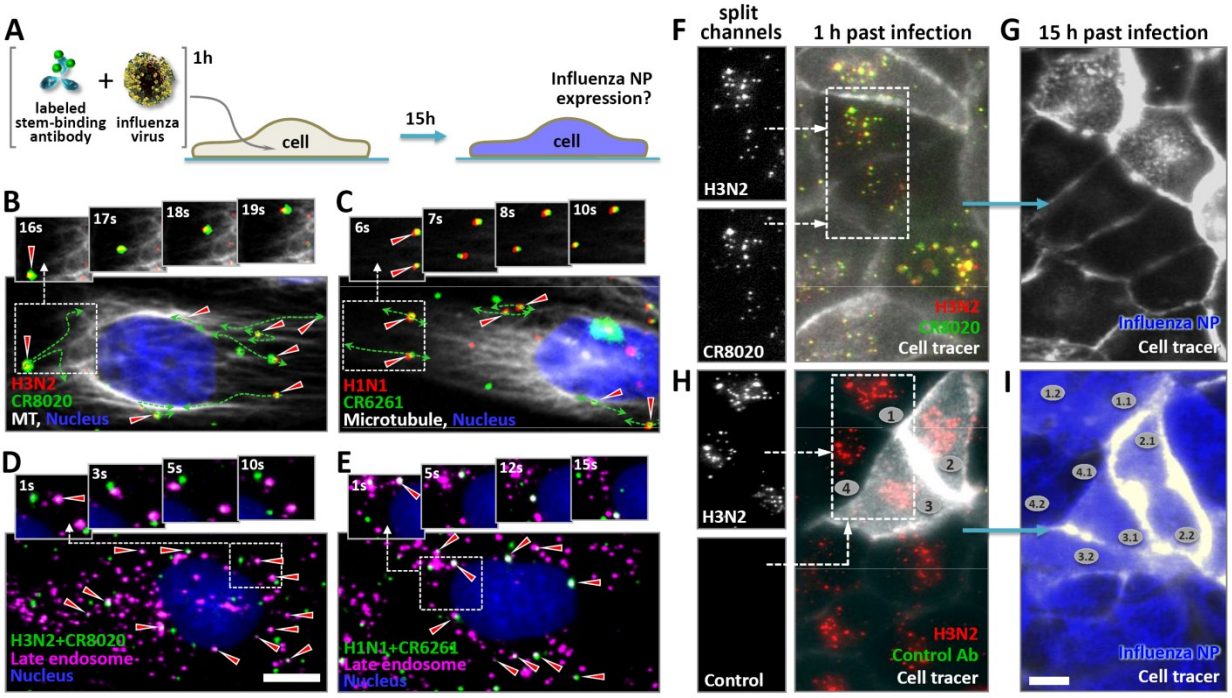

Figure 2-1 – *Stem-binding bnAbs are internalized into live cells in complex with viral particles, reach late endosomes, and prevent infection.* ***A****) Experimental layout. Fluorescently labeled viruses and antibodies were pre-incubated and subsequently added to live cells and tracked. Whether or not cells were eventually infected was determined by staining for influenza NP after tracking individual cells for 15 hours.* ***B*** *and* ***C****) Stills of movies (Movies M1-1 and M1-2) showing the joint and directed motion of R18-labeled A/Aichi/2/1968-X31 (H3N2) (red) and AF647-labeled CR8020 (green) (B), and R18-labeled A/Puerto Rico/8/1934 (H1N1) virus (red) and AF647-labeled CR6261 (green) (C), along TubulinTracker-stained microtubules (white) of live MDCK cells (nucleus, blue) approximately 30 minutes after addition of the pre-incubated virus-antibody mixtures. Dashed lines outline the trajectories of the virus-antibody complexes (red triangles) as seen in movies M1-1 and M1-2.* ***D****) A/Aichi/2/1968-X31 (H3N2) virus was pre-incubated with AF647-labeled CR8020 (green) before addition to live MDCK cells labeled with LysoTracker (magenta) and imaged when virus-antibody complexes reached the perinuclear region. Arrows indicate co-localization of virus-antibody complexes with low-pH vesicles (white).* ***E****) As in (D), except that here A/Puerto Rico/8/1934 (H1N1) virus and AF647-labeled CR6261 were used.* ***F****) R18-labeled A/Aichi/2/1968-X31 (H3N2) virus (red) was incubated with AF647-labeled CR8020 (green) before addition to live MDCK cells expressing a GFP-cell tracer (grey cell outline). Virus-antibody complexes (co-localization shown in yellow, compare also split channels in the inset) were detected in live cells 30 minutes after inoculation.* ***G****) To determine whether internalized virus-antibody complexes prevent infection, the fate of individual cells was assessed by tracking them over night (imaged in 30 min intervals). 15 hours post-incubation (hpi) the same cells (including their progeny) were fixed and stained for expression of influenza nuclear protein (NP, blue).* ***H****) Incubation of R18-labeled A/Aichi/2/1968-X31 (H3N2) virus (red) with non-binding AF647-labeled CR6261 did not result in internalization of antibody. Only viral particles were detected in live cells 30 minutes after addition of the virus-antibody mixture and*

*(**Figure 2-1 Continued**) infection was not prevented, as demonstrated by the expression of NP (blue) in these same cells 15 hours later **I**). Examples of progeny cells are indicated with numbers. Scale bars B-E equal 10 µm, F-I equal 25 µm.*

2.2.2 Stem-binding bnAbs prevent membrane fusion

The finding that stem-binding bnAbs reach late endosomes in complex with the virus is congruent with the assumption that such antibodies can prevent infection by blocking fusion of the viral and endosomal membranes. To directly observe the interference of viral fusion by bnAbs, a single particle fusion assay was applied (Figure 2-2A). Hereto, the envelope membrane of virus particles were fluorescently labeled at a density of lipophilic dye molecules that led to fluorescence self-quenching [24,25]. Labeled viruses were subsequently incubated with various concentrations of stem-binding bnAbs (optionally fluorescently labeled). Virus-antibody complexes were then bound to receptor proteins embedded in a target membrane and imaged. Upon lowering of the pH, HA molecules of individual viral particles incubated with a non-binding control antibody or low concentrations of bnAbs undergo conformational change and mediate membrane fusion. This event is observed as a rapid temporary increase in fluorescence signal (Figure 2-2B,C, yellow triangles; Movie M1-5). Increasing bnAb concentrations dramatically decrease the number of fusing virus particles (Figure 2-2D-G, Movie M1-6), demonstrating the direct inhibition of membrane fusion by stem-binding bnAbs.

2.2.3 Preventing proteolytic cleavage of HA is an additional mechanism of neutralization for some stem-binding bnAbs

The inhibition of the fusion between the virus and the endosome is a mechanism shared by all neutralizing stem binding bnAbs described to date. Inhibiting the cleavage of HA0 into HA1 and HA2 fragments removes the fusogenic potential of HA and is a second mechanism adding to the potency of some of the stem binding Abs. Stem-binding bnAbs CR8020 and FI6 recognize epitopes which partially overlap with the fusion peptide and bind close to the cleavage

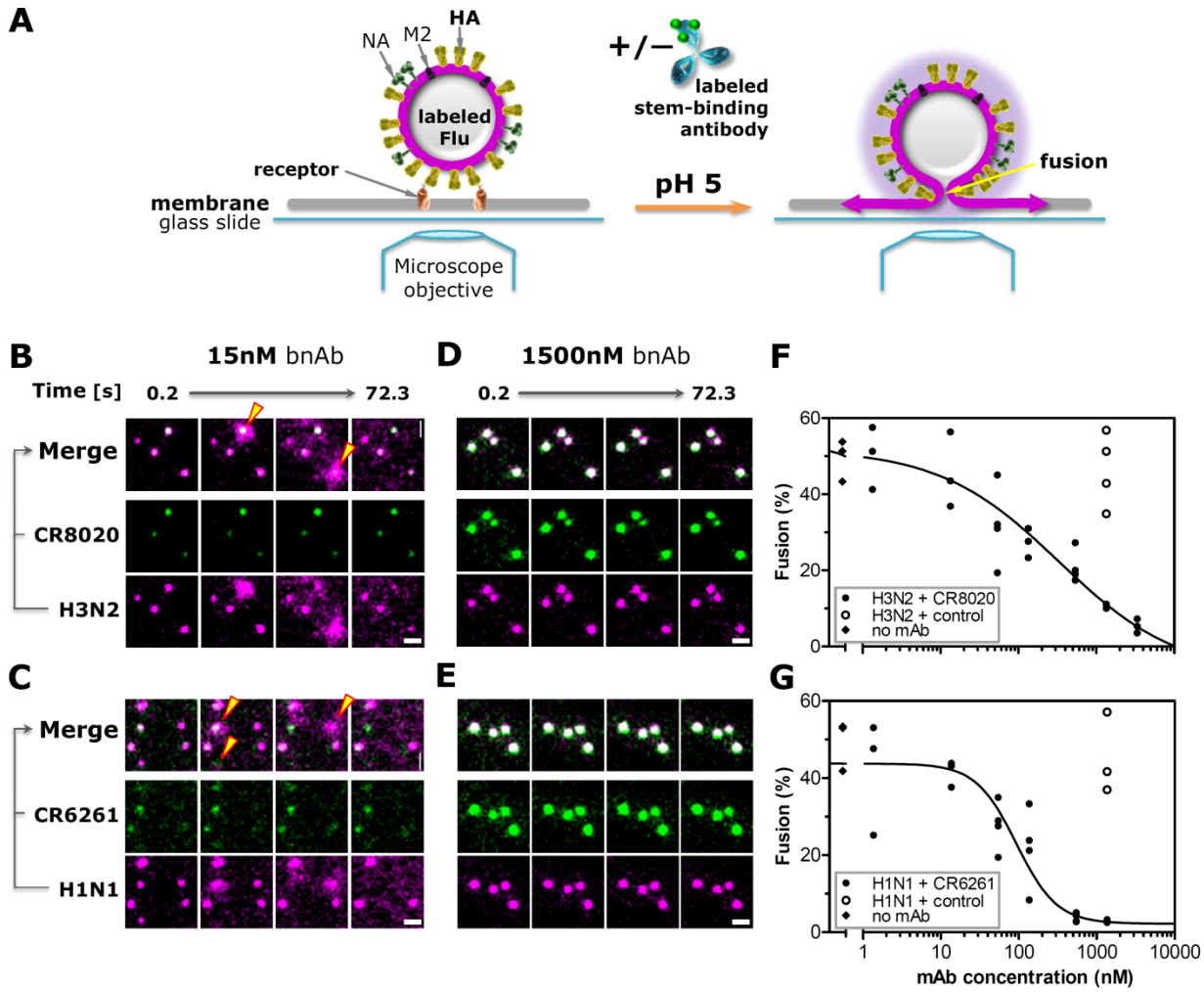

Figure 2-2 – *Stem-binding bnAbs prevent membrane fusion in an in vitro single particle fusion assay.* ***A****) Assay setup in microfluidic chamber mounted on an inverted fluorescent microscope. (****B*** *and* ***D****) Stills of movies of individual R18-labeled A/Aichi/2/1968-X31 (H3N2) or (****C*** *and* ***E****) A/Puerto Rico/8/1934 (H1N1, Movie M1-5 and M1-6) virus particles (magenta) incubated with AF488-labeled bnAbs (green) and bound to sialic acid decorated proteins embedded in a supported lipid bilayer where they co-localize (white, merge). Upon lowering the pH from 7.4 to 5.0 (t=0 seconds), viruses incubated with only 15 nM CR8020 or CR6261 undergo HA-mediated fusion with the target membrane, visualized as a rapid increase in signal due to fluorescence dequenching followed by diffusion of R18 molecules away from the fusion site (B and C, yellow triangles), whereas no fusion events occur when viruses are incubated with 1500 nM bnAbs (D and E). Scale bars equal 3 μm; illumination conditions and image contrast settings are identical in B-E. (****F*** *and* ***G****) The percentage of H3N2 and H1N1 particles undergoing fusion after the pH drop decreases with increasing concentrations of CR8020 and CR6261, respectively (black symbols). In contrast, high concentrations of bnAbs used as non-binding control antibody have no effect on the percentage of fusion (open symbols).*

site of HA [8,9]. Both have been reported to not only inhibit the conformational change of HA, but to also prevent trypsin from cleaving the extracellular domain of purified HA *in vitro* [8,9]. To test the contribution of inhibiting HA cleavage on the potency of CR8020, we generated a batch of H3N2 virus of which the HA proteins were uncleaved by harvesting the virus after a single round of infection in the absence of trypsin. As expected, such 'uncleaved' virus was only infectious on MDCK cells after treatment with trypsin (Figure 2-3A). Next, we compared the potency of CR8020 against this virus treated with trypsin either before, or after addition of the antibody (Figure 2-3B). When CR8020 was added before cleavage, a nine-fold increase in potency was found compared to when antibody was added to previously cleaved virus (Figure 2-3C,D). This difference shows that the *in vitro* neutralizing potency of CR8020 is based on prevention of both fusion and cleavage. However, although porcine trypsin is widely used to render influenza viruses infectious in cell culture, in human lungs cleavage is thought to be mediated by membrane-bound proteases such as TMPRSS-2, and -4 and Human Airway Trypsin [26] and potentially also by secreted proteases like tryptase Clara, miniplasmin, and ectopic anionic trypsin [3]. Human lung derived Calu-3 cells form polarized epithelia and express TMPRSS-2 and -4 [27]. These cells allow the propagation of influenza virus in the absence of trypsin, indicating that cellular serine proteases are capable of mediating cleavage of progeny virus (Figure A1-3A). Interestingly, uncleaved virus is not infectious when added to Calu-3 cells, suggesting that cell-associated proteases are unable to cleave the HA of 'incoming' virus particles (Figure A1-3B). In order to compare the cleavage status of the HA on viral particles produced in the presence and absence of CR8020, we infected Calu-3 cells with H3N2 virus and added the antibody two hours later. In this way we prevented interference of the antibody with the initial infection, but allowed it to bind immediately to newly expressed HA molecules on the cell surface. Virus particles were harvested from the supernatant 20 hours post infection and analyzed by Western blot. Whereas in the presence of a non-binding control antibody (CR6261) a portion of the HA molecules on viral particles were cleaved, as indicated

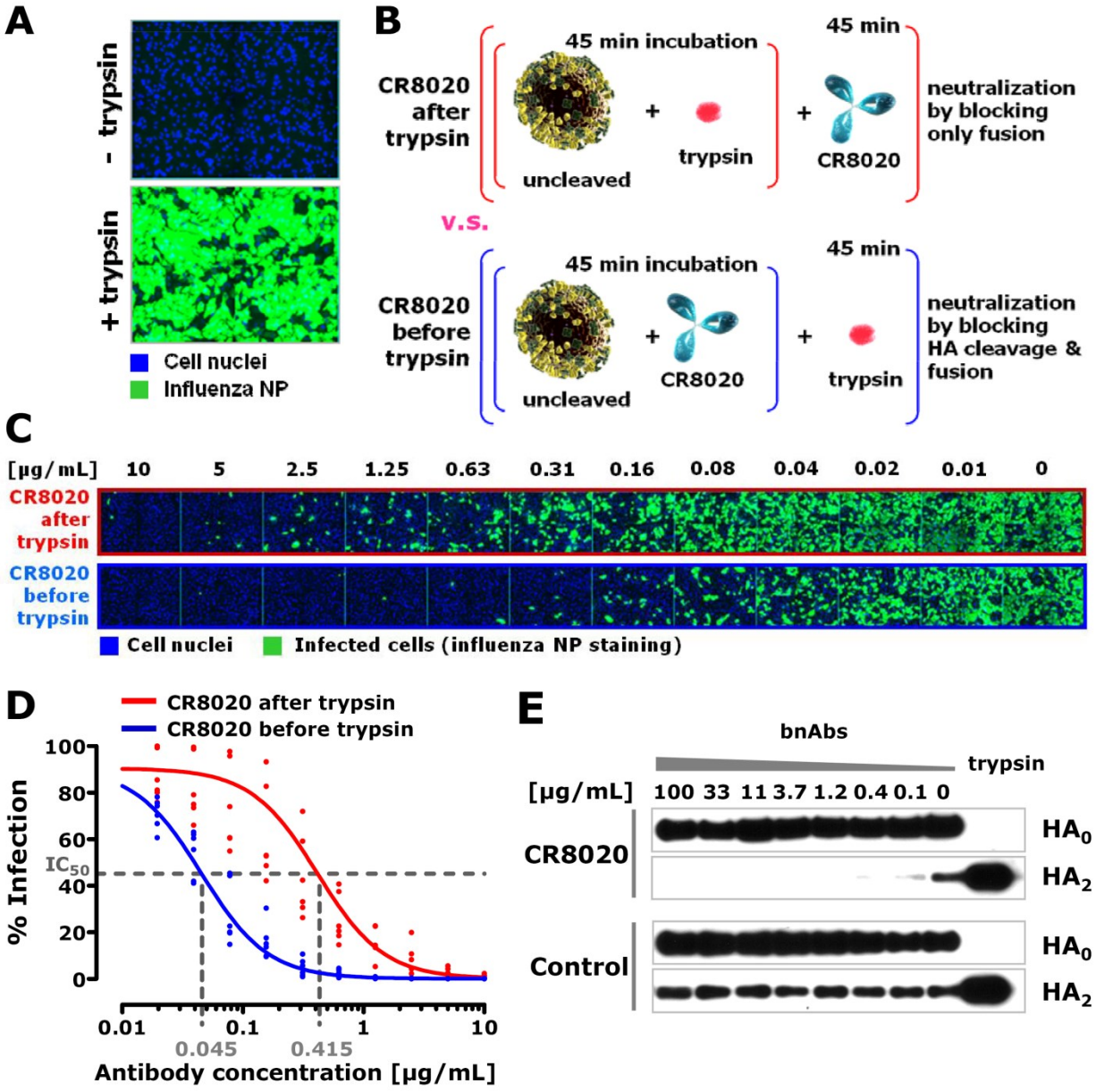

Figure 2-3 *– Blocking HA cleavage by CR8020 has an additive effect on virus neutralization in vitro.* ***A****) Expression of influenza NP (green) in MDCK cells (nuclei labeled with DAPI in blue) 16 hours after inoculation with A/Wisconsin/67/2005 (H3N2) virus of which the HA was uncleaved (top) or cleaved by prior incubation with trypsin (bottom).* ***B****) Experimental layout to study the additive effect of cleavage inhibition on the potency of CR8020 in vitro.* ***C****) A/Wisconsin/67/2005 (H3N2) virus was either first incubated with trypsin and then with a serial dilution of neutralizing antibody (i.e. CR8020 after trypsin), or the virus was first incubated with serial dilutions of antibody and then treated with trypsin (i.e. CR8020 before trypsin). After 18 hours of infection, cells (nuclei stained with DAPI, blue) were stained for infection (NP expression, green).* ***D****) Graph shows numerical analysis of results; normalized percentage of infection versus antibody concentration was used to compare the IC_{50} values for each condition. Change in IC_{50} is 9.2-fold (95 % C.I. 6.8-12.3).* ***E****) Calu-3 cells (polarized human lung epithelia) were infected with cleaved*

*(**Figure 2-3 Continued**) A/Wisconsin/67/2005 (H3N2). Virus was washed away after 2 hours, and cells were incubated with test and control antibody for 18 hours in the absence of trypsin. Newly produced viral particles released into the culture supernatant were harvested and the HA cleavage status was analyzed by Western blot (using rabbit polyclonal anti-HA serum). The presence of the HA2 band is indicative for cleavage (the HA1 band is not efficiently stained by the polyclonal serum).*

by the presence of the HA2 band, CR8020 efficiently blocked HA cleavage at a concentration as low as 0.4 µg/mL (Figure 2-3E). Interestingly, not all HA molecules incorporated in viral particles need to be cleaved to allow spread of infection in Calu-3 cells, as apparent from the observation that virus spreading in these cells in the absence of trypsin (Figure A1-3A) contains both cleaved and uncleaved HA (Figure 2-3E). Nevertheless, in the presence of sufficient amounts of CR8020, newly budded viral particles contain only uncleaved HA molecules, rendering them non-infectious. This shows, in a physiological situation, that CR8020 inhibits cleavage and spread of influenza virus and that a single type of antibody can act intra-cellularly (fusion inhibition) as well as extra-cellularly (cleavage inhibition).

2.2.4 HA head-binding antibodies not only block attachment, but also viral egress

Head-binding neutralizing antibodies are well-documented to prevent viral attachment to the receptor. However, we have recently described two bnAbs, CR8033 and CR8071, which bind to the globular head of influenza B HA and are able to inhibit viral egress [10]. Whereas CR8033 also interferes with attachment of the virus to its cellular receptor, egress inhibition appears to be the only neutralization mechanism of CR8071. Since both head- and stem-binding antibodies can bind to HA on the surface of infected cells (Figure A1-1C), we hypothesized that egress inhibition is a more common mechanism of action for antibodies directed against HA of influenza A and B. To test this, cells were infected and three hours later, various stem- and head-binding antibodies were added (Table A1-1). Delaying the addition of antibodies ensured unhindered initial infection and allowed assessment of the effect on egress

only. Twenty hours after infection, the amounts of newly produced viral particles present in the supernatants and cell lysates were analyzed. Since the presence of the neutralizing antibodies would interfere with assays assessing virus titers (e.g. $TCID_{50}$), we used Western blot analysis to determine the amount of virus. As observed with influenza B specific antibodies CR8033 and CR8071, the presence of head-binding antibodies against influenza A viruses of the H1N1 (CR9020, CH65 and 2D1) and H3N2 (CR8057) subtypes led to a significant reduction in the amount of viral particles released into the supernatant (shown by the absence of HA), while the production and accumulation of HA in the cell was not affected (Figure 2-4A,B and Figure A1-5A). In contrast, the presence of HA stem-binders (CR6261 and CR8020) had no effect on the amount of viral particles released into the supernatant. Thus, egress inhibition appears to be a common mechanism of antibodies directed against the head region of HA of both influenza A and B viruses. Since head-binding antibodies are dominant in the response to infection or vaccination, we were interested to see whether polyclonal serum (besides the well-documented inhibition of receptor interaction) could also inhibit viral egress. Indeed, addition of HA-specific polyclonal mouse serum to infected cells caused a concentration dependent reduction of viral particles in the supernatant, without affecting the accumulation of HA in the cell (Figure 2-4C).

Confirmation that head-binding antibodies inhibit egress comes from Scanning EM (SEM) images showing that whereas separate budding particles are present at the surface of infected cells in the presence of stem-binding antibody CR6261, large aggregates of particles are visible in the presence of each of the head-binding antibodies (Figure 2-4E and Figure A1-4, A1-5C). Transmission EM (TEM) images further reveal that the aggregated virions resemble fully formed free virus particles, with an electron dense core due to the vRNPs and spike proteins on the surface (Figure 2-4F,G and Figure A1-4, A1-5D,E). Moreover, completely formed viral particles surrounded by an endosomal membrane were detected in the cytoplasm near the surface, suggesting that un-budded particles can be re-internalized (red triangles in

Figure 2-4 – *HA head binding antibodies inhibit influenza virus egress. (**A**) Calu-3 cells were infected with A/Puerto Rico/8/1934 (H1N1) and 3 hours later stem-binding antibody CR6261 or head-binding antibody CH65 was added. Twenty hours later, the amounts of HA present in the cell supernatant (S) and lysate (L) were analyzed by Western blot (HA0 band shown). (**B**) As in (A) except that cells were infected with A/Wisconsin/67/2005 (H3N2) virus and stem- and head-binding antibodies CR8020 and CR8057, respectively, were used. (**C**) Naïve mice were immunized and boosted twice with DNA encoding the HA of influenza A/Brisbane/59/2007 (H1N1) virus. Serum was collected and added to MDCK cells 3 hours after infection with the same virus. The amount of newly produced particles in culture supernatants and cell lysates were analyzed 20 hours later by Western blot (HA0 band shown). As positive and negative controls 1 µg/mL of CR9020 and CR8057 were included, respectively. (**D**) Fab fragments of head-binding antibodies CH65 and CR8057 were added 3 hours after infection of MDCK cells with A/Puerto Rico/8/1934 (H1N1) and A/Wisconsin/67/2005 (H3N2) virus, respectively, and 20 hours later the amounts of HA present in the supernatant were analyzed as above. (**E**) SEM images of the surface of MDCK cells infected with influenza A/New Caledonia/20/1999 (H1N1), A/Wisconsin/67/2005 (H3N2), or influenza B/Florida/04/2006 virus and subsequently incubated (from 3 hours post infection) with CR6261 (50 µg/mL, 333 nM), CH65 (10 µg/mL, 67 nM), CR8057 (0.5 µg/mL, 3 nM) or CR8033 (2.5 µg/mL, 17 nM) respectively. Representative images of three independent experiments are shown. Scale bar 1 µm. (**F** and **G**) As in (E) except TEM images of ultrathin sectioned MDCK cell (re-internalized particles indicated with red triangles). Scale bar in (F) 500 nm and in (G) 100 nm.*

(Figure 2-4 Continued)

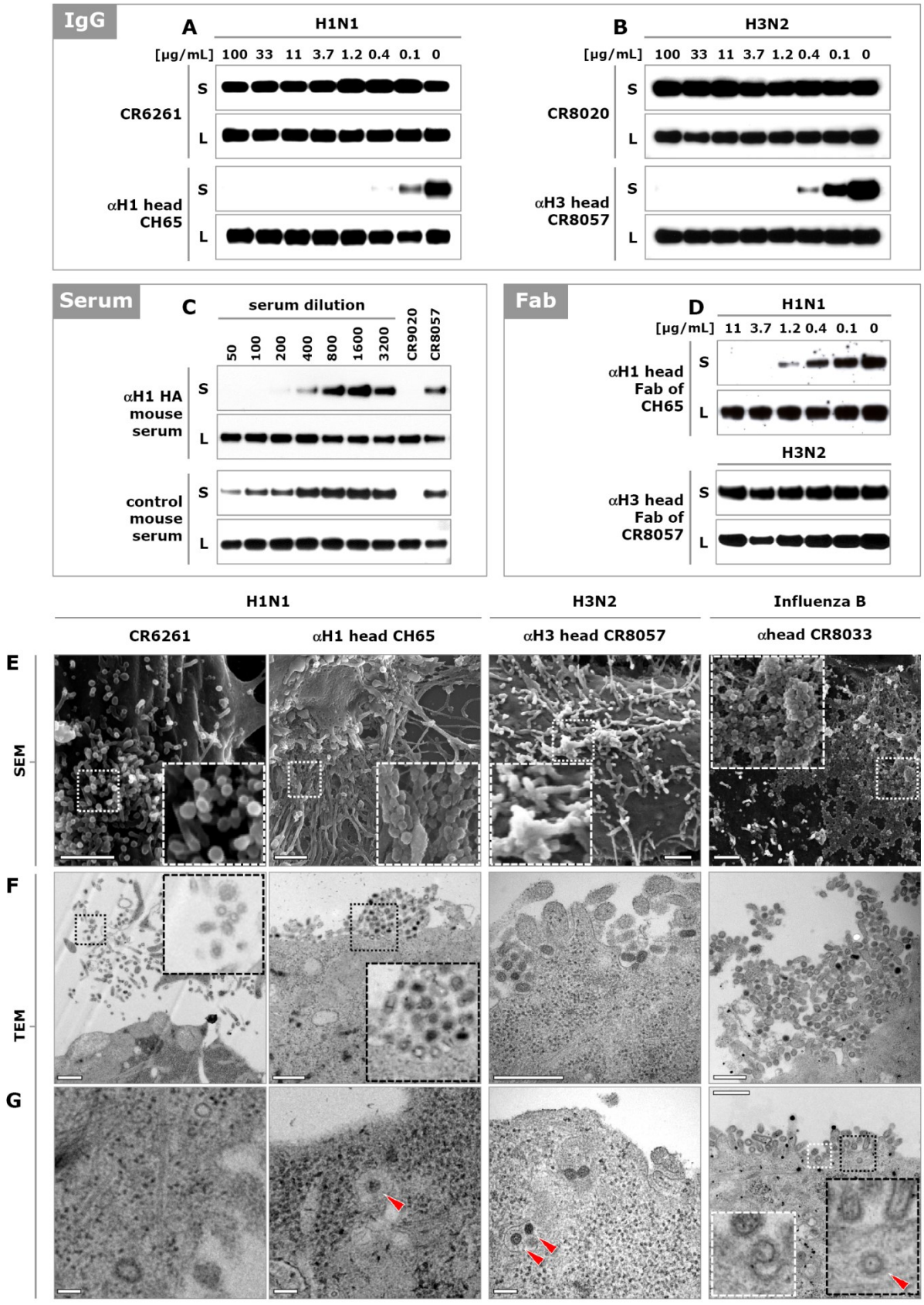

Figure 2-4G and Figure A1-5E). In all these aspects, the phenotype is similar to what is seen with the antiviral drug zanamivir, which inhibits egress by blocking the enzymatic activity of the neuraminidase (NA) protein (Figure A1-5C-E).

We hypothesized that HA head-binding antibodies inhibit egress by cross-linking of newly formed virions to each other and to HA on the cell membrane. In line with this hypothesis, the presence of the monovalent Fab fragments of CR8057, CR8033 and CR8071 had no effect on the amount of HA in the supernatant of cells infected with H3N2 and influenza B virus, respectively (Figure 2-4D and Figure A1-5B). Interestingly however, the Fab fragment of CH65 did result in a reduction of HA in the supernatant of cells infected with H1N1 virus, similar to the IgG molecule. Considering the phenotypic resemblance with zanamivir, one may speculate that CH65 prevents NA from performing its function through steric hindrance, rather than through cross-linking newly formed virions. However, it is also possible that all these antibodies inhibit egress in the same way (be it through hindrance of NA or otherwise), but that differences in affinity, or the orientation in which they bind to HA determines whether the Fab alone or the larger IgG molecule is required. Either way, our results show that many, if not all, head-binding neutralizing antibodies, next to preventing attachment to the receptor, also inhibit egress.

2.3 Discussion

The *in vivo* activity of antiviral antibodies is thought to be a combination of direct mechanisms of action (e.g. neutralization) and indirect mechanisms of action, generally mediated by immune cells (e.g. NK cells) or complement factors interacting with the Fc-tail of the bound antibodies and inducing cell toxicity [28,29]. In this study, we focused on the direct mechanisms of action of bnAbs as a consequence of their binding to different epitopes on HA. By using live cell imaging and infectious viruses we distinguish four physiologically relevant mechanisms by which anti-HA antibodies can interfere with the pivotal functions of HA and neutralize the virus: inhibition of receptor binding, inhibition of membrane fusion, inhibition of

HA0 cleavage and inhibition of egress. These mechanisms, being so diverse and tailored to different stages in the life-cycle of the influenza virus (Figure 2-5A), are not readily captured in a single assay format. Consequently, when assessing the potency of a particular antibody, antiviral, or a (universal) vaccine, it will be necessary to use various assays. Indeed, the use of HAI and standard microneutralization assays is one of the reasons why the existence of bnAbs has long gone undetected [30]. Likewise, some of the head-binding antibodies described previously may in addition to preventing attachment also inhibition egress [11,13,31–33]. Because the epitopes of the bnAbs studied here (and several others) are known, we can link their mechanisms of action to specific regions on the HA molecule (Figure 2-5B). Although this link is not absolute in the sense that only antibodies binding to these regions exert these mechanisms [34], the bnAbs show us highly conserved sites where interference with crucial processes involving HA is possible (Figure 2-5A,B). This information may be exploited to design broad-spectrum anti-influenza virus molecules since the broad reactivity of these antibodies means that antivirals mimicking their mechanisms of action will be broadly active, provided that they bind to the same highly conserved regions on HA.

Figure 2-5 – *Mechanisms of action of bnAbs map to conserved regions on HA and thereby reveal conserved vulnerabilities of influenza virus. (**A**) Influenza virus life cycle highlighting the four distinct mechanism of actions of HA head-binding (green) and stem-binding (blue) bnAb. (Panel **B**, left) X-ray structure of an uncleaved H3 trimer (A/Hong Kong/1/68 PDB 1HA0) in a space filling representation. For clarity, only one monomer of the trimer is colored (HA1 green, HA2, yellow). The head region, comprising lectin and vestigial esterase domains, and the stem region, containing the fusion machinery, are indicated with dotted black lines. The receptor binding site is plotted in blue and the cleavage site in pink. The regions around these sites (solid orange lines) are the footprints of sialic acid and trypsin, respectively. To roughly estimate the trypsin footprint, a trypsin structure (PDB 1YF4) was docked on the HA cleavage site such that the cleaved HA arginine overlapped with the bound arginine from 1YF4. HA amino-acids within 5A from trypsin were then taken as an approximation of the footprint. (Panel **B**, right) Footprints, indicated by solid cyan lines, of the bnAbs studied here superimposed on HA: CH65 and CR6261 footprints are plotted on HA from A/South Carolina/1/1918 (PDB ID 3GBN), and the CR8020 footprint on A/Hong Kong/1/1968 HA (PDB ID 3SDY). For the flu B antibodies, the B/Brisbane/60/2008 structure (PDB ID 4FQM) is used. Each of the HA structures has been colored with amino-acid conservation index, corresponding to their respective virus groups: H1 – group1, H3 – group 2 and B – entire influenza B. Conservation was calculated based on the NCBI flu database set as of December 2011, assuming a number of conservative substitutions [8]. Red color corresponds to more than 99 % conservation, white to less than 60 % conservation. Additional human antibodies of which the epitopes and/or mechanism(s) of action are known are indicated on the far right.*

(Figure 2-5 Continued)

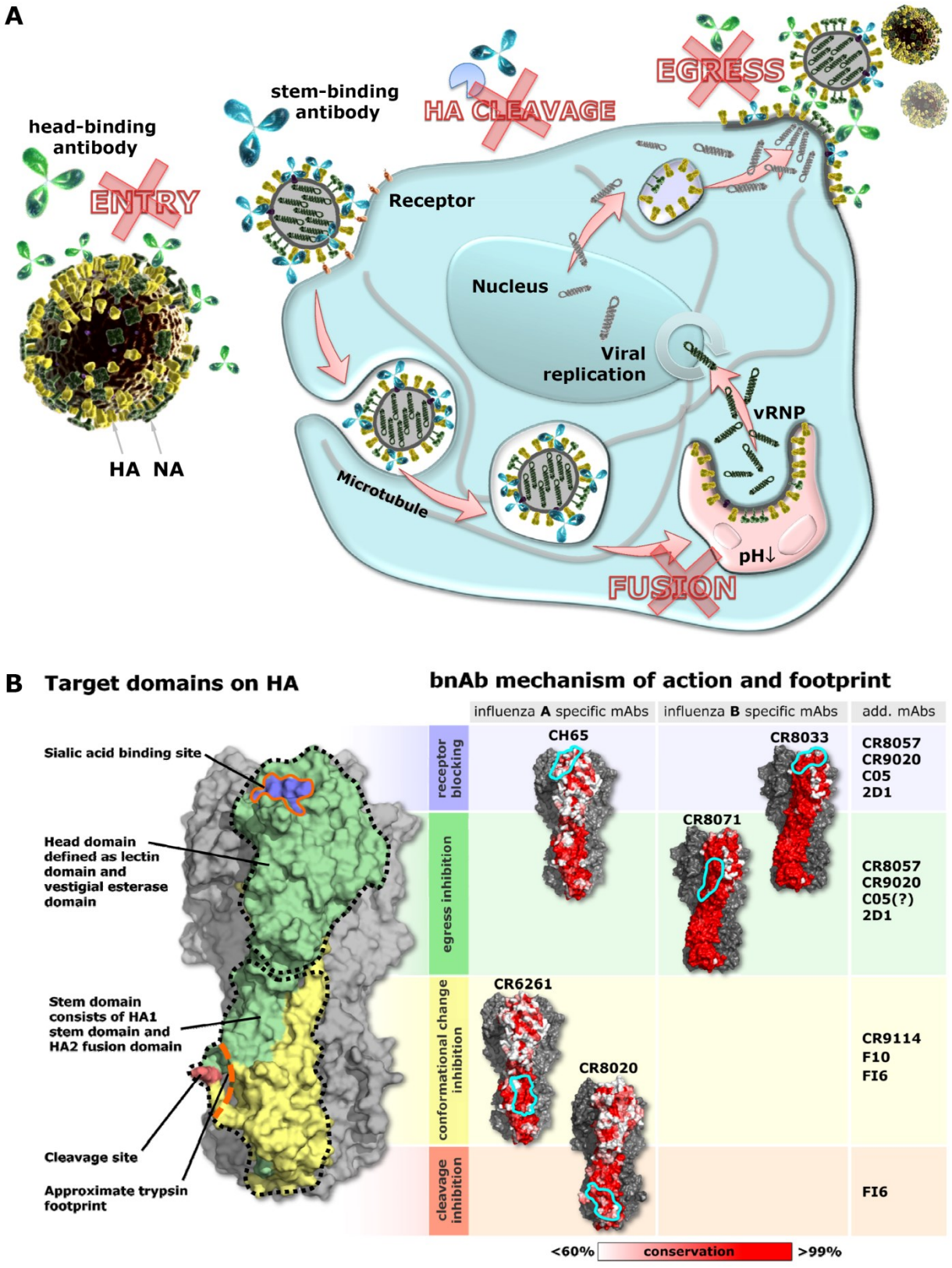

2.4 Materials and Methods

2.4.1 Cell Culture

Suspension PER.C6® (sPER.C6®) cells [35,36] were cultured in Adenovirus Expression Medium (AEM, Invitrogen) supplemented with 4 mM L-glutamine and passaged twice weekly. Cells were cultured at 37°C, 10 % CO_2 in a shaking incubator. The canine kidney cell line MDCK (ATCC, CCL-34) was cultured in Dulbecco's Modified Eagle Medium (DMEM) supplemented with 10 % fetal bovine serum and 2 mM L-Glutamine and passaged twice weekly. The lung adenocarcinoma cell line Calu-3 (ATCC, HTB-55) was cultured in the same medium supplemented with Non Essential Amino Acids and passaged once a week. Cells were cultured at 37°C, 10 % CO_2. All culture reagents were purchased from Invitrogen (Carlsbad).

2.4.2 Viruses

Purified wild type influenza viruses A/Puerto Rico/8/1934 (H1N1) and A/Aichi/1968-X31 (6:2 reassortant of A/Puerto Rico/8/1934 with the HA and NA segments of A/Aichi/1968 (H3N2)) propagated in eggs were purchased from Charles River Laboratories and used for live cell imaging. Stock samples were certified to contain 2 mg of protein per mL and stored at -80 ºC. A/New Caledonia/20/1999 (H1N1), A/NYMC/X-181 (6:2 reassortant of A/Puerto Rico/8/1934 with the HA and NA segments of A/California/07/2009 (H1N1)), A/Puerto Rico/8/1934 (H1N1), A/New Caledonia/20/1999 (H1N1), A/Brisbane/59/2007 (H1N1), A/Wisconsin/67/2005 (H3N2), A/Aichi/2/1968-X31 (H3N2), A/NYMC/X-161B (A/Puerto Rico/8/1934 with the HA and NA segments of A/Wisconsin/67/2005 (H3N2)), and B/Florida/04/2006 were grown by infecting sPER.C6® cells with virus at MOI $1x10^{-4}$ in infection medium (AEM and VP-FSM (2:1), supplemented with 2.6 mM L-glutamine and 3 µg/mL trypsin (all reagents from Invitrogen)). After 72 h of incubation, virus containing cell culture supernatant was harvested by centrifugation at 4000 g for 10 min. Virus aliquots were stored at -80 ºC. For colocalisation and

entry studies in live cells, A/New Caledonia/20/1999 and A/NYMC/X-161B were purified by ultracentrifugation at 27,000 rpm for 2 h at 4 ºC through a 25 % sucrose cushion. The virus pellet was resuspended in NTE buffer (150 mM NaCl, 10 mM Tris, 1mM EDTA), pH 7.4 overnight at 4 ºC before aliquotting and storage at -80 ºC.

Uncleaved viruses were produced by infecting sPER.C6® cells with cleaved virus at MOI 2 for 2 h in infection medium without trypsin. Cells were subsequently washed extensively with 10 % FBS in PBS and incubated in infection medium in the absence of trypsin. Virus supernatant was harvested by centrifugation at 4000 g for 10 min. All incubations were done at 35 ºC, 10 % CO_2, on a shaking platform. Uncleaved status of HA was confirmed by Western blotting after probing with H1-HA or H3-HA specific polyclonal serum and infection assays to confirm the absence of infection without prior treatment with 5 µg/mL trypsin for 30 min at 37 ºC.

All viruses were specifically titrated to reach > 90 % infection in each of the experimental conditions. Controls confirmed the successful infection in every experiment.

2.4.3 Antibodies (IgG expression, Fabs and polyclonal sera)

Fully human IgG1 antibodies CR6261, CR8020, CR8033, CR8057, CR9020, CR11054, and CR11055 were constructed and expressed as described previously (Ekiert et al., 2011). Fab fragments were obtained by IdeS digestion of antibodies, followed by purification via protein G (GE Healthcare), cation exchange (MonoS, GE Healthcare), and gel filtration (Superdex200, GE Healthcare). All antibodies and Fab fragments were more than 97 % pure and monomeric. Influenza A nucleoprotein (NP) specific monoclonal mouse antibody was obtained from Abbiotec (clone 5D8) and for influenza B NP from Santa Cruz (sc-52027). Goat $F(ab')_2$ anti-mouse- or anti-human Alexa Fluor conjugated secondary antibodies (Invitrogen) were used for fluorescent imaging at 2 µg/mL. HA specific rabbit polyclonal serum for Immunoblot analysis was obtained from Protein Sciences. Secondary HRP-coupled anti-rabbit F(ab')2-fragment were purchased from Jackson Immuno Research Laboratories (111-036-047). Polyclonal sheep sera

directed against B/Florida/4/2006 (07/356, sheep 478 and 479) were obtained from the NIBSC and derived from sheep immunized with the respective purified HA. HA-specific polyclonal serum was derived from mice immunized intramuscularly three times at a 3-week interval with 50 µg plasmid DNA encoding full-length A/Brisbane/59/07 HA, codon-optimized for mammalian expression, mixed with 50 µg plasmid DNA encoding murine Granulocyte Macrophage-Colony Stimulating Factor (GM-CSF).

In all experiments antibodies were either used at a range of concentrations or at sufficiently high concentration to neutralize the virus under the given experimental settings. This was confirmed by neutralization controls in every experiment. Imaging also confirmed that the used antibody concentrations were sufficient to binding nearly 100 % of viral particles including infectious and potentially non-infectious particles (Figure 2-1, Figure A1-1, Table A1-2).

2.4.4 Virus labeling

Purified and concentrated viruses were diluted in HNE buffer (5 mM Hepes, 140 mM NaCl, 0.2 mM EDTA, pH 7.4) for labeling. The lipophilic fluorescent dye, Octadecyl Rhodamine B chloride (R18, Molecular Probes) dissolved in DMSO or DMSO alone as a mock labeled control was added to the samples to a final dye concentration of 1-2µM and 0.4-0.5 % DMSO. The samples were mixed for 2-3h at room temperature, protected from light. Unincorporated dye was removed by passing the virus-dye solution through a PD-10 desalting column (GE Healthcare). Fractions containing labeled virus were pooled and labeling verified by fluorescence microscopy.

To confirm that labeling did not affect the infectivity of viruses, labeled- and mock-labeled virus samples were compared in imaged based infection assays (Figure A1-6). Only batches of labeled virus showing less than 2 fold differences in titer were used.

2.4.5 Antibody labeling

For imaging studies, HA-specific monoclonal antibodies were fluorescently labeled according to manufacturer's guidance with the amine reactive dyes (Molecular Probes) Alexa Fluor 488 (AF488) or Alexa Fluor 647 (AF647). Briefly, dye dissolved in DMSO was added to antibodies diluted in sodium bicarbonate buffer to a basic pH. For each antibody different dye concentrations where tested to avoid over-labeling. Contents were mixed and incubated for ~2h protected from light. Free dye was removed from the sample by desalting and buffer exchange using PD-10 sephadex G-25 columns (GE Healthcare). Antibodies were labeled with 3-8 dyes per IgG molecule.

The biological activity of all labeled antibodies was confirmed and compared to unlabeled antibodies in viral neutralization assays before they were used in imaging experiments. Only batches of labeled antibodies showing less than 2 fold differences in titer where used.

2.4.6 Virus Neutralization Assay (VNA)

MDCK cells were seeded on the day of experiment at 40,000 cells/well into 96-well flat bottom plates. Antibodies were serially diluted, mixed with an equal volume of viral inoculum and incubated for 2 h at 37 ºC in medium (DMEM supplemented with 2 mM L-glutamine and 3 µg/mL trypsin-EDTA). The mixture (~100 $TCID_{50}$/well) was then added to confluent MDCK monolayers in quadruplicate. Cells were cultured for 72h before supernatant was added to an equal volume of 1 % Turkey red blood cells and incubated for 1h at room temperature in a 96-well V-bottom plate. The absence of hemagglutination was defined as protection. Titers were determined using the Spearman-Kärber formula.

2.4.7 Hemagglutination inhibition (HI) Assay

Virus was diluted to 8 HA units/50μL and 25μL was combined in quadruplicate wells with an equal volume of antibody serially diluted in PBS. Plates were incubated for 1h at 37 ºC in 96-well V-bottom plates. 50 μL of 1 % Turkey red blood cells was then added to each well and incubated for 1h at room temperature. Button formation was scored as evidence of hemagglutination inhibition. Titers were determined using the Spearman-Kärber formula.

2.4.8 Imaging

All experiments were performed using black flat bottom 96-well imaging plates (BD Falcon) which were sealed with oxygen permeable film (Sigma Aldrich) before imaging. Images were taken after laser-based auto-focusing using a Pathway 855 high content imager (Becton Dickinson) equipped with different objectives (Olympus: 4X 0.16 NA, 20X 0.75 NA, and 40X 0.90 NA). Movies were taken with the 40X objective at4 frames/s while alternating between two channels over the duration of 3-5 min. For the overnight tracking of cells images were automatically taken at pre-defined positions over the duration of ~15 h at ~30 min intervals. Confirming infection (NP expression) after fixation and staining of the cells was carried out at the same pre-defined positions with the 40X objective, and also throughout the well with a 20X objective to determine the percentage of infected cells. Images of individual channels where overlaid and movies were compiled using ImageJ software [37]. Due to limited recording speed and alternating channels the registration of fast moving particles is not perfectly synchronized leading sometimes to the artificial separation of virus and antibody signal in adjacent movie frames. To determine the percentage of infected cells, image channels (e.g. cell nucleus and cytoplasm) were analyzed and segmented using Attovision software (Becton Dickinson) followed by the IC_{50} value calculation by SPSS software (IBM) and graphs plotted using GraphPad Prism software.

2.4.9 Imaged based infection assay

Cells were infected with an MOI of 3 for at least 15 h and then rinsed twice with PBS followed by fixation with 80 % ice cold acetone for 10 min. After removing the acetone and drying the wells the plates were washed 3 times with 300 µL per well wash buffer (PBS, 0.05 % Tween-20) then incubated for 1 h with mouse anti-influenza NP antibody (1 µg/mL) in antibody dilution buffer (1 % BSA, 0.1 % Tween-20 in PBS) at room temperature. After washing three times with 300 µL wash buffer the wells were incubated with 2 µg/mL goat-anti mouse AF488 labeled secondary antibody and 1 µg/mL 4',6-diamidino-2-phenylindole (DAPI) for 1 h. After three wash steps buffer was replaced with 100 µL PBS containing 0.25 mM Sodium Azide, plates sealed, and imaged.

2.4.10 HA-specific staining of particles and infected cells

All staining steps described below were performed for 1h at room temperature in the dark. *Viral particles*: R18-labelled A/New Caledonia/20/99 (H1N1), A/Puerto Rico/8/34 (H1N1), A/NYMC/X-161B (H3N2) or A/Aichi/68-X31 (H3N2) virus was diluted in CO_2-independent medium (Invitrogen) supplemented with 2 mM L-glutamine and spotted onto glass bottom 96-well imaging plates for 30 min at 37 ºC before washing with PBS and staining with anti-HA specific antibodies at 5 µg/mL in 1% BSA/PBS, followed by detection with 2 µg/mL goat anti-human-Alexa Fluor 647 secondary antibody. Wells were washed four times with medium before replacing with CO_2-independent (phenol red free) medium (Invitrogen) supplemented with 2 mM L-glutamine for imaging.

Infected cells: MDCK cells were infected overnight with virus serially diluted in DMEM supplemented with 2 mM L-glutamine before fixing with either 3% paraformaldehyde (PFA) in PBS or ice cold 80% acetone for 10 min. Staining was carried out as mentioned for viral particles under both permeabilizing (acetone) and non-permeabilizing (PFA) conditions. Under

permeabilizing conditions, cells were also stained for influenza NP to confirm the presence of viral infection. Nuclei were counterstained with 0.1 µg/mL DAPI.

2.4.11 Virus entry inhibition

An immunofluorescence entry assay was designed to assess the ability of HA head-binding antibodies to prevent viral internalization into cells. R18-labelled H1N1 or H3N2 (MOI 3) was pre-incubated with Alexa-Fluor 647 labeled HA-specific antibodies to a final concentration of 30 µg/mL (200 nM) for 1h at 37 ºC before being added to MDCK cells seeded in 96-well black-sided imaging plates (Becton Dickinson). MDCK cells stably expressing a GFP cell marker (OriGene, Rockville, USA) were incubated with virus for 15 min at 37 ºC followed by treatment of the cells with 0.05 U/well neuraminidase (Sigma) for 5 min at 37 ºC to remove non-internalized viruses. Cells were washed twice with PBS before imaging live in CO_2-independent medium supplemented with 2 mM L-glutamine.

2.4.12 Virus internalization

An immunofluorescence internalization assay was designed to assess the ability of HA stem-binding antibodies to be internalized into cells in complex with infectious virus particles. A pre-determined amount of R18-labelled H1N1 or H3N2 virus giving rise to 90-100 % infection under the following experimental conditions was pre-incubated with Alexa-Fluor 647 labeled HA-specific bnAbs to a final concentration of 30 µg/mL (200 nM) for 1h at 37 ºC. MDCK cells were treated for 5min at 37 ºC with the cell permeant nuclear counterstain Hoechst 33342 (10 µg/mL, Invitrogen), followed by treatment with 3µM tubulin tracker green reagent (Molecular Probes) for 30 min at 37 ºC to stain the microtubules. Cells were then incubated for 15 min at 37 ºC with the prepared virus-antibody mixture, followed by treatment with 0.05U/well neuraminidase (Sigma Aldrich) for 5 min at 37 ºC. All reagents were diluted in CO_2-independent medium supplemented with 2 mM L-glutamine. Cells were washed four times in medium before imaging live in CO_2-

independent medium supplemented with 2 mM L-glutamine and the glucose oxidase/catalase oxygen scavenging system (GODCAT, 1 % glucose, 0.5 mg/mL glucose oxidase, 40 µg/mL catalase; all reagents from Sigma) to prevent photobleaching [38]. To avoid a decrease in cell viability and viral replication the exposure with light and oxygen scavenging system was limited to two hours and the medium then replaced. Movies were captured at manually selected positions with a 40X 0.90 NA objective.

2.4.13 Virus colocalization

Mock-labelled H1N1 or H3N2 virus was pre-incubated with Alexa-Fluor 647 labeled anti-HA bnAbs to a final concentration of 30 µg/mL (200 nM) for 1h at 37 ºC. Immediately prior to infection, MDCK cells were treated for 5 min at 37 ºC with the cell permeant nuclear dye Hoechst 33342 (Invitrogen) at 10 µg/mL. Cells were then infected with the virus-mAb mixture (MOI 3) mixed 1:1 with 100 nM Lysotracker Red reagent (Molecular Probes) for 15 min at 37 ºC, followed by treatment with 0.05 U/well neuraminidase (Sigma Aldrich) for 5 min at 37 ºC. All reagents were diluted in CO_2-independent medium supplemented with 2 mM L-glutamine. Cells were washed four times with medium before imaging live in CO_2-independent medium supplemented with 2 mM L-glutamine and the glucose oxidase/catalase oxygen scavenging system.

2.4.14 Colocalization analysis

To determine percentage colocalization between R18-labelled virus and AF647-labelled antibodies, images were analyzed using ImageJ software with the particle analysis plugin – 3D Object Counter [39].

2.4.15 Overnight cell tracking

A pre-determined amount of R18-labelled H1N1 or H3N2 virus giving rise to 90-100 % infection under the following experimental conditions, was pre-incubated with Alexa-Fluor 647 labeled anti-HA bnAbs to a final concentration of 30 µg/mL (200 nM) for 1h at 37 ºC. MDCK cells stably expressing a GFP cell marker, were seeded into 96-well black-sided imaging plates and subsequently infected with the virus-mAb mixture for 15min at 37 ºC, followed by treatment with 0.05 U/well neuraminidase for 5 min at 37 ºC. All reagents were diluted in CO_2-independent medium supplemented with 2 mM L-glutamine. Cells were washed extensively before imaging live for 15 h in CO_2-independent medium supplemented with 2 mM L-glutamine and 1 % FBS. The following day, cells were fixed with ice cold 80 % acetone for 10min and stained for influenza A NP expression as previously described to confirm infection inhibition in the presence of neutralizing antibody.

2.4.16 Single particle fusion assays

Fusion experiments were executed as described in the supporting information. Briefly, R18-labeled viruses were pre-incubated with either AF488 labeled or unlabeled bnAb. A proteoliposome solution was added to the microfluidic flow cell to form a glass-supported planar lipid bilayer. Virus-bnAb mixture was added to the flow cell and viruses were immobilized onto the planar lipid bilayer (Figure A1-2). Fluorescein-labeled streptavidin was then added followed by washing. Viral fusion was initiated by rapid injection of a pH5 buffer and recorded using an inverted TIRF microscope setup. Fusion events were detected as a sharp temporary increase in the fluorescence. Fusion percentage was calculated as the number of fusion events divided by the total number of virions observed in a field of view.

2.4.17 HA-cleavage inhibition

To study the additive effect of HA-cleavage inhibition, uncleaved A/Wisconsin/67/05 (H3N2, MOI 3) was either first incubated with trypsin (Gibco) at 1.5 µg/mL, followed by incubation with antibodies serially diluted from 0 - 10 µg/mL (0 - 67 nM), or, first incubated with antibodies serially diluted from 0 - 10 µg/mL, followed by incubation with trypsin at 1.5 µg/mL. FBS was added to a final concentration of 10 % after trypsin treatment to inhibit trypsin activity and all incubation steps were carried out for 45 min at 37 ºC. Virus-antibody mixtures were then added to confluent MDCK monolayers and allowed to incubate overnight. HA cleavage status was verified by Western blot analysis with a portion of the treated samples (data not shown). Cells were fixed with ice cold 80 % acetone for 10 min and stained for influenza A NP expression as described above. Calu3 cells were infected with cleaved A/Wisconsin/67/05 (H3N2) or A/New Caledonia/20/99 (H1N1) with an MOI 3 in DMEM supplemented with 2 mM L-Glutamine. Three hours post infection cells were washed twice with PBS and incubated overnight with a concentration range (0-100 µg/mL) of test or control antibody in 50 µL medium and incubated overnight. The following day, the medium of three replicate wells was pooled and spun down for 10 min at 200 x g to remove cell debris. One well from each triplicate was used to obtain cell lysate by resuspending the cell layer in 150 µL lysis buffer (50 mM Tris-HCl, 150 mM NaCl, 5 mM EDTA, 1 % Triton X-100, pH 7.5). As a positive control for HA cleavage, supernatant from cells infected with virus in the absence of antibody was used and treated with 5 µg/mL trypsin for 30 min at 37 ºC for complete HA cleavage. Samples were then subject to Western blot analysis. To confirm viral infection, plates were also fixed and stained with ice cold 80 % acetone for 10 min and stained for Influenza A NP expression.

2.4.18 Statistical analyses

Single-particle fusion, and cleavage inhibition data were analyzed using a 4-parameter logistic model in which for variance stabilization the '*transform both sides'* approach was used as described previously [40]. For transformation, a logit transformation was selected:

$$logit[F] = logit\left[D + \frac{A - D}{1 + \left({}^{X}/_{10^{c}}\right)^{B}}\right]$$

where F represents the proportion fusing virions over total virions, D and A represent respectively the upper and lower asymptote, B represents a slope factor, X represents the antibody concentration (nM) and C represents the inflection point (estimated on a $\log_{10}$ scale). For stabilization of the model fusion data obtained without antibody present was placed at an *infinite* low antibody concentration. Conditions with no events were set to 1 fusion event.

To be able to determine the effect of trypsin on the potency of CR8020, the model was modified to include an indicator variable in the estimation of the inflection point that takes the value 0 for data before trypsin and a 1 for data after trypsin (C + ID*Δc). The difference, in location, between the dose-response curves is then indicated by Δc and represents a difference in potency of the mAb under these conditions. Statistical analysis was performed using IBM SPSS statistics (version 20).

2.4.19 SDS-PAGE and Immunoblotting

Relative amounts and cleavage status of hemagglutinin in the samples were determined by Western blotting. First 2 µL reducing agent (Invitrogen) and 5 µL 4x loading buffer (Ivitrogen) was added to 13 µL sample followed by 10 min incubation at 90 ºC. Proteins in each sample were resolved by 4-12% Bis-Tris SDS-PAGE (NUPAGE, Invitrogen) followed by trans-blotting onto a PVDF membrane (0.45 µm, P-Immobilon, Millipore, Massachusetts) in transfer buffer (NUPAGE, Invitrogen) containing 5 % methanol at 30 V for 60 min. The membrane was blocked

by incubation in blocking solution containing 4 % non-fat dry milk (Bio-Rad) in TBST (20 mM Tris-HCl, 150 mM NaCl, 0.2 % Tween 20) overnight at 4 ºC. The blocked membrane was incubated with rabbit anti-HA1 or -HA3 polyclonal serum, 60 ng/mL for 1 h at room temperature and washed 3 times with TBST. Subsequently, the membrane was incubated with goat anti-rabbit peroxidase conjugated $F(ab')_2$ fragment (1:3,000 v/v) for 1 h at room temperature. After three washes with TBST, the membranes were incubated for 5 min with ECL-Plus substrate solution (GE Healthcare). Stained proteins were visualized using Amersham Hyperfilms (GE Healthcare).

2.4.20 Egress inhibition assay

Four hours prior to the experiment, 40,000 MDCK cells per well were seeded in DMEM/glutamine into flat bottom 96 well imaging plates (BD Falcon). The amount of virus needed to achieve 90-100 % infection was titrated in a separate experiment. The required amount of virus was added to the cells washed twice with PBS and incubated at 37 °C, 5 % CO_2. After three hours, the supernatants were removed and cells were washed twice with PBS to remove non-internalized virus particles. Cells were replenished with 50 µL infection medium containing serial diluted antibodies. After incubation for 16 – 18 h at 37 °C, 5 % CO2, the supernatants were harvested, spun down to remove debris (200 x g for 10 min). The remaining cells were lysed (Tris HCl pH 7.5, 150 mM NaCl, 5 mM EDTA, 1 % (v/v) Triton-X). Lysate and supernatant samples were treated with loading buffer and reducing agent, incubated for 10 min at 90 °C, and analyzed by SDS-PAGE and Western blot to determine the amount of virions produced and released into the supernatant. As a control for infection, replicate identically-treated wells were fixed with 80 % acetone and the number of infected cells was assessed using the imaged based infection assay (data not shown).

2.4.21 Scanning electron microscopy of influenza virus infected cells

MDCK cells seeded on coverslips (sterile 15 mm thermanox plastic, Thermo Scientific, #174969) were infected with a pre-determined amount of virus (separate experiment) to yield 90 – 100 % infected cells 18 h post infection. Three hours after the initial infection, the supernatants were removed; cells were washed thrice with PBS, before media containing the indicated concentration of antibodies were added. After an additional 15 h, the cell culture medium was removed and cells were fixed in phosphate buffered 2.5 % glutaraldehyde buffer pH 7.4 for 1 – 2 h and stored at 4 °C until further analysis. The coverslips were rinsed in PBS followed by distilled water and then dehydrated in 70 %, 95 %, anhydrous ethanol and finally in acetone and subjected to critical point drying in acetone and liquid CO_2. Finally, the cells were mounted on alumina stubs and coated with a thin layer of carbon and examined in a Zeiss Ultra 55 SEM field emission microscope using an accelerating voltage of 3 keV and InLens detection at Vironova, Sweden.

2.4.22 Transmission electron microscopy of influenza virus infected cells

MDCK cells seeded on coverslips were infected with a pre-determined amount of virus (separate experiment) to yield 90 – 100 % infected cells 18 h post infection. Three hours after the initial infection, the supernatants were removed; cells were washed thrice with PBS, before media containing the indicated concentration of antibodies were added. After an additional 15 h, the cell culture medium was removed and cells were fixed in phosphate buffered 2.5 % glutaraldehyde buffer for 1 – 2 h and stored at 4 °C until further analysis. The samples were subsequently scraped and pelleted using a table top centrifuge, before being washed twice in 0.1 M phosphate buffer and chemically post-fixed with 2 % osmium tetroxid (OsO4) in 0.1 M phosphate buffer for 2 h at 4 °C followed by stepwise dehydration with ethanol, followed by LX 112-embedding by stepwise infiltration and polymerization at 60 °C. Microtome sections of ~ 60 nm were prepared and applied to one-slot formvar nickel grids. The sections were finally

post-stained with uranyl acetate and Reynold's lead citrate before being imaged with a FEI Tecnai 10 electron microscope run at 100 kV accelerating voltage using a 2k x 2k Veleta CCD camera (Olympus Soft Imaging Systems) at Vironova, Sweden.

2.5 References

1. Burton DR, Poignard P, Stanfield RL, Wilson IA (2012) Broadly neutralizing antibodies present new prospects to counter highly antigenically diverse viruses. Science 337: 183-186.

2. Gerhard W (2001) The role of the antibody response in influenza virus infection. Curr Top Microbiol Immunol 260: 171-190.

3. Bertram S, Glowacka I, Steffen I, Kuhl A, Pohlmann S (2010) Novel insights into proteolytic cleavage of influenza virus hemagglutinin. Rev Med Virol 20: 298-310.

4. Gamblin SJ, Skehel JJ (2010) Influenza hemagglutinin and neuraminidase membrane glycoproteins. J Biol Chem 285: 28403-28409.

5. Throsby M, van den Brink E, Jongeneelen M, Poon LL, Alard P, et al. (2008) Heterosubtypic neutralizing monoclonal antibodies cross-protective against H5N1 and H1N1 recovered from human IgM+ memory B cells. PLoS One 3: e3942.

6. Ekiert DC, Bhabha G, Elsliger MA, Friesen RH, Jongeneelen M, et al. (2009) Antibody recognition of a highly conserved influenza virus epitope. Science 324: 246-251.

7. Sui J, Hwang WC, Perez S, Wei G, Aird D, et al. (2009) Structural and functional bases for broad-spectrum neutralization of avian and human influenza A viruses. Nat Struct Mol Biol 16: 265-273.

8. Ekiert DC, Friesen RH, Bhabha G, Kwaks T, Jongeneelen M, et al. (2011) A highly conserved neutralizing epitope on group 2 influenza A viruses. Science 333: 843-850.

9. Corti D, Voss J, Gamblin SJ, Codoni G, Macagno A, et al. (2011) A neutralizing antibody selected from plasma cells that binds to group 1 and group 2 influenza A hemagglutinins. Science 333: 850-856.

10. Dreyfus C, Laursen NS, Kwaks T, Zuijdgeest D, Khayat R, et al. (2012) Highly conserved protective epitopes on influenza B viruses. Science 337: 1343-1348.

11. Whittle JR, Zhang R, Khurana S, King LR, Manischewitz J, et al. (2011) Broadly neutralizing human antibody that recognizes the receptor-binding pocket of influenza virus hemagglutinin. Proc Natl Acad Sci U S A 108: 14216-14221.

12. Krause JC, Tsibane T, Tumpey TM, Huffman CJ, Basler CF, et al. (2011) A broadly

neutralizing human monoclonal antibody that recognizes a conserved, novel epitope on the globular head of the influenza H1N1 virus hemagglutinin. J Virol 85: 10905-10908.

13. Ekiert DC, Kashyap AK, Steel J, Rubrum A, Bhabha G, et al. (2012) Cross-neutralization of influenza A viruses mediated by a single antibody loop. Nature 489: 526-532.

14. Friesen RH, Koudstaal W, Koldijk MH, Weverling GJ, Brakenhoff JP, et al. (2010) New class of monoclonal antibodies against severe influenza: prophylactic and therapeutic efficacy in ferrets. PLoS One 5: e9106.

15. Koudstaal W, Koldijk MH, Brakenhoff JP, Cornelissen LA, Weverling GJ, et al. (2009) Pre- and postexposure use of human monoclonal antibody against H5N1 and H1N1 influenza vir us in mice: viable alternative to oseltamivir. J Infect Dis 200: 1870-1873.

16. Ekiert DC, Wilson IA (2012) Broadly neutralizing antibodies against influenza virus and prospects for universal therapies. Curr Opin Virol 2: 134-141.

17. Julien JP, Lee PS, Wilson IA (2012) Structural insights into key sites of vulnerability on HIV-1 Env and influenza HA. Immunol Rev 250: 180-198.

18. Nabel GJ, Fauci AS (2010) Induction of unnatural immunity: prospects for a broadly protective universal influenza vaccine. Nat Med 16: 1389-1391.

19. Reading SA, Dimmock NJ (2007) Neutralization of animal virus infectivity by antibody. Arch Virol 152: 1047-1059.

20. Han T, Marasco WA (2011) Structural basis of influenza virus neutralization. Ann N Y Acad Sci 1217: 178-190.

21. Corti D, Lanzavecchia A (2013) Broadly neutralizing antiviral antibodies. Annu Rev Immunol 31: 705-742.

22. Okuno Y, Isegawa Y, Sasao F, Ueda S (1993) A common neutralizing epitope conserved between the hemagglutinins of influenza A virus H1 and H2 strains. J Virol 67: 2552-2558.

23. Brandenburg B, Zhuang X (2007) Virus trafficking - learning from single-virus tracking. Nat Rev Microbiol 5: 197-208.

24. Floyd DL, Harrison SC, van Oijen AM (2009) Method for measurement of viral fusion kinetic s at the single particle level. J Vis Exp 31: e1484.

25. Floyd DL, Ragains JR, Skehel JJ, Harrison SC, van Oijen AM (2008) Single-particle kinetics of influenza virus membrane fusion. Proc Natl Acad Sci U S A 105: 15382-15387.

26. Bottcher E, Matrosovich T, Beyerle M, Klenk HD, Garten W, et al. (2006) Proteolytic activation of influenza viruses by serine proteases TMPRSS2 and HAT from human airway epithelium. J Virol 80: 9896-9898.

27. Bottcher-Friebertshauser E, Stein DA, Klenk HD, Garten W (2011) Inhibition of influenza

virus infection in human airway cell cultures by an antisense peptide-conjugated morpholino oligomer targeting the hemagglutinin-activating protease TMPRSS2. J Virol 85: 1554-1562.

28. Burton DR (2002) Antibodies, viruses and vaccines. Nat Rev Immunol 2: 706-713.

29. Hangartner L, Zinkernagel RM, Hengartner H (2006) Antiviral antibody responses: the two extremes of a wide spectrum. Nat Rev Immunol 6: 231-243.

30. Thomson CA, Wang Y, Jackson LM, Olson M, Wang W, et al. (2012) Pandemic H1N1 Influenza Infection and Vaccination in Humans Induces Cross-Protective Antibodies that Tar get the Hemagglutinin Stem. Front Immunol 3: 87.

31. Rigg RJ, Carver AS, Dimmock NJ (1989) IgG-neutralized influenza virus undergoes primary, but not secondary uncoating in vivo. J Gen Virol 70 (Pt 8): 2097-2109.

32. Edwards MJ, Dimmock NJ (2000) Two influenza A virus-specific Fabs neutralize by inhibiting virus attachment to target cells, while neutralization by their IgGs is complex and occurs simultaneously through fusion inhibition and attachment inhibition. Virology 278: 423-435.

33. Yu X, Tsibane T, McGraw PA, House FS, Keefer CJ, et al. (2008) Neutralizing antibodies derived from the B cells of 1918 influenza pandemic survivors. Nature 455: 532-536.

34. Barbey-Martin C, Gigant B, Bizebard T, Calder LJ, Wharton SA, et al. (2002) An antibody that prevents the hemagglutinin low pH fusogenic transition. Virology 294: 70-74.

35. Jones D, Kroos N, Anema R, van Montfort B, Vooys A, et al. (2003) High-level expression of recombinant IgG in the human cell line per.c6. Biotechnol Prog 19: 163-168.

36. Sanders BP, Edo-Matas D, Custers JH, Koldijk MH, Klaren V, et al. (2013) PER.C6((R)) cells as a serum-free suspension cell platform for the production of high titer poliovirus: a potential low cost of goods option for world supply of inactivated poliovirus vaccine. Vaccine 31: 850-856.

37. Schneider CA, Rasband WS, Eliceiri KW (2012) NIH Image to ImageJ: 25 years of image analysis. Nat Methods 9: 671-675.

38. Vaughan JC, Brandenburg B, Hogle JM, Zhuang X (2009) Rapid actin-dependent viral motility in live cells. Biophys J 97: 1647-1656.

39. Bolte S, Cordelieres FP (2006) A guided tour into subcellular colocalization analysis in light microscopy. J Microsc 224: 213-232.

40. Findlay JW, Dillard RF (2007) Appropriate calibration curve fitting in ligand binding assays. Aaps J 9: E260-267.

Chapter 3

Jason Otterstrom [1,2], Martin Koldijk [3], Jarek Juraszek [3], Chan Tang [3], Samaneh Mashaghi [2], Boerries Brandenburg [3], Antoine M. van Oijen [2]

1) Harvard University Biophysics Program, Harvard Medical School, Boston, MA, 02115, USA

2) Centre for Synthetic Biology, Zernike Institute for Advanced Materials, University of Groningen, Groningen, 9747AG, The Netherlands

3) Crucell Vaccine institute, Janssen Center of Excellence for Immunoprophylaxis, Leiden, 2333 CN, The Netherlands

Experimental design was conceived by Dr. Antoine van Oijen, Dr. Boerries Brandenburg and myself. I designed and constructed the fluorescence microscope, performed experiments, and wrote data extraction and analysis programs. Together with Dr. Martin Koldijk, we statistically analyzed the data. Jarek Juraszek performed Monte Carlo modeling (Appendix 2) and together we interpreted the results in light of experimental data. Together with Samaneh Mashaghi, we performed the full fusion experiments (Appendix 2). Together with Dr. Antoine van Oijen, we wrote the thesis chapter. I used data obtained to make all figures in this chapter, in Appendix 2 and the supplemental movie M2-1.

Chapter 3

Single-Particle Studies Quantitatively Relate Influenza Membrane-Fusion Kinetics with Stoichiometry of Neutralizing Antibodies

Abstract

Neutralization of influenza virus infectivity as a direct action of antibody binding is of key importance in the design of next-generation vaccines and prophylaxes. The two novel antibodies CR6261 and CR8020 have recently been shown to inhibit influenza A hemagglutinin (HA)-mediated membrane fusion through epitope binding and efficiently neutralize infection [1]. Here, we directly correlate the number of antibodies or Fab fragments bound to a virion with that virus particle's capacity for membrane fusion using single-particle fluorescence microscopy. Individual virus particles bound by labeled antibodies or their Fab fragments are visualized during their fusion to a planar supported bilayer. The fluorescence intensity arising from the virus-bound antibodies or Fab is directly proportional to the number present on the viral surface and so provides access to the stoichiometry required for fusion inhibition. We find fusion inhibition by both antibody and Fab with stoichiometries that leave large numbers of unbound HA epitopes on the viral surface. Simultaneous kinetic measurements of the fusion process reveal that those few particles capable of fusion at high antibody/Fab coverage display significantly slower hemifusion kinetics. Overall, our results support a membrane fusion mechanism requiring the stochastic, coordinated action of multiple HA trimers and a model of fusion inhibition by stem-binding antibodies through disruption of inter-HA coordination.

3.1 Introduction

Antibodies neutralizing the infection from a broad spectrum of influenza viruses are seeding new hopes for more effective – and perhaps universal – vaccines to thwart annual influenza A epidemics [2-5]. Influenza is an enveloped virus decorated with large numbers of the fusion protein hemagglutinin (HA) embedded in its viral membrane (Figure 3-1A). HA is a protein of keen interest because it is a critical antigenic target of the immune system and antibodies targeting it can exhibit direct neutralizing activity [1,6-9][9]. Furthermore, HA represents a model system for the study of protein-mediated membrane fusion [10]. Decades of investigation have elucidated the main principles of HA-mediated membrane fusion, but a number of open questions still remain [10] and the ways HA-antibody interactions can disrupt the fusion process are still in need of thorough characterization [11,12].

The HA protein is a homotrimeric transmembrane protein with each protomer consisting of two separate, disulfide-linked domains [13,14]. The HA1-containing “head” domain distal from the viral envelope contains a binding site for sialic acid moieties that allow a virus to bind to a target cell. The HA2-containing “stem” is comprised mostly of the envelope-proximal ectodomain and the transmembrane domain. During infection, influenza viruses are initially taken into a cell by clathrin-mediated endocytosis. In response to the low pH of late endosomes, the stem undergoes drastic conformational changes that serve to mediate fusion between the viral envelope and the endosomal membrane to release the viral genome into a cell and initiate infection. Influenza A HA is classified into 17 subtypes that are collected into two phylogenetically distinct groups [15,16] – Group 1 and Group 2 – and hence exhibits substantial antigenic drift. Head-binding antibodies typically recognize variable loop regions surrounding the receptor site and thus show strain-specific neutralization [5,9,17], though some can neutralize a limited set of viral strains [18-20]. In contrast, stem-binding antibodies recognize an epitope region that is highly conserved between influenza strains [21] and possess a broad neutralization capacity that can span an entire phylogenetic group [6,7,18,22-24] or

even across the two groups [8,18,25]. Antibodies against such conserved regions are of interest for their use as anti-flu therapeutics and for rational design of vaccines, HA-binding proteins and small molecules [2-5,26].

Two well characterized broadly neutralizing, stem-binding antibodies are the Group 1 HA-specific CR6261 and the Group 2 HA-specific CR8020 [6,7,22]. They are effective in neutralizing influenza infection from a broad range of strains both prophylactically and therapeutically in animal models [7,27]. We recently demonstrated that binding of HA by these antibodies directly resulted in inhibition of HA-mediated viral membrane fusion [1]. Due to epitope similarity, fusion inhibition is likely to be an effect shared by the other known broadly neutralizing, stem-binding antibodies C179, F10, FI6v3, 39.29, 81.39 and CR9114 [8,18,23-25]. The ability of antibodies to block fusion confirms the accessibility of their membrane-proximal epitope on intact viruses despite the dense packing of surface proteins (Figure 3-1A), and was also recently shown by cryo-electron tomography [28]. An open question regarding stem-binding antibodies is the binding stoichiometry required for virus neutralization.

Neutralization stoichiometry is at least partly dependent on the binding affinity, K_d, for the antibody to its epitope [5,29]. Though of key importance to determining an antibody's neutralization efficacy, K_d on the a viral surface in its structurally and physiologically relevant context is often not known. [5,30]. Moreover, virus pleiomorphy and high surface protein density can occlude many epitopes, blocking antibody accessibility and reducing avidity for the epitope. A previous stoichiometry measurement on influenza using quantification through radioisotope labeling of neutralizing antibodies found that infectivity could be reduced by 50% with as few as ~50 antibody molecules, but reductions to 0.05% infectivity required more than 1200 antibodies [31]. These results are in line with multi-hit and coating models describing stoichiometry, which predict large numbers of epitopes must be bound for a virus to be neutralized, rather than single-hit models involving a critical site vulnerable to neutralization [11,12,32]. The antibodies used in these studies, however, were poorly characterized in terms of epitope mapping and their

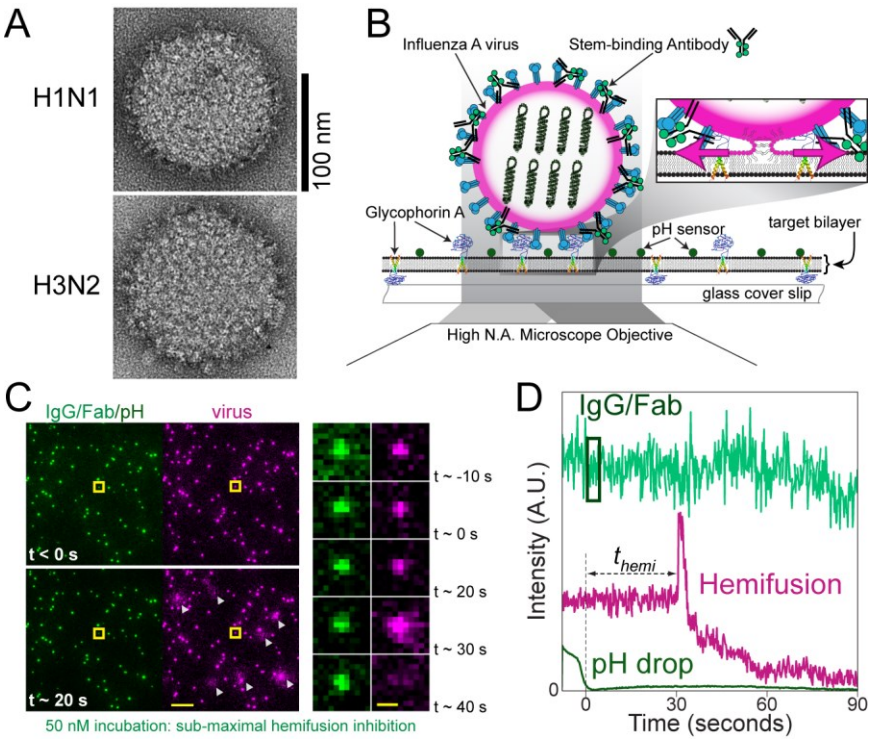

Figure 3-1 – *Experimental design and readouts.* ***A****) Transmision electron micrographs at 45,000x of two influenza A viruses, H1N1 on top and H3N2 on the bottom.* ***B****) Schematic depiction of experimental design. Alexa 488-labeled IgG (or Fab) are bound to R18-labeled influenza A viruses (magenta-edged sphere). Viruses are then immobilized on a glass-supported planar bilayer through interaction with glycophorin A; pH-sensitive fluorescein (pK_a 6.4) is also bound to the bilayer surface. Fluorescence is excited and detected via objective TIRF microscopy. Zoom-in: acidification of the virus particles causes membrane fusion to occur that results in escape of the R18 dye from the viral membrane into the target bilayer through a hemifusion intermediate and produces a dequenching signal.* ***C****) Left: false-color still frames from a fusion movie at time points before (upper) and 20 seconds after (lower) the pH drop; scalebar = 10 μm. For each frame, the left half-image visualizes IgG/Fab (green spots, 50 nM incubation) and fluorescein (diffuse background), while the right half-image simultaneously visualizes the R18-labeled viruses (magenta) and their low pH-induced dequenching (white triangles). Right: image montage of the virus highlighted by the yellow square. Subsequent frames from the fusion movie show a virus covered with a sub-inactivating number of IgG molecules (green) fusing to the bilayer, seen as a flash of R18 intensity (magenta) followed by its diffusion outward (scalebar = 1 μm).* ***D****) Fluorescence time trajectory for the highlighted virus in (C) where time t = 0 is set after the average green fluorescence intensity sharply decreases upon arrival of the fusion-inducing pH 5.0 buffer. The virus-bound IgG/Fab fluorescence used for stoichiometry measurements is indicated by the dark-green box, located 1 second after the pH drop and enclosing 3 seconds worth of fluorescence information. Hemifusion is observed for this virus particle by the abrupt increase in R18 fluorescence. The time to hemifusion, t_{hemi}, occurs for this virus at t ≈ 30 seconds.*

precise mechanism of action. Furthermore, the traditional viral plaque assays that were used are prone to complicating factors, such as dependencies on cell type and cell confluency [11], and the potential to miss single-round infection [33]. Additionally, neutralization arose from a convolution of cell-binding inhibition, inhibition of membrane fusion, aggregation of virus particles and the abrogation of post-entry events that cannot be directly delineated from one another [9,12].

We previously adapted our single-particle viral fusion assay [34] to incorporate high concentrations of CR6261 and CR8020 to demonstrate that these antibodies act directly to inhibit HA-mediated membrane fusion [1]. The experimental design of the single-particle fusion assay described in [1] is extended to quantify the number of CR6261 or CR8020 antibodies (IgG) or their Fab-fragments (Fab) that must bind to a virus for membrane fusion to be inhibited. We find that under conditions of maximal hemifusion inhibition, virus particles rendered non-fusogenic likely contain many HA trimers that are unbound and could be triggered by low pH. Furthermore, binding of the neutralizing IgG/Fab molecules causes a delay in the kinetics of membrane fusion. The high temporal resolution and single-particle nature of our methodology are crucial in gaining access to this information and provide insight into the mechanism of HA-mediated fusion that is difficult to obtain via conventional approaches [35].

3.2 Results

3.2.1 Fluorescently labeled IgG and Fab inhibit hemifusion.

Low pH-induced HA-mediated hemifusion of a virion to a planar target bilayer is visualized as a rapid fluorescence burst at the site of a virus particle, as depicted in Figure 3-1 and previously described [34,36]. Prior to immobilization on the bilayer surface, R18 labeled viruses (A/Puerto Rico/8/34 H1N1 or A/Aichi/68-X31 H3N2) were incubated with the broadly neutralizing, stem-binding antibodies CR6261 or CR8020 (collectively: IgG), or their Fab fragments (crF6261 or crF8020, respectively), at varying concentrations. Viral infectivity

following R18 labeling was previously confirmed (Appendix 1), so that the viruses used here are infectious particles. Incubation conditions ensured that IgG/Fab binding equilibrium had been achieved prior to immobilization and dissociation over the course of the experiment was found to be negligible (Figure A2-1, Appendix 2). Immobilization of the virus on the glass-supported bilayer was not hampered by IgG/Fab binding (Figure A2-2). We have previously reported a sigmoidal, dose-dependent reduction in the hemifusion efficiency of H1N1 or H3N2 viral strains upon binding of these IgG that was influenza-group specific [1]. Here, the use of antibodies covalently labeled with pH-insensitive Alexa Fluor 488 dye molecules (CR6261af488 and CR8020af488, 5 dyes/IgG; Figure A2-3 and Table A2-1) also showed a dose-dependent reduction in the hemifusion efficiency (Figure 3-2A). A similar sigmoidal dose-dependent decrease in hemifusion efficiency resulted from viral incubation with Alexa 488-labeled Fab fragments of these two antibodies (crF6261af488 and crF8020af488, 2.4 dye/Fab; Figure A2-3 and Table A2-1). Since hemifusion efficiency is reduced by Fab as well as IgG, we conclude that inhibition of influenza HA-mediated fusion does not require bivalent binding, but arises solely from epitope recognition.

Separately, we found that viral content release was inhibited to a similar extent as hemifusion, indicating that hemifusion is a functional readout for full fusion (Figure A2-4). Under conditions where few IgG were bound to the virus and full fusion occurred, antibody-labeled hemagglutinin proteins could be seen to diffuse into the target bilayer after successful content release (Movie M2-1), demonstrating successful merger of the viral membrane with the target supported bilayer.

3.2.2 Maximal hemifusion inhibition by IgG binding occurs below full epitope occupancy

The stoichiometry of IgG/Fab binding is determined as a quotient of two intensity measurements. The dividend is the integrated fluorescence intensity arising from virus-bound IgG/Fab immediately after the pH drop (Figure 3-1C), which is proportional to the number of

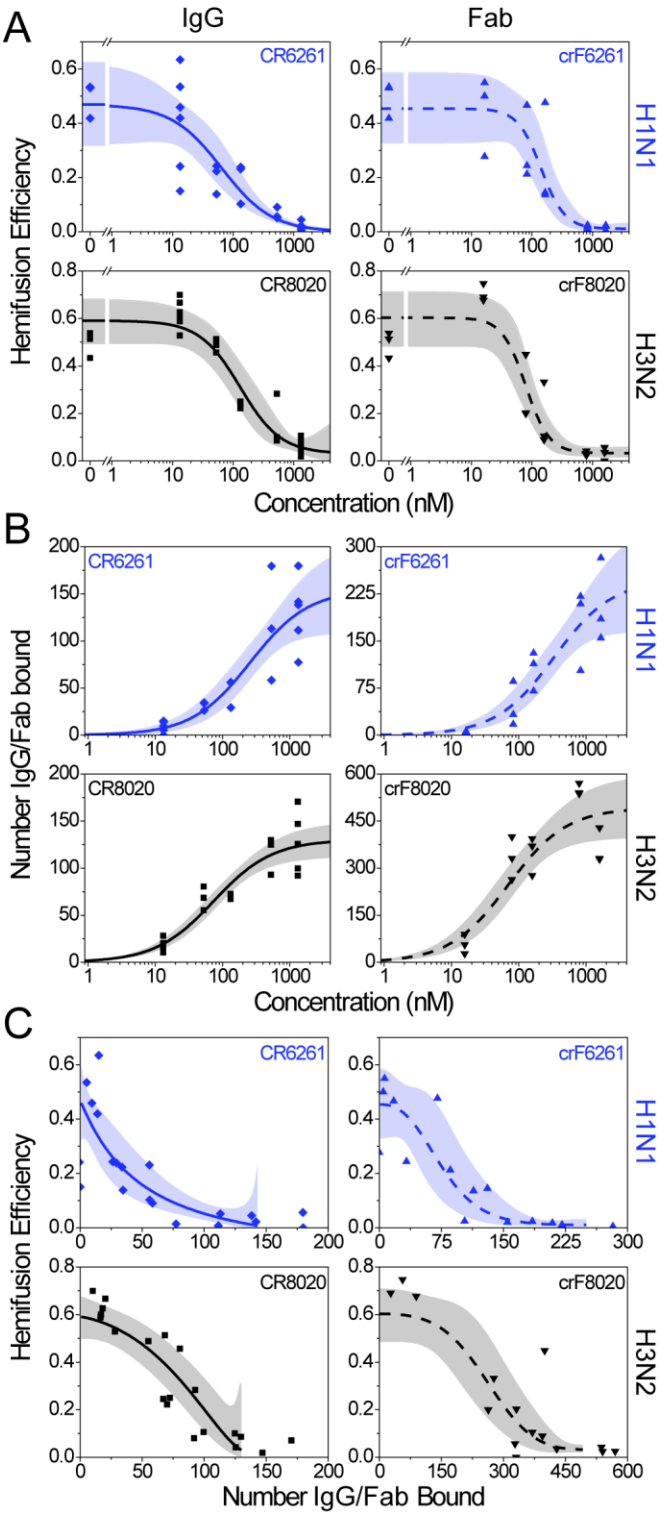

Figure 3-2 *– Hemifusion inhibition and antibody stoichiometry. In each panel IgG inhibition and binding data are in the left column graphs (solid fit lines), Fab data are in the right column (dashed fit lines); the upper rows are the H1N1 strain (blue) and lower rows are H3N2 (black). Each data point represents a single experimental run, best-fit lines are in blue or black and their 95% confidence bands are in light blue or grey.* ***A****) Hemifusion efficiency decreases as the concentration of neutralizing IgG or Fab is increased.* ***B****) The number of neutralizing IgG or Fab bound to virions increases as the concentration used for incubation with virus increases.* ***C****) Plot of hemifusion data (A) versus the number of IgG or Fab bound to the viral surface (B) allows for estimation of the number of IgG/Fab required for a given reduction in hemifusion efficiency. Fit lines used are: logistic function (A), hyperbolic function (B) and a combination of these two (C) (Table A2-2 and Appendix 2). Fit lines in (C) are truncated at high coverage that correspond to the plateau values obtained in (A) and (B) at high IgG or Fab concentrations.*

Table 3-1 – Summary of stoichiometric and kinetic results*

Virus	Neutralizing Molecule	Number of IgG/Fab bound at maximal hemifusion inhibition	Number of IgG/Fab bound at half-maximal hemifusion inhibition	Fractional occupancy at half-maximal inhibition **	Fold-increase of hemifusion time: upper plateau relative to lower
H1N1	CR6261 IgG	155 (107–202)	31 (8–69)	0.20 (0.04–0.48)	2.2 (1.6–3.0)
	crF6261 Fab	248 (158–338)	74 (39–119)	0.30 (0.12–0.55)	2.7 (1.6–4.5)
H3N2	CR8020 IgG	130 (112–149)	83 (62–107)	0.64 (0.46–0.84)	2.1 (1.5–2.9)
	crF8020 Fab	493 (394–592)	261 (192–340)	0.53 (0.36–0.73)	2.6 (2.2–3.0)

* values in parenthesis report 95% confidence intervals.

** calculated as the quotient of the number of IgG/Fab bound at half-maximal hemifusion inhibition and the number bound at maximal hemifusion inhibition.

IgG/Fab present. The divisor is the integrated intensity from individual IgG/Fab, which is obtained separately by visualizing the molecules under identical illumination conditions in the absence of virus and target bilayer (Figure A2-5). Dividing these two intensity measurements provides the number of molecules bound to an individual virion. IgG/Fab labeling efficiency was >99% for IgG and ~90% for Fab (Figure A2-3 and Table A2-1). Numbers of bound IgG/Fab were corrected for the presence of a small amount of unlabeled molecules using these percentages. The total internal reflection fluorescence (TIRF) conditions utilized were in a range where the fluorescence emanating from the virus-bound IgG/Fab was independent of TIR angle (Figure A2-5), while still allowing for suppression of background fluorescence and high signal-to-noise.

Figure 3-2B shows a sigmoidal increase in the mean number of IgG or Fab molecules bound to all viruses (*i.e.* fusing and non-fusing) upon increasing IgG/Fab concentrations. The upper plateau from a fit to the data provides an estimate for the average number of IgG/Fab molecules that are needed to maximally inhibit HA-mediated hemifusion. These and other stoichiometric values are summarized in Table 3-1 with all calculated fit parameters reported in Table A2-2. For both virus strains, we find that more Fab molecules are required to achieve maximal hemifusion inhibition compared with IgG. The H3N2 strain has ~3.8-fold more Fab than IgG under conditions of maximal hemifusion inhibition, while the H1N1 strain has ~1.6-fold more Fab than IgG.

We estimated the number of HA trimers on each virus for comparison to the number of IgG/Fab bound at maximal hemifusion neutralization. Electron microscopy of the H1N1 and H3N2 viral strains indicated that they are morphologically similar (Figure 3-1A) and each have an average envelope diameter of 125 nm (Figure A2-6). Using results from recent cryoelectron tomography reconstruction of virus particles similar to those used here [28,37], we estimate there are ~375 HA trimers on each virus. This value agrees with previous estimates that were in the range of 300-500 trimers per 120 nm diameter virus particle [38-40]. With data from Table 3-1 we estimate a binding stoichiometry of 0.41 CR6261 IgG per HA and 0.35 CR8020 IgG per HA at maximal hemifusion inhibition. For the Fab, we estimate a binding stoichiometry of 0.69 crF6261 Fab per HA and 1.31 crF8020 per HA. These observations are consistent with predictions that the physical size and bivalent binding of IgG molecules would lower their stoichiometries relative to the smaller and monovalent Fab fragments [28].

Steric interactions between surface proteins and IgG/Fab molecules as they pack together on a viral surface were investigated *in silico* using a simulation designed to study protein packing and prevent protein overlap. To this end, thousands of random, two-dimensional, protein dense viral surfaces were generated through a Monte Carlo procedure (Figure A2-7) utilizing the crystallographic dimensions of the envelope proteins (HA, NA, M2) at appropriate relative concentrations. Increasing numbers of IgG/Fab were bound to HA in accord with their co-crystal structure [7,22]. The number of IgG/Fab bound to HA when overlap minimization could no longer be achieved was taken as the maximum number of molecules sterically allowed on the viral surface.

Simulations indicated that 270-300 IgG molecules could sterically fit on a viral surface. Though the viral surface was represented in 2D, these values were in excellent agreement with 3D cryoEM tomography predictions that 75% of the 375 HA were available for binding [28]. The simulations revealed that bivalent IgG binding prevailed until ~175 molecules were present on the viral surface, at which point monovalent binding became dominant. These simulation results

suggest that the experimentally determined 155 CR6261 or 130 CR8020 IgG bound at maximal hemifusion neutralization (Table 3-1) would bind bivalently to abrogate the fusogenicity of approximately 310 or 260 HA trimers, respectively. As such, we conclude that not all sterically available epitopes need to be bound for influenza viruses to be inhibited from undergoing membrane fusion. As such, it is likely that fusion-competent HA trimers remain on the surface of virions whose fusogenicity is inhibited through IgG binding. Lastly, simulation results indicated that approximately 500 Fab molecules sterically fit on the surface of an influenza particle. This value agrees with the experimentally measured number of crF8020 Fab bound, however only about half as many crF6261 bind at maximal hemifusion inhibition. This difference is discussed in the following section.

3.2.3 Low occupancies can significantly reduce the extent of hemifusion.

Combining measurements of hemifusion efficiency with the calculated number of virus-bound IgG or Fab molecules allows us to directly correlate the inhibition of HA-mediated hemifusion on a per bound-molecule basis. Data and fits displayed in Figures 3-2A and 3-2B are combined and shown in Figure 3-2C showing this correlation (data fitting in Appendix 2). Directly relating coverage with hemifusion efficiencies allows for estimation of the number of IgG/Fab molecules needed to reduce the likelihood of a virus undergoing hemifusion by half (half-maximal hemifusion inhibition, Table 3-1). Similar to the requirements for maximal hemifusion inhibition, more Fab than IgG are needed for half-maximal fusion inhibition.

We define the fractional occupancy to determine the fraction of available binding sites on the viral surface that IgG or Fab molecules must occupy for the likelihood of hemifusion to be reduced by half. It is the quotient of the number of IgG/Fab bound at half-maximal hemifusion inhibition and the number bound at maximal hemifusion inhibition (Table 3-1). We find that the fractional occupancies are similar between 6261 IgG and Fab, and also between 8020 IgG and Fab. There is a difference in the hemifusion response to increasing fractional occupancy

between the two viral strains, however, with the H1N1 strain showing a higher susceptibility to hemifusion inhibition at lower fractional occupancies compared to the H3N2 strain.

Discrepancies in response to IgG/Fab binding could arise from differences in avidity and/or accessibility of the IgG/Fab for their epitopes on the two viral strains, or from inter-strain variation in surface protein density or composition [40,41]. An additional rationale for the differing responses could relate to a notable difference in the behavior of the 6261 and 8020 epitopes upon exposure of HA to low pH [7,42]. The 6261 epitope primarily comprises the 'A' α-helix (HA2 residues 38-55) that participates in the loop-to-helix transition undergone by HA and remains contiguous throughout the unfolding and refolding process. In contrast, the 8020 epitope is split during low pH conformational changes with the 'G' α-helix (HA2 residues 145-153) remaining membrane proximal and the β-sheet near the fusion peptide (HA2 residues 32-36) being extended distally from the viral membrane to allow insertion of the fusion peptide into a target. Such a difference in epitope behavior may allow the H3 HA to more readily escape from the conformationally inactivated state imposed by 8020 binding, consistent with its more robust hemifusion response to both the IgG and the Fab (Figure 3-2C). An H3 hemagglutinin trimer being better able to "slip its handcuffs" may also relate to the similarity in the number of IgG molecules required for maximal hemifusion inhibition of the two strains, while there is a nearly 2-fold discrepancy between the Fab (Table 3-1). If double binding was needed to ensure H3 does not escape the inactivated state, then it follows that more monovalent 8020 Fab than 6261 Fab would be needed, while a comparable number of bivalent 8020 and 6261 IgG could engage in double HA binding.

3.2.4 IgG/Fab binding delays the time to hemifusion

The time to hemifusion is measured as the time between disappearance of the fluorescein signal (pH drop) and the onset of lipophilic dye escape from the site of viral fusion

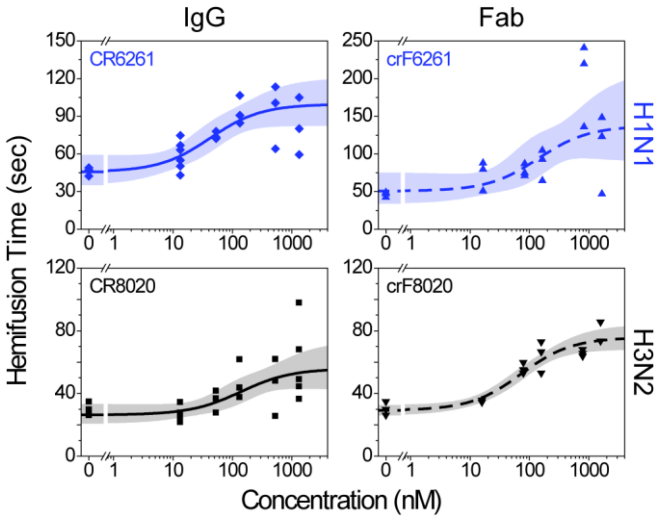

Figure 3-3 *– Hemifusion is delayed at higher IgG/Fab concentrations. Data are displayed as in Figure 3-2, and are fit with a hyperbolic function having a constant offset (Table A2-2). Fold-increases in hemifusion times between zero and the highest IgG/Fab concentrations are listed in Table 3-1.*

(Figure 3-1C). Concomitant with a decreasing efficiency of hemifusion and increasing numbers of bound IgG/Fab, we find that the time required for the remaining fusion-competent particles to undergo hemifusion becomes longer as the concentration of IgG/Fab increases (Figure 3-3).

The hemifusion times increase from their base-line values at zero IgG/Fab to plateau values at high IgG/Fab concentrations in a sigmoidal fashion. The baseline hemifusion time in the absence of IgG/Fab was 46 seconds for the H1N1 strain and 30 seconds for the H3N2 strain. At the highest IgG concentrations both viral strains show an upper plateau for hemifusion times that is an approximately 2-fold increase over their baseline values (Table 3-1). When bound by the corresponding Fab, both virus strains exhibit slightly larger increases, showing more than a 2.5-fold increase over their baselines. Differences between the delays caused by IgG and Fab may result from differences in their physical size and/or their HA binding valencies. A bivalently binding IgG abrogates the fusogenicity of trimers that are neighbors and may interfere with fusion processes that occur over long time scales, but that are left intact by the monovalent Fab. The observation of an upper plateau for all cases is consistent with inactivation of HA membrane fusion capacity upon prolonged exposure to acidic conditions [43]. It suggests that viral HA have a temporal window-of-opportunity following acidification to induce fusion before they become inactivated.

3.3 Discussion

We describe a new method for quantitatively determining the numbers of broadly neutralizing, stem-binding antibodies or their Fab fragments bound to individual influenza virus particles. The experimental design allows for direct correlation between the stoichiometry of antibody binding and its functional impact on viral fusogenicity and kinetics. Our stoichiometry results indicate that maximal inhibition of membrane fusion by IgG does not require all sterically available epitopes to be bound, which may leave pH sensitive HA trimers on the surface of a non-fusogenic virion. Fab molecules are also capable of inhibiting HA-mediated membrane

fusion, albeit with higher stoichiometry, demonstrating that bivalent IgG binding is not a requisite for inhibition of membrane fusion. Concomitant with decreasing hemifusion efficiency at higher IgG/Fab coverage, we observe a 2- to 2.5-fold kinetic delay in the hemifusion process. These observations are consistent with a molecular model for fusion inhibition whereby blockage of HA's low-pH conformational triggering by IgG/Fab binding prevents the accumulation of triggered HA into a sufficient density for membrane fusion to occur and is depicted in Figure 3-4.

The presence of sterically available HA epitopes on the surface of a fusion-inhibited virus is consistent and in support of a mechanism of HA-mediated membrane fusion requiring a coordinated action between multiple HA's for membrane fusion to be productive [34,36,44,45]. That the fusogenicity of a single HA could be abrogated by removal of coordination partners without IgG or Fab having to directly bind that particular HA implies the existence of a network of inter-HA connectivities on the viral surface (Figure 3-4). In this context, network connections at neutral pH would be established by the relative geometry and distance between neighboring HA. Network connections become stochastically activated upon acidification when neighboring HA undergo their conformational extension and latch on to a target membrane. If a sufficient number of HA trimers are physically close enough in space and are refolding within a close enough window of time, then they are able to coordinate their work and mediate the onset of lipid hemifusion. If HA is exposed to low pH for extended periods of time, however, it inactivates by non-productively refolding and also disrupts the HA coordination network. Thus, timing of the entire fusion process represents the interplay between 1) low pH-induced, stochastic firing of individual HA trimers; 2) stochastic coordination between HA post-firing to mediate productive membrane fusion; and 3) low pH-induced inactivation of the activated HA (Figure 3-4).

Predictions from a recent study by Ivanvovic *et al.* [36] simulating the stochastic inter-HA coordination mechanism are consistent with our findings that hemifusion kinetics are delayed by binding of either IgG or Fab molecules. They found that increasing proportions of non-fusogenic

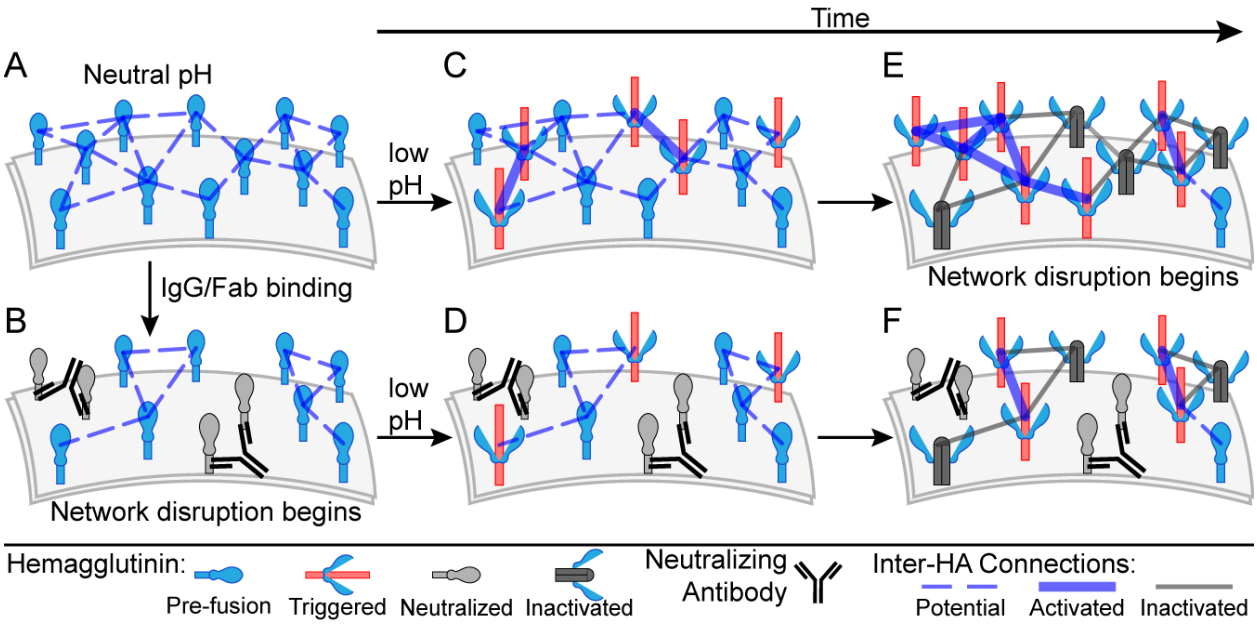

Figure 3-4 – *Cartoon illustrating inter-HA network disruption by IgG binding that leads to fusion inhibition.* ***A****) Fusogenic HA at neutral pH in the pre-fusion conformation (light blue spikes) initially have network connectivities (blue dashed lines) dictated by their spatial geometry relative to one another.* ***B****) Binding of IgG (black 'Y') inactivates the HA (light grey spikes) by preventing their low pH-induced conformational changes and disrupts the network between neighboring HA.* ***C*** *and* ***D****) Exposure to low pH conditions triggers HA to unfold into fusion-competent conformations (red spikes) and activates the inter-HA network (thick blue lines) between neighboring, triggered HA.* ***E*** *and* ***F****) Continued low pH exposure causes HA inactivation by non-productive re-folding (dark grey spikes), also removing inter-HA connections (grey lines). Network disruption begins prior to low pH activation in the presence of IgG/Fab binding (B, D and F), but in their absence it begins only in late stages after network activation (E). Productive fusion would arise at locations with a sufficiently high density of activated inter-HA connectivities. Both IgG/Fab binding and low pH inactivation can inhibit membrane fusion even in the presence of fusogenic HA.*

HA on the simulated viral surface caused slower kinetics due to disruption of inter-HA coordination. Binding of 6261 or 8020 IgG/Fab on the surface of our infectious virus particles increases the proportion of inactive HA on the surface of our infectious viruses [1], slowing hemifusion kinetics. Thus, 6261 and 8020 IgG/Fab inhibit membrane fusion through disruption of the coordination network between neighboring HA trimers.

It is of interest that the delay in hemifusion time imparted by Fab is longer than that for IgG. The aforementioned simulation [36] indicated that increasingly larger fractions of non-fusogenic proteins gave rise to progressively slower kinetics. The larger delay in hemifusion time observed with Fab suggests that more HA may be rendered non-fusogenic when viral fusion is inhibited by Fab as compared to IgG. A need for fewer HA to be inactivated by IgG to achieve maximal hemifusion inhibition compared to Fab implies that, indeed, HA's nearest neighbors are critical for maintenance of the trimer's capacity to mediate fusion.

Our single-particle studies detect a subtle difference between the susceptibility of the H1N1 and H3N2 viruses to hemifusion inhibition upon IgG/Fab binding that is not borne out in the physiological context of infection. Both IgG molecules are similarly capable of prophylactically preventing and therapeutically treating lethal influenza infection in mice [6,7]. As well, since the influenza virus has a high multiplicity of infection (MOI) [1], data in Figure 3-2C and Table 3-1 indicate that low fractional occupancies could be sufficient to decrease the fusogenic virus population below the MOI needed for a sustained infection. Moreover, the stem-binding antibodies are up to nine-fold more potent in neutralizing viral infection by preventing proteolytic cleavage that activates HA compared to neutralization through fusion inhibition alone [1]. Lastly, the observed delay in fusion time would lead to extended exposure of a virus to the harsh environment of late endosomes, conditions which could lead to viral degradation prior to successful membrane perforation. As such, the high epitope coverage we measure is likely not necessary to stop infection in viral neutralization assays. Rather, using high IgG/Fab epitope

coverage here has provided novel insight into the mechanism of inter-HA coordination mediating membrane fusion and the mechanism for fusion inhibition by stem-binding antibodies.

Steric interference on the viral surface may also contribute to fusion inhibition upon antibody binding, but comparison of Fab versus IgG stoichiometry does not necessarily shed clear light on the subject. The ~67% reduction in protein mass through use of a Fab also comes at the expense of one paratope, whose effect in neutralizing nearest neighbors could be important. As well, the ~50 kDa Fab are still quite large and comparable to the size of a single HA1/HA2 monomer. The use of peptides [3] or small molecules [26] capable of inhibiting HA's low pH conformational changes would be valuable for delineating HA-inactivation versus steric effects and could be studied using the experimental design described here.

3.4 Materials and Methods

Microfluidic flow cells were used for all experiments and were constructed using cleaned microscope cover slips (25 x 25-mm, No. 1, VWR, USA) affixed to a quartz top using double-sided tape (Grace Bio-Labs), as previously described [34] or non-permanently adsorbed to a single-use multi-channel PDMS (polydimethylsiloxane; Dow Corning, Slygard 184) chip, which was formed by standard PDMS cast molding techniques [46,47].

Proteoliposomes containing the sialoglycoprotein glycophorin A (GYPA; full-length with a GST tag, Abnova, Taipei City, Taiwan) were formed as previously described [1] by mixing lipids solubilized in detergent with the GYPA. Removal of detergent with Bio-Beads (SM-2 absorbent, Bio-Rad Laboratories, Inc.) formed multilaminar proteoliposomes, which were incubated in the glass-bottomed microfluidic channels for 45 minutes to form contiguous, planar bilayers through spontaneous rupture. The bilayers enabled virus immobilization and prevented non-specific adhesion of labeled IgG/Fab molecules.

Influenza A virus strains R/8/34 (H1N1) and Aichi/68/X:31 (H3N2) propagated in SPF eggs were purchased from Charles River (North Franklin, Connecticut, USA; 2 mg/ml total viral

protein) and used without further purification. Labeling was performed for three hours by diluting virus stocks 1:3 into Hepes buffer, then adding octadecyl rhodamine B lipophilic dye (R18, Invitrogen Inc.) dissolved in dimethyl sulfoxide (DMSO) to a final concentration of 1 μM dye and <0.5% v/v DMSO. Unincorporated dye was removed using PD-10 desalting columns (GE Healthcare). Fractions of 200 μl were collected and the three with the highest particle count were pooled into a single volume and used for fusion experiments.

Alexa 488 labeling of IgG and Fab was done according to manufacturer specifications (Invitrogen) to obtain high degrees of protein labeling.

Fusion experiments were conducted as previously described [1] by incubating labeled viruses with labeled IgG/Fab for 45-60 minutes, then immobilizing them on a bilayer formed within a microfluidic cell, followed by fluorescein-labeled streptavidin (Invitrogen). Immobilized viruses were observed using a 60x, TIRF objective on an Olympus IX-71 inverted microscope equipped with 488 nm and 561 nm lasers (Sapphire models, Coherent Inc.) aligned in objective-based TIR mode. Green and red emissions were simultaneously visualized on either half of an EMCCD camera (Hamamatsu Photonics K.K.) using either a home-built or commercial dual-view (Photometrics, Tucson, AZ, USA) system. HA-mediated fusion was initiated by adding pH 5.0 citric acid buffer and fusion events recorded continuously with 200 ms exposure time. Fluorescence intensity arising from individual IgG/Fab molecules adsorbed to clean glass and in pH 5.0 buffer was done under identical illumination conditions.

Data analysis was performed using custom MATLAB (Mathworks Inc.) scripts, similar to those previously described [1,34]. Briefly, viruses were identified in the red R18, then paired with locations separately identified in the green Alexa 488 channel. Recorded fusion movies were corrected for laser illumination profile and fluorescence background before fluorescence extraction. The fusion-inducing pH drop was identified to set time t=0 (Figure 3-1). Lipid mixing trajectories were analyzed manually to select those particles

showing dequenching behavior upon escape of the self-quenched R18 dye into the target bilayer. Experiments showing fewer than 25 virions in a field of view were rejected. For stoichiometry calculations, green-channel trajectories were averaged for 15 frames (three seconds) beginning one second after the pH drop (Figure 3-1D). The number of virus-bound IgG/Fab molecules was quantified as a ratio of their integrated intensity when bound to the integrated intensity of IgG/Fab individually (Appendix 2, Figure A2-5). The time to hemifusion is calculated as the elapsed time from pH drop to the onset of hemifusion dequenching.

3.5 References

1. Brandenburg B, Koudstaal W, Goudsmit J, Klaren V, Tang C, et al. (2013) Mechanisms of hemagglutinin targeted influenza virus neutralization. PLoS One In Press.

2. Burton DR, Poignard P, Stanfield RL, Wilson IA. (2012) Broadly neutralizing antibodies present new prospects to counter highly antigenically diverse viruses. Science 337: 183-186.

3. Fleishman SJ, Whitehead TA, Ekiert DC, Dreyfus C, Corn JE, et al. (2011) Computational design of proteins targeting the conserved stem region of influenza hemagglutinin. Science 332: 816-821.

4. Steel J, Lowen AC, Wang TT, Yondola M, Gao Q, et al. (2010) Influenza virus vaccine based on the conserved hemagglutinin stalk domain. MBio 1: 10.1128/mBio.00018-10.

5. Han T, Marasco WA. (2011) Structural basis of influenza virus neutralization. Ann N Y Acad Sci 1217: 178-190.

6. Throsby M, van den Brink E, Jongeneelen M, Poon LL, Alard P, et al. (2008) Heterosubtypic neutralizing monoclonal antibodies cross-protective against H5N1 and H1N1 recovered from human IgM+ memory B cells. PLoS One 3: e3942.

7. Ekiert DC, Friesen RHE, Bhabha G, Kwaks T, Jongeneelen M, et al. (2011) A highly conserved neutralizing epitope on group 2 influenza A viruses. Science 333: 843-850.

8. Corti D, Voss J, Gamblin SJ, Codoni G, Macagno A, et al. (2011) A neutralizing antibody selected from plasma cells that binds to group 1 and group 2 influenza A hemagglutinins. Science 333: 850-6.

9. Knossow M, Gaudier M, Douglas A, Barrere B, Bizebard T, et al. (2002) Mechanism of neutralization of influenza virus infectivity by antibodies. Virology 302: 294-298.

10. Harrison SC. (2008) Viral membrane fusion. Nat Struct Mol Biol 15: 690-8.

11. Klasse PJ, Sattentau QJ. (2002) Occupancy and mechanism in antibody-mediated neutralization of animal viruses. J Gen Virol 83: 2091-2108.

12. Reading SA, Dimmock NJ. (2007) Neutralization of animal virus infectivity by antibody. Arch Virol 152: 1047-1059.

13. Wilson IA, Skehel JJ, Wiley DC. (1981) Structure of the haemagglutinin membrane glycoprotein of influenza virus at 3 A resolution. Nature 289: 366-373.

14. Waterfield M, Scrace G, Skehel J. (1981) Disulphide bonds of haemagglutinin of asian influenza virus. Nature 289: 422-424.

15. Tong S, Li Y, Rivailler P, Conrardy C, Castillo DA, et al. (2012) A distinct lineage of influenza A virus from bats. Proc Natl Acad Sci U S A 109: 4269-4274.

16. Gamblin SJ, Skehel JJ. (2010) Influenza hemagglutinin and neuraminidase membrane glycoproteins. J Biol Chem 285: 28403-28409.

17. Bizebard T, Gigant B, Rigolet P, Rasmussen B, Diat O, et al. (1995) Structure of influenza virus haemagglutinin complexed with a neutralizing antibody. Nature 376: 92-94.

18. Dreyfus C, Laursen NS, Kwaks T, Zuijdgeest D, Khayat R, et al. (2012) Highly conserved protective epitopes on influenza B viruses. Science 337: 1343-1348.

19. Ekiert DC, Kashyap AK, Steel J, Rubrum A, Bhabha G, et al. (2012) Cross-neutralization of influenza A viruses mediated by a single antibody loop. Nature 489: 526-532.

20. Lee PS, Yoshida R, Ekiert DC, Sakai N, Suzuki Y, et al. (2012) Heterosubtypic antibody recognition of the influenza virus hemagglutinin receptor binding site enhanced by avidity. Proc Natl Acad Sci U S A 109: 17040-17045.

21. Krystal M, Elliott RM, Benz EW,Jr, Young JF, Palese P. (1982) Evolution of influenza A and B viruses: Conservation of structural features in the hemagglutinin genes. Proc Natl Acad Sci U S A 79: 4800-4804.

22. Ekiert DC, Bhabha G, Elsliger MA, Friesen RH, Jongeneelen M, et al. (2009) Antibody recognition of a highly conserved influenza virus epitope. Science 324: 246-51.

23. Sui J, Hwang WC, Perez S, Wei G, Aird D, et al. (2009) Structural and functional bases for broad-spectrum neutralization of avian and human influenza A viruses. Nat Struct Mol Biol 16: 265-273.

24. Okuno Y, Isegawa Y, Sasao F, Ueda S. (1993) A common neutralizing epitope conserved between the hemagglutinins of influenza A virus H1 and H2 strains. J Virol 67: 2552-2558.

25. Nakamura G, Chai N, Park S, Chiang N, Lin Z, et al. (2013) An in vivo human-plasmablast enrichment technique allows rapid identification of therapeutic influenza A antibodies. Cell Host Microbe 14: 93-103.

26. Vanderlinden E, Goktas F, Cesur Z, Froeyen M, Reed ML, et al. (2010) Novel inhibitors of influenza virus fusion: Structure-activity relationship and interaction with the viral hemagglutinin. J Virol 84: 4277-4288.

27. Friesen RH, Koudstaal W, Koldijk MH, Weverling GJ, Brakenhoff JP, et al. (2010) New class of monoclonal antibodies against severe influenza: Prophylactic and therapeutic efficacy in ferrets. PLoS One 5: e9106.

28. Harris AK, Meyerson JR, Matsuoka Y, Kuybeda O, Moran A, et al. (2013) Structure and accessibility of HA trimers on intact 2009 H1N1 pandemic influenza virus to stem region-specific neutralizing antibodies. Proc Natl Acad Sci U S A 110: 4592-4597.

29. Fleury D, Barrere B, Bizebard T, Daniels RS, Skehel JJ, et al. (1999) A complex of influenza hemagglutinin with a neutralizing antibody that binds outside the virus receptor binding site. Nat Struct Biol 6: 530-534.

30. Klasse PJ. (2009) Neutralization of infectivity. In: Mahy BWJ, van Regenmortel MHV, editors. Desk Encyclopedia of General Virology. Oxford, U.K.: Academic Press. pp. 404-410.

31. Taylor HP, Armstrong SJ, Dimmock NJ. (1987) Quantitative relationships between an influenza virus and neutralizing antibody. Virology 159: 288-298.

32. Parren PW, Burton DR. (2001) The antiviral activity of antibodies in vitro and in vivo. Adv Immunol 77: 195-262.

33. Brooke CB, Ince WL, Wrammert J, Ahmed R, Wilson PC, et al. (2013) Most influenza a virions fail to express at least one essential viral protein. J Virol 87: 3155-3162.

34. Floyd DL, Ragains JR, Skehel JJ, Harrison SC, van Oijen AM. (2008) Single-particle kinetics of influenza virus membrane fusion. Proc Natl Acad Sci U S A 105: 15382-15387.

35. Otterstrom J, van Oijen AM. (2013) Visualization of membrane fusion, one particle at a time. Biochemistry .

36. Ivanovic T, Choi JL, Whelan SP, van Oijen AM, Harrison SC. (2013) Influenza-virus membrane fusion by cooperative fold-back of stochastically induced hemagglutinin intermediates. eLife Sciences 2. 10.7554/eLife.00333.

37. Harris A, Cardone G, Winkler DC, Heymann JB, Brecher M, et al. (2006) Influenza virus pleiomorphy characterized by cryoelectron tomography. Proc Natl Acad Sci U S A 103: 19123-19127.

38. Tiffany JM, Blough HA. (1970) Models of structure of the envelope of influenza virus. Proc Natl Acad Sci U S A 65: 1105-12.

39. Inglis SC, Carroll AR, Lamb RA, Mahy BW. (1976) Polypeptides specified by the influenza virus genome I. evidence for eight distinct gene products specified by fowl plague virus. Virology 74: 489-503.

40. Moules V, Terrier O, Yver M, Riteau B, Moriscot C, et al. (2011) Importance of viral genomic composition in modulating glycoprotein content on the surface of influenza virus particles. Virology 414: 51-62.

41. Shaw ML, Stone KL, Colangelo CM, Gulcicek EE, Palese P. (2008) Cellular proteins in influenza virus particles. PLoS Pathog 4: e1000085.

42. Bullough PA, Hughson FM, Skehel JJ, Wiley DC. (1994) Structure of influenza haemagglutinin at the pH of membrane fusion. Nature 371: 37-43.

43. Weber T, Paesold G, Galli C, Mischler R, Semenza G, et al. (1994) Evidence for H(+)-induced insertion of influenza hemagglutinin HA2 N-terminal segment into viral membrane. J Biol Chem 269: 18353-18358.

44. Mittal A, Bentz J. (2001) Comprehensive kinetic analysis of influenza hemagglutinin-mediated membrane fusion: Role of sialate binding. Biophys J 81: 1521-1535.

45. Danieli T, Pelletier SL, Henis YI, White JM. (1996) Membrane fusion mediated by the influenza virus hemagglutinin requires the concerted action of at least three hemagglutinin trimers. J Cell Biol 133: 559-69.

46. Delamarche E, Bernard A, Schmid H, Michel B, Biebuyck H. (1997) Patterned delivery of immunoglobulins to surfaces using microfluidic networks. Science 276: 779-781.

47. Xia Y, Whitesides G. (1998) Soft lithography. Annu Rev Mater Sci 28: 153-184.

Page intentionally left blank.

Chapter 4

Fusion Tracker: Principles and Development of Computational Tools for the Automated Analysis of Influenza Virus Membrane Fusion Events

Abstract

Observation of membrane fusion events mediated by the hemagglutinin surface protein of influenza viruses has provided a wealth of information regarding the functioning of these fusion proteins. The experimental design is conceptually straightforward: label the viral membrane and lumen with fluorophores that escape the confines of the particle only upon successful membrane fusion to a target bilayer. Release of the membrane dye upon fusion of the viral outer leaflet to the target bilayer indicates hemifusion and loss of the lumen dye indicates full fusion and expulsion of the viral contents. In practice, the fluorescence signals recorded from observation of fusion events (trajectories) can be complicated, confounding and difficult to interpret. Significant effort is required to discriminate true fusion events from noise and non-events. Currently, separation of the fluorescence trajectories into true fusion events and non-events is performed manually and depends upon visual inspection of the data, potentially leading to bias and errors. An automated analysis algorithm has been developed based upon maximum likelihood estimators and least squares fitting to address such bias and errors. It has the added benefit of also reducing the time involved in extraction of membrane fusion kinetic data. Programmatic implementation of the algorithm is robust and results in the ability to extract kinetics of the hemifusion process comparable to those published previously, which were extracted by manual trajectory selection.

4.1 Introduction

Single-molecule experiments probing biochemical kinetics provide a window into the fine, physical details underpinning the function of proteins. Though successfully designing and carrying out experiments detecting single molecules is difficult, it is only half of the story. Once fluorescence recordings of a biochemical event are obtained, the fluorescence signals must be extracted and interpreted in the context of the process being observed. While experimental design allows prediction for the type of fluorescence changes that should occur following a biochemical reaction, many complicating factors can make event detection of real events complicated, tedious and time consuming. Herein lies the elephant in the room: the raw data from single-molecule biophysical experiments are complex and heterogeneous, and necessitate both biological and technical knowledge for their interpretation to be correct. As a result of this complexity, data analysis can represent a significant barrier to obtaining results once a successful experiment is completed.

Visualizing the process of membrane fusion mediated by the influenza virus surface spike protein hemagglutinin upon exposure to an acidic environment relies upon recording two fluorescence signals. One is a lipid signal arising from fluorescent lipid dyes incorporated into the phospholipid envelope of an influenza virus. The second is a fluorescence signal from an aqueous dye staining the lumen of the viral particle. Both signals are stably incorporated into the virus particles until hemagglutinin successfully fuses the viral membrane to a target membrane [1-3]. Kinetics of the fusion process are measured as the elapsed time between virus particle acidification and release of either the lipid or content dye from the virus, as well as the time between the lipid and content release signals. Lipid dye release indicates the onset of hemifusion, or lipid mixing, between the virus and a target, while content dye release indicates the onset of pore formation and the creation of a corridor through which the viral contents can escape from the lumen. The time between these two events is the lifetime of the transient

hemifusion intermediate (hemifusion lifetime), wherein only the proximal leaflets of the virus and target are fused, while the distal leaflets remain separate (Figure 4-1).

The state of the art to extract these waiting times is to manually analyze the fluorescence intensity from each individual virus over time – its fluorescence trajectory - and separate out those trajectories depicting true fusion events from those that do not. The selection process is guided by visual inspection [1-4] of the trajectories and involves creating hundreds of plots of the form depicted in Figure 4-1C. A researcher then decides whether any of the given trajectories appear to show characteristics of membrane fusion based upon their personal experience. The characteristics a trajectory must possess have not been defined quantitatively, though they can be described qualitatively. True hemifusion signals typically include a large and rapid intensity increase corresponding to dequenching of the lipid dye, termed the hemifusion time, followed by a relatively gradual signal dissipation as the lipid dye diffuses from the viral envelope into the planar, target bilayer (Figure 4-1). Pore formation signals include only a large signal dissipation indicating the contents of the viral lumen have been released, defining the pore formation time, and which ideally follows a hemifusion event.

Extraction of waiting times from fluorescence signals selected in this fashion have provided valuable insight into the mechanism of hemagglutinin-mediated fusion [1-3,5,6]. These studies, though, focused primarily on the time of lipid dequenching and content dissipation and not on the kinetics involved with lipid signal dissipation. Modeling the waiting time distribution for hemifusion dequenching by a gamma distribution allows for extraction of two valuable pieces of kinetic information: the speed of the rate limiting step in the multi-step fusion process, and the number of rate limiting steps that are required for fusion to have occurred [1]. The gamma distribution is:

$$p_{\Gamma}(t|k,N) = \frac{k^N t^{N-1}}{\Gamma(N)} \exp(-k\,t) \tag{4-1}$$

where k is the speed of the rate limiting step and N is the number of steps in the reaction.

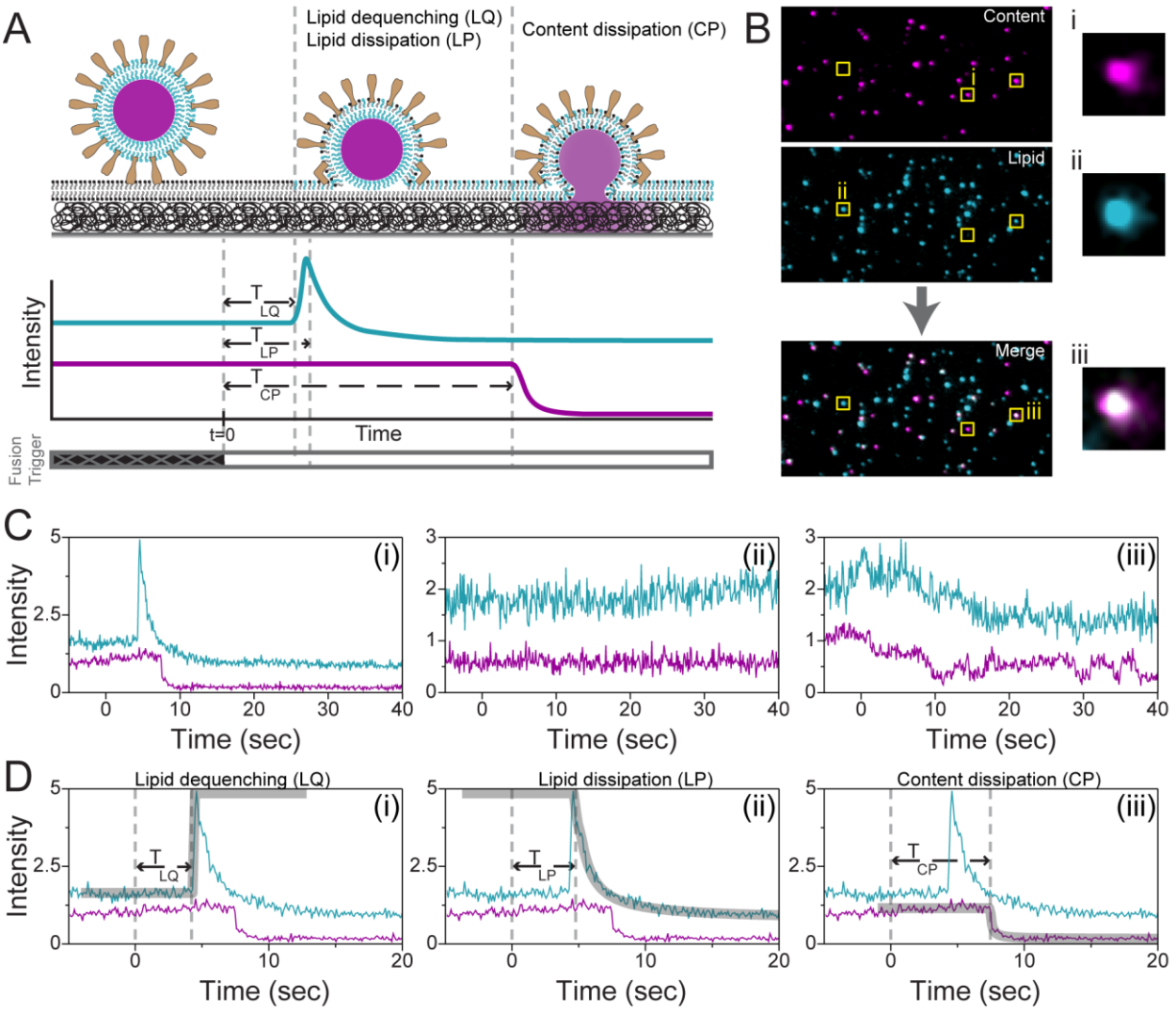

Figure 4-1 *– Experimental setup and fluorescence read out that Fusion Tracker software is designed to analyze.* ***A****) Cartoon of a dual-labeled virus particle having a lipid dye (blue) and a content dye (purple), along with an idealized fluorescence trajectory, adapted from* [7] *and Chapter 1. The virus is immobilized upon a planar bilayer supported by dextran as in* [1] *and provides a constant level of fluorescence emission. Following a stimulus that acts as a fusion trigger, the hemagglutinin proteins on the viral surface (brown) mediate fusion of the proximal leaflets of the viral and target bilayers. Initial merger and lipid mixing causes a lipid dequenching signal (LQ), observed as a sharp fluorescence increase. Shortly after dequenching, the lipid dye diffuses away from the site of fusion, causing a lipid dissipation signal (LP). Once the distal leaflets of the virus and target bilayers have merged, the contents of the virus are lost, causing a content dissipation signal (CP). Time points corresponding to these three events in the idealized trajectory are indicated with labeled arrows.* ***B****) Sections of an image from a two-color membrane fusion recording, 50 x 25 μm in size, are shown in false color. Channels are aligned as described in the text with the content signal in the top part (purple) of the image and lipid signal in the bottom (blue). Merger of the two emission channels allows for co-localization of the dual-labeled virus signals (merged image, bottom). Small 2 x 2 μm regions highlighted by the*

*(**Figure 4-1 Continued**) yellow squares show that some virus particles have only a content signal (i) and others have only a lipid signal (ii), but many have both fluorescent labels (iii, white). **C**) Sample fluorescence trajectories that are typically analyzed visually. It is straightforward to distinguish an exemplary trajectory (i) for a virus particle undergoing LQ, LP (blue) and CP (purple) from a trajectory that clearly does not show any fusion activity (ii). Determining the fusion behavior for the virus trajectory shown in (iii) using consistent and quantitative criteria is not straightforward, as it shows characteristics of both lipid dissipation and content dissipation. **D**) Portions of the fusion trajectory in (C.i) are adequately captured by the model functions described in the text (gray, transparent fit lines). i) Equation 4-2 models the sharp signal increase upon lipid dequenching. ii and iii) Equation 4-3 models the dissipative fluorescence losses in the lipid (ii) and content (iii) signals. Fit lines in (i) and (ii) are extended beyond the fluorescence signal to facilitate visualization of the fitting model as described in Equations 4-2 and 4-3.*

Previous studies have demonstrated that *N* is fairly constant over a range of pH values used to induce fusion and typically varies from a value of 2–4 [1,3]. The *N* parameter is interpreted to represents the number of hemagglutinin proteins required for hemifusion to occur. Mathematically, *N* governs the shape of the distribution and under- or over-sampling portions of a distribution will give rise to large discrepancies in the determined *N* value. Sampling errors can occur due to unexpected intensity fluctuations typical in single-molecule trajectories and because of viral movement prior to membrane fusion. This movement is both Brownian and directed, the latter arising from a drag force upon the particle caused by flow of fusion-inducing low-pH buffer into the experimental chamber [3]. Drag-induced rolling of the virus on the surface of a bilayer comes to a halt as the hemagglutinin proteins extend into the bilayer, fixing a virus into position for fusion. Since previous studies extracted fluorescence intensity using a fixed region of interest in the fusion recordings [1], rather than particle tracking, arrival of a virus particle could mimic the fluorescence signal of a virus undergoing solely dequenching. Hence, the extracted fusion kinetics and the interpretations they imply are strongly dependent upon the reproducibility with which an investigator will consistently select or reject the same type of fluorescence signals.

Other single-molecule approaches have attempted to overcome the human element in data selection and waiting time extraction by designing and utilizing statistical models for determining significant changes in fluorescence trajectories. These mathematical tools have been applied in an automated analysis format to study fluorophore photobleaching [8], quantum dot blinking [9], microtubule assembly via optical trapping [10] and helicase unwinding of DNA via FRET [11]. Single-molecule trajectories from these studies are largely step-like in character, showing discrete intensity heights that characterize distinct molecular states. Statistically significant deviations from those heights can be detected by change-point analysis [12], an approach that looks for a higher likelihood of transitioning between two molecular states rather than remaining in one at every time point within a trajectory. With this tool, it is possible to identify the number of molecular states visited by an individual molecule. In automatically analyzing these stepping trajectories, the investigators do not set *a priori* presumptions about the number or locations of the states, the only requirement is that they be statistically resolvable within the noise of the experimental system.

In contrast, trajectories of membrane fusion represent a continuum of fluorescence intensity levels as the hundreds of fluorophores initially trapped within the virus particle are rapidly redistributed to the target and/or surroundings. However, the underlying principle of a state change remains, however. As a consequence, determining when a virus transitions from a non-fused into a fused state should be amenable to analysis by similar logic and statistical tools. This chapter represents the first attempt at adapting the change-point analysis tool [12] to automatically separate trajectories depicting true fusion events from those that do not without human intervention. The assumptions of the statistical model are reversed from their use in identification of discrete stepping levels, in that viruses are assumed to have their lipid or content signal in only one of two states: either fused or non-fused. With this presumption, mathematical models approximating the shape of fluorescence trajectories during successful

fusion events can be fit to the data and allow for identification of fusion events from noise (Figures 4-1 and 4-6).

Dequenching signals are modeled as sigmoidal functions having the form:

$$\text{Dequenching}(t, \boldsymbol{p}) = p_2 + (p_1 - p_2) \times \left(1 + \exp\left(\frac{4\,(t - p_3)}{p_4}\right)\right)^{-1} \quad (4\text{-}2)$$

where $\boldsymbol{p}$ is a vector containing these parameters: p_1, the plateau intensity value before dequenching; p_2, the plateau value after dequenching; p_3, the inflection point of the intensity increase; and p_4, the duration of the dequenching event. Dissipation signals are modeled with the Gaussian function describing two-dimensional diffusion, so as to capture information regarding lipid dye diffusion upon hemifusion:

$$\text{Dissipation}(t, \boldsymbol{p}) = p_1 - p_2 \times H(t - p_3) \times \exp\left(\frac{-r^2}{4\,p_4\,(t - p_3)}\right) \quad (4\text{-}3)$$

where r is the radius around a virus particle in μm that is used for fluorescence intensity integration, and $\boldsymbol{p}$ is a parameter vector representing: p_1, the intensity value before dissipation; p_2, size of the signal loss upon dissipation (*i.e.* initial intensity minus final intensity); p_3, the frame indicating the onset of signal dissipation; and p_4, the two-dimensional diffusion constant in μm^2/second. $H(t- p_3)$ is the Heaviside function and is invoked to remove the contribution of the exponential at times less than p_3. Fits of Equations 4-2 and 4-3 as determined by the algorithm described are depicted in Figures 4-1 and 4-6.

As shown here, these models sufficiently describe fluorescence trajectories of membrane fusion and allow automated separation of fusing events from non-fusion. In addition, the designed analysis algorithm outlined in Figure 4-2 also performs particle tracking to reduce the confounding influence of viral motion. Tracking also allows for extraction of the kinetics of hemagglutinin unfolding as a result of acidification [3] in an automated fashion. Further, by fitting the trajectories to mathematical models, we are able to access the rich kinetic details present in the trajectories that has not yet been investigated. Kinetic information such as the

diffusion constant for dye release, the elapsed time until hemifusion dissipation, elapsed time between hemifusion dequenching and dissipation and the duration of a dequenching event can now be readily extracted and subject to analysis (see Chapter 5). The intent of the program design is that workers in the field of single-particle membrane fusion can utilize the software or its theoretical foundations to increase data throughput while also standardizing data analysis when extracting membrane fusion kinetics. Here, the theory underlying the selection algorithm and its application to the case of analyzing membrane fusion is described in detail. This chapter together with Appendix 3 will allow future investigators to utilize, adapt and expand the back-end analysis program that has been developed.

4.2 Algorithm design

The analysis platform is conceptually laid out in Figure 4-2, which shows the main steps involved in automated analysis of a fluorescence recording of the membrane fusion events arising from immobilized virus particles. It is designed to accept one split-field, dual emission channel recording (one fluorescent reading for the lipid signal and the second for the content signal, Figure 4-1) and perform two sequential types of analysis. The first type is image analysis where labeled virus particles are detected, they are tracked as the fluid flow causes them to roll upon the bilayer surface, and their fluorescence over time is extracted (termed fluorescence trajectory). This step also involves a number of calculations to correct the fluorescence levels in each recorded frame. The second type is decision analysis to determine which of the trajectories represents a true fusion event and which do not. The theoretical basis of the statistics used for making trajectory selection decisions is discussed first, followed by an overview of image analysis and details of the decision algorithm that uses the statistical tests to select particle trajectories.

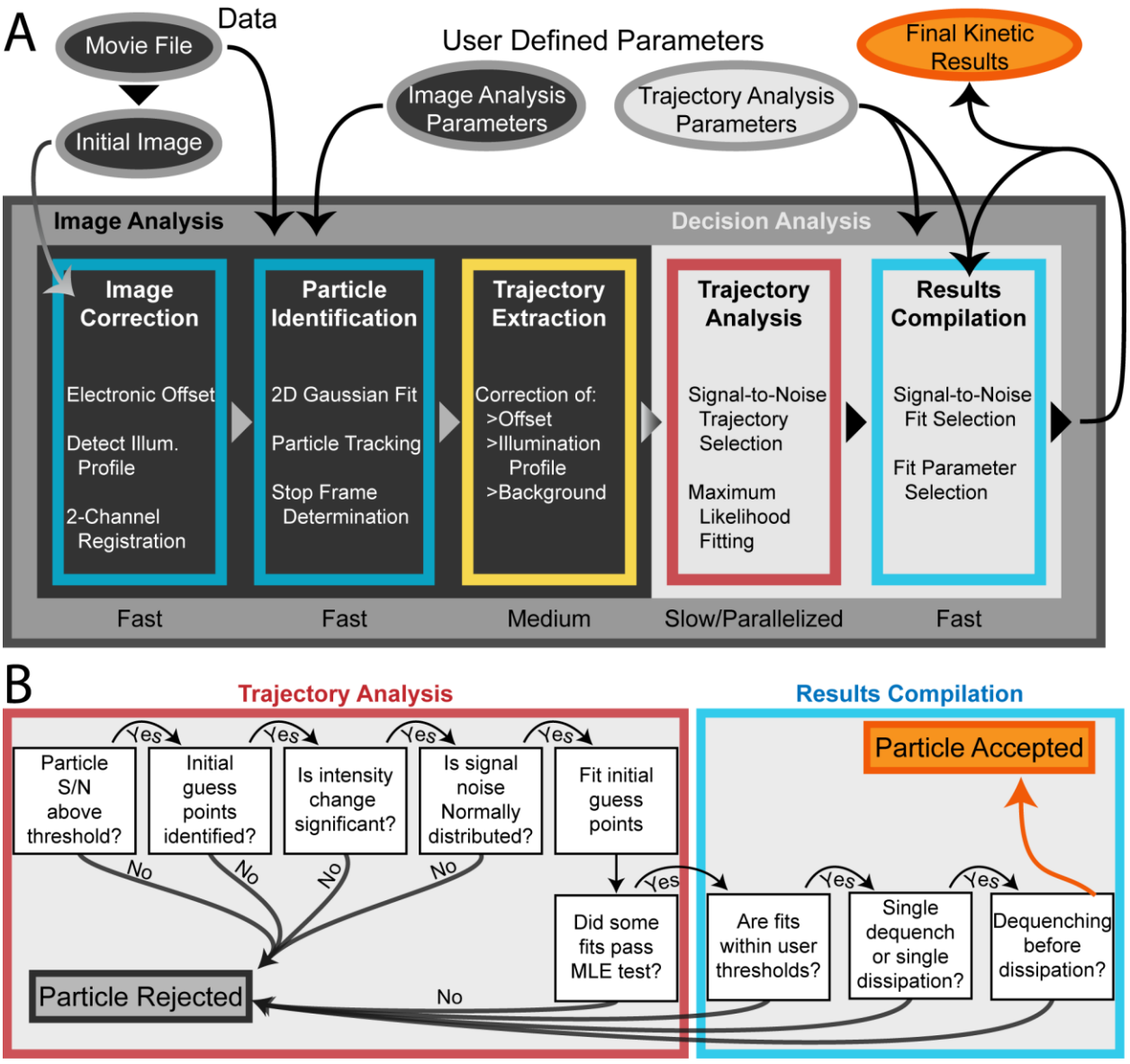

Figure 4-2 *– Schematic outline of data flow and trajectory selection implemented in the designed analysis program.* ***A****) Image Analysis serves to correct the images for the illumination profile and fluorescence background. Extracted fluorescence trajectories from identified and tracked particles are subjected to decision analysis algorithms that separate trajectories of virions undergoing membrane fusion from those that do not. Results are compiled in a fashion that user-defined trajectory analysis parameters can be iteratively altered to trim data without having to repeat the slow MLE-based trajectory analysis. Principal steps in the boxes are color coded to indicate the processing speed of each sub-step. Blue is rapid requiring less than one minute, yellow is intermediate requiring 2-5 minutes and red can require upwards of one hour. The red step has been parallelized to reduce computational time, but can still be time consuming depending on available computational power.* ***B****) Outline of the sequential steps comprising the Boolean decision function spanning the two portions of the Decision Analysis algorithm. This function chooses which individual particle trajectories are accepted for inclusion in reported kinetics or are rejected.*

4.2.1 Statistical tests

Statistical tests can be used for automated decision making by allowing for rejection of a null hypothesis with a certain degree of confidence or significance, α. This value represents the theoretical frequency of incorrectly or falsely rejecting the null hypothesis of a test. As depicted in Figure 4-2, a series of statistical tests has been concatenated to define a Boolean decision function designed to determine which of the extracted fluorescence trajectories represent fusion events falling within the definitions of the function.

Two tests are used in defining the decision function comprising the analysis algorithm. One is the Student's *t*-test, which is used to test if the mean of a single distribution is zero or if the mean value of two distributions is equal (i.e. the mean of their difference is zero). It is a valid test when estimating the mean of a sample to determine if it derives from a Normal distribution. While single fluorophores exhibit Poisson-based shot noise, fluorescently labeled virus particles have hundreds of individual fluorophores. As such, they collectively give rise to a noise profile that is the convolution of hundreds of Poisson distributions and is approximately a normal distribution, in agreement with the Central Limit Theorem. The "normalcy" of the integrated signal noise is shown in Figure 4-3 and supports the assumption of normally distributed noise in the trajectories of integrated fluorescence.

The *t*-test is used to in a number of instances, with null hypothesis rejection leading either to acceptance or rejection of a particle or trajectory under inspection. Specifically, it is used to check that the intensity noise of the trajectories is sufficiently Normal and null hypothesis rejection leads to particle rejection. Subsequently, it is used to ensure that changes in intensity around a point of interest are statistically relevant with null hypothesis rejection leading to acceptance of an intensity change.

The second statistical test is a maximum likelihood estimator test (MLE). This test estimates the optimal parameters when fitting a mathematical model to data and determines if the fit is statistically relevant as compared to a fit by a null model. Briefly, a domain of the

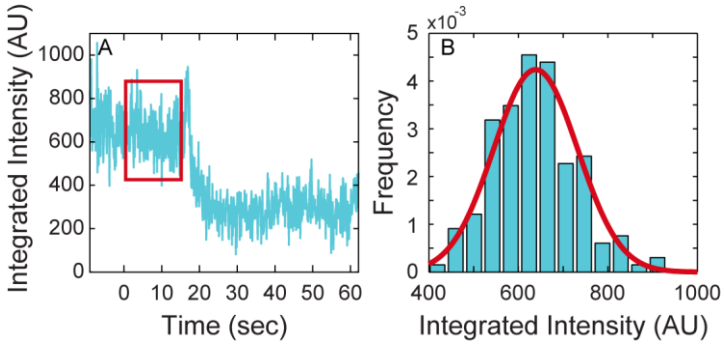

Figure 4-3 – *The integrated fluorescence signal of the virus particles is normally distributed.* ***A****) Fluorescence trajectory of hemifusion for a single influenza virion showing a dequenching intensity increase rapidly followed by signal dissipation caused by outward movement of the lipid dye. This trajectory is subsequently analyzed in Figures 4-5 and 4-6. The time between t = 0 and the first possible event point (Figure 4-5) is highlighted with a red box. Intensity within this region is plotted in (B) and corresponds to the intensity used to test for normalcy of the signal noise (Figure 4-2B).* ***B****) Distribution of the integrated fluorescence intensity values from the box in (A). It is well-fitted by a Normal distribution having* μ *= 638 AU,* σ *= 94.1 AU. Fitting results in an adjusted* R^2 *of 0.909 and the distribution passes a Student's t-test with a p-value of 0.929 and passes an Anderson-Darling test for normalcy with p = 0.644.*

fluorescence trajectory containing a point of interest is fit by two functions: 1) a model describing a change in the intensity; and 2) a null model that describes the absence of a change. The fitting domain selected from the trajectory is varied to obtain a number of fits for comparison to each other. The domain where the change model is both statistically significant and maximally better than the null model is taken to be the location of an event. If these conditions are not met, it is determined that no intensity change has occurred.

The change-point algorithm recently described by Yang [12] described the use of MLE to identify points of sudden changes in intensity in acquired fluorescence trajectories. In his description, extreme values of a ratiometric likelihood estimator occur at frames where there is a sudden change in fluorescence intensity. The likelihood ratio is defined as:

$$Likelihood\ Ratio = \frac{L_N(There\ IS\ a\ change)}{L_N(There\ is\ NO\ change)} = \frac{L_N(Model)}{L_N(Null)} \qquad (4\text{-}4)$$

where L_N is the function describing the likelihood of obtaining the observed intensities in N frames given a particular fit function. The MLE test involves calculating the likelihood value that a change occurs at a particular point within a trajectory, dividing it by the null likelihood that there is not a change at that point, and comparing their ratio to an analytical threshold set through a user-defined α value. If the likelihood ratio is above the threshold, then it may be considered a real event, otherwise it is considered not to have a change in signal intensity.

In the analysis algorithm described here, there being a *change* in fluorescence intensity corresponds to a dequenching or dissipation event, described by the mathematical models in Equations 4-2 and 4-3. There being *no change* in fluorescence intensity is taken to correspond to gradual intensity changes described by a simple line of the form $y = B*t+A$. This null model was selected because those particles that clearly do not show fusion upon visual inspection often show no obvious change in intensity throughout their trajectory and visually appear to change linearly in time. Photobleaching usually does not cause a significant non-linear effect in the extracted trajectories due to the low laser power used in observing viral fusion events (

typically ~1 W/cm^2). As such, bleaching in the trajectories often appears more linear than exponential, in accord with the Taylor series of the exponential function.

The likelihood function, L_N, is defined in terms of the joint density function, *g*, describing the probability of obtaining the observed values $\boldsymbol{Z} = \{z_1, z_2, z_3, \ldots, z_N\}$ in each of *N* frames given input parameters, θ, appropriate for the density function. Since each frame in a recording is obtained independently, the likelihood, L_N, can be described as:

$$L_N(\theta|Z) = g(Z|\theta) = g(z_1|\theta) \times g(z_2|\theta) \times \ldots \times g(z_N|\theta) = \prod_{f=1}^{N} g(z_f|\theta) \quad (4\text{-}5)$$

where θ represents the parameters describing the probability density function *g*. The $\boldsymbol{Z}$ values used in the algorithm are the residual values $z_f = y_f - model_f(\boldsymbol{p})$, obtained as the difference between the recorded fluorescence intensity values in each frame, y_f, and the fit to one of the models. The *model* can be from Equations 4-2 or 4-3, or the null model (straight line), and $\boldsymbol{p}$ is the vector of parameters at time *t=f* used in *models* from Equations 4-2 or 4-3, or *B* and *A* for the *model* of the null fit.

Model fits from Equations 4-2 or 4-3 may be relevant for only a short interval within a particular trajectory, notably when a dequenching event is rapidly followed by a dissipation event as in Figure 4-1. To this end, model fitting is performed from an initial frame *n* to a final frame *m* within the trajectory so as to detect short-lived and subsequent events, where the total length of the trajectory is *N* and $1 \le n < m \le N$. Computationally, it is much faster to compute the logarithm of the likelihood ratio, which converts the quotient into a difference and the products in to summations. Incorporating these changes, Equation 4-4 becomes:

$$\ln[Likelihood\ Ratio]_{n,m} = \sum_{f=n}^{m} \ln\left[g_{model}(z_f|\theta)\right] - \sum_{f=n}^{m} \ln\left[g_{null}(z_f|\theta)\right] \quad (4\text{-}6)$$

Using the assumption that the signal noise of the highly-labeled virus particles is Normally distributed, *i.e.* $g(z_f|\theta = \{\mu_z, \sigma\}) = \left(1/\sqrt{2\pi\sigma^2}\right) \times \exp\left(-(z_f - \mu_z)/2\sigma^2\right)$, and

presuming that a perfect fit results in an average residual value of zero, *i.e.* μ_z = 0, the two summations each acquire the form:

$$\sum_{f=n}^{m} \ln\left[g\left(z_f|\theta=\{0,\sigma\}\right)\right] = -\frac{S}{2}\ln[2\pi\sigma^2] - \frac{1}{2\sigma^2}\sum_{f=n}^{m}\left[y_f - model_f(\boldsymbol{p})\right]^2 \quad (4\text{-}7)$$

Here, $S = m\text{-}n\text{+}1$ and is the total number of frames used for fitting, σ is the signal noise determined for the fluorescence trajectory and $\boldsymbol{p}$ is the vector of fit parameters determined by least squares fitting. Calculation of the log likelihood ratio, then, is the difference between the sum of the squares of the residuals to the model fit (Equation 4-2 or 4-3) and the sum of the squares of the residuals to the null, linear fit.

The domain giving rise to optimal model fitting is determined by varying either *n* or *m* over a range *[a, b]* to obtain a set of log-likelihood ratio values. If *n* is varied, then values for *a* and *b* are restricted to $1 \le a < b < m$, and likewise if *m* is varied, then $n < a < b \le N$. The maximum of the set of log-likelihood ratio values is used to define the test statistic

$$Q_S = 2 \times \max_{a\le n,m\le b}\left\{\ln[Likelihood\ Ratio]_{n,m}\right\} \quad (4\text{-}8)$$

where the notation $a \le n, m \le b$ is to indicate that for either *n* or *m* being varied, the one being varied must lie between *[a,b]*, while the other is fixed and not confined to this restriction. This test statistic is then compared to the analytical threshold $C_{S,1\text{-}\alpha}$ that depends on the number of frames, *S*, used to determine Q_S and the user-defined significance level, α. As described by Yang, $C_{S,1\text{-}\alpha}$ is obtained by numerically solving for it in the expression (Equation 8 in [12]):

$$\frac{1}{2}C_{S,1-\alpha}^2 \exp\left(-\frac{1}{2}C_{S,1-\alpha}^2\right)\left[T - \frac{2}{C_{S,1-\alpha}^2}T + \frac{4}{C_{S,1-\alpha}^2}\right] = 1-\alpha \quad (4\text{-}9)$$

where for simplification the dependence on the number of frames, *S*, is simplified using: $T = \ln[(1\text{-}h^2)/h^2]$ and $h = \ln[S]^{3/2}/S$. This expression for $C_{S,1\text{-}\alpha}$ is only valid if the noise profile of the underlying data is Normally distributed, hence analyzed particles analyzed must be ensured to have Normally distributed signal noise. The MLE-based Boolean test then returns the result of the test:

$$\text{if}\begin{cases}\sqrt{Q_S} \geq C_{S,1-\alpha}, \text{ accept } model \text{ fit with parameters } \boldsymbol{p} \text{ between } n \text{ and } m \\ \sqrt{Q_S} < C_{S,1-\alpha}, \text{ reject } model \text{ fit}\end{cases} \quad (4\text{-}10)$$

Additionally, the fit parameters in the vector ***p*** must satisfy the condition of a signal increase for dequenching ($p_2 > p_1$, Equation 4-2) or a signal decrease for dissipation ($p_2 > 0$, Equation 4-3). In addition to being used for determination of optimal fitting parameters for dequenching and dissipation fusion events, this MLE test is used for determination of the rolling stop frame of the particles moving in buffer flow.

4.2.2 Image analysis

Image analysis begins by detecting a number of image correction factors, localizing virus particles, tracking their movement and finally extracting their fluorescence over the duration of recording. The recorded images are corrected for electronic offset, Gaussian illumination profile of the excitation beam and fluorescence background across a field of view. These corrections result in images that are flat with respect to the illumination beam and that have the peak of their pixel intensity distribution centered at zero.

Virus particles are initially localized by averaging a user-defined number of frames after the viruses have stopped rolling (see Appendix 3). The positions they assume at this point in a recording are obtained the using a merger of the two emission channels and are typically the same as the location where they undergo fusion. Registration of the two channels is performed by calculating the cross correlation between the two channels [13] to obtain a rigid [row, column] offset translation for moving from any position in one channel to the corresponding position in the other channel. Channel merger prior to particle identification allows for localization of all viruses, even if they contain only one of the two fluorescence signals, *i.e.* if a virus is only lipid-labeled or only content-labeled (Figure 4-1).

Intensity peaks corresponding to virions are detected in the merged image using a discoidal filter [14]. This filter draws two concentric circles around each pixel in an image – r_{in}

and r_{out} where $r_{in} < r_{out}$, and the outer circle's pixels do not include those of the inner circle – and filtered image is the difference between the average pixel intensities within these two radii. Virus particles are localized as clusters of bright fluorescence peaks that lie above a threshold value in the filtered image and have a minimal size (user-defined) or larger. The threshold is set as $\mu+m*\sigma$ where μ and σ are the average and standard deviation of the pixel values in the discoidally filtered image, respectively, and m is a user-defined multiplication factor (Appendix 3). The locations of these peaks are transferred to the merged image of the two channels, where each intensity peak is fit with a 2D Gaussian function [15]. Fitting is performed to obtain the size of the fluorescence spot, quantified as the width, σ_w, of the Gaussian fit. Large particles are excluded from analysis, with 'large' defined as lying above a $\mu+m*\sigma$ threshold, with μ and σ being the average and standard deviation of the particles widths and m being user defined (Appendix 3).

Once these initial virus locations are identified, virus movement throughout the course of the recorded movie is tracked. Tracking information is used to correct for microscope drift and to determine the frame when rolling viruses come to a stop [3]. Tracking of the virus particles is greatly facilitated by the high degree of labeling of the virus particles. Because they each have hundreds of fluorophores, the particles do not exhibit blinking and are thus present in every recorded frame up until they undergo fusion.

Identification of the rolling stop-frame utilizes a MLE test for two distance trajectories: the distance of a virus in each frame relative to its initial position and the distance relative to its final position. Both of these data appear sigmoidal in time with the former showing an increase as the virus gets farther away from its initial location, and the latter showing a decrease as the virus gets closer to its final location (Figure 4-4). Only those particles having a maximal displacement within their distance curve larger than a user-defined number of pixels are considered for stop-frame determination. To find the stop frame, both distance curves are fit with the sigmoid of

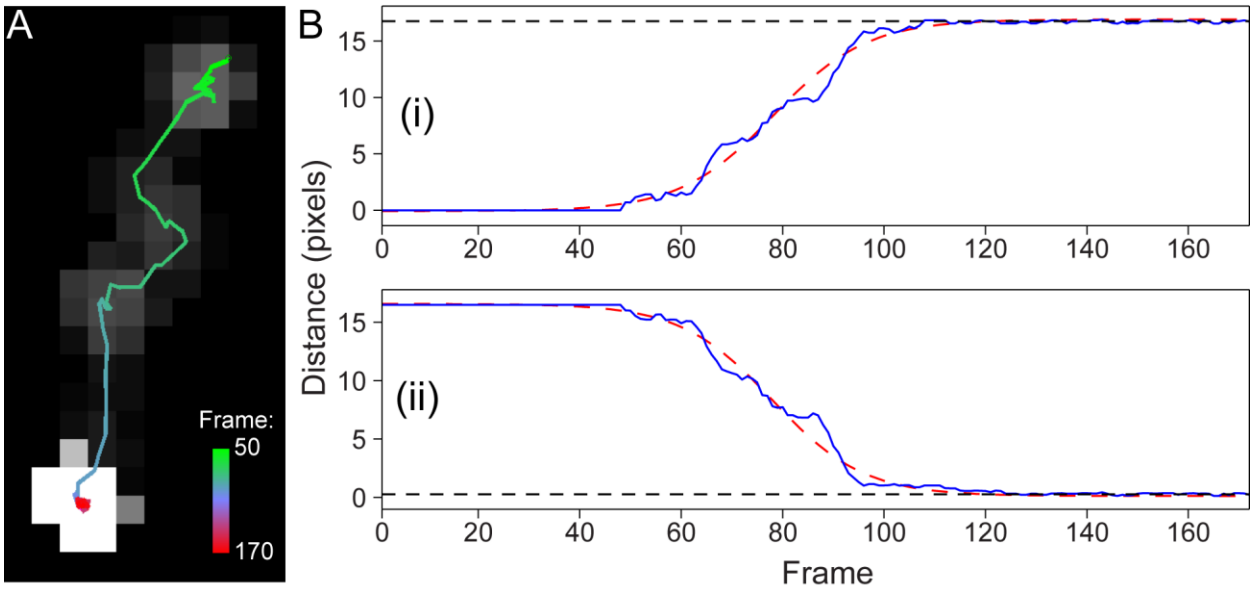

Figure 4-4 – *Tracking of virus particles allows for calculation of the frame where the virus stops rolling.* ***A****) Tracking trajectory of a virus particle. The grey-scale image shows the path of a virion with the grey-scale value set relative to the time the virus spent at each location. The overlaid trajectory found through particle tracking begins when the particle starts moving in frame 50 (green) and ends at frame 170 after the particle has stopped rolling (red).* ***B****) Distance trajectories used to identify the rolling stop frame. The distance from the virus' initial position (i) and from its final position (ii) are shown in blue; position trajectories are smoothed for fitting, but is not plotted for clarity. Movement trajectories are well fit by sigmoidal functions (red dashed lines). The lower bound of the upper plateau in (i) and the upper bound of the lower plateau in (ii) are black dashed lines. The first passage frame of the trajectory beyond these thresholds is taken as the rolling stop frame. Here, it was found to be frame 109 in (i) and 127 in (ii), so the reported value is 118.*

Equation 4-2, which allows for estimation of the upper and lower plateau values of the respective sigmoids. Comparison of the sigmoidal fit to that of a fit to a straight line (*i.e.* constant position) allows for calculation of a Q_S test statistic for comparison to a $C_{S,1-\alpha}$ threshold from Equations 4-8 and 4-9, respectively. If the test of Equation 4-10 is passed, then fit parameters are tested to ensure they correspond to sigmoidal increases/decreases. Two frames are identified: the first frame when the distance curve passes the lower bound of the upper plateau when analyzing distance from the initial position (Figure 4-4B.i); and the first frame below the upper bound of the lower plateau when analyzing distance from the final position (Figure 4-4B.ii). When these two frames are not equal, their mean value is recorded. Particles found moving in both channels have the average of all four stop-frames reported.

Virus particle locations in every frame of the recording allows for extraction of each particle's fluorescence intensity throughout the movie without interference from particle movements. All pixels within a distance that is a multiple of the previously calculated width, σ_w, are utilized for signal integration and trajectory compilation (Appendix 3). For instance, if the user defined a value of m = 2, then all pixels within a distance of $2\sigma_w$ from the center of the Gaussian fitting are used for signal integration. This distance corresponds to r in Equation 4-3. Integration of the pixel intensities for each viral particle provides a unique dual fluorescence time-trajectory that captures the full fusion behavior of each individual virus particle. These trajectories are then subjected to a Boolean decision function (Figure 4-2B) that selects which trajectories indicate successful membrane fusion and which do not.

4.2.3 Decision analysis

Decision analysis begins, as outlined in Figure 4-2B, by rejecting dimmer particles because they often give rise to poorly interpretable trajectories. Dim particles are identified according to their signal-to-noise, calculated at the beginning of a trajectory. Those particles

whose ratio is below a user-defined threshold are rejected (Appendix 3). The noise profile of the trajectory itself is tested for how closely it corresponds to a Normal distribution by subjecting it to a Student's *t*-test. Those particles determined to have a non-Normal noise profile are rejected. This test is necessary, since the likelihood ratio calculated in Equation 4-6 and the analytical threshold used for Q_S comparison are dependent upon the assumption of Normally distributed noise [12].

Trajectories having a satisfactorily Normal noise profile are smoothed using a Fourier filter [16] and the smoothed trajectory analyzed using two sliding-window based filters. These filters identify time points corresponding to large signal increases or large signal decreases, as depicted in Figure 4-5.*ii-v*. The use of sliding window filters to initially select a few key points of interest reduces the required computational overhead by focusing the least squares fits to domains that are most likely to have an event detected. The alternative would be to scan the entire trajectory, which can be more than 1500 frames in length, from beginning to end and determine if a dequenching or dissipation event was fit significantly at some point within the trajectory.

One filter is a Savitzky-Golay (SG) filter (built-in MATLAB function) acting upon the first derivative of the smoothed trajectory. It is a digital filter that fits a line through all points within a window that slides through the length of the trajectory. The other filter is a sliding window difference filter that calculates the difference between the average signal in a window immediately prior to and immediately after each point in the trajectory, akin to the smoothed trajectory's first derivative. A threshold is defined for the output of each filter (Figure 4-5) as $\mu \pm m^*\sigma$, where μ and σ are the average value and standard deviation of the filtered first derivative, respectively, and m is a user-defined multiplication factor. Regions of the filtered first derivatives lying above the upper threshold designate possible intensity increases and regions below the lower threshold are possible intensity decreases. The peak value above or below the

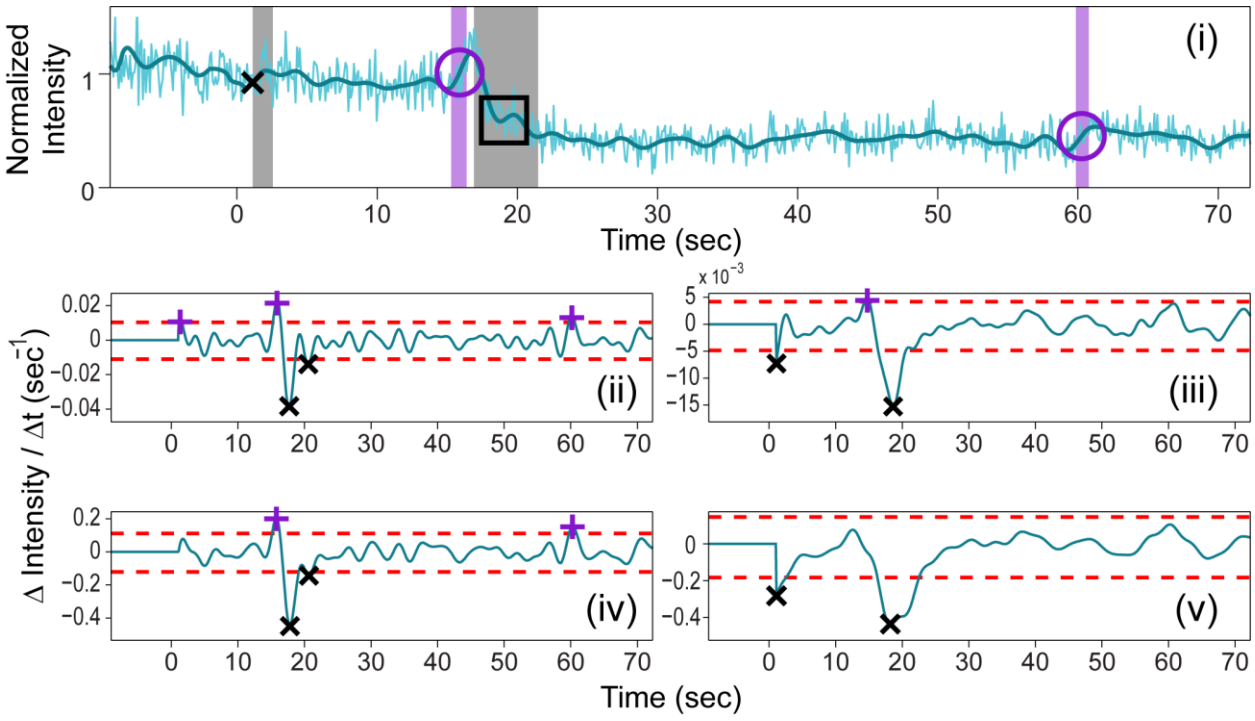

Figure 4-5 – *Filtering by two sliding window-based filters allows identification of initial points of interest that may be fusion events.* ***i****) The trajectory of Figure 4-3 is analyzed by the Savitzky-Golay (SG) derivative filter (****ii*** *and* ***iii****), and by a sliding window difference filter (****iv*** *and* ***v****) to identify time points that may correspond to fusion events. Raw data is shown as light blue and smoothed data used for intensity change identification is the overlaid heavy blue line. Identified points of interest that are sent for MLE-based fitting are indicated as purple circles for intensity increases or as black squares for intensity decreases. The confidence intervals ascribed to each potential event point are set by the collective domains of the first derivative above or below the thresholds in ii-v and are indicated by the filled purple or grey box underlying each circle or square, respectively. For instance, the decrease near t = 20 is identified repeatedly in (ii-v), with a large domain in (v) lying beyond the threshold, hence it has a large confidence range.* ***ii*** *through* ***v****) The smoothed first derivative data of the trajectory in (i) is shown as a blue line; thresholds determined as* $\mu \pm 2^{*}\sigma$ *of this first derivative are shown as dashed red lines. The first derivative is set to zero for t < 0. ii and iv) A window size of 17 frames is used and identifies two increases of interest (purple cross) near t ~ 15 and 60 seconds and two decreases (black 'x') both near t ~ 20 seconds. The increase near t=0 is found only in the SG filter and is rejected. iii and v) A window size of 51 frames is used and identifies two decreases near t ~ 0 and 20 seconds. The decrease near t=0 is rejected because the intensity change at its location is determined non-significant by the Boolean decision function of Figure 4-2B, hence a square is not placed at its location in (i).*

threshold is taken as the possible event point and a pseudo-confidence interval around each point is defined as the first and last frame where the filtered derivative surpasses the threshold.

While these filters have the advantage of being computationally fast, they will almost invariably return a possible event point, though the event point returned may appear spurious and uninteresting upon visual inspection. Often, a number of these undesirable possible event points are identified by one of the two filters, but they are less often identified by both filters. Increases/decreases detected by both filter types are thus selected as initial points for possible events (Figure 4-5). Such discrimination constitutes the first level of event point selection. These initial "guesses" are screened to confirm that the signal intensities before and after the event frames are statistically significant using a *t*-test.

Different filter window sizes are useful for detecting different signals – small windows for short events and large windows for long events. Dequenching events are rapid and short-lived (Figure 4-5.*ii*,*iv*), while signal dissipation events arising from diffusion are longer-lived events (Figure 4-5.*iii,v*). To detect both signals in a single trajectory, the window used for filtering the first derivative to detect events is increased from an user-defined initial value until the window size is large enough that no events are detected above or below the thresholds. Points whose pseudo-confidence regions overlap are grouped together to define initial guesses for plausible event points.

Finally, these initial guess points are used as initialization parameters for least squares fitting of the raw fluorescence trajectories to the model functions of Equations 4-2 and 4-3 for identification of dequenching or dissipation, respectively. The behavior of these empirical, mathematical models mirrors that observed in the fluorescence trajectories obtained from fusing virions (Figures 4-1 and 4-6). Extracted fit parameters provide estimates for the kinetics associated with an individual fusion event and are determined with upper and lower confidence bounds (see Appendix 3). When dissipation occurs during hemifusion detection, it corresponds to the outward diffusion of the lipid dye into the target bilayer away from the site of hemifusion.

The dissipation Equation 4-3 has been used previously to extract the two dimensional diffusion constant of the lipid dye [5] following a dequenching event. In the case of pore formation, dissipation of the signal from the contents of the virus could be ascribed to the diffusion of the dye in the area between the coverslip and the bilayer created by the dextran cushion. In the analysis described here (and in Chapter 5), it is treated only as a rate of signal loss and is not directly interpreted with a physical meaning.

For each initial guess point, a domain surrounding it is defined and taken as a section of the whole trajectory to be used for fitting, as described in the *Statistical Tests* section. Edges of the domains defined by *n* and *m* are varied between *a* and *b* in such a way that, ideally, the trajectory information is well approximated by the null model at one extreme and gradually fit with increasing likelihood by the model function of interest. For dequenching, the starting frame, *n*, is fixed as either the left-most edge of the trajectory or the upper bound for the immediately preceding guess point, and the end frame, *m*, is varied from the lower bound of the guess point being probed up to either the next guess point or the end of the trajectory. For dissipation, *n* is varied from either the left edge of the trajectory or the upper bound of the immediately preceding guess point up to the upper bound of the guess point being probed, and *m* is fixed as either the lower bound of the subsequent guess point or the end of the trajectory. In this fashion, the MLE-based statistical test determines 1) the statistically optimal fitting domain and 2) the corresponding best fit parameters that extract valuable kinetic information. If the MLE test is not passed, then the fit at the guess point is rejected.

The existence of an analytical threshold in the MLE test is useful because it is conceptually easy to understand and define. In practice, however, the values for $C_{S,1-\alpha}$ obtained are often quite small compared to many values of Q_S that are calculated. It often occurs that the four-parameter models of Equations 4-2 or 4-3 produce Q_S values indicating a statistically better fit to the data that is not corroborated by visual inspection of the resulting fit line. This discrepancy arises because the four parameter fit lines are better able to accommodate

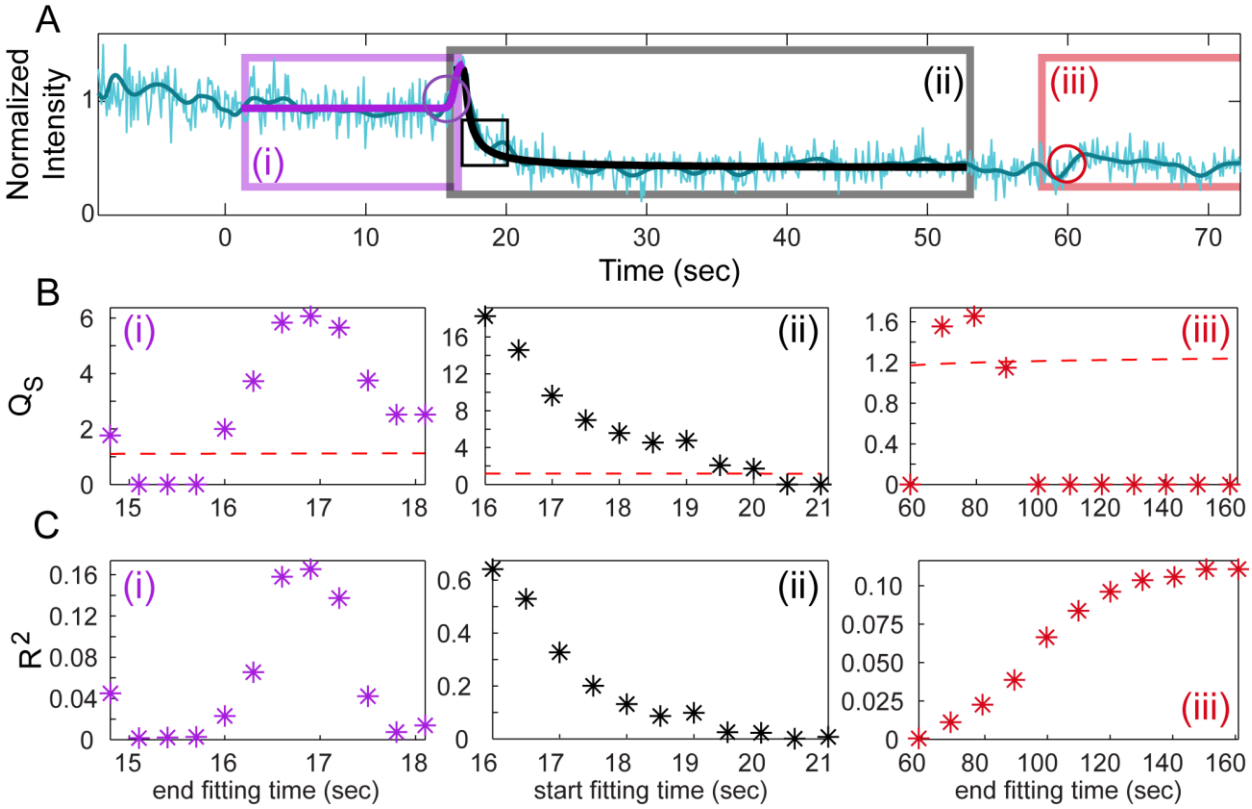

Figure 4-6 – *Dequenching and dissipation signals are automatically fit and detected using maximum likelihood estimators.* ***A****) Trajectory from Figure 4-3 is analyzed using the three points of interest identified in Figure 4-5 to perform the MLE test within the domains indicated by the purple, black and red boxes. Equation 4-2 is used for the points in (i) and (iii); Equation 4-3 is used for (ii). Intensity increase in (i) and decrease in (ii) are found to be dequenching and dissipation events shown as thick purple and black lines, respectively. The increase in (iii) is rejected and not fit.* ***B****) Values for the Q_S estimator as one edge of the fitting domain is varied to find maximal values above the analytical threshold, shown as dashed red lines. In (i) and (iii) the starting time point for fitting is fixed and the end time point of the fitting box is varied to find where Q_S becomes maximal. In (ii) the end time point is fixed and the starting time point is varied.* ***C****) R^2 values for the fits performed within the indicated domains and corresponding to Q_S values in (B). Maximal values of Q_S and R^2 correspond for (i) and (ii), but not for (iii), hence (i) and (ii) are accepted and (iii) is rejected.*

intensity fluctuations than is the two parameter linear null model. To reduce the occurrence of this type of error, a model fit passing the MLE test of Equation 4-10 is compared to its R^2 value, both of which depend upon the fitting residuals, z_f. Situations where the fit should be accepted show a maximal Q_S value that corresponds to a nearly maximal R^2 value (Figure 4-6.*i,ii*). At those points that should be rejected however, the Q_S value rises above the $C_{S,1-\alpha}$ threshold, but the overall R^2 value of the fit is not yet maximal and the Q_S value falls back below the $C_{S,1-\alpha}$ value shortly after this fluctuant point (Figure 4-6.*iii*).

To help ensure fits to fluctuant points are rejected, the MLE test is performed twice. The first round of MLE testing determines at what starting/ending frame the Q_S value is maximal and, also, where the R^2 value is maximal. In the second round, the average of these two starting/ending positions is used to set the appropriate edge of the fitting domain and the MLE test performed again. If the frame giving maximal Q_S and R^2 values are in close proximity, then it is likely that the second round Q_S value will also be larger than the threshold. If they are far apart, however, it is likely that the large Q_S value occurred due to a fluctuant point and the second round Q_S value will be below the threshold and the fit to the guess point rejected.

Fit parameters determined by the sequential MLE tests are checked to ensure that a dequenching fit corresponds to an intensity increase, and that dissipation fits correspond to an intensity decrease. In this fashion, fluorescence trajectories are determined to have a dequenching or dissipative signal without any manual intervention. Parallel processing is utilized to perform MLE-based fitting of multiple trajectories simultaneously on separate CPU cores, which greatly reduces the overall required computational time. It was found that with a single processing core, approximately 400 single-channel trajectories of 1500 frames required approximately one hour of processing time.

4.2.4 Extracted fusion kinetics

Kinetic information extracted from the fluorescence trajectories selected to represent membrane fusion events is in the form of waiting times. These times are the elapsed time between the detected pH drop and the onset of signal dequenching or the onset of signal dissipation. The time points extracted are depicted schematically in Figure 4-1. Once the slow MLE-based fitting procedure has been completed, selection of trajectories to acquire fusion kinetics is computationally fast and can be iterated to filter out trajectories based on user-defined parameters. Statistically significant dequenching and dissipation fits can be selected based on signal-to-noise thresholds of the resulting fit parameters or by setting absolute limits for the permitted values of the p_4 fit parameters (see Appendix 3). In both Equations 4-2 and 4-3, the p_4 parameter determines the duration of a particular event and certain limits may be desirable. Fast or slow events could indicate strange behavior, such as detachment of a virion from the bilayer in the case of dissipation or influx of fluorescence from neighboring virions in the case of dequenching, respectively. The p_4 parameter is useful also for extraction of physical properties relevant to the fusion process. For dequenching, this parameter describes the width of the dequenching event. For dissipation, this parameter describes the diffusion constant of the fluorescent signal, a quantity of potential use when observing movement of lipid signal dissipation.

For dequenching fits, the elapsed time between the pH drop and dequenching is determined to be the first time point when the MLE-determined fit is greater than the upper bound for the p_1 parameter. This time constitutes the moment when the intensity increase is above the base line. In previous studies [1,2] and in Chapters 2 and 3 the hemifusion time was taken as the point where the first derivative of the trajectory was maximal as determined using only a SG filter. The current time point determination reproduces the previously observed kinetics because this first passage time is, necessarily, near the region where the trajectory will have its largest first derivative. The p_3 parameter could also have been used, but in this case

the fluorescence signal is already increasing and the parameter does not truly capture the first moment when the signal can be confidently determined to be increasing.

For dissipation fits, the elapsed time between the pH drop and the onset of dissipation is taken to be the p_3 parameter resulting from the fits. This is the moment in the trajectory when the Heaviside function allows the diffusion equation to match with the observed fluorescence loss. This definition for the onset of signal dissipation more reliably captures the initiation point than does the previous determination of dissipation time, which was the minimum value of the trajectory's first derivative again determined by a SG filter. Empirically, this moment occurred closer to the mid-point of a dissipative signal. It is expected that extraction of the onset time for dequenching or dissipation in the manner described here will be systematically smaller than time points identified only by a SG filter, though the absolute difference will be small relative to the speed of relevant fusion kinetics.

The fitting-based algorithm now provides access to additional kinetic information not previously considered in viral membrane fusion studies. These kinetic data include: the lipid signal dissipation time, elapsed time between lipid dequenching and lipid dissipation (Figure 4-1), elapsed time between lipid dissipation and content dissipation and the duration of the lipid dequenching event.

4.3 Results validation

Accumulation of waiting times from the selected fusion trajectories into distributions provides insight into the biochemical mechanism underlying membrane fusion. There is no absolute "gold standard," however, for reliably comparing acquired distributions. Rather, comparison of the results acquired by this automated algorithm must be compared to those resulting from manual trajectory selection. To validate the kinetics obtained from trajectories selected using the algorithm described here, the waiting time distribution of hemifusion dequenching obtained by the algorithm from a single fusion recording is compared to

distributions acquired from two independent, manual trajectory selections of the same recording. Only the hemifusion dequenching time is compared between the different analysis methods because too few hemifusion lifetime and pore formation events are observed in a single fusion recording to allow comparison of these event distributions. The fusion recording used for validation is of X31 influenza A fusing to a bilayer comprised of DOPC*, POPC** and Cholesterol in a 2:2:1 ratio at a pH of 5.0 and is one included by Floyd *et al.* in their publication originally describing the single-particle membrane fusion assay [1]. The results from automated analysis are compared to a third manual selection found to be over-correcting for particle motion and under-sampling the earliest time bins, which serves as a negative control.

Figure 4-7 presents the results of the comparison of the hemifusion waiting time distributions obtained through automated analysis to those obtained manually. The first manual selection indicated as 'Manual #1' was performed by Daniel Floyd and the selected data were later aggregated with additional experimental data to obtain his final published results [1]. I performed the second manual selection (Manual #2) by visually inspecting both the extracted fluorescence trajectory and each virus particle at its location in the recorded fusion movie. This particle-by-particle selection using both pieces of information required approximately 2.5-3 hours to screen approximately 300 particles and allows comparison of the time involved in such scrutinous trajectory selection. I also performed the trajectory selection giving rise to the 'erroneous' waiting time distribution prior to the more careful trajectory selection giving rise to 'Manual #2.' Selection giving the erroneous distribution involved only visual inspection of the extracted fluorescence trajectories. The difference in particle selection was found to arise from over-estimation of particle motion in the early portion of the fluorescence trajectory, which led to excessive trajectory rejection and under-sampling of early fusion events. Each distribution in Figure 4-7 includes time points from approximately 100 particles, which is twice the estimated

* 1,2-dioleoyl-sn-glycero-3-phosphocholine (DOPC);
** 1-palmitoyl-2-oleoyl-sn-glycero-3-phosphocholine (POPC)

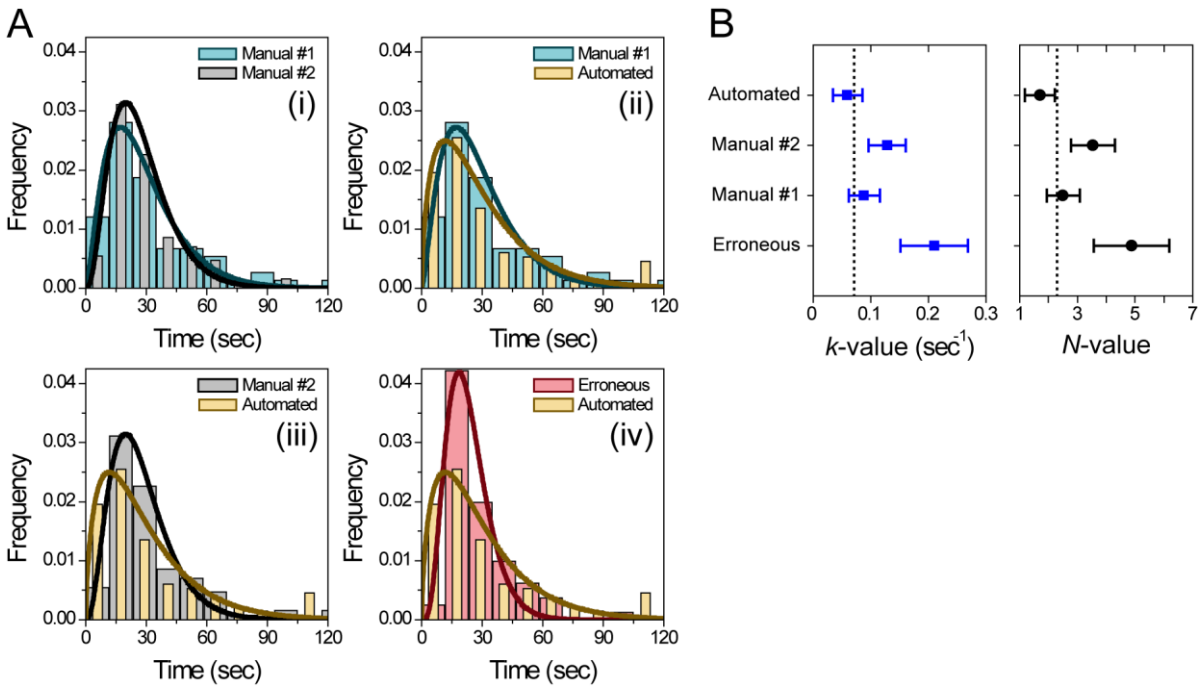

Figure 4-7 – *Kinetic data compiled from automated analysis reproduces results obtained from accepted, manual data selection.* ***A****) Hemifusion waiting time distributions are shown with corresponding fits by the gamma distribution. Accepted manual selections #1 and #2 are shown in light blue and grey with fits in blue and black, respectively. Automated analysis is shown in yellow with a yellow fit line. The erroneous manual selection is shown in red with a dark red fit line. Reports of a t-test comparing the distribution means is reported in Table 4-1.* ***B****) Gamma distribution fitting parameters k and N for the fits shown in (A) are shown with error bars representing 95% confidence bounds for the fits. Values for k and N published in* [1] *are shown for reference as vertical dashed lines.*

number of data points needed to distinguish an *N* value of 2 from a value of 4, under the assumption of equal trajectory selection [17].

Automated particle selection accounts for particle motion by incorporation of a particle tracking algorithm and, thus, early time bins should be unaffected by virus rolling. Full analysis of the two-color fusion recording, including fluorescence trajectory extraction followed by selection by the Boolean decision function, required approximately 25 minutes on a computer containing two CPU's. For the analysis considered here, the fits of hemifusion dequenching were required to give fit parameters having a signal-to-noise of at least one with no additional data filtering to restrict values for the dequenching time (p_4, Equation 4-2). The signal-to-noise requirement was varied from values of one to five with no effect on the results obtained.

The hemifusion waiting time distribution extracted by the automated algorithm matches nicely to the distributions measured for both Manual #1 and Manual #2, as can be observed in Figure 4-7A.*i*,*ii*,*iii*. The erroneous distribution stands apart from the other three distributions, a visual observation captured both in comparisons of the distribution means by a *t*-test (Table 4-1) and in the extracted *k* and *N* values.

Table 4-1 – Statistical comparison of kinetic distributions using the Student's *t*-test

Comparison	*t*-test *p*-value
Manual #1 vs. Manual #2	0.799
Manual #1 vs. Automated	0.693
Manual #2 vs. Automated	0.866
Manual #1 vs. Erroneous	0.170
Manual #2 vs. Erroneous	0.087
Automated vs. Erroneous	0.129

Fit parameters obtained by modeling the three distributions in Figure 4-7A.*i*,*ii*,*iii* with a gamma distribution (Figure 4-7B) are in good accord with each other, lying within each other's 95% confidence intervals. They are also in good correspondence with the published values of k = 0.071 and N = 2.3 [1]. The erroneous distribution of Figure 4-7A.*iv* gives rise to k and N values that do not agree with *i*, *ii* and *iii* or with the published values. The trend of greater similarity between Manual #1 and Manual #2 with the automated distribution is observed in the larger *t*-test *p*-values indicating greater degrees of similarity than for any of them with the erroneous distribution. While the *p*-values obtained for comparison with the erroneous distribution do not fall below the commonly accepted p = 0.05 level to establish a statistically significant difference, they are substantially smaller than the values obtained in comparing distributions in Figure 4-7A.*i*,*ii*,*iii*. Based on the agreement between the kinetics extracted by the automated algorithm and those obtained by manual analyses, the automated selection of fusion trajectories is thus considered to be comparable to that performed manually.

4.4 Future development

Algorithm design and testing to this point indicate it is robust and can be operated in batch processing to sequentially analyze multiple fusion recordings without the need for user intervention. Testing the algorithm to provide the data included in this chapter, along with the analysis described in Chapter 5, required the automated analysis of 74 separate fusion experiments consisting of 24,391 individual virus particles. Not only is the time required for data analysis reduced by nearly 6-fold and made more reproducible through use of this program, additional kinetic time points and parameters can now be studied. Detection of the time when a lipid signal undergoes dissipation following dequenching allows for two additional intermediate times to be probed: the time between lipid dequenching and dissipation (as observed in Figures 4-1 and 4-6) and the time between lipid dissipation and content signal dissipation. Both of these values are related to the hemifusion lifetime and the point where lipid merger has begun, but

viral contents have not yet been released. As well, the two-dimensional diffusion constant of the lipid dye escaping from the viral envelope may provide information regarding the nature of the hemifusion stalk formed upon initial membrane merger. To make this programmatic algorithm more amenable to use in the field of membrane fusion, however, additional development will be required.

One fundamental development is expansion of the recording conditions that can be accepted by the program, principally for particle detection. At present, only two channel movies having dually labeled virus particles can be accepted as an input. The emission channels must be separated into the top-half and bottom half of each frame, with the pore formation occurring in the red (longer wavelength) channel on top and the hemifusion occurring in the green (shorter wavelength) channel on bottom. Single color and other split-field orientations such as green-top and red-bottom, or left-right orientations with the green or red on either side of each image, should be incorporated to allow input flexibility. As described in Appendix 3, all of the scripts requiring a particular image layout have options defined for the various orientations described, but have yet to be tested. Additionally, accommodation of full image recordings, rather than split-field, should be included, since detection setup allows for the largest possible field of view.

For particle detection, the currently implemented program uses a merger of the two channels to locate particles. An alternative two-color identification strategy that needs to be accommodated is localization of viruses in only one channel, *i.e.* red channel, that are then transferred to the green channel. This method as used in Chapter 3 allowed measurement of the fluorescence arising from fluorescently labeled antibodies bound to the immobilized virus particles even if the fluorescence signal from the antibodies was too faint to be readily detected. As well, single-color fusion experiments to follow solely hemifusion or pore formation need to be accommodated.

To facilitate the definition of the analysis conditions and parameters to be used, a graphical/guided user interface (GUI) is in need of development. The GUI should allow users to

define the image and trajectory analysis parameters described in Appendix 3 in an intuitive and understandable fashion. One suggested method would be to ask a user to define parameters sequentially, first by loading a fusion recording and acquiring a sample image that can be used for determination of filtering parameters for particle detection. Once particles are detected and tracked, particles known to the user to be ideal fusion trajectories should be chosen through a point-and-select method. The fluorescence trajectory of these nicely fusing virions can be plotted and the trajectory selection parameters defined to ensure that the few tested trajectories visualized are accepted by the Boolean decision function.

Additional validation metrics should also be evaluated. While it was shown here that the kinetics extracted by the automated algorithm are comparable to those resulting from manual selection, the error of trajectory selection has not been evaluated or compared to manual selection. As such, the true positive/negative and false positive/negative selection percentages remain to be determined for the algorithm. These ratios should also be determined for analysis of movies of varying quality, where the focus and brightness of the recordings is varied.

Though the limitations of this analysis method have yet to be fully evaluated, the proof-of-principle validation for the power of the maximum likelihood estimator-based selection criteria in choosing fusion trajectories has been achieved. Further advancement of the algorithm described here is sincerely hoped for and given the imparted advantages of increased data throughput and of improved reproducibility of the analyzed data, it is certainly warranted.

4.5 References

1. Floyd DL, Ragains JR, Skehel JJ, Harrison SC, van Oijen AM. (2008) Single-particle kinetics of influenza virus membrane fusion. Proc Natl Acad Sci U S A 105: 15382-15387.

2. Ivanovic T, Rozendaal R, Floyd DL, Popovic M, van Oijen AM, et al. (2012) Kinetics of proton transport into influenza virions by the viral M2 channel. PLoS One 7: e31566.

3. Ivanovic T, Choi JL, Whelan SP, van Oijen AM, Harrison SC. (2013) Influenza-virus membrane fusion by cooperative fold-back of stochastically induced hemagglutinin intermediates. eLife Sciences 2. 10.7554/eLife.00333.

4. Floyd DL, Harrison SC, van Oijen AM. (2009) Method for measurement of viral fusion kinetics at the single particle level. J Vis Exp (31). pii: 1484. doi: 10.3791/1484.

5. Wessels L, Elting MW, Scimeca D, Weninger K. (2007) Rapid membrane fusion of individual virus particles with supported lipid bilayers. Biophys J 93: 526-538.

6. Imai M, Mizuno T, Kawasaki K. (2006) Membrane fusion by single influenza hemagglutinin trimers. kinetic evidence from image analysis of hemagglutinin-reconstituted vesicles. J Biol Chem 281: 12729-12735.

7. Otterstrom J, van Oijen AM. (2013) Visualization of membrane fusion, one particle at a time. Biochemistry .

8. McGuire H, Aurousseau MR, Bowie D, Blunck R. (2012) Automating single subunit counting of membrane proteins in mammalian cells. J Biol Chem 287: 35912-35921.

9. Zhang K, Chang H, Fu A, Alivisatos AP, Yang H. (2006) Continuous distribution of emission states from single CdSe/ZnS quantum dots. Nano Lett 6: 843-847.

10. Kerssemakers JW, Munteanu EL, Laan L, Noetzel TL, Janson ME, et al. (2006) Assembly dynamics of microtubules at molecular resolution. Nature 442: 709-712.

11. Myong S, Bruno MM, Pyle AM, Ha T. (2007) Spring-loaded mechanism of DNA unwinding by hepatitis C virus NS3 helicase. Science 317: 513-516.

12. Yang H. (2012) Change-point localization and wavelet spectral analysis of single-molecule time series. In: Komatsuzaki T, Kawakami M, Takahashi S, Yang H, Silbey RJ, editors. Single-Molecule Biophysics: Experiment and THeory. COMMERCE PLACE, 350 MAIN STREET, MALDEN 02148, MA USA: WILEY-BLACKWELL. pp. 219-243.

13. Guizar M. (2008) Efficient subpixel image registration by cross-correlation (http://www.mathworks.nl/matlabcentral/fileexchange/18401-efficient-subpixel-image-registration-by-cross-correlation), MATLAB central file exchange. Retrieved June 13, 2013.

14. Hedde PN, Fuchs J, Oswald F, Wiedenmann J, Nienhaus GU. (2009) Online image analysis software for photoactivation localization microscopy. Nat Methods 6: 689-690.

15. Yildiz A, Forkey JN, McKinney SA, Ha T, Goldman YE, et al. (2003) Myosin V walks hand-over-hand: Single fluorophore imaging with 1.5-nm localization. Science 300: 2061-2065.

16. Ben-Ezra S. (2009) FFT filter - clean your signals and display results! (http://www.mathworks.nl/matlabcentral/fileexchange/25017-fft-filter-clean-your-signals-and-display-results), MATLAB central file exchange. Retrieved July 19, 2013.

17. Floyd DL, Harrison SC, van Oijen AM. (2010) Analysis of kinetic intermediates in single-particle dwell-time distributions. Biophys J 99: 360-366.

Chapter 5

Polyunsaturated Lipids Enhance Influenza Hemagglutinin Membrane Fusion Kinetics and Efficiency as Revealed by Single Virus-Particle Observation

Abstract

Biological membranes where membrane fusion is rapid and frequent possess substantially different lipid compositions compared to more static plasma membranes, likely reflecting the dynamic nature of the membrane fusion process. They contain larger amounts of polyunsaturated fatty acids (PUFA) that are characterized by high degrees of acyl chain flexibility and water permeation in contrast to monounsaturated fatty acids (MUFA). Here, a planar phosphatidylcholine bilayer comprised of either MUFA or PUFA lipids is formed on a dextran support and serves as a target for fusion by influenza viruses via hemagglutinin (HA)-mediated fusion. Individual virus particles are observed using a dual-color fluorescence microscopy-based fusion assay that simultaneously records lipid- and content-mixing events [1]. Automated and quantitative analysis reveals that fusion to MUFA bilayers frequently produces a long-lived state of restricted hemifusion where viral and bilayer lipids are fused, but do not freely intermix. HA is capable of forming a fusion pore through the restricted hemifusion intermediate wherein viral content is released after lipids initially begin to mix, but prior to free intermixing of the viral and bilayer lipids. When fusing to PUFA bilayers, viruses are less prone to enter a restricted hemifusion state, and release their contents more rapidly and more efficiently. It is postulated that the confined lipid diffusion present during the restricted hemifusion state results from the formation of a molecular fence created by the influenza fusion peptide and cholesterol present at the site where fusion takes place.

5.1 Introduction

Infection of a cell by the influenza virus begins when the virus binds to the surface of its target, enters the cell via clathrin-mediated endocytosis, then perforates the endosomal membrane to release its viral genome into the cytosol and begin cellular hijacking. Both of these initial steps in the infection process are mediated by the viral surface protein hemagglutinin (HA) [2]. The HA fusion protein represents a model system for understanding viral membrane fusion, where energetic barriers separating the final fusion product [3,4] must be crossed without the use of ATP or other external energy source. As a result, viral HA are highly dependent upon both the sequence and structure of the protein itself [5] and the properties of the membrane to which it will mediate fusion [6].

HA is a homotrimeric transmembrane protein embedded at high copy number into the phospholipid membrane of the influenza virus. Each HA monomer is initially produced in a fusion inactive form, HA0, that upon proteolytic cleavage forms two disulfide-linked domains, HA1 and HA2, that constitute the pre-fusion form of the protein [7]. The HA1 domain is located distal from the viral membrane and contains a sialic acid receptor binding pocket that serves to bind a virus to the surface of target cells [2][8]. The viral membrane-proximal HA2 domain represents the primary fusion machinery of HA, containing the highly conserved N-terminal fusion peptide and the viral membrane embedded C-terminal transmembrane region (Figure 5-1A) [9]. HA2 is capped by the HA1 domain and locked into a metastable conformation at neutral pH. Upon exposure to acidic conditions below pH 5.5 in the late endosome of a cell, the HA2 undergoes a massive conformational change, unfurling the hydrophobic fusion peptide from its initial position in a pocket near the viral membrane and inserting it into the target membrane [10,11]. This extended intermediate of HA acts to couple the viral and target bilayers and has been detected only indirectly [5]. Subsequent re- folding of the extended conformation back upon itself is thought to bring the two membranes into close apposition through formation of a nipple-like structure that facilitates the onset of lipid mixing between the proximal leaflets (Figure

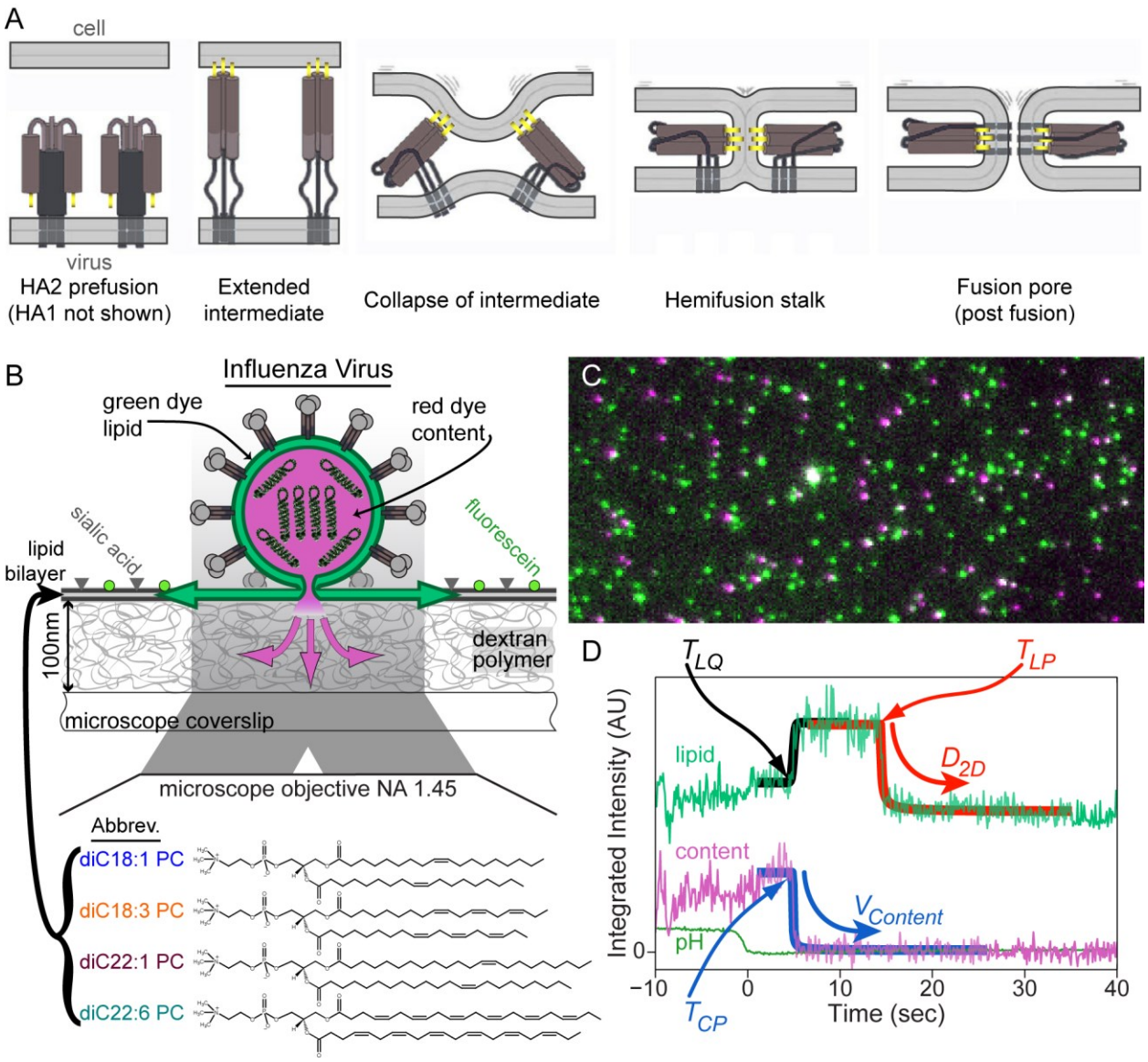

Figure 5-1 – *Experimental design for visualizing membrane hemifusion and full fusion of influenza virus particles to target bilayers of varying composition.* ***A****) A proposed mechanism for HA-mediated membrane fusion, focusing only on the HA2 domain (panel adapted from ref.* [10]*). Left to right: the HA2 domain is folded at neutral pH to sequester the fusion peptide (yellow) into a hydrophobic pocket; upon acidification the HA2 domain unfolds into the extended intermediate to embed the exposed fusion peptide into the target membrane; the extended structure collapses to bring the apposed membranes into close proximity, presumably through formation of a dimple structure* [3]*; lipid mixing begins with a lipidic hemifusion stalk that unites the proximal leaflets of the two membranes and allows dequenching to occur (D); a fusion pore is opened through action of the HA transmembrane domain to allow escape of viral contents.* ***B****) As described in* [1] *influenza virus particles are dually labeled with a green lipophilic dye in their envelope (blue-green) and a red aqueous dye marking the viral lumen (magenta). Virions are immobilized on a dextran-supported planar phospholipid bilayer through specific interaction of HA with sialic acid moieties presented by gangliosides. Bilayers are comprised of one of four PC*

*(**Figure 5-1 Continued**) lipid types (shown below the experimental diagram) in a 4:1 molar ratio with cholesterol. The pH-sensitive fluorescein dye (bright green) is attached to the bilayer surface and serves as an internal pH meter. **C**) Dual colored viruses are observed simultaneously in two emission channels that are super-imposed here. Fluorescence from the viral envelope and lumen are false-colored green and magenta, respectively. Many viruses contain only one signal, but some (white) contain both fluorescence signals and report on both lipid mixing and pore formation. **D**) Onset times for fusion events relative to loss of fluorescein signal (t=0, acidification time) are extracted from fluorescence trajectories after fitting. The lipid dequenching time (black), T_{LQ}, is determined by fitting a portion of the lipid trajectory (blue-green) with Equation 5-2. Lipid dissipation time (red), T_{LP}, and the rate of outward lipid diffusion into the bilayer, D_{2D}, are determined by fitting the same trajectory with Equation 5-3. Content dissipation time (blue), T_{CP}, and the rate of content signal loss, $V_{content}$, are determined by fitting the content trajectory (magenta) with Equation 5-3. Fits are determined in an automated fashion using maximum likelihood estimators (Chapter 4 and reference* [12]*). The trajectory for this particular virion depicts the restricted hemifusion state, indicated by a delay between lipid dequenching and dissipation. Pore formation occurrs through a restricted hemifusion intermediate and prior to free intermixing of the viral and target bilayers. The fusion of this particle is seen in Supplementary Movie M4-1.*

5-1A) [2,3,10,11]. The state of initial lipid mixing is defined as hemifusion and is described in terms of a highly curved stalk. Following lipid mixing, the palmitoylated C-terminal transmembrane domain acts to facilitate the opening of a fusion pore connecting the viral lumen with the cytosol for release of the viral genome [13,14].

Lipid head groups and their contribution to spontaneous membrane curvature have been demonstrated to play an important role in facilitating or inhibiting the fusion process. Formation of a hemifusion stalk is inhibited by lipids having positive curvature, such as lysophosphatidylcholine (LPC), while negative curvature oleic acid or lipids having phosphatidylethanolamine (PE) head groups facilitate its formation [6,15,16]. Fusion pores have the opposite curvature and their formation is also lipid dependent, being facilitated by positive curvature and inhibited by negative curvature [15,17]. In comparison to the zero-curvature phosphatidylcholine (PC) lipids, PE and plasmalogen lipid species have been demonstrated to be generally more fusogenic [16,18].

The fatty acid (FA) composition of phospholipids comprising lipid bilayers has received less attention in terms of their contribution to the fusion mechanism. Biological membranes undergoing critical membrane fusion events, such as those of synaptic vesicles [19], the gray matter of the cerebral cortex [20], and sperm plasma membranes [21], contain large amounts of the omega-3 polyunsaturated fatty acid (PUFA) docosahexaenoic acid (22:6) and its metabolic precursor linolenic acid (18:3) . The presence of PUFA is important for proper health of the tissues they form and PUFA deficiencies correlate with presence of disease, such as Alzheimer's [22] and infertility [23]. As well, the PE and plasmalogen lipids in these tissues are common reservoirs of PUFA [20,24].

The influenza virus lipidome is primarily composed of 16 to 18-carbon length saturated and monounsaturated lipids present principally in PC and glycosphingolipids [25,26]. A minor amount of the influenza membrane does consist of PUFA, though, being 14% of all PC and 39% of PE [26]. The composition of the influenza virus is quite important for proper virus stability and infectivity [27], and directed lipid oxidation through the use of small molecules has been demonstrated to neutralize influenza viruses [28]. Since PUFA lipids are particularly sensitive to oxidation, they may be critical targets of such targeted oxidation.

Incorporation of unsaturated lipids into *in vitro* systems for the study membrane fusion serves to increase the rate of fusion [18,29-31] compared to bilayers of monounsaturated FA (MUFA). Lipid membranes consisting of phospholipids having PUFA show greater acyl chain fluctuations [32], and larger degrees of lipid fluidity and water permeation [33-35] than those of MUFA. It has been postulated that the enhanced acyl chain dynamics may allow for filling of voids created during fusion since PUFA more readily form the inverted hexagonal lipid phase that is similar to hemifusion stalk [36].

The dual color viral fusion assay originally described in [1] is adapted here to study the effect of MUFA and PUFA acyl chains on the kinetics of HA-mediated membrane fusion. Briefly, X31 influenza viruses were labeled with a green lipophilic dye staining their membrane and a

red water soluble sulforhodamine B (SRB) dye staining their lumen. The green lipid dye incorporates into the virus particle at concentrations sufficient to enable self-quenching and a marked decrease of the fluorescence intensity when incorporated into the viruses. As depicted in Figure 5-1B, labeled viruses were immobilized upon dextran-supported bilayers [1] were comprised of 20% cholesterol and 80% symmetric diacyl PC lipids having one of the four following fatty acid chains: 1,2-dioleoyl-PC (diC18:1), 1,2-dilinolenoyl-PC (diC18:3), 1,2-dierucoyl-PC (diC22:1), 1,2-didocosahexaenoyl-PC (diC22:6). Disappearance of the fluorescein signal upon acidification of the virus (pH drop) indicates the synchronization of the fusion process for all viruses and sets time t = 0 seconds. Shortly thereafter, the virus particles fuse with the target bilayers and the fluorescence emitted during the fusion process is recorded in two spectrally separated channels (Figure 5-1C).

Lipid mixing of the viral lipids with the target is observed to occur with two distinct signals: lipid dequenching and lipid dissipation (Figure 5-1D). Dequenching of the green lipophilic dye corresponds to the onset of a hemifusion stalk. The signal arises from initial mixing between viral and bilayer lipids that alleviates neighbor-neighbor dye molecule quenching and thereby increase emitted fluorescence. Following dequenching, dissipation of the lipid signal is observed as the lipid dye continues to escape from the viral envelope and freely diffuses outward from the site of fusion. Content release is observed as a loss of fluorescence signal in the red fluorescence channel and occurs as the small SRB molecules rapidly escape the viral lumen through a pore formed in the viral envelope.

A key development since this viral fusion assay was first described by Floyd *et al.* [1] is the automated analysis script described in Chapter 4. In addition to making data selection more rapid and objective, it also provides additional kinetic information that has not yet been investigated. Specifically, the time between pH drop and lipid dissipation, which has only been qualitatively noted in previous studies [1,5,37], is now readily accessible for kinetic study. The rate of signal dissipation for the lipid and content signals similarly provide information about the

mobility of the dyes being observed. These rates of signal loss are also reported by the automated analysis script and can now be studied with large numbers of identified events.

This chapter details the kinetics found for various steps in the fusion process and their dependencies on the degree of unsaturation present in the target bilayer. Overall, the polyunsaturated lipids substantially affect the fusion process after the lipid dequenching event. As such, the additional information about dissipation onset and rate that can now be accessed is crucial to detect the impact that acyl chain polyunsaturation has on the fusion process.

5.2 Results

5.2.1 Lipid dequenching and initial mixing

Movement of the fluorescent dye from the viral membrane into the proximal leaflet in the target bilayer relieves concentration-dependent dye quenching and gives rise to a sharp fluorescence increase (dequenching) in the fluorescence trajectory of a virion. The moment taken as the onset of lipid dequenching, T_{LQ}, is indicated in Figure 5-1D and its extraction from the fluorescence trajectory of the lipid dye is described in the *methods* section. As observed in Figure 5-2A, lowering the pH used to stimulate HA-mediated hemifusion causes more than a 10-fold decrease in the time for the onset of the initial stage of lipid mixing, in agreement with previous fusion studies [1]. In varying the lipid composition of the target bilayer, it is observed that the median time to fusion is slowest for the diC22:1PC lipid, while the other three lipid compositions show faster kinetics. Inspection of the waiting time distributions themselves shows a subtle effect, however, with the diC18:1 and diC18:3 distributions being nearly identical (Figure 5-2B) and the diC22:1 and diC22:6 showing comparatively broader distributions (Figure 5-2C).

All of the hemifusion waiting-time distributions show a notable rise and decay, though, which is characteristic of a multi-step biochemical process. This behavior is expected and consistent with other investigations of HA-mediated hemifusion [1,5,38-40] and is interpreted to

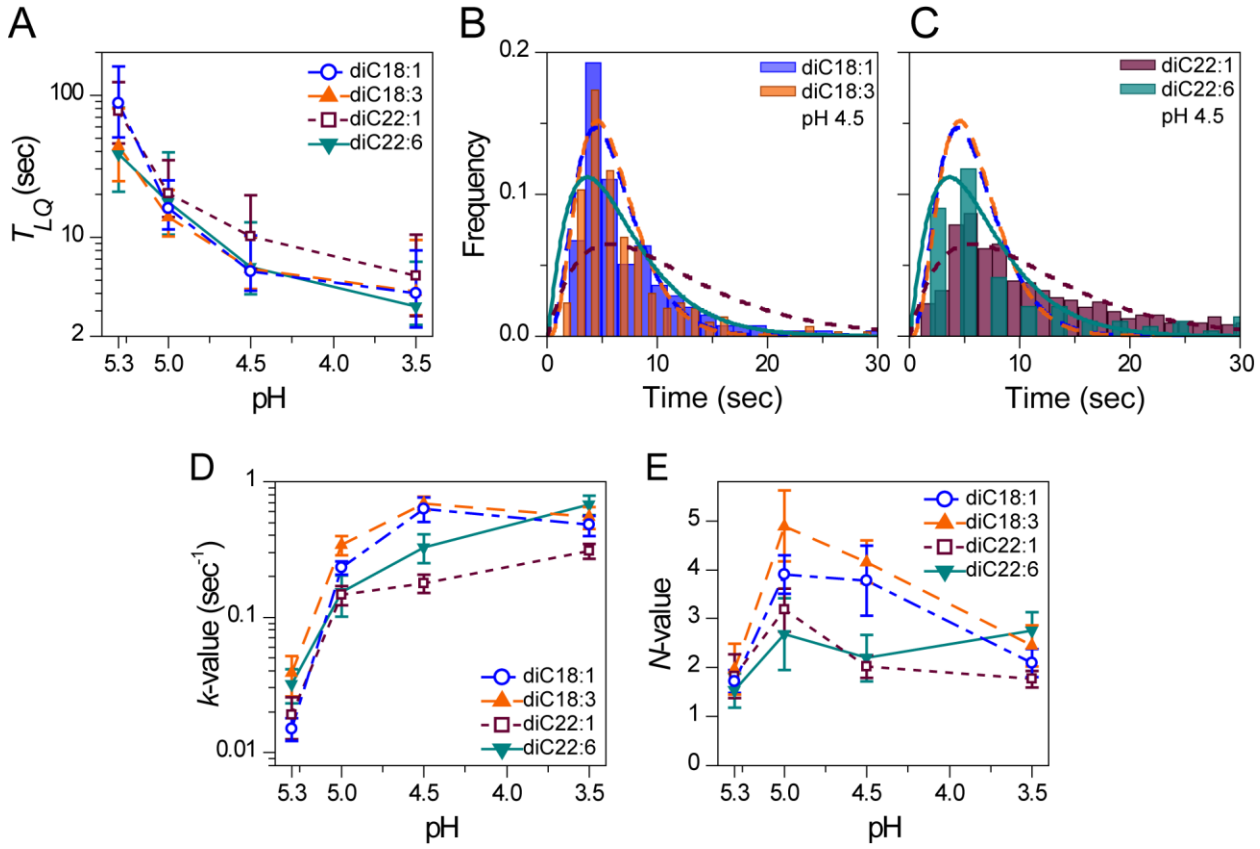

Figure 5-2 – *The kinetics of initial lipid mixing between the virus and its target are subtly faster for fusion to bilayers comprised of shorter acyl chains.* ***A****) The time between pH drop and lipid dequenching, indicating the time for onset of initial lipid mixing between the virus and target bilayer. Target bilayers are comprised of 18:1 (blue open circles), 18:3 (orange filled upward triangles), 22:1 (red open squares) or 22:6 (cyan filled downward triangles) diacyl PC phospholipids. Data points are median values ± interquartile range for distributions of all dequenching times.* ***B*** *and* ***C****) Distribution of waiting times for lipid signal dequenching during fusion to bilayers having acyl chains of 18 (B) or 22 (C) carbons in length at pH 4.5. Colors as in (A) and fit lines are to a gamma distribution.* ***D*** *and* ***E****) Fit parameters from analysis of waiting time distributions by a gamma function (Equation 5-1) showing the rate of the rate-limiting step, k, in (D) and the number of rate-limiting steps, N, in (E). Colors as in (A); data points are values found for fits to distributions of all observed dequenching events for the relevant condition ± 90% confidence intervals. Connecting lines are guides for the eye.*

be the coordinated participation of multiple HA trimers in driving the hemifusion process. Use of the gamma distribution to extract detailed kinetic information about the multi-step biochemical reaction of HA-mediated hemifusion has been previously described [1,41]. The gamma distribution is:

$$p_\Gamma(t|k,N) = \frac{k^N t^{N-1}}{\Gamma(N)} \exp(-k\,t) \tag{5-1}$$

where *k* is the rate of the rate-limiting step in the multi-step process and *N* is the number of rate-limiting steps that occur. Gamma distribution fit lines to the hemifusion waiting-time distributions for the four lipids at pH 4.5 are also shown in Figure 5-2 and highlight the differences between the distributions.

Comparing the *k* value extracted for fusion to the four lipid types as the fusion-inducing pH is lowered from 5.3 to 3.5 recovers two previously observed [1] kinetic regimes (Figure 5-2D). At higher pH values, the rate-limiting step shows a pH dependency, becoming nearly 10-fold faster as the pH is lowered from pH 5.3 to pH 5.0. Below pH 5.0, however, the rate *k* changes comparatively little, staying within the same order of magnitude. It is therefore interpreted that the pH-induced conformational unfolding of the hemagglutinin protein dominate the kinetic process between pH 5.3 and 5.0, whereas below pH 5.0 re-folding of HA to induce membrane merger becomes the rate limiting step. Re-folding is necessarily influenced by the properties of the target membrane given the substantial geometrical changes it must undergo [42,43].

Kinetic differences observed upon variation of the target bilayer composition are consistent with this interpretation and show a lipid-dependent separation of *k* values between pH 5.0 and pH 3.5 (Figure 5-2D). In line with Figure 5-2B, target bilayers of diC18:1 and diC18:3 lipids show similar *k* values that are, generally, faster than the *k* values for diC22:1 and diC22:6 in the lipid-dominated low-pH kinetic regime. This observation suggests that there is a subtle kinetic advantage for the shorter lipids during the onset of initial lipid mixing. The difference in

rates may be partially related to a hydrophobic mismatching between the 16-18-carbon length viral membrane and the thicker target bilayers of 22-carbon length acyl chains [25,26,44]. Bilayers having 18-carbon length acyl chains, on the contrary, would have a thickness comparable to that of the virus and would also have more favorable interactions with the hemagglutinin transmembrane region. At pH 3.5, when HA is running at maximum velocity, the increased amount of acyl chain disorder presented by the diC22:6 PUFA may overcome the hydrophobic mismatch effect and drive the system yet faster.

The number of HA's participating in the fusion process, *N*, extracted from gamma distribution analysis confirms that multiple HA's consistently participate in the fusion process. The *N* value is significantly larger than one at all pH values and is largely contained between values of 2 and 5, consistent with previous reports for the number of HA required to drive hemifusion [1,5,38]. Overall, the distributions of waiting times between pH drop and initiation of lipid mixing suggest a subtle enhancement of lipid mixing kinetics when a virus fuses to a target bilayer comprised of acyl chains similar in length to those of the viral envelope.

5.2.2 Lipid dissipation and full lipid intermixing

Dissipation of the lipid signal occurs once the lipophilic dye molecules initially contained in the viral membrane are able to freely intermix with the lipids of the proximal leaflet of the target bilayer after the initial mixing giving a dequenching signal. In this state, the lipophilic dyes diffuse radially outward from the site of fusion into the target bilayer. The moment taken as the onset of lipid dissipation, T_{LP}, is indicated in Figure 5-1D and its extraction from the fluorescence trajectory of the lipid dye is described in the *methods* section.

In decreasing from a fusion pH of 5.3 to 3.5, the time for free lipid intermixing decreases by nearly 10-fold for all target lipid compositions tested (Figure 5-3A). This fold-decrease is in rough agreement with the decrease in time until initial lipid mixing indicated by dequenching (Figure 5-2A). In stark contrast, though, is the significant lipid dependency evident in Figure 5-

3A. In the case of lipid dissipation, the degree of acyl unsaturation plays an important role in governing the kinetics of the onset of free lipid intermixing, rather than its length. At fusion pH's 4.5 and 3.5 target bilayers comprised of PUFA undergo free lipid intermixing at a time 4-5 fold faster than MUFA bilayers.

Between the MUFA bilayers, the diC18:1 undergoes free lipid intermixing slightly faster than the diC22:1. This trend is consistent with a better hydrophobic mismatch between the viral membrane and the shorter 18-carbon acyl chain as was observed in Figure 5-2D. Alternatively, the diC22:1 may exhibit a comparatively higher degree of acyl chain order compared to the diC18:1, given that it has a longer stretch of saturated hydrocarbon linkages between its PC head group and its *cis* unsaturated at carbon 13. As well, it's gel-to-liquid transition temperature of +13ºC [Avanti Lipids published value] is substantially higher than the -17ºC transition temperature of diC18:1, consistent with the diC22:1 having a greater propensity for acyl chain order [45]. For the PUFA bilayers, the more highly unsaturated and disordered diC22:6 shows faster intermixing between the viral and target bilayers than the diC18:3. The slightly shorter time to free lipid intermixing may be related to the extended region of saturated hydrocarbon linkages directly below the PC head group of diC18:3 that is absent in diC22:6 (Figure 5-1B). In accord with this, the transition temperature of diC18:3 is slightly higher at -60ºC compared to -68ºC for diC22:6. These results indicate that the kinetics governing the onset of full lipid intermixing is highly dependent on the degree of acyl unsaturation and, likely, disorder.

The rate of lipid signal dissipation is the two-dimensional diffusion constant for the lipophilic dye as is escapes from the viral membrane into the target bilayer through the lipidic hemifusion stalk. Figure 5-2B demonstrates that the rate of dye diffusion into target bilayers of different composition has a marked dependency on the composition of the target bilayer. The 2D diffusion constant of the lipid dye is largest for the highly disordered diC22:6, followed by the diC18:3, then diC18:1 and diC22:1. This ordering corresponds to the kinetics for the onset of lipid dissipation observed in Figure 5-3A where diC22:6 is the fastest and diC22:1 is the

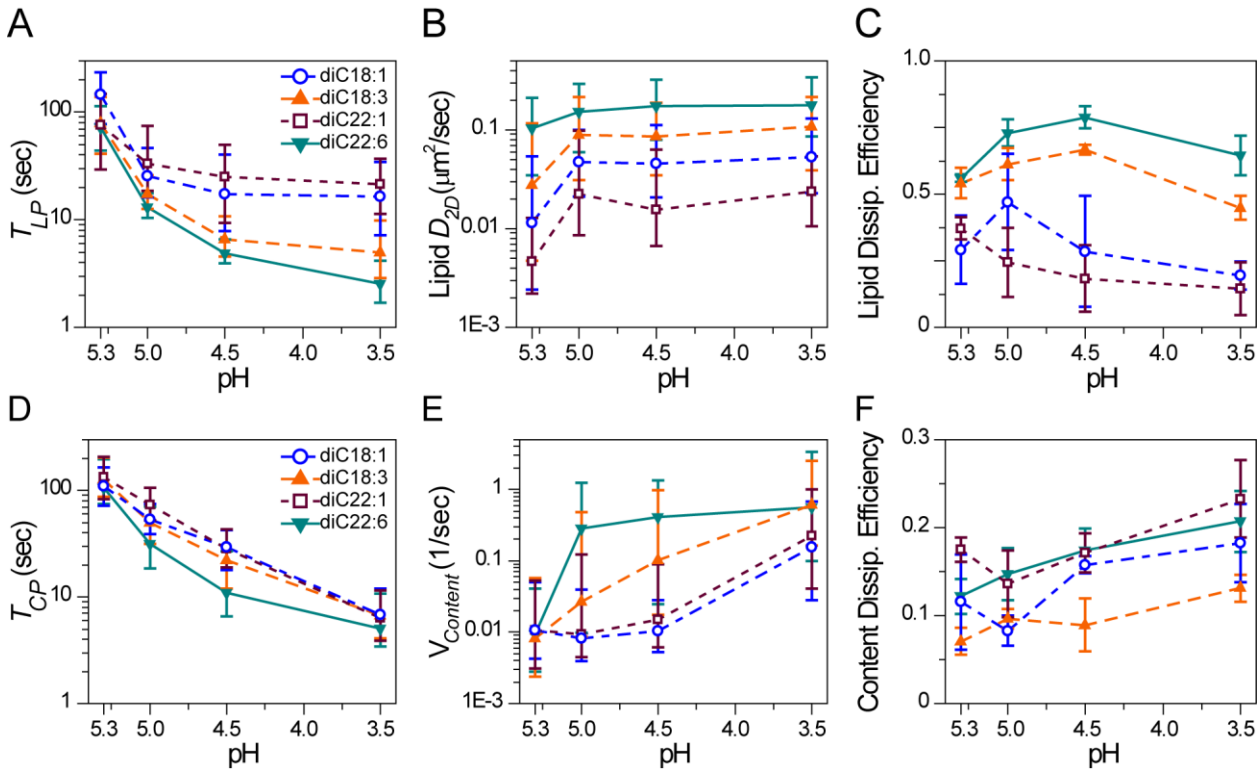

Figure 5-3 – *Polyunsaturated acyl chains cause substantially faster onset of free lipid intermixing and lead to faster content release. Colors as in Figure 5-2.* ***A*** *and* ***D****) Elapsed time between pH drop and the onset of lipid signal dissipation (A) or the onset of content signal dissipation (D) is plotted versus the pH used to induce membrane fusion. The former in (A) represents the onset of full lipid intermixing between the viral envelope and target bilayer, and the latter in (D) represents the opening of a fusion pore large enough for escape of the small molecule dye out of the lumen of the virus.* ***B*** *and* ***E****) Fit parameter for the rate of dissipative loss of the lipid signal (B) or of the content signal (E) as depicted in Figure 5-1. Lipid signal dissipation provides measurement for the diffusion constant of the lipid dye as it leaves the site of initial fusion and spreads into the target bilayer. The rate of content signal loss represents a qualitative read-out for the rate of fusion pore expansion.* ***C*** *and* ***F****) Efficiency of lipid (C) or content (F) signal dissipation calculated as the number of particles per experiment showing a detectable dissipation signal divided by the total number of virus particles identified. Data points in A, B, D and E are medians ± interquartile range for distributions of all events measured, data in C and F are mean values from all experiments performed ± standard deviation.*

slowest. The correlation between larger 2D diffusion constants measured for the different lipids and a shorter time to onset of free lipid intermixing is statistically significant for pH values 5.0, 4.5 and 3.5 (Appendix 4, Figure A4-1). This correlation exists only when comparing different experimental conditions, however, and no correlation was found between the time an individual virus undergoes free lipid intermixing and the 2D diffusion constant measured for its signal dissipation. Because the diffusion constant depends on lipid packing, head group area and acyl chain ordering [33], the data in Figure 5-3A and B confirm that the onset of free lipid intermixing occurs faster for those lipids showing a lower degree of lipid packing and acyl chain ordering.

The efficiency of full lipid intermixing is calculated as the number of virus particles producing a lipid dissipation signal divided by the total number of virus particles observed in an experiment. It is observed in Figure 5-3C viruses fusing to bilayers of PUFA show a significantly higher efficiency in undergoing free lipid intermixing as compared to bilayers of MUFA. The highest efficiency is largely correlated with the larger diffusion constants and faster kinetics to the onset of lipid dissipation. Hence, viruses fusing to bilayers of polyunsaturated lipids undergo free lipid intermixing at a higher rate and with higher efficiency than during fusion to bilayers of monounsaturated lipids. The enhancement in kinetics and efficiency imparted by the PUFA is correlated to the higher degree of acyl chain disorder and mobility of lipids within the bilayer.

5.2.3 Content dissipation and fusion pore opening

Dissipation of the content signal indicates the opening of a fusion pore large enough for the small SRB dyes to pass through and escape the viral lumen and mixing of the distal leaflets of the viral and target bilayers. The moment taken as the onset of content dissipation, T_{CP}, is indicated in Figure 5-1D and its extraction from the fluorescence trajectory of the content dye is described in the *methods* section. The elapsed time between the pH drop and the onset of content release shows a pH dependency, occurring faster at lower pH in accord with the faster onset of initial lipid mixing and dequenching (Figure 5-3D). The kinetics for the onset of content

release show that the viral content is released slightly earlier during fusion to a bilayer of diC22:6 lipids, but the lipid dependency is not as pronounced as observed for lipid signal dissipation. Interpreting pore-formation waiting time distributions with the gamma distribution (Equation 5-1) is extremely challenging [1,41] and was not undertaken. Overall, the kinetics for the onset of pore formation are not heavily dependent upon the acyl chain composition of the target bilayer.

The rate of content signal dissipation provides a qualitative measure for how rapidly the fusion pore is opening, since a larger pore will allow more SRB dye molecules to escape per unit time. As can be seen in Figure 5-3E, the rate of content release is found to have a notable pH and lipid dependency. It is unlikely that the rate of content release is reporting on the opening of multiple fusion pores, given that their formation is energetically costly (15-20 k_BT) and considered to be a rare nucleation event [46].

At pH 5.3, the rate of content release is equivalent for all the lipids tested, with the lipid dependency being observed for pH 5.0 and below. Hemagglutinin transmembrane domains have been demonstrated to be essential for the productive formation of a fusion pore [13]. As such, the pH-dependent conformational rearrangements undertaken by HA in mediating membrane fusion are likely to be important contributors to the observed pH dependency. Faster content release at lower pH may be attributed to a higher degree of synchronization among the HA trimers in undergoing conformational changes since these changes will be driven to occur more rapidly.

For pH 5.0 and below, the fastest content release is observed for fusion of viruses to the diC22:6 PUFA, followed by the diC18:3 PUFA. Content release is comparable between the diC18:1 and diC22:1 MUFA and substantially slower than for either PUFA for fusion below pH 5.0. Unfortunately, It is not possible to directly calculate the diameter of the fusion pore allowing release of the content dye because the precise number of fluorophores present in the viral lumen is unknown. Content labeling, as described in *methods*, involves passive diffusion of the

SRB dye into the virus, and hence it also escapes passively giving lower degrees of labeling in viruses over time. Further, the contents of the virus particles are tightly packed with the RNA-nucleoprotein genome and M1 capsid, leaving unknown space for the SRB dyes to sterically fit. Qualitatively, however, the rate of content signal loss can be used to compare the relative sizes of the fusion pores that form, with the larger pores giving rise to faster loss of the content signal [47]. Hence, it is concluded that expansion of the fusion pore is most rapid when viruses are fusing to target bilayers comprised of PUFA lipids.

The efficiency of fusion pore opening is slightly pH dependent, being more efficient at lower pH values. This, again, may be attributed to greater synchronization between HA trimers at lower pH. Notably, there is no clear trend in terms of lipid dependency, neither with respect to acyl chain length or degree of unsaturation. This observation suggests that the opening of a fusion pore itself is not dependent upon the lipid type, but is instead driven by the HA transmembrane domain. Once a pore is opened, though, the PUFA lipids facilitate its expansion to allow rapid release of the viral lumen contents.

5.2.4 Comparing the fusion time points

Comparison of the three fusion time points – lipid dequenching, lipid dissipation and content dissipation – to each other allows for reconstruction of the order of events en route to productive membrane fusion. It is observed in Figure 5-4A that for pH values of 5.3 and 5.0 both the MUFA and PUFA bilayers show similar trends wherein first lipid dequenching occurs, followed by lipid dissipation and, finally, content dissipation. At pH 4.5 and below, however, there is a notable difference between the two lipid classes.

The PUFA bilayers continue to show a close correspondence between lipid dequenching and lipid dissipation, both of which occur more rapidly at lower pH. In contrast, the MUFA bilayers demonstrate a flattening out of the time to lipid dissipation that results in a considerable delay between lipid dequenching and lipid dissipation. On a molecular level, it represents a

delay between initial lipid mixing and free lipid intermixing, indicating there is a confinement of the lipid diffusion between the viral and target bilayers. A confinement of outward lipid diffusion following initial lipid contact has been described previously as restricted hemifusion [48]. The duration of the restricted hemifusion is long enough that the content dissipation, in fact, occurs before free lipid intermixing for MUFA bilayers at pH 3.5. An example of this order of events is depicted in the fluorescence trajectory of Figure 5-1D wherein a lipid dequenching signal is clearly observed, but the lipids do not diffuse away from the virus until several seconds after the dequenching event.

The restricted hemifusion state appears to have a dependency on lipid type and on the pH used to incite fusion, since it is longer-lived for viruses fusing to target bilayers comprised of MUFA lipids at pH 4.5 and below. This combination of dependencies suggests that it is both the interaction of HA with the target bilayer together with the bilayer's intrinsic properties that cause and maintain the state of confined lipid diffusion. The pH dependency in particular may indicate that the number of HA N-terminal fusion peptides inserted into the bilayer could play a role. For fusion to PUFA bilayers this confined state is very short lived at all pH values, noted by the close agreement of the lipid dequenching and lipid dissipation populations. This observation indicates that large amounts of polyunsaturated lipids disrupt the molecular configurations necessary to maintain a state of confined lipid diffusion around the site where lipid mixing is initiated.

It is consistently observed that the formation of a fusion pore follows the dequenching signal for all experimental conditions probed. Hence, a lipidic hemifusion intermediate between the proximal leaflets of the viral and target bilayers precedes the opening of a fusion pore, in agreement with previous observations [1,48]. The surprising observation that the formation of a fusion pore can occur before the free intermixing of lipids in the proximal leaflets indicates that the HA trimers are able to form a fusion pore through a restricted hemifusion intermediate. Such

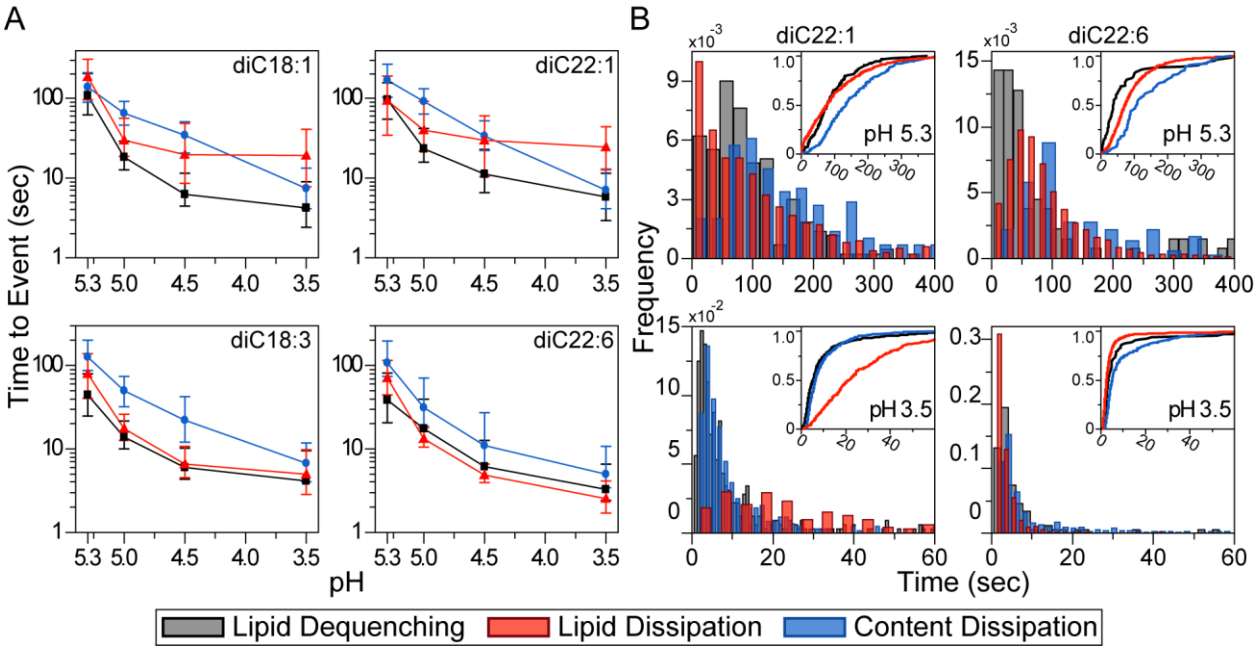

Figure 5-4 – *HA can induce pore formation prior to full lipid intermixing when mediating fusion to monounsaturated lipids at low pH. Data for elapsed time to lipid dequenching is shown in black, to lipid dissipation in red and to content dissipation in blue.* ***A****) Elapsed time between pH drop and the three membrane fusion events extracted from the fluorescence trajectories. Data points are medians ± interquartile range for distributions of all event times measured. The number of events detected for each fusion condition is described in Table A4-1 of Appendix 4. The lipid used in the target bilayer is indicated in the respective plot with bilayers of monounsaturated lipids in the top row and polyunsaturated lipids in the bottom row.* ***B****) Distribution of the three event times for fusion to the bilayers comprised of acyl chains 22-carbons in length. The top row is at the pH of 5.3 and the bottom row at pH 3.5. The left column corresponds to diC22:1PC and the right column to diC22:6PC. Each plot is the probability distribution of all events detected for a particular combination of pH and lipid. Insets into the plots are the cumulative density distributions corresponding to the probability distributions and highlight the delay in lipid dissipation after content dissipation during fusion at pH 3.5 to the bilayer of monounsaturated diC22:1PC.*

behavior is consistent with the data of Figure 5-3F wherein the opening of a fusion pore depends on the action of HA and not on the acyl chain composition of the target.

Inspection of the waiting time distributions for the three fusion time points under differing experimental conditions in Figure 5-4B confirms that the restricted hemifusion state is long lived for MUFA bilayers at low pH. For fusion at pH 5.3, both the diC22:1 MUFA and diC22:6 PUFA lipids show similarly broad waiting time distributions for lipid dequenching, lipid dissipation and content dissipation. At pH 3.5 both diC22:1 and diC22:6 lipids have distributions for the content release time that remain closely associated with the lipid dequenching distributions, though with a slight delay. The two signals also have similar widths for both lipid types, as observed at the higher pH. The waiting time distribution for lipid dissipation does not show such consistency between the lipid types or the high and low pH values. For diC22:6 the lipid dissipation remains closely associated with the lipid dequenching signal and shows a similar width in the distribution. In contrast, the diC22:1 lipid dissipation distribution is exceptionally broad relative to the width of the lipid dequenching distribution. It is so broad that a considerable population is still present at times greater than 30 seconds post pH drop, a time when most content dissipation has already occurred. The delay in time to lipid dissipation is equally stark in the inset cumulative distribution of Figure 5-4B for diC22:1 at pH 3.5. In contrast, the inset diC22:6 cumulative distributions at pH 3.5 are quite similar.

Analysis of the entire population of observed fusion events indicates the influenza HA trimers are capable of forming a fusion pore through a restricted hemifusion state since content signal dissipation can precede lipid signal dissipation. Moreover, it appears that termination of a restricted hemifusion state to allow lipid signal dissipation is highly dependent upon the acyl chain composition of the target bilayer and the pH used to stimulate fusion. The lipid dequenching signal to indicate initial mixing of the proximal leaflets and the content dissipation signal to indicate opening of a fusion pore both show only a subtle or no lipid dependency, respectively (Figure 5-2 and Figure 5-3). For these observations to be true, however, they must

be consistent on the level of single particles showing at least two of the three fusion time points (dual-event particles). As such, measurement of elapsed time between lipid dequenching and lipid dissipation, and between lipid dissipation and content dissipation in dual-event particles should show a lipid dependency. There should be no lipid dependency in the elapsed time between lipid dequenching and content dissipation.

5.2.5 Dual-event particles confirm population level observations

Most of the virus particles observed show only one of the three fusion events (Figure 5-1) with sufficient signal-to-noise to permit detection. A considerable minority of particles, though, shows at least two of the three fusion events being compared in Figure 5-4; the number of virus particles showing two events is included in Table A4-1. These fusion events are valuable because they allow for direct observation of the transient intermediate that exists between two of the fusion events. Such intermediates are accessible only through observation of viral membrane fusion at the single-particle level and hence support the justification for pursuing this type of experimental design. The kinetics of dual event particles correspond very well with the kinetics of the population as a whole (Figure A4-2), indicating that particles showing two fusion events are not a kinetic population separate from single-event particles.

The confinement lifetime for a dual-event particle can be defined as the elapsed time between the lipid dequenching signal and the lipid dissipation signal: $T_{Confine} = T_{LP} - T_{LQ}$. It represents the time when the proximal leaflets have hemifused enough to give rise to a dequenching signal, but outward lipid diffusion has not yet occurred. In accord with population data, the confinement lifetime shows a pronounced lipid dependency for pH 4.5 and below (Figure 5-5A). The confinement lifetime is shorter for viruses fusing to bilayers comprised of PUFA lipids. The distribution of confinement lifetimes is well represented by a single exponential distribution (Figure 5-5B), indicating that a single rate-limiting step separates the state of initial lipid mixing that gives dequenching from the final state of free lipid intermixing.

Extraction of the decay constant for the confinement lifetime by fitting with an exponential distribution (Figure 5-5C) reinforces the observation that the state of confined lipid diffusion is rapidly disrupted when the target bilayer has large amounts of PUFA lipids. The decay constant also clearly shows a pH dependency for the release of confined lipid diffusion, suggestive of a role by HA in the restricted hemifusion state.

The hemifusion lifetime was previously defined [1] as the elapsed time between lipid dequenching and content dissipation: $T_{HL} = T_{CP} - T_{LQ}$. Though the nomenclature of a hemifusion lifetime would suggest the end of a hemifused state, the data in Figure 5-4 indicate that a restricted hemifusion state does not necessarily end with the content dissipation signal. Nonetheless, this terminology will be utilized here for consistency with the previous study. The hemifusion lifetime thus represents the time when the proximal leaflets have hemifused, but a fusion pore large enough for escape of small molecule dyes has not yet formed. In accord with the population data, the hemifusion lifetime does not show a lipid dependency (Figure 5-5D). Instead, only a pH dependency is observed. Such a pronounced pH dependency was not observed previously [1] and may be the result of alterations made to the geometry of the microfluidic channel used and the increase in flow rate during influx of the low pH buffer (see *methods*). Nevertheless, the distribution of hemifusion lifetimes shows a single exponential character, as was observed previously [1] (Figure 5-5E). Extracting the hemifusion lifetime decay constants reinforces both the presence of a pH dependency and absence of a lipid dependency in the transition from initial lipid mixing to initial pore formation.

The final intermediate state that can be extracted from dual-event particles is the inter-dissipation time: $T_{dsp} = T_{CP} - T_{LP}$. When this value is less than zero, it represents the time that a fusion pore was open to allow content release while lipid diffusion was confined. When T_{dsp} is greater than zero, it represents the time that the proximal leaflets of the virus and target bilayer are fully intermixed while the distal leaflets are unmerged and the viral contents are contained.

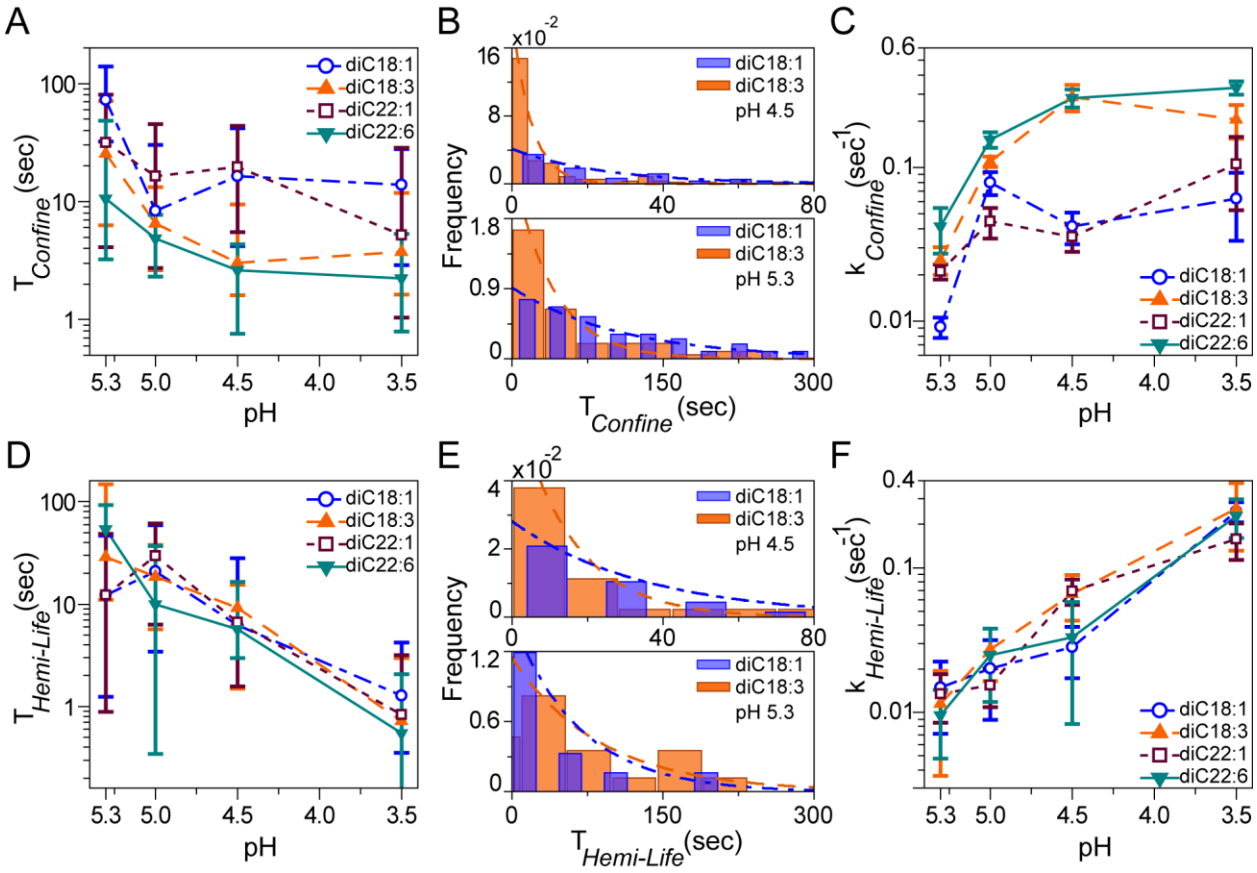

Figure 5-5 – *Particles showing two events confirm that the confinement lifetime is longer during fusion at low pH to bilayers of monounsaturated lipids, while the hemifusion lifetime has no lipid dependency. Data points in A and D are median values ± interquartile range, and in C and F they are fit values ± 95% confidence intervals. Color scheme as in figure 5-2.* ***A****) Confinement lifetime is defined as the elapsed time between lipid dequenching and lipid dissipation for particles showing both signals. A pH and lipid dependency in the confinement lifetime can be observed.* ***B****) The distributions for confinement lifetimes providing the data in (A) are well fit by a single exponential distribution. The confinement lifetimes for diC18:1PC and diC18:3PC at pH 4.5 are shown with their corresponding fit lines.* ***C****) Rate of confinement decay from exponential fits to the confinement lifetime distributions.* ***D****) Hemifusion lifetime is defined as the elapsed time between lipid dequenching and content signal dissipation for particles showing both signals. A pH dependency can be observed, but no lipid dependency.* ***E****) Distributions of hemifusion lifetimes are well described by single exponential distributions, as described previously* [1]*. Hemifusion lifetimes for diC18:1PC and diC18:3PC at pH 4.5 are shown with their corresponding fit lines.* ***F****) Rate of hemifusion decay from exponential fits to hemifusion lifetime distributions.*

The inter-dissipation time distributions did not show trends overtly indicative of any particular waiting time distribution. As such, the cumulative distributions of the inter-dissipation times were compared in Figure 5-6A. For each pH value used to induce fusion a larger portion of the cumulative distributions for the monounsaturated lipids are below zero as compared to the polyunsaturated lipids. A more overt comparison is performed in Figure 5-6B where the percentile of inter-dissipation times falling below zero is directly compared between MUFA and PUFA bilayers over the range of pH values. At all pH values for the 18-carbon length lipids and at pH 4.5 and below for the 22-carbon length acyl chains, the MUFA lipids showed a higher percentile of instances when content release occurred prior to free intermixing of the viral and target lipids, *i.e.* $T_{CP} < T_{LP}$, than the PUFA lipids. These observations are in accord with the kinetics extracted on the population level that the influenza HA is capable of forming a fusion pore through a restricted hemifusion intermediate, which occurs more commonly during fusion to bilayers having large amounts of monounsaturated lipids.

5.3 Discussion and future direction

It is widely accepted that membrane fusion mediated by HA initiates with lipid mixing in the formation of a hemifusion stalk that is subsequently opened into a fusion pore in a manner depending on both lipids and the HA transmembrane domain [1,5,6,13,42,48-50]. The results presented here agree with this order of events and provide insight into the effect of polyunsaturated lipids on the kinetics of the membrane fusion and the mechanism of the fusion process itself. We find two principal kinetic effects arising from the presence of PUFA in target bilayers. The first is to enhance the rate and efficiency of free lipid intermixing between the virus and target (Figure 5-3). The second is to substantially increase the rate of content loss during pore formation, which is surprisingly not accompanied by an increase in pore formation

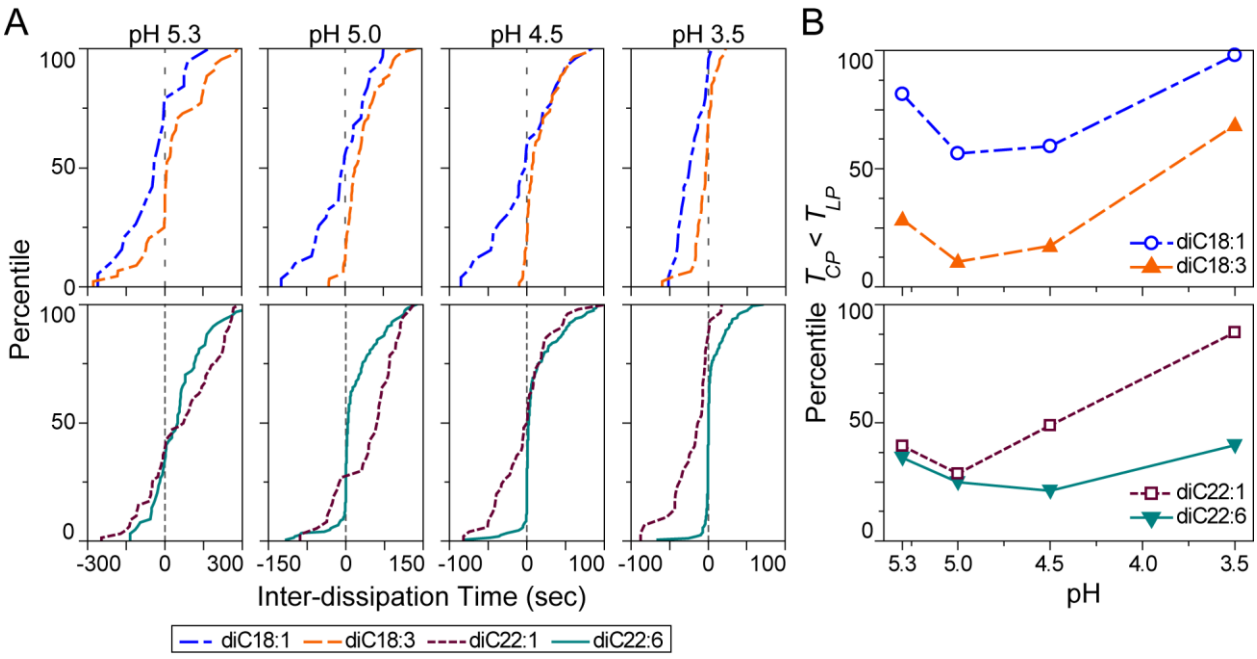

Figure 5-6 – *Particles showing two events confirm content release is more likely to occur prior to full lipid intermixing during fusion to bilayers of monounsaturated lipids at low pH. Color scheme as in Figure 5-2.* ***A****) Cumulative distributions of inter-dissipation times for the 18-carbon (top row) and 22-carbon (bottom row) length acyl chains at varying pH values (columns).* ***B****) Percentile corresponding to an inter-dissipation time of zero in (A), which is the percentile of dual-event particles where content dissipation occurred prior to lipid dissipation ($T_{CP} < T_{LP}$). Fusion to monounsaturated lipids shows higher percentiles of content dissipation prior to lipid dissipation than polyunsaturated lipids.*

efficiency. Previous studies of viral fusion at the single-particle level did not focus on the rate of content release or the kinetics for the onset of lipid dissipation. The observations made here were enabled through the use of the automated data selection algorithm described in Chapter 4 that extracts a large amount of kinetic data from the information-rich fluorescence trajectories.

Mechanistically, it is observed that lipid mixing can lead to a state of restricted hemifusion evidenced by a delay between the lipid dequenching and dissipation signals (Figure 5-4). While such a state has been reported in previous studies of cell-cell fusion mediated by HA [31,48,50], we demonstrate that persistence of a restricted hemifusion state is modulated by the composition of the target bilayer to which a virus is fusing. The restricted hemifusion is longer lived during fusion to bilayers having monounsaturated acyl chains while it more rapidly transitions to a state of free lipid intermixing when the target is comprised of polyunsaturated acyl chains (Figure 5-5). Further, we find that HA is capable of opening fusion pores large enough for small molecule dyes to pass through while engaged in a restricted hemifusion state (Figure 5-4 and Figure 5-6).

Previous investigations of the restricted hemifusion state suggested that it involved confined lipid diffusion and demonstrated that it required the presence of large numbers of activated HA trimers [48]. Specifically, cleaving the unfolded HA allowed lipids to freely diffuse away from the fusion site. It was postulated that a ring of HA trimers in the viral membrane form to drive membrane fusion and act as a molecular fence surrounding the initial hemifusion stalk that restricts lipid movement.

Data presented here are consistent with a dependency on activated HA to form a restricted hemifusion state [48] as observed in the pH dependency for the onset of delayed lipid dissipation during fusion to MUFA bilayers (Figure 5-4). At high pH, when fewer HA are likely to stochastically unfold per unit time, a state of restricted hemifusion is not observed. The restricted hemifusion state is entered only at the lower pH values, when many fusion peptides could be expected to insert into the target bilayer in a short period of time.

Our observation that the restricted hemifusion state is disrupted by the presence of PUFA in the target bilayer suggests that the molecular fence confining lipid diffusion is present in the target bilayer, however, and not in the viral membrane. Data in Figure 5-3 indicate that higher lipid mobility correlates with faster onset of free lipid intermixing and an end to a restricted hemifusion state. As such, molecular species that decrease lipid mobility may be sufficient to give rise to confined lipid diffusion observed during restricted hemifusion. It is postulated that the molecular fence confining lipid diffusion is formed by two components and lies within the footprint of the virus immobilized on a target bilayer. One component is HA fusion peptide that becomes inserted into the target bilayer in large numbers following acidification of the virus. The second is cholesterol that escapes from the viral membrane and enters the target bilayer upon the initial lipid mixing causing dequenching. Both of these hydrophobic molecular species have been measured to increase acyl chain order and reduce the free volume present in bilayers containing monounsaturated lipids [44,45,51,52]. Such ordering of the acyl chains results in lower lipid mobility [33] and could give rise to a state of confined lipid diffusion depicted in Figure 5-7.

Viral structures revealed by cryoelectron tomography indicate that there are enough fusion peptides present in the footprint of a virus to influence lipid mobility. The spherical viruses were described to have a radius of 75 nm from their center to the tip of their spike proteins and contain around 375 HA trimers [53]. If the viral footprint consists of a hemisphere where all available fusion peptides are inserted and the area per lipid is taken to be 70 $Å^2$ (approx. value for both diC18:1 [54] and diC22:1 [45]), then the resulting peptide:lipid ratio in the viral footprint would be approximately 1:100. Significant free volume reduction and acyl chain ordering in membranes of diC18:1 have been measured at the 1:100 ratio [51]. Interaction between the influenza fusion peptide and PUFA containing membranes has yet been investigated, but simulations of protein transmembrane domain at high concentrations in PUFA bilayers have indicated a substantial reduction in lipid mobility within the bilayer due to molecular crowding

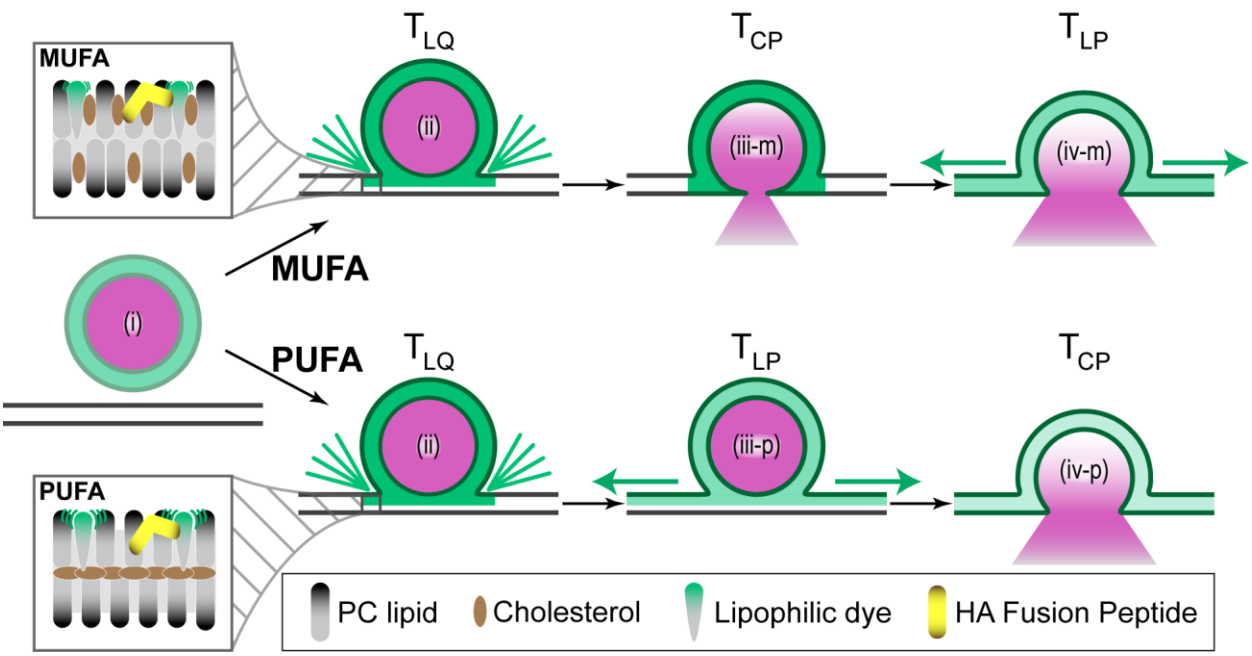

Figure 5-7 – *Model for the creation of an HA fusion peptide-cholesterol molecular fence restricting lipid diffusion away from a site of fusion.* ***i****) Pre-fusion immobilization of a virus to a target bilayer when lipophilic dyes are in a quenched state.* ***ii****) Upon acidification, a virus initially enters a state of confined lipid mixing and gives rise to a dequenching signal. This state is initially entered when fusing to a bilayer comprised of either monounsaturated fatty acids (MUFA, top path) or polyunsaturated fatty acids (PUFA, bottom path). Zooming in on the lipids (grey-black) near the perimeter of the hemifusion stalk highlights the composition-dependent orientation of cholesterol (CH, brown) in the bilayer. For MUFA bilayers, CH is oriented normal to the plane of the bilayer and interacts with acyl chains to increase acyl chain ordering and reduce lipid mobility* [44]*. For PUFA bilayers, CH is oriented parallel to the plane of the bilayer* [58,59] *where it may interact with acyl chains to a lesser extent, allowing higher lipid mobility* [33]*. In both cases, the HA fusion peptide (yellow) can act to increase acyl chain ordering and as a large steric hindrance to diffusion. Evolution of the fusion process from (ii) then depends on lipid type. The commonly observed sequence of fusion events at pH 3.5 is depicted in (****iii****) and (****iv****). For MUFA bilayers (iii-m), the restricted hemifusion state persists when a nascent fusion pore opens to release the SRB content dye. Outward lipid diffusion (iv-m) occurs at a later time following sufficient expansion of the fusion pore. For PUFA bilayers (iii-p), the system quickly escapes from the restricted hemifusion state to allow outward lipid diffusion. Nascent fusion pores expand rapidly (iv-p) to quickly release the SRB dye contained in the viral lumen. Note: All dimensions in the two zoom-in sections are scaled relative to an estimated 70 Å^2 per phosphatidylcholine (PC) lipid molecule and HA trimers are excluded for clarity.*

and steric effects [55,56]. To estimate the relative area occupied by the fusion peptides, we take the fusion peptide to be a rectangular block in the 2D area of the bilayer having a projected length of 26 Å and width of approximately 8 Å (PDB: 2JRD [57], viewing perpendicular to the plane of the target bilayer). The fusion peptides then have an area equivalent to approximately 3 lipid molecules and would occupy approximately 3% of the bilayer area, which may introduce steric effects and reduce lipid mobility. Such ordering and steric effects of the fusion peptide could contribute to the dependency of the restricted hemifusion intermediate on the amount of activated HA present.

The viral envelope of egg-derived X31 viruses, as used here, have been found to consist of ~50 mol% cholesterol [27]. The target bilayer was designed to have 20 mol% cholesterol. If these two mix in equal proportions lipid dequenching occurs, then the approximate cholesterol concentration in the area of the viral footprint would be near 35 mol% cholesterol. Acyl chain order and lipid-cholesterol lateral area was found to increase for both diC18:1 and diC22:1 lipids at this concentration [44]. Further, membranes containing MUFA have been shown to have a larger reduction in lateral diffusion upon addition of cholesterol compared to membranes containing PUFA [33]. Specifically, evidence suggests that the acyl chains of the monounsaturated lipid molecules are compressed by cholesterol's rigid sterol rings [60] as it orients parallel to the plane of the acyl chains [61]. Cholesterol has a pronouncedly different interaction with diacyl PUFA phospholipids, however, becoming sequestered to the middle of a bilayer perpendicular to the plane of the acyl chains [58,59]. Hence, when a virus is fusing to the PUFA bilayers the cholesterol is removed from an area where it can interact with lipids or the fusion peptide and cannot contribute to the formation of a molecular fence constricting lipid diffusion, as depicted in Figure 5-7. The sequestration of cholesterol by PUFA lipids could explain why the restricted hemifusion was observed less frequently when viruses fused to bilayers of diC18:3 and diC22:6.

Release from the restricted hemifusion state to allow free lipid intermixing could occur through two paths. In one path, the local lipid composition in the footprint of the virus does not permit formation of a molecular fence to confine lipid diffusion. This situation could be expected to arise more frequently during fusion to bilayers of PUFA due to cholesterol sequestration. In the second path, expansion of the fusion pore alleviates the restricted hemifusion state. Presumably, the concentration of both the fusion peptide and cholesterol would have to be at a critical concentration or higher for a molecular fence to be created and maintained. As the fusion pore expands, the area surrounding a hemifusion stalk also expands thereby decreasing the local fusion peptide and cholesterol concentration. When expansion reduces the local concentrations below a critical value, the fence breaks and lipid molecules exhibit free intermixing, giving rise to the lipid dissipation signal (Figure 5-7). Data here suggest that fusion pores expand more rapidly for the bilayers of PUFA (Figure 5-3E) and lipid dissipation would thereby occur faster. Hence, both scenarios are consistent with the data presented that bilayers of polyunsaturated lipids give rise to earlier onset of free lipid intermixing.

Testing this model would consist of performing two additional experimental variations. To assess the contribution of the influenza fusion peptide to the onset of a restricted hemifusion state, the number of fusion peptides inserting into a target could be reduced by use of small molecules [62] or peptides [63] that block HA low pH conformational changes. These peptides bind to influenza HA and prevent their low pH conformational changes. Their small size has the advantage over neutralizing antibodies in avoiding additional steric effects that could inhibit fusion. Assessing the contribution of cholesterol would involve reducing the cholesterol content in the target bilayer to zero. *A priori*, it is unclear if this reduction would be sufficient to observe a statistically significant change in the kinetics of the restricted hemifusion state, since cholesterol can still be contributed by the virus. Removing some cholesterol from the virions may be possible, though it has been previously found that cholesterol depletion markedly affects fusion by the influenza virus [64]. Incorporating either of these experimental variations while fusing

virions to bilayers of diC18:1 or diC22:1 at pH 3.5 would be expected to reduce the delay between lipid dequenching and dissipation signals (Figure 5-4A). Such a change should be accompanied by an increase in the rate of confinement decay (Figure 5-5C) as the restricted hemifusion state should last for shorter amounts of time and reduce the percentile of dual events having $T_{CP} < T_{LP}$ (Figure 5-6B).

Opening a fusion pore through a hemifusion diaphragm is energetically costly [46] and simulations have found that it can be triggered by the movement of water molecules across an unstable bilayer [65]. It is thus surprising that we do not find an enhanced efficiency of pore opening during fusion to the PUFA bilayers, though it is known that polyunsaturated lipids have higher degrees of water penetration [35]. In contrast, addition of positive curvature LPC lipid to the inner leaflet of red blood cells did increase the efficiency of pore opening and content release [48]. It may suggest that PUFA are important in a biological context for helping drive open a nascent fusion pore to avoid premature closing or flickering, while the lipid head group separately affects the likelihood that a fusion event will occur. Such speculation is in line with the presented data of faster content release (Figure 5-3E). Additionally, it may help explain why large amounts of polyunsaturated lipids are present in synaptic vesicles and sperm membranes [21,34] and why they are typically incorporated into the highly fusogenic plasmalogen or PE type lipids [20].

In summary, the fusion of influenza viruses to target bilayers of varying acyl chain composition was studied at the single-particle level using fluorescence microscopy. Fluorescence trajectories of the fusion events were analyzed using an automated fitting-based algorithm to identify the various time points along the fusion pathway and the rate of signal change. Extracted kinetics indicate that fusion to monounsaturated lipids leads to a long-lived restricted hemifusion state wherein lipid diffusion is confined. Influenza HA is capable of forming a fusion pore through a restricted hemifusion intermediate. Lastly, fusion to polyunsaturated lipids leads to more rapid escape from a restricted hemifusion state and results in faster release

of viral contents. Future work will investigate a proposed model for the combined effect of influenza fusion peptides and cholesterol in creating a restricted hemifusion state.

5.4 Materials and methods

5.4.1 Materials

X31 influenza virus particles propagated in the allantoic cavity of fertilized chicken eggs were purified in the lab of Prof. J. Skehel and kindly sent at a concentration of 10 mg/ml total viral protein for use in the fusion assay. Virus particles were dual-labeled in two subsequent steps. Red sulforhodamine B dye (Sigma-Aldrich) dissolved in deionized water at 20 mM was mixed with 5 μl of purified virus to a final dye concentration of 13 mM and incubated either over night at room temperature or for 48 hours at 4ºC. Free dye was removed by passing the virus-dye solution through a PD-10 sephadex column (GE Healthcare). Fractions of 200 μl were collected and those containing the highest virus concentrations were visible by eye and appeared red. The two most intensely red fractions were pooled together and mixed with green, lipophilic octadecyl rhodamine 110 (Rh110) to a final dye concentration 0.06 mg/ml (*i.e.* 3 μl of dye solution per 100 μl of content-labeled virus). The Rh110 dye was synthesized in-house [1] and dissolved in DMF at 2 mg/ml. Content-labeled virus was mixed with Rh110 for 2-3 hours, then the dual labeled viruses were separated by passage through another PD-10 column. The three brightest fractions were pooled together and used in the same day.

Phospholipids used for the formation of planar bilayers were purchased from Avanti Polar Lipids (Alabama, USA) and used without further purification or treatment: ovine wool cholesterol, 1,2-dioleoyl-*sn*-glycero-3-phosphocholine (diC18:1), 1,2-dilinolenoyl-*sn*-glycero-3-phosphocholine (diC18:3), 1,2-dierucoyl-*sn*-glycero-3-phosphocholine (diC22:1) and 1,2-didocosahexaenoyl-*sn*-glycero-3-phosphocholine (diC22:6). Lipid formulations included 19.7 mol% cholesterol, 79.3 mol% PC lipid, 1 mol% bovine brain disialoganglioside GD1a (Sigma),

and 0.0022 mol% N-((6-(biotinoyl)amino)hexanoyl)-1,2-dihexadecanoyl-snglycero- 3-phosphoethanolamine (biotin-X DHPE, Life Technologies).

5.4.2 Liposome preparation

To prepare liposomes, lipids dissolved in chloroform were mixed at appropriate ratios and the chloroform subsequently removed. For the monounsaturated diC18:1 and diC22:1, removal was performed drying under an argon flow, followed by vacuum desiccation for two hours. Lipid mixtures containing the polyunsaturated diC18:3 and diC22:6 were found to undergo extensive oxidation during vacuum desiccation. Instead, chloroform was removed by a constant flow of argon for 1-1.5 hours. Once dried, the lipid mixtures were suspended in HNE buffer (5 mM hepes, 140 mM NaCl, 0.1 mM EDTA, pH 7.4), subjected to repeated freeze/thawing cycles and extruded using polycarbonate membrane filters having a 100 nm pore diameter (Avanti Polar Lipids). Liposomes were prepared fresh the day of use at 2.5 mM total lipid.

5.4.3 Dextran functionalized cover slips

Dextran functionalized microscope cover slips were prepared similar to previous description [1]. Briefly, glass cover slips (25 x 25 mm, No. 1.5, VWR Scientific) were cleaned by subsequent 15 minute sonication treatments of detergent, acetone, ethanol, and 1M KOH. Cover slips were rinsed and dried at 110ºC for one hour, then cleaned in an oxygen plasma cleaner. Cleaned cover slips were functionalized with (3-glycidooxypropyl) trimethoxysilane (Gelest Inc, Morrisville, PA, USA) dissolved into isopropanol at 0.2% by volume. Functionalized cover slips were cured for 1 hour at 80ºC, then covered with dextran (dextran 500; Pharmacosmos A/S; mean MW 5 x 10^5 Da) dissolved in deionized water at 0.3 g/ml and allowed to react for two days.

5.4.4 Microfluidic channels

Microfluidic channels for the fusion experiments were formed by PDMS (polydimethylsiloxane, Dow Corning, Sylgard 184) using common cast molding techniques [66,67]. First, a silicon wafer having a relief pattern corresponding to five non-intersecting channels was prepared using standard photolithographic techniques and SU-8 negative photoresist. PDMS was mixed at a 9:1 ratio of elastomer to curing agent, degassed to remove bubbles, poured on top of the silicon master and allowed to cure either at 60ºC for four hours or under desiccation at room temperature for 48 hours. Solid blocks of PDMS containing the relief pattern were easily removed from the silicon wafer and cut to fit the glass cover slips. Each chip housed five microfluidic channels having inner dimensions 0.5(w) x 0.2 (h) x 10(l) mm and separated by 0.5 mm. PDMS chips were used to form the experimental flow channel by adsorbing them to a dextran-functionalized cover slip. Leakage between channels was prevented by applying pressure to the PDMS chip using a specially designed flow cell holder and microscope stage adaptor. Inlet and outlet polyethylene tubing (PE20 and PE60, respectively; Intramedic) was coupled to each microfluidic channel to allow rapid buffer exchange using a negative pressure syringe pump (Harvard Apparatus Model 11 syringe pump).

5.4.5 Microscope design

Fluorescence microscopy was performed using an inverted fluorescence microscope (Nikon TE-2000U) equipped with a high numerical aperture (NA = 1.45) 60x oil-emersion objective. Dual-labeled viruses were illuminated by 488 nm and 561 nm lines from an argon/krypton gas laser (Coherent Innova 70C) that were focused onto the back focal-plane of the microscope objective and aligned into objective-based total internal reflection (TIR) mode. Green and red emitted fluorescence was filtered using a 500-to-540 nm and 600-to-640 nm dual band-pass emission filter (Chroma Technology). The colors were spectrally separated using a

dichroic mirror and each emission channel was focused onto separate regions of a 512 x 512 pixel electron multiplying CCD camera (Andor Technology DV 887-BI, 16 μm pixel size).

5.4.6 Fusion assay

Fusion experiments were performed at room temperature, which fluctuated between 21-23ºC. Microfluidic channels comprised of a dextran-functionalized cover slip adsorbed to a PDMS chip were mounted to the microscope stage. The flow channel was initially hydrated by flowing in HNE buffer, then the liposome solution was added and allowed to incubate with the dextran surface for a minimum of 20 minutes. Dual-labeled virus particles were diluted between 20 and 50-fold in HNE, then added to the flow chamber, which also flushed out excess lipids. Virus particles were allowed to bind to the surface until the coverage density was such that approximately 200-400 particles were visible in a field of view. Streptavidin-fluorescein conjugates at a concentration of 4 μg/ml in HNE was added to the flow chamber to wash out unbound virus particles. Finally, video recording was begun and the low pH buffer (10 mM citric acid, 140 nM NaCl, 0.2 mM EDTA) was added to the flow chamber to induce HA-mediated fusion. Lipids and virus solutions were flowed into the flow channel at a flow rate of 100 μl/min and the low pH buffer at 500 μl/min. Frame exposure time was 50 ms for fusion at pH 3.5, 100 ms for fusion at pH 4.5 and 5.0 and 200 ms for fusion at pH 5.3. Laser power was adjusted to ensure a similar photon count rate per frame (*i.e.* intensity was double for pH 3.5 compared to pH 4.5, and was half for pH 5.3 compared to pH 4.5).

In comparison to the original implementation of this viral fusion assay [1], a number of modifications were incorporated. The microfluidic channels were constructed by PDMS chips rather than being created by hand through the use of quartz tops and double-sided tape. Repeated use of PDMS chips ensured that the flow channels of all experiments had identical geometries. Incorporation of multiple channels also allowed for more robust and high-throughput

data acquisition. A syringe pump with a definable flow rate was used for buffer exchange rather than a peristaltic pump that had an unknown flow rate, but that was estimated to have been approximately 100 μl/min. Addition of the low-pH buffer was therefore approximately 5-fold faster for the experiments performed here than in the original experimental setup, though the flow profile was still parabolic given the dimensions of the flow channel [68].

5.4.7 Data extraction and analysis

Disappearance of the fluorescein signal upon acidification of the virus is defined as the pH drop and sets time $t = 0$ seconds. To identify the frame where the pH drop occurs, the sigmoidally-decreasing fluorescein signal was analyzed as previously described [1]. Briefly, the slope at the inflection point is determined and the frame when it crosses base-line fluorescence once all fluorescein signal has dissipated is set as the pH drop frame.

The fluorescence trajectories of individual virus particles were extracted and analyzed using the MATLAB-based Fusion Tracker automated analysis software package described in Chapter 4. In brief, virus particles in the fluorescence recordings were identified through discoidal filtering [69] and then fit with two-dimensional Gaussian functions to determine their width. A circle of twice the Gaussian width centered at particle's location was used for integration of the particle's fluorescence intensity. Fluorescence intensity extracted from each frame of a recording was corrected for the laser illumination profile, background fluorescence and channel cross-talk. The acquired fluorescence trajectories (emitted fluorescence intensity over time) were fed into the Boolean decision function described in Chapter 4. This function identifies trajectories having potential events based on a particle's inherent signal-to-noise, its noise profile characteristics and on the existence of large, rapidly occurring intensity changes. Portions of the trajectory identified to contain large intensity changes were fit with one of two functions that serve 1) to determine the timing and rate of an event and 2) to separate transient signal fluctuations from true fusion events.

Large intensity increases in trajectories of the green, lipid channel were fit using a sigmoidal function defined as the dequenching equation:

$$\text{Dequenching}(t, \boldsymbol{p}) = p_2 + (p_1 - p_2) \times \left(1 + \exp\left(\frac{4\,(t - p_3)}{p_4}\right)\right)^{-1} \quad (5\text{-}2)$$

where $\boldsymbol{p}$ is a vector containing the parameters: p_1, the plateau intensity value before dequenching; p_2, the plateau value after dequenching; p_3, the inflection point of the intensity increase; and p_4, the duration of the dequenching event. The moment for the onset of lipid dequenching, T_{LQ}, is determined to be the first frame when the value of the dequenching fit rises above the upper 95% confidence bound of the p_1 parameter.

Large intensity decreases in both the lipid and content signal trajectories were fit using the dissipation equation:

$$\text{Dissipation}(t, \boldsymbol{p}) = p_1 - p_2 \times H(t - p_3) \times \exp\left(\frac{-r^2}{4\,p_4\,(t - p_3)}\right) \quad (5\text{-}3)$$

where r is the radius around a virus particle in μm that is used for fluorescence intensity integration, and $\boldsymbol{p}$ is a parameter vector representing: p_1, the intensity value before dissipation; p_2, size of the signal loss upon dissipation (*i.e.* initial intensity minus final intensity); p_3, the frame indicating the onset of signal dissipation (*i.e.* $p_3 = T_{LP}$ or T_{CP} for the lipid or content signal, respectively); and p_4, the rate of signal loss. For lipid signal dissipation, p_4 is the two-dimensional diffusion constant in μm^2/second [70], while for content signal dissipation it is simply the rate of intensity loss and is not interpreted to correspond to a physical constant. $H(t-p_3)$ is the Heaviside function and is invoked to remove the contribution of the exponential at times less than p_3..

The fitting of portions of trajectories with Equations 5-2 or 5-3 was performed by an automated analysis script that determines the most statistically relevant region for fitting using a maximum likelihood estimator [12]. This estimator takes the quotient of probabilities for obtaining the residuals found by fitting the trajectory with Equations 5-2 or 5-3 and the

probability for the residuals found by fitting the same trajectory with a straight line. An analytical threshold is set by defining an acceptable false-positive rate and if the ratio is larger than this threshold, then the fit is accepted, otherwise the fit is rejected. Statistically relevant fits were used to determine the signal-to-noise of the detected event and fits falling below a defined threshold value were rejected. The threshold for lipid dequenching fits was varied between 1.0-2.5, while the threshold for either lipid or content dissipation was set at 2.0. Lipid signal trajectories were permitted to have a single dequenching event that occurred prior to a single dissipation event. If more than one dequenching event was detected, then both dequenching fits were thrown out. Similarly for dissipation events. If a lipid dissipation event was detected prior to the lipid dequenching event, the particle was rejected. Content signal trajectories were allowed to have a single dissipation event only.

Fusion time points extracted from accepted fits of the trajectories were aggregated together for kinetic analyses presented in Figure 5-2 through 5-6. All fitting was performed in MATLAB using least squares fitting and the error reported for determined fit values corresponds to the 95% confidence interval for the relevant parameter.

5.5 References

1. Floyd DL, Ragains JR, Skehel JJ, Harrison SC, van Oijen AM. (2008) Single-particle kinetics of influenza virus membrane fusion. Proc Natl Acad Sci U S A 105: 15382-15387.

2. Skehel JJ, Wiley DC. (2000) Receptor binding and membrane fusion in virus entry: The influenza hemagglutinin. Annu Rev Biochem 69: 531-69.

3. Kuzmin PI, Zimmerberg J, Chizmadzhev YA, Cohen FS. (2001) A quantitative model for membrane fusion based on low-energy intermediates. Proc Natl Acad Sci U S A 98: 7235-40.

4. Markvoort AJ, Marrink SJ. (2011) Lipid acrobatics in the membrane fusion arena. Curr Top Membr 68: 259-294.

5. Ivanovic T, Choi JL, Whelan SP, van Oijen AM, Harrison SC. (2013) Influenza-virus membrane fusion by cooperative fold-back of stochastically induced hemagglutinin intermediates. eLife Sciences 2. 10.7554/eLife.00333.

6. Chernomordik LV, Leikina E, Frolov V, Bronk P, Zimmerberg J. (1997) An early stage of membrane fusion mediated by the low pH conformation of influenza hemagglutinin depends upon membrane lipids. J Cell Biol 136: 81-93.

7. Bertram S, Glowacka I, Steffen I, Kuhl A, Pohlmann S. (2010) Novel insights into proteolytic cleavage of influenza virus hemagglutinin. Rev Med Virol 20: 298-310.

8. Wiley DC, Wilson IA, Skehel JJ. (1981) Structural identification of the antibody-binding sites of hong kong influenza haemagglutinin and their involvement in antigenic variation. Nature 289: 373-378.

9. Wilson IA, Skehel JJ, Wiley DC. (1981) Structure of the haemagglutinin membrane glycoprotein of influenza virus at 3 A resolution. Nature 289: 366-373.

10. Harrison SC. (2008) Viral membrane fusion. Nat Struct Mol Biol 15: 690-8.

11. Bullough PA, Hughson FM, Skehel JJ, Wiley DC. (1994) Structure of influenza haemagglutinin at the pH of membrane fusion. Nature 371: 37-43.

12. Yang H. (2012) Change-point localization and wavelet spectral analysis of single-molecule time series. In: Komatsuzaki T, Kawakami M, Takahashi S, Yang H, Silbey RJ, editors. Single-Molecule Biophysics: Experiment and THeory. COMMERCE PLACE, 350 MAIN STREET, MALDEN 02148, MA USA: WILEY-BLACKWELL. pp. 219-243.

13. Melikyan GB, White JM, Cohen FS. (1995) GPI-anchored influenza hemagglutinin induces hemifusion to both red blood cell and planar bilayer membranes. J Cell Biol 131: 679-691.

14. Sakai T, Ohuchi R, Ohuchi M. (2002) Fatty acids on the A/USSR/77 influenza virus hemagglutinin facilitate the transition from hemifusion to fusion pore formation. J Virol 76: 4603-4611.

15. Bailey A, Zhukovsky M, Gliozzi A, Chernomordik LV. (2005) Liposome composition effects on lipid mixing between cells expressing influenza virus hemagglutinin and bound liposomes. Arch Biochem Biophys 439: 211-221.

16. Chernomordik L, Chanturiya A, Green J, Zimmerberg J. (1995) The hemifusion intermediate and its conversion to complete fusion: Regulation by membrane composition. Biophys J 69: 922-929.

17. Melikyan GB, Brener SA, Ok DC, Cohen FS. (1997) Inner but not outer membrane leaflets control the transition from glycosylphosphatidylinositol-anchored influenza hemagglutinin-induced hemifusion to full fusion. J Cell Biol 136: 995-1005.

18. Glaser PE, Gross RW. (1994) Plasmenylethanolamine facilitates rapid membrane fusion: A stopped-flow kinetic investigation correlating the propensity of a major plasma membrane

constituent to adopt an HII phase with its ability to promote membrane fusion. Biochemistry 33: 5805-5812.

19. Ikemoto A, Ohishi M, Hata N, Misawa Y, Fujii Y, et al. (2000) Effect of n-3 fatty acid deficiency on fatty acid composition and metabolism of aminophospholipids in rat brain synaptosomes. Lipids 35: 1107-1115.

20. Farooqui AA, Horrocks LA. (2001) Plasmalogens, phospholipase A2, and docosahexaenoic acid turnover in brain tissue. J Mol Neurosci 16: 263-72; discussion 279-84.

21. Zalata AA, Christophe AB, Depuydt CE, Schoonjans F, Comhaire FH. (1998) The fatty acid composition of phospholipids of spermatozoa from infertile patients. Mol Hum Reprod 4: 111-118.

22. Hashimoto M, Hossain S. (2011) Neuroprotective and ameliorative actions of polyunsaturated fatty acids against neuronal diseases: Beneficial effect of docosahexaenoic acid on cognitive decline in alzheimer's disease. J Pharmacol Sci 116: 150-162.

23. Safarinejad MR, Hosseini SY, Dadkhah F, Asgari MA. (2010) Relationship of omega-3 and omega-6 fatty acids with semen characteristics, and anti-oxidant status of seminal plasma: A comparison between fertile and infertile men. Clin Nutr 29: 100-105.

24. Richardson UI, Wurtman RJ. (2007) Polyunsaturated fatty acids stimulate phosphatidylcholine synthesis in PC12 cells. Biochim Biophys Acta 1771: 558-563.

25. Gerl MJ, Sampaio JL, Urban S, Kalvodova L, Verbavatz JM, et al. (2012) Quantitative analysis of the lipidomes of the influenza virus envelope and MDCK cell apical membrane. J Cell Biol 196: 213-221.

26. Blom TS, Koivusalo M, Kuismanen E, Kostiainen R, Somerharju P, et al. (2001) Mass spectrometric analysis reveals an increase in plasma membrane polyunsaturated phospholipid species upon cellular cholesterol loading. Biochemistry 40: 14635-14644.

27. Polozov IV, Bezrukov L, Gawrisch K, Zimmerberg J. (2008) Progressive ordering with decreasing temperature of the phospholipids of influenza virus. Nat Chem Biol 4: 248-255.

28. Vigant F, Lee J, Hollmann A, Tanner LB, Akyol Ataman Z, et al. (2013) A mechanistic paradigm for broad-spectrum antivirals that target virus-cell fusion. PLoS Pathog 9: e1003297.

29. Ehringer W, Belcher D, Wassall SR, Stillwell W. (1990) A comparison of the effects of linolenic (18:3 omega 3) and docosahexaenoic (22:6 omega 3) acids on phospholipid bilayers. Chem Phys Lipids 54: 79-88.

30. Talbot WA, Zheng LX, Lentz BR. (1997) Acyl chain unsaturation and vesicle curvature alter outer leaflet packing and promote poly(ethylene glycol)-mediated membrane fusion. Biochemistry 36: 5827-5836.

31. Zhukovsky MA, Leikina E, Markovic I, Bailey AL, Chernomordik LV. (2006) Heterogeneity of early intermediates in cell-liposome fusion mediated by influenza hemagglutinin. Biophys J 91: 3349-3358.

32. Eldho NV, Feller SE, Tristram-Nagle S, Polozov IV, Gawrisch K. (2003) Polyunsaturated docosahexaenoic vs docosapentaenoic acid-differences in lipid matrix properties from the loss of one double bond. J Am Chem Soc 125: 6409-6421.

33. Filippov A, Oradd G, Lindblom G. (2007) Domain formation in model membranes studied by pulsed-field gradient-NMR: The role of lipid polyunsaturation. Biophys J 93: 3182-3190.

34. Stillwell W, Wassall SR. (2003) Docosahexaenoic acid: Membrane properties of a unique fatty acid. Chem Phys Lipids 126: 1-27.

35. Huster D, Jin AJ, Arnold K, Gawrisch K. (1997) Water permeability of polyunsaturated lipid membranes measured by 17O NMR. Biophys J 73: 855-864.

36. Teague WE, Fuller NL, Rand RP, Gawrisch K. (2002) Polyunsaturated lipids in membrane fusion events. Cell Mol Biol Lett 7: 262-264.

37. Otterstrom J, van Oijen AM. (2013) Visualization of membrane fusion, one particle at a time. Biochemistry .

38. Danieli T, Pelletier SL, Henis YI, White JM. (1996) Membrane fusion mediated by the influenza virus hemagglutinin requires the concerted action of at least three hemagglutinin trimers. J Cell Biol 133: 559-69.

39. Kozlov MM, Chernomordik LV. (1998) A mechanism of protein-mediated fusion: Coupling between refolding of the influenza hemagglutinin and lipid rearrangements. Biophys J 75: 1384-96.

40. Bentz J. (2000) Minimal aggregate size and minimal fusion unit for the first fusion pore of influenza hemagglutinin-mediated membrane fusion. Biophys J 78: 227-245.

41. Floyd DL, Harrison SC, van Oijen AM. (2010) Analysis of kinetic intermediates in single-particle dwell-time distributions. Biophys J 99: 360-366.

42. Chernomordik LV, Kozlov MM. (2008) Mechanics of membrane fusion. Nat Struct Mol Biol 15: 675-683.

43. Chernomordik LV, Kozlov MM. (2003) Protein-lipid interplay in fusion and fission of biological membranes. Annu Rev Biochem 72: 175-207.

44. Kucerka N, Pencer J, Nieh MP, Katsaras J. (2007) Influence of cholesterol on the bilayer properties of monounsaturated phosphatidylcholine unilamellar vesicles. Eur Phys J E Soft Matter 23: 247-254.

45. Kucerka N, Perlmutter JD, Pan J, Tristram-Nagle S, Katsaras J, et al. (2008) The effect of cholesterol on short- and long-chain monounsaturated lipid bilayers as determined by molecular dynamics simulations and X-ray scattering. Biophys J 95: 2792-2805.

46. Tolpekina TV, den Otter WK, Briels WJ. (2004) Nucleation free energy of pore formation in an amphiphilic bilayer studied by molecular dynamics simulations. J Chem Phys 121: 12060-12066.

47. Lai Y, Diao J, Liu Y, Ishitsuka Y, Su Z, et al. (2013) Fusion pore formation and expansion induced by Ca2+ and synaptotagmin 1. Proc Natl Acad Sci U S A 110: 1333-1338.

48. Chernomordik LV, Frolov VA, Leikina E, Bronk P, Zimmerberg J. (1998) The pathway of membrane fusion catalyzed by influenza hemagglutinin: Restriction of lipids, hemifusion, and lipidic fusion pore formation. J Cell Biol 140: 1369-1382.

49. Knecht V, Marrink SJ. (2007) Molecular dynamics simulations of lipid vesicle fusion in atomic detail. Biophys J 92: 4254-4261.

50. Zimmerberg J, Blumenthal R, Sarkar DP, Curran M, Morris SJ. (1994) Restricted movement of lipid and aqueous dyes through pores formed by influenza hemagglutinin during cell fusion. J Cell Biol 127: 1885-1894.

51. Haque ME, Koppaka V, Axelsen PH, Lentz BR. (2005) Properties and structures of the influenza and HIV fusion peptides on lipid membranes: Implications for a role in fusion. Biophys J 89: 3183-3194.

52. Filippov A, Oradd G, Lindblom G. (2003) The effect of cholesterol on the lateral diffusion of phospholipids in oriented bilayers. Biophys J 84: 3079-3086.

53. Harris A, Cardone G, Winkler DC, Heymann JB, Brecher M, et al. (2006) Influenza virus pleiomorphy characterized by cryoelectron tomography. Proc Natl Acad Sci U S A 103: 19123-19127.

54. Tristram-Nagle S, Petrache HI, Nagle JF. (1998) Structure and interactions of fully hydrated dioleoylphosphatidylcholine bilayers. Biophys J 75: 917-925.

55. Javanainen M, Hammaren H, Monticelli L, Jeon JH, Miettinen MS, et al. (2013) Anomalous and normal diffusion of proteins and lipids in crowded lipid membranes. Faraday Discuss 161: 397-417; discussion 419-59.

56. Parton DL, Tek A, Baaden M, Sansom MS. (2013) Formation of raft-like assemblies within clusters of influenza hemagglutinin observed by MD simulations. PLoS Comput Biol 9: e1003034.

57. Lai AL, Tamm LK. (2007) Locking the kink in the influenza hemagglutinin fusion domain structure. J Biol Chem 282: 23946-23956.

58. Harroun TA, Katsaras J, Wassall SR. (2008) Cholesterol is found to reside in the center of a polyunsaturated lipid membrane. Biochemistry 47: 7090-7096.

59. Kucerka N, Marquardt D, Harroun TA, Nieh MP, Wassall SR, et al. (2010) Cholesterol in bilayers with PUFA chains: Doping with DMPC or POPC results in sterol reorientation and membrane-domain formation. Biochemistry 49: 7485-7493.

60. Alwarawrah M, Dai J, Huang J. (2010) A molecular view of the cholesterol condensing effect in DOPC lipid bilayers. J Phys Chem B 114: 7516-7523.

61. Yeagle PL. (1985) Cholesterol and the cell membrane. Biochim Biophys Acta 822: 267-287.

62. Vanderlinden E, Goktas F, Cesur Z, Froeyen M, Reed ML, et al. (2010) Novel inhibitors of influenza virus fusion: Structure-activity relationship and interaction with the viral hemagglutinin. J Virol 84: 4277-4288.

63. Fleishman SJ, Whitehead TA, Ekiert DC, Dreyfus C, Corn JE, et al. (2011) Computational design of proteins targeting the conserved stem region of influenza hemagglutinin. Science 332: 816-821.

64. Sun X, Whittaker GR. (2003) Role for influenza virus envelope cholesterol in virus entry and infection. J Virol 77: 12543-12551.

65. Smeijers AF, Markvoort AJ, Pieterse K, Hilbers PA. (2006) A detailed look at vesicle fusion. J Phys Chem B 110: 13212-13219.

66. Delamarche E, Bernard A, Schmid H, Michel B, Biebuyck H. (1997) Patterned delivery of immunoglobulins to surfaces using microfluidic networks. Science 276: 779-781.

67. Xia Y, Whitesides G. (1998) Soft lithography. Annu Rev Mater Sci 28: 153-184.

68. Stone HA. (2007) Introduction to fluid dynamics for microfluidic flows. In: Lee H, Westervelt RM, Ham D, editors. CMOS Biotechnology Series on Integrated Circuits and Systems. : Springer US. pp. 5 - 30.

69. Hedde PN, Fuchs J, Oswald F, Wiedenmann J, Nienhaus GU. (2009) Online image analysis software for photoactivation localization microscopy. Nat Methods 6: 689-690.

70. Wessels L, Elting MW, Scimeca D, Weninger K. (2007) Rapid membrane fusion of individual virus particles with supported lipid bilayers. Biophys J 93: 526-538.

Page intentionally left blank.

Chapter 6

Conclusions and Outlook

6.1 Conclusions

Protein-mediated membrane fusion is a critical biological process for breaching the phospholipid bilayers that compartmentalize cells, cellular substructures and virus particles. As discussed in Chapter 1, single-particle studies visualizing membrane fusion are providing detailed insights into the mechanism, kinetics and timing of the fusion process, thereby complementing previous ensemble and structural studies. These latter types of studies investigating fusion by the influenza hemagglutinin (HA) protein, in particular, have resulted in a number of mechanistic models for the molecular events that occur during membrane fusion [1-3]. Though insightful, these early studies only accessed average measurements over a population of virus particles or fusion as mediated by HA expressed on cell surfaces rather than incorporated into infectious particles. The single-particle fusion assay originally developed by Floyd *et al*. allowed for real-time visualization of the membrane fusion process as mediated by HA [4]. Their results revealed the kinetic nature of previously invisible intermediate states and established a conceptual framework for interpreting single-particle fusion kinetics [5]. Subsequent use of this assay advanced knowledge of viral lumen acidification via the M2 channel during fusion [6] and of the kinetic underpinnings of HA's low-pH conformational changes that engage a virus particle with a target membrane [7]. The work described in this dissertation demonstrates the utility of the single-particle fusion assay as a platform for the study of viral fusion inhibitors (Chapters 2 and 3) and provides insight into the lipid dependency of the fusion process after HA conformational unfolding (Chapter 5). Lastly, prototype software has been developed to rapidly and reproducibly analyze recordings of viral membrane fusion, extracting fusion kinetics in a fully automated fashion (Chapter 4).

Neutralization of influenza infection through antibody binding can occur through numerous pathways such as inhibition of target cell binding, fusion inhibition or prevention of progeny virus release. Because these effects are not necessarily mutually exclusive, discerning a mechanism of action directly related to antibody binding is challenging in ensemble fusion assays or with viral infection assays [8,9]. Incorporation of the broadly neutralizing, stem-binding antibodies CR6261 and CR8020 into the fusion assay, as described in Chapter 2, served to directly demonstrate that binding of these antibodies to their epitope inhibits HA-mediated membrane fusion. This direct visualization confirmed that the IgG molecules are able to recognize and bind their epitope on infectious virus particles and produce a functional effect. It also validates ensemble biochemical experiments of solubilized HA (*i.e.* not on a virus) indicating that antibody binding prevents HA's low-pH conformational change [10,11].

Adapting the fusion assay and associated analysis in Chapter 3 for the use of fluorescently labeled antibodies at high concentrations enabled simultaneous measurement of binding stoichiometry and its functional effect on membrane fusion. Both stoichiometric and kinetic results indicate that not all HA trimers on a virus need to be bound by antibody or Fab for fusion to be inhibited. This observation is in accord with models for HA-mediated membrane fusion requiring the concerted action of multiple HA trimers [4,12,13]. Furthermore, it suggests the molecular mechanism for fusion inhibition occurs via disruption of pH-triggered HA aggregation into a requisite geometry and of sufficient number for membrane fusion to ensue. This mechanism of fusion inhibition is likely to be shared by other broadly neutralizing, stem-binding antibodies because of overlap and similarities in their epitopes on the HA protein [10,11,14-16]. Overall, Chapters 2 and 3 serve as proof-of-concept studies demonstrating that the study of fusion inhibitors using the single-particle fusion assay provides both direct conformation of fusion inhibition and detailed information on the inhibition mechanism.

Lipidomics studies indicate the lipid composition of biological membranes frequently undergoing fusion events have substantially larger amounts of unsaturated lipids compared to

those of more other membranes [17,18]. Simply identifying their presence or studying the biophysical characteristics of the lipids through NMR or SAXS [19,20], however, does not provide insight into their function in the fusion process. The role of acyl-chain unsaturation was addressed in Chapter 5 where the target bilayers formed upon a dextran cushion were comprised of lipids having either polyunsaturated fatty acids (poly-UFA) or the more common monounsaturated fatty acids (mono-UFA). Kinetic analysis revealed that the rate of content release and the onset of full lipid intermixing between viral and target bilayers are heavily affected by the presence of poly-UFA. Viruses fusing to poly-UFA bilayers show faster content loss than for mono-UFA bilayers, which suggests that poly-UFA lipids may facilitate the rapid expansion of a fusion pore. When fusing to mono-UFA bilayers at low pH, where lipid effects are most prevalent, viruses more readily entered a state of restricted hemifusion wherein lipids were not allowed to freely diffuse between the viral and target bilayers. Escape from this state was significantly more rapid during fusion to poly-UFA bilayers. Interestingly, HA is capable of forming a fusion pore despite the restricted lipid movement and with kinetics that are insensitive to target bilayer composition. The restricted hemifusion state is postulated to arise from acyl chain ordering due to the presence of HA fusion peptide and cholesterol in the area immediately surrounding a fusion site. These observations suggests that the mechanism of pore formation mediated by the HA transmembrane domain may be largely insensitive to acyl chain ordering and lipid phase at the hemifusion diaphragm.

Extracting large amounts of kinetic data from fluorescence recordings of viral membrane fusion is an arduous task. To facilitate reproducible data extraction and analysis, a MATLAB-based software package was designed and implemented to automatically identify fusion events from the viruses' fluorescence trajectories. As described in Chapter 4, automated analysis of trajectories using statistical analysis, Boolean tests and maximum likelihood predictors [21] can identify fusion events to extract kinetics that are comparable to scrutinous manual selection.

Achieving the implementation of such a program addresses the need for a more unified approach to data analysis in the field of single-particle membrane fusion identified in Chapter 1.

6.2 Outlook and future directions

Steric contributions to the inhibition of membrane fusion by stem-binding antibodies remain to be fully resolved. The use of Fab fragments for comparison to the three-fold larger IgG molecules in Chapter 3 indicated that more Fab molecules are required for a similar degree of fusion inhibition. Using Fab to compare with IgG, however, alters both the size of the inhibitory molecule along with its binding valency. Given the influenza group-specific similarities in the fractional occupancies between IgG and Fab, relative to the stoichiometry of maximal fusion inhibition, HA binding and hence binding valency is certainly a major contributor to the inhibitory effect. Nonetheless, Fab fragments are still fairly large and could act to sterically occlude the close apposition of target and viral membranes in a fashion similar to full IgG. Measuring the binding stoichiometry of small HA-binding peptides shown biochemically to block HA's low-pH conformational change [22] would provide good insight into the effect of steric occlusion. Their size of ~12 kDa should allow them to be fluorescently labeled without affecting their binding avidity. If HA binding is the principle determinant for the functional observation of hemifusion inhibition, then similar numbers of peptides as Fab fragments would be required for comparable reductions in fusion efficiency. If steric factors play a significant role, however, the numbers of peptides should be substantially higher than the number of Fab needed, since by molecular weight they are approximately one quarter a Fab and less than one-tenth of an IgG.

A separate measurement to probe the steric occlusion required to inhibit membrane fusion would be to incubate the virus with acylated-PEG molecules. These amphiphilic molecules have been used to form planar bilayers tethered to a PEG surface (see Appendix 2 and [23]). The hydrophobic acyl group should incorporate into the viral envelope, similar to R18, and allow the PEG polymer to occupy space between HA trimers without affecting their pH

sensitivity. Fluorescently labeled PEG would allow for stoichiometric measurements that could be directly coupled to the volume they occupy on the viral surface.

Fusion-inhibiting small peptides [22] or small molecules [24] could also be utilized to probe the model for the restricted hemifusion state presented in Chapter 5. There, this state is proposed to arise, in part, due to the large amount of HA fusion peptide near a fusion site. These fusion inhibitors would reduce the number of HA fusion peptides that become inserted into the target bilayer with minimal steric effects. If the local fusion peptide concentration is critical to the onset of the restricted hemifusion state during fusion to mono-UFA bilayers at low pH, then increasing concentrations of fusion inhibiting molecules should affect kinetics related to lipid dissipation. A reduction in the confinement lifetime of Figure 5-5 and in the inter-dissipation time measured in Figure 5-6 would be anticipated. Such reductions would bring the trends in the fusion kinetics for mono-UFA bilayers more in line with those of poly-UFA bilayers. Cholesterol is also postulated to play a role in the restricted hemifusion state and it can easily be removed from the target bilayer. Problematically, cholesterol is likely to be added locally to the fusion site upon hemifusion of the viral and target membranes such that little kinetic change may result. While cholesterol could potentially be removed from the influenza viruses using cyclodextrin, this has been shown to substantially reduce the virus's fusogenicity [25].

Extension of the single-particle fusion assay to visualize the fusion of virus particles to surface-immobilized vesicles would provide a number of opportunities to study new aspects of pore formation. Preliminary results obtained by a master's student in the van Oijen group, Kumar Sourav Das, indicate that such fusion geometry is possible for the use with influenza. Further, it has been demonstrated in the study of SNARE-mediated fusion [26,27]. Liposomes have two advantages over a planar bilayer. Firstly, both leaflets of a properly immobilized liposome are fluid and free from interactions with any surfaces. Secondly, and importantly, they can encapsulate buffers and probes that may be able to investigate the rate of fusion pore expansion.

One approach would be to visualize the escape of the viral genome using a labeled RNA or DNA hairpin whose fluorescence changes upon binding to the viral RNA. The kinetics of fusion pore opening presented in Chapter 5 report the release of a small sulforhodamine dye. This molecule can fit through a pore substantially smaller than the eight massive ribonucleoprotein complexes (RNP) comprising the viral genome, but which are the essential elements for establishment of viral infection. To detect release of the RNP two components could be loaded into a liposome. One is an RNA or DNA hairpin labeled on either end with either a FRET (fluorescence resonance energy transfer) pair, as in [27], or a dye with a quenching agent [28]. The second is a small molecule, membrane impermeable protein denaturant that would first enter the viral lumen through a nascent pore and denature the RNP. Denaturation of the RNP should release the RNA from association with proteins so that it may interact with the hairpin to form an RNA hybrid, causing a rapid FRET decrease or dequenching fluorescence increase. Alternatively, high salt concentrations within a liposome could allow for dissociation of the proteins that are electrostatically bound to the viral RNA, though this may interfere with hybridization. Combined with fluorescence dequenching upon lipid mixing, readout of RNP release would provide insight into the kinetics and efficiency of the pore expansion process.

In his Ph.D. dissertation, Dr. Dan Floyd [29] described preliminary results on development of a FRET-based experimental system to visualize the initial membrane fluctuations prior to the onset of hemifusion. His design utilized zero-mode waveguides to create a localized evanescent field for fluorescence excitation whose width was less than the diameter of a virus particle. Such dimensions would, in theory, allow for reasonable signal-to-noise FRET measurements between the viral and target bilayers labeled with appropriate lipophilic dyes. An alternative excitation strategy would be the use of stimulated emission depletion microscopy (STED) [30]. With this type of microscope design, a sub-diffraction sized spot of illumination

could be created to generate FRET between the two bilayers and record the onset of hemifusion with higher time resolution than what can be achieved using CCD cameras.

By and large, however, the biggest area for expansion of the utility of the single-particle viral fusion assay is its application to new virus types. Preliminary work on chikungunya virus being performed in the van Oijen lab is looking promising. The self-contained nature of the disposable PDMS microfluidic channels makes this assay potentially safe and amenable for fusion studies on more lethal viruses, such as HIV or even Ebola. As well, it is plausible that immobilized liposomes filled with quenched calcein dye could be used to investigate the membrane penetration mechanism of non-enveloped viruses. Finally, further development of the analysis software described in Chapter 4 would make data analysis less technically demanding and, hopefully, enhance assay accessibility to the virology field in general.

6.3 References

1. Chernomordik LV, Leikina E, Frolov V, Bronk P, Zimmerberg J. (1997) An early stage of membrane fusion mediated by the low pH conformation of influenza hemagglutinin depends upon membrane lipids. J Cell Biol 136: 81-93.

2. Chernomordik LV, Frolov VA, Leikina E, Bronk P, Zimmerberg J. (1998) The pathway of membrane fusion catalyzed by influenza hemagglutinin: Restriction of lipids, hemifusion, and lipidic fusion pore formation. J Cell Biol 140: 1369-1382.

3. Kuzmin PI, Zimmerberg J, Chizmadzhev YA, Cohen FS. (2001) A quantitative model for membrane fusion based on low-energy intermediates. Proc Natl Acad Sci U S A 98: 7235-40.

4. Floyd DL, Ragains JR, Skehel JJ, Harrison SC, van Oijen AM. (2008) Single-particle kinetics of influenza virus membrane fusion. Proc Natl Acad Sci U S A 105: 15382-15387.

5. Floyd DL, Harrison SC, van Oijen AM. (2010) Analysis of kinetic intermediates in single-particle dwell-time distributions. Biophys J 99: 360-366.

6. Ivanovic T, Rozendaal R, Floyd DL, Popovic M, van Oijen AM, et al. (2012) Kinetics of proton transport into influenza virions by the viral M2 channel. PLoS One 7: e31566.

7. Ivanovic T, Choi JL, Whelan SP, van Oijen AM, Harrison SC. (2013) Influenza-virus membrane fusion by cooperative fold-back of stochastically induced hemagglutinin intermediates. eLife Sciences 2. 10.7554/eLife.00333.

8. Klasse PJ, Sattentau QJ. (2002) Occupancy and mechanism in antibody-mediated neutralization of animal viruses. J Gen Virol 83: 2091-2108.

9. Reading SA, Dimmock NJ. (2007) Neutralization of animal virus infectivity by antibody. Arch Virol 152: 1047-1059.

10. Ekiert DC, Bhabha G, Elsliger MA, Friesen RH, Jongeneelen M, et al. (2009) Antibody recognition of a highly conserved influenza virus epitope. Science 324: 246-51.

11. Ekiert DC, Friesen RHE, Bhabha G, Kwaks T, Jongeneelen M, et al. (2011) A highly conserved neutralizing epitope on group 2 influenza A viruses. Science 333: 843-850.

12. Danieli T, Pelletier SL, Henis YI, White JM. (1996) Membrane fusion mediated by the influenza virus hemagglutinin requires the concerted action of at least three hemagglutinin trimers. J Cell Biol 133: 559-69.

13. Mittal A, Bentz J. (2001) Comprehensive kinetic analysis of influenza hemagglutinin-mediated membrane fusion: Role of sialate binding. Biophys J 81: 1521-1535.

14. Corti D, Voss J, Gamblin SJ, Codoni G, Macagno A, et al. (2011) A neutralizing antibody selected from plasma cells that binds to group 1 and group 2 influenza A hemagglutinins. Science 333: 850-6.

15. Sui J, Hwang WC, Perez S, Wei G, Aird D, et al. (2009) Structural and functional bases for broad-spectrum neutralization of avian and human influenza A viruses. Nat Struct Mol Biol 16: 265-273.

16. Dreyfus C, Laursen NS, Kwaks T, Zuijdgeest D, Khayat R, et al. (2012) Highly conserved protective epitopes on influenza B viruses. Science 337: 1343-1348.

17. Ikemoto A, Ohishi M, Hata N, Misawa Y, Fujii Y, et al. (2000) Effect of n-3 fatty acid deficiency on fatty acid composition and metabolism of aminophospholipids in rat brain synaptosomes. Lipids 35: 1107-1115.

18. Zalata AA, Christophe AB, Depuydt CE, Schoonjans F, Comhaire FH. (1998) The fatty acid composition of phospholipids of spermatozoa from infertile patients. Mol Hum Reprod 4: 111-118.

19. Teague WE, Fuller NL, Rand RP, Gawrisch K. (2002) Polyunsaturated lipids in membrane fusion events. Cell Mol Biol Lett 7: 262-264.

20. Eldho NV, Feller SE, Tristram-Nagle S, Polozov IV, Gawrisch K. (2003) Polyunsaturated docosahexaenoic vs docosapentaenoic acid-differences in lipid matrix properties from the loss of one double bond. J Am Chem Soc 125: 6409-6421.

21. Yang H. (2012) Change-point localization and wavelet spectral analysis of single-molecule time series. In: Komatsuzaki T, Kawakami M, Takahashi S, Yang H, Silbey RJ, editors. Single-Molecule Biophysics: Experiment and THeory. COMMERCE PLACE, 350 MAIN STREET, MALDEN 02148, MA USA: WILEY-BLACKWELL. pp. 219-243.

22. Fleishman SJ, Whitehead TA, Ekiert DC, Dreyfus C, Corn JE, et al. (2011) Computational design of proteins targeting the conserved stem region of influenza hemagglutinin. Science 332: 816-821.

23. Reich C, Andruzzi L. (2010) Preparation of fluid tethered lipid bilayers on poly(ethylene glycol) by spin-coating. Soft Matter 6: 493-500.

24. Vanderlinden E, Goktas F, Cesur Z, Froeyen M, Reed ML, et al. (2010) Novel inhibitors of influenza virus fusion: Structure-activity relationship and interaction with the viral hemagglutinin. J Virol 84: 4277-4288.

25. Sun X, Whittaker GR. (2003) Role for influenza virus envelope cholesterol in virus entry and infection. J Virol 77: 12543-12551.

26. Yoon TY, Okumus B, Zhang F, Shin YK, Ha T. (2006) Multiple intermediates in SNARE-induced membrane fusion. Proc Natl Acad Sci U S A 103: 19731-19736.

27. Diao J, Su Z, Ishitsuka Y, Lu B, Lee KS, et al. (2010) A single-vesicle content mixing assay for SNARE-mediated membrane fusion. Nat Commun 1: 54.

28. Piestert O, Barsch H, Buschmann V, Heinlein T, Knemeyer J, et al. (2003) A single-molecule sensitive DNA hairpin system based on intramolecular electron transfer. Nano Lett 3: 979-982.

29. Floyd DL. (2010) Single particle studies of influenza viral membrane fusion. Thesis (Ph.D., Division of Medical Sciences (Biological Chemistry and Molecular Pharmacology))--Harvard University, 2010.

30. Klar TA, Jakobs S, Dyba M, Egner A, Hell SW. (2000) Fluorescence microscopy with diffraction resolution barrier broken by stimulated emission. Proc Natl Acad Sci U S A 97: 8206-8210.

Appendix 1 – Supplementary information for Chapter 1

This appendix contains the following supplementary information:

A1.1 Supporting materials and methods for the single particle fusion assay

A1.2 Supplementary figures

A1.3 Supplementary tables

A1.4 Supplementary movies descriptions

A1.5 Supplementary references

A1.1 Supporting materials and methods for the single particle fusion assay

A1.1.1 Microfluidic flow cell construction

Microfluidic flow cells were constructed for fusion experiments using cleaned glass microscope cover slips (25 x 25-mm, No. 1, VWR) and either a PDMS (polydimethylsiloxane; Dow Corning, Slygard 184) chip or a quartz top affixed with double sided tape (Grace Bio-Labs) as described previously [1,2]. A PDMS chip was used with unlabeled antibodies, while the quartz was used for AF488-labeled antibody experiments. PDMS chips formed by standard PDMS cast molding techniques [3] housed five parallel channels of dimensions 0.5(w) x 0.2 (h) x 10(l) mm and were non-permanently adsorbed to the clean glass cover slips. Holes were punched into the chip to allow insertion the PE20 inlet and PE60 outlet tubing (BD Intramedic; I.D = 0.38 mm and 0.76 mm, respectively). The PDMS chip with glass bottom was clamped in a home-built PDMS-chip housing and affixed to the microscope stage with a custom adaptor.

A1.1.2 Proteoliposome Preparation

Chloroform solutions of 1,2-dioleoyl-*sn*-glycero-3-phosphocholine (DOPC) (Avanti Polar Lipids), cholesterol (Avanti Polar Lipids) and *N*-((6-(biotinoyl)amino)hexanoyl)-1,2-

dihexadecanoyl-*sn*-glycero-3-phosphoethanolamine triethylammonium salt (Biotin-X DHPE, Invitrogen) were mixed in a molar ratio of 0.8:0.2:2.5x10^{-5}. The lipid mixture was dried under an argon stream, then for two hours under vacuum. Lipids were resuspended in HNE buffer to 5 mg/mL, freeze/thawed five times with liquid nitrogen, then extruded (mini-extruder, Avanti) using 0.2 μm pore size filters at ~40 °C. Triton X-100 (VWR) was added to a final concentration of 0.5 % (w/v) and incubated in the liposome suspension at 37 °C for 15 min then on ice for 15 min. Sialoglycoprotein glycophorin A (GYPA) – full-length recombinant protein with a GST tag (Abnova) – was added to solubilized lipids at a lipid:protein molar-ratio of approximately 1:40,000 and allowed to mix at 4 °C for 30 min. Triton-X detergent was removed by two successive two hour incubations with Bio-Beads (SM-2 absorbent, Bio-Rad Laboratories, Inc.) at 4 °C using 200 mg Bio-Beads per 300 μL of solution. Glycophorin A membrane protein was used in lieu of membrane-bound gangliosides, such as GD1a, because we found that the H1N1 virus strain did not become immobilized upon planar bilayers containing sialic acid presented in this fashion.

A1.1.3 Microscope Setup

Single-particle fusion assays were conducted on an inverted dual color fluorescent microscope (Olympus IX-71) equipped with a 60x NA 1.49 oil immersion objective (Olympus APON60OTIRF), and both 488 nm blue and 561 nm yellow continuous-wave solid state lasers (Sapphire models, Coherent Inc.) aligned in objective-based Hi-Lo total internal reflection (TIR) mode [4]. Emitted fluorescence light was filtered using a custom-ordered microscope filter cube (Chroma Ltd.) allowing passage of wavelengths: 495 to 550 and 570 to 710. The green fluorescein/AF488 and red R18 emitted fluorescence signals were spectrally separated in a home-build dual view setup utilizing a long-pass dichroic mirror (Thorlabs DMLP567), passed through band-pass filters (Chroma ET525-50m and ET605-70m, respectively) and focused onto either half of an EMCCD camera (Hamamatsu Photonics K.K., Image-EM model C9100-13).

A1.1.4 Fusion Experiment

R18-labeled viruses were diluted 10-fold into a solution of either 100 % Alexa Fluor-488 labeled or 100 % unlabeled antibodies, bringing the antibodies to the desired final concentration, and then incubated at room temperature for 30 min prior to flow cell addition. The proteoliposome solution was added to the microfluidic flow cell mounted to the microscope stage using negative pressure from a syringe pump (New Era Pump Systems Inc., NE-1000) connected via a six-valve manifold (Qosina, Edgewood, NY, USA) and allowed to incubate for 30 min at room temperature, spontaneously forming a glass-supported planar lipid bilayer Figure 2-2A). The fusion experiments were executed as reported previously [1, 2] in a fashion similar to wherein virus in the antibody solution was added to the flow cell and viruses were observed to immobilize upon the fluid, continuous, planar bilayer. Fluorescein-labeled streptavidin (Invitrogen) was subsequently added at a concentration of 6 μg/mL with unlabeled antibodies or at 0.2 μg/mL with labeled. This was followed by a 2 minute wash at 100 μL/min with clean HNE buffer to remove unbound viruses, unbound antibodies and unbound streptavidin-fluorescein. Viral fusion was initiated by rapid injection of a citric acid buffer (10 mM citric acid, 140 mM NaCl, 0.2 mM EDTA, pH 5.0) at 200 μL/min and recorded using Metavue imaging software (Life Science Imaging Ltd.) at an acquisition rate of 5 Hz and maximal EM gain until all fusion events had ceased. Images in figure 2 and supplementary movies S5 and S6 were created using ImageJ.

A1.1.5 Data Analysis

Recorded fusion movies were processed and analyzed in a fashion similar to that previously described [1, 2]. Individual viral particles were identified and their fluorescent trajectories extracted using home-written MATLAB code. Arrival of the acidic buffer led to disappearance of the fluorescein signal and synchronization of viral fusion. The onset of fusion

between the virus and target bilayer was visualized by sudden increases in the R18 signal, caused by fluorescence dequenching, followed by outward diffusion of the R18 molecules into the target bilayer away from the fusion site. Red-channel fluorescent trajectories (fluorescence at a spot over time) of the viruses were extracted from recorded movies and plotted for manual selection. Trajectories showing clear dequenching spikes followed by dissipative signal loss were directly classified as fusing virions. Trajectories showing characteristics of dequenching and/or dissipative signal loss, but with poorer signal strength, were subjected to further manual inspection. In this case, a virus particle in question is observed in the recorded fusion movie. Viruses showing a rapid outward movement of lipid molecules away from the virus identifiable by eye were also classified as fusing virions. The percent hemifusion in each experiment was calculated as the number of particles in a field of view determined to undergo fusion divided by the total number of particles initially detected in the same field of view. Experiments of fusion at each antibody concentration were conducted at least three times and experiments having fewer than 25 particles detected in a field of view were not included in the final analysis. Additionally, experiments showing 25 fusing particles or fewer were subjected to two rounds of particle selection to reduce the likelihood of false-event selection.

A1.2 Supplementary figures

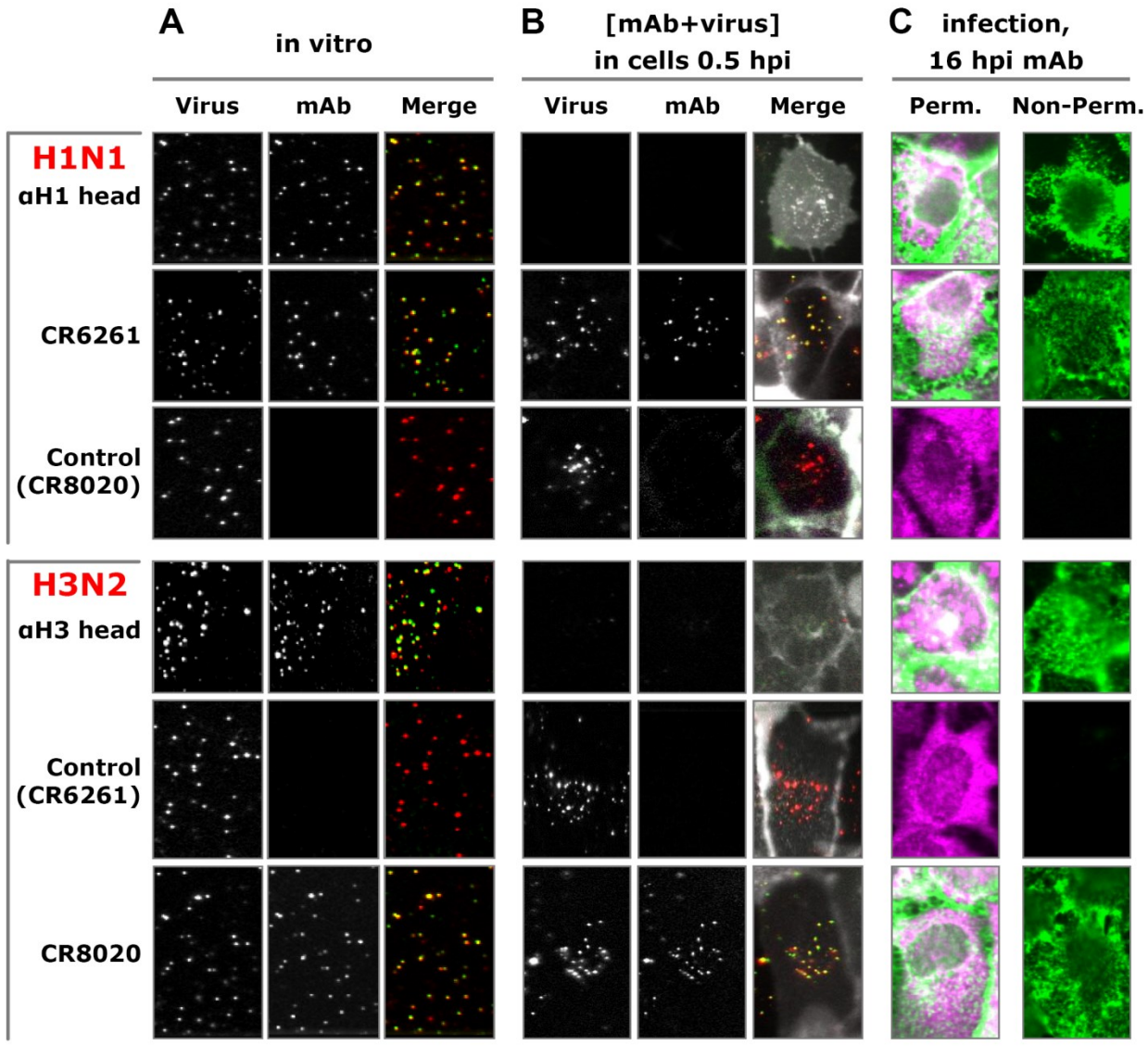

Figure A1-1 – *Stem-binding bnAbs co-localize with influenza particles in vitro and in live cells, bind on the surface of infected cells. (**A**) Influenza A/Puerto Rico/8/1934 (H1N1) and A/Aichi/2/1968-X31 (H3N2) viruses were labeled with the lipophilic dye octadecyl rhodamine B (R18, red), spotted onto glass, and incubated with fluorescently labeled antibodies CR6261 or CR8020. Head-binding control antibodies, CR9020 (binding to head region of a narrow spectrum of H1 HAs) and CR8057 (binding to the head region of a narrow spectrum of H3 HAs) were used in combination with R18-labeled A/New Caledonia/22/1999 (H1N1) and A/Wisconsin/67/2005 (H3N2), respectively. Antibodies CR6261 and CR8020 served as non-binding controls on H3N2 and H1N1 viruses, respectively. Virus-antibody complexes were bound to the glass bottom of 96 well plates and imaged. R18-labeled virus and AF647-labeled*

*(**Figure A1-1 Continued**) antibody are shown in separate channels in grayscale and in the merged image in red and green, respectively. Antibodies co-localize with the virus to which they bind in vitro. (**B**) Live MDCK cells expressing a GFP cell marker (grey) were incubated for ~20 min (at 37ºC) with viral particles (red) pre-incubated with antibodies and imaged as in (A). To allow detection of internalized particles only, non-internalized particles were removed by neuraminidase treatment. Whereas head-binding antibodies prevent internalization, stem-binding bnAbs co-localize with internalized viral particles (yellow). (**C**) MDCK cells were infected, fixed 15 hours later, and subsequently stained with anti-HA antibodies as in (A) and anti-influenza A nucleoprotein (NP) antibody to confirm infection (magenta, only detectable under permeabilizing conditions). Infected cells were also incubated with fluorescently labeled bnAb (green) to demonstrate their ability to bind surface-expressed HA and budding viral particles.*

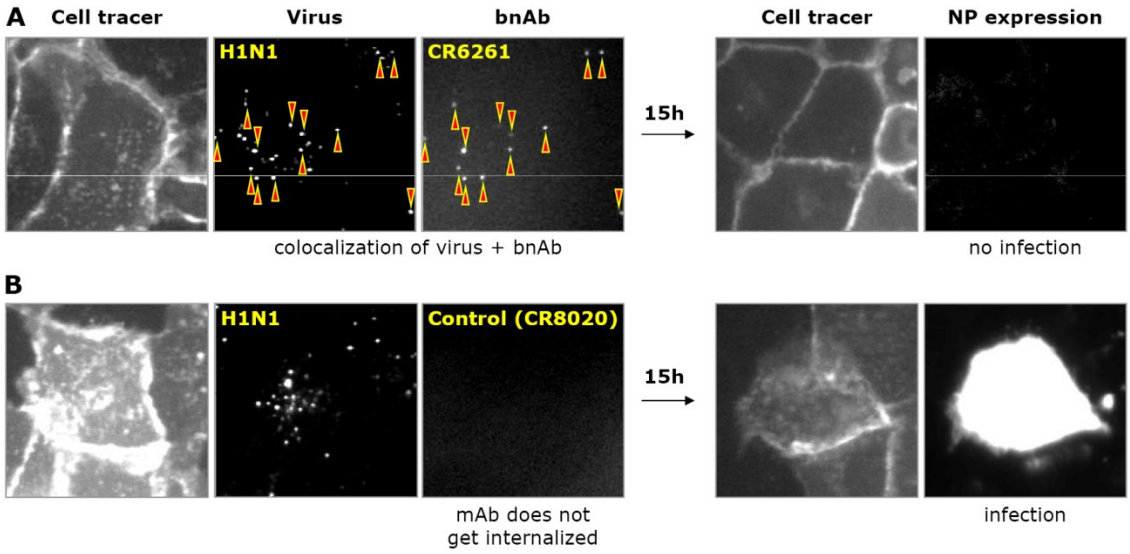

Figure A1-2 – *CR6261 is internalized into live cells in complex with H1N1 viral particles and prevents infection. (**A**) Separate channels (in grey scale) of a three color image showing live MDCK cells expressing a GFP-cell tracer incubated with R18-labeled A/Puerto Rico/8/1934 (H1N1) virus in complex with AF647-labeled CR6261. Internalized virus-antibody complexes (red triangles) were detected in live cells 30 min after inoculation. Individual cells were tracked over 15 hours before being fixed and stained for influenza nuclear protein (NP) to detect infection. (**B**) Control experiment showing that incubation of R18-labeled A/Puerto Rico/8/1934 (H1N1) virus with non-binding AF647-labeled CR8020 did not result in internalization of antibody. Only viral particles are detectable inside live cells 30 min after inoculation and 15 hours later these cells were infected as evident from the expression of NP.*

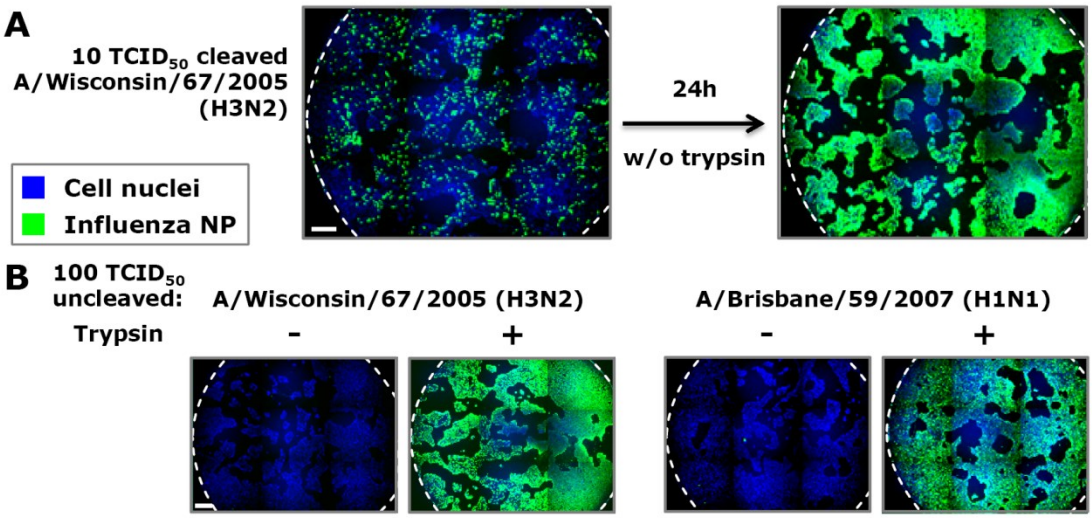

Figure A1-3 – *Calu-3 cells support the propagation of influenza virus in the absence of trypsin, but cannot be infected by uncleaved virus. (**A**) Calu-3 cells were infected with 10 $TCID_{50}$ cleaved A/Wisconsin/67/2005 (H3N2) influenza virus in the absence of trypsin. 24 hours after infection cells (nuclei blue) were fixed and stained for influenza NP (green) as indication for infection. (**B**) 100 $TCID_{50}$ of uncleaved A/Wisconsin/67/2005 and A/Brisbane/59/2007 (harvested from MDCK cells in the absence of trypsin) were added to Calu-3 cells with or without trypsin. Uncleaved virus is not infectious but can be rendered infectious when treated with trypsin. Images (A and B) show an entire well.*

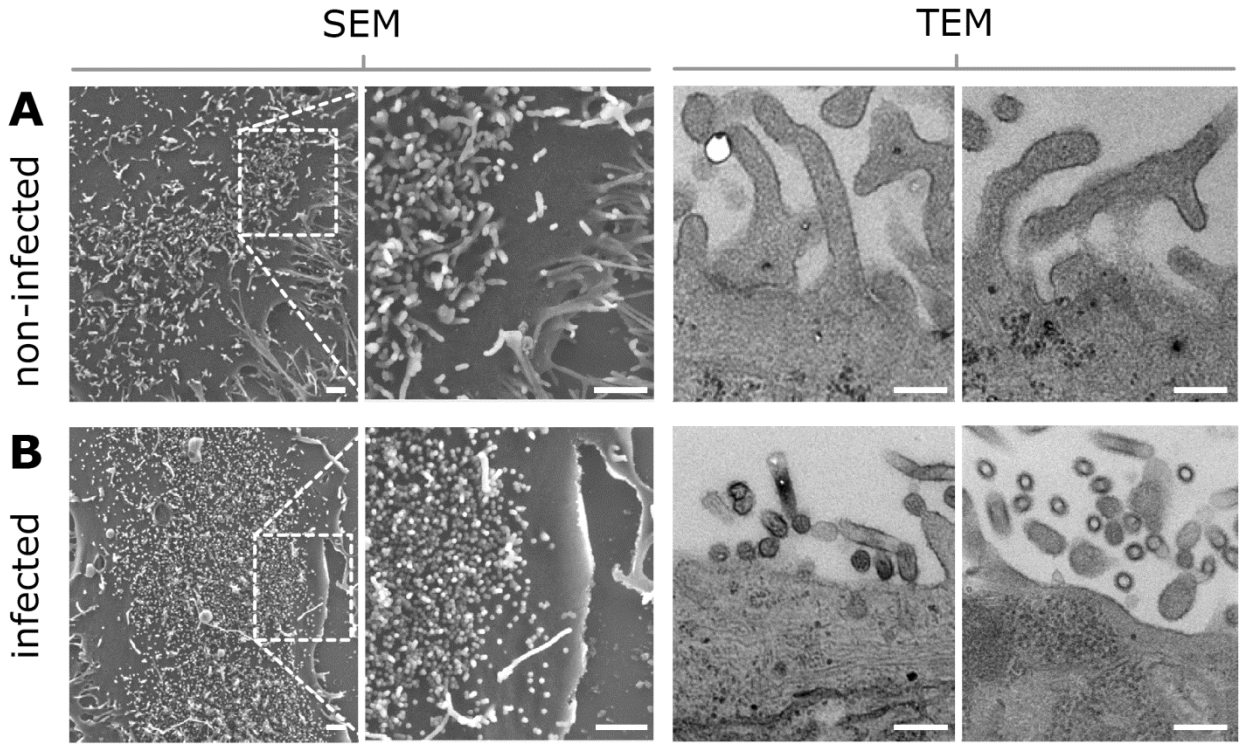

Figure A1-4 – Influenza virus egress. Scanning electron microscopy (SEM) and transmission electron microscopy (TEM) images of the surface of (**A**) non-infected or (**B**) influenza (B/Florida/04/2006) virus infected MDCK cells. High numbers of spherical viral particles are budding off the surface and are clearly distinguishable form microvilli or smooth cell protrusions by size, electron density, and their double membrane. Scale bar in SEM is 1 µm and in TEM 200 nm.

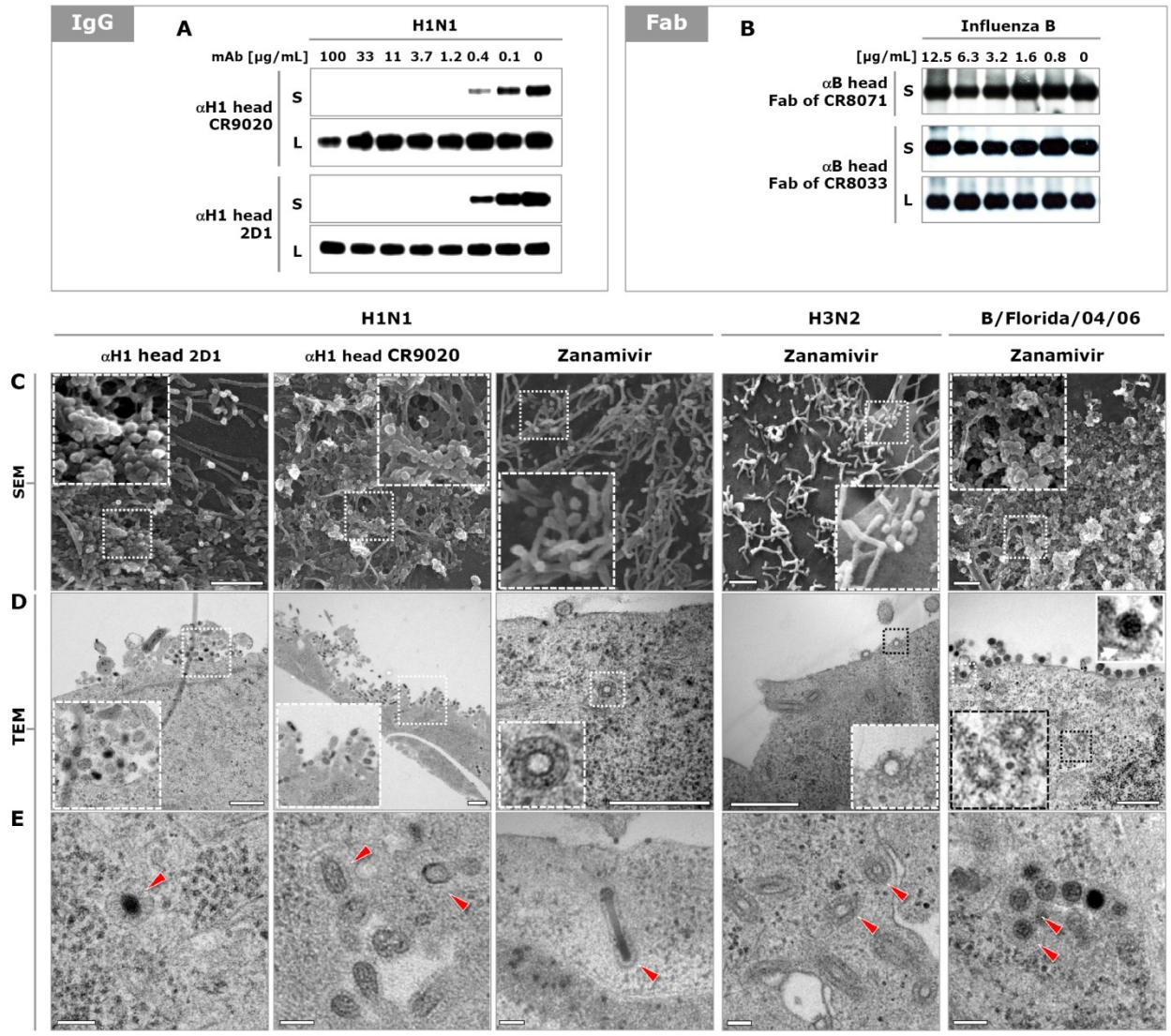

Figure A1-5 – *HA head binding antibodies inhibit influenza virus egress. (**A**) Calu-3 cells were infected with A/Puerto Rico/8/1934 (H1N1) and 3 hours later head-binding antibody CR9020 or 2D1 was added. Twenty hours later, the amounts of HA present in the cell supernatant (S) and lysate (L) were analyzed by Western blot (HA0 band shown). (**B**) As in (**A**) except MDCK cells were infected with B/Florida/04/2006 and the Fab fragments of CR8071 and CR8033 were used in the egress assay. (**C**) SEM images of the surface of MDCK cells infected with influenza A/California/07/2009 (H1N1), A/New Caledonia/20/1999 (H1N1), A/Wisconsin/67/2005 (H3N2), or influenza B/Florida/04/2006 virus and subsequently incubated (from 3 hours post infection) with 2D1 (5 µg/mL), CR9020 (15 µg/mL), and Zanamivir (0.5µM) respectively. Representative images of three independent experiments are shown. Scale bar (**C**) 1µm. (**D-E**) As in (**B**) except TEM images of ultrathin sectioned MDCK cell (re-internalized particles indicated with red triangles). Scale bar in (**D**) 500 nm and in (**E**) 100 nm.*

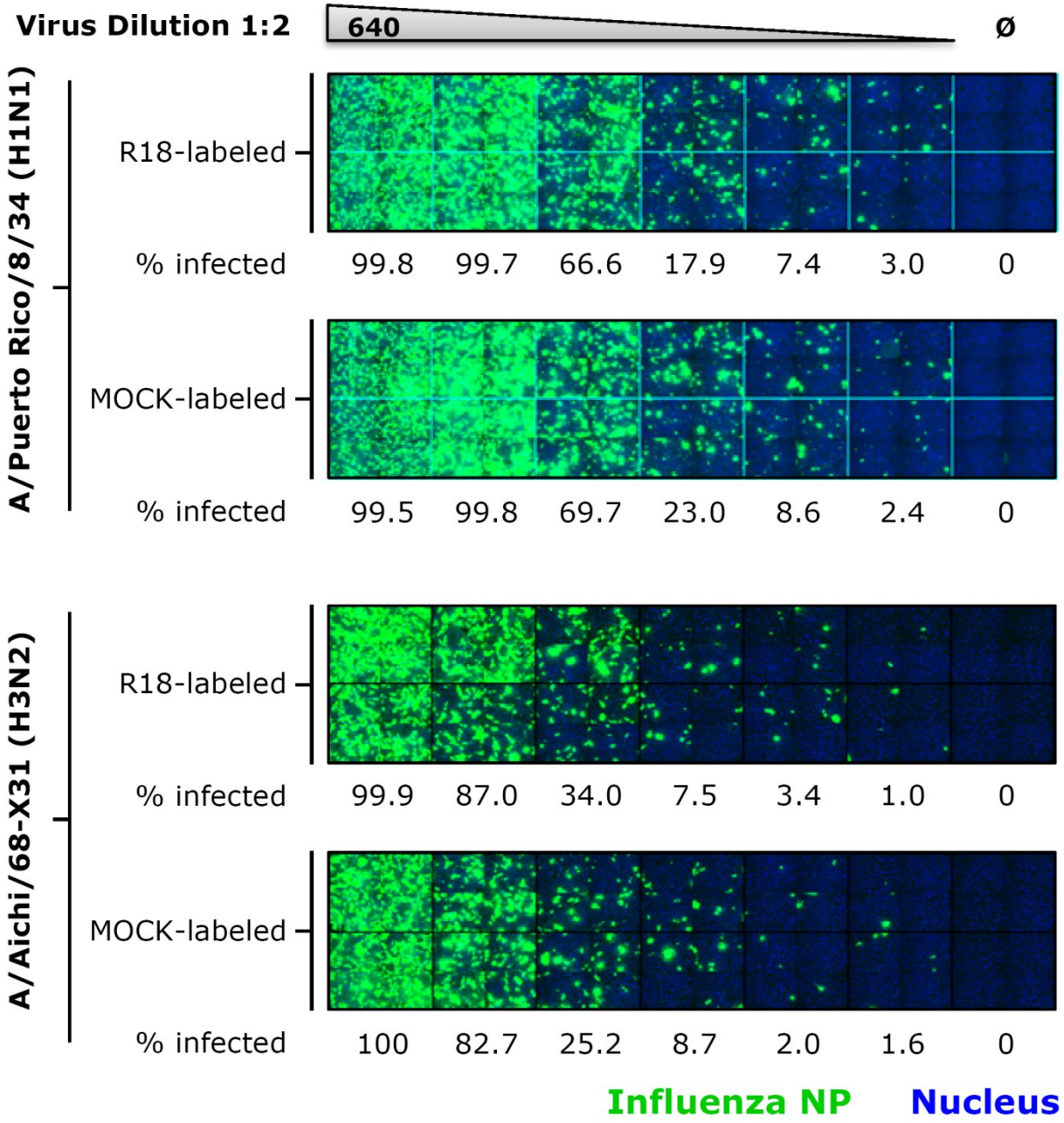

Figure A1-6 – R18 labeled influenza virus remain infectious. MDCK cells were infected with R18- or MOCK-labeled A/Puerto Rico/8/1934 (H1N1) or A/Aichi/2/1968-X31 (H3N2) and the number of infected cells (nucleus stained with DAPI, blue) for each virus was determined by staining for influenza NP expression (green).

A1.3 Supplementary tables

Table A1-1 – Characteristics of bnAbs, control antibodies, and Fabs used in this study.

IgG1s/ Fabs	HA Epitope	VNA titer [µg/mL]		HAI titer [µg/mL]				Breadth[h]	Ref.
		H1N1	H3N2	B	H1N1	H3N2	B		
CR6261	Stem	3.58 [a]	-	-	-	-	-	broad A-G1	[5]
CR8020	Stem	-	2.2 [b]	-	-	-	-	broad A-G2	[6]
CR8033	Head	-	-	0.02[c]	-	-	0.22[c]	broad B	[7]
CR8033 Fab	Head	-	-	2.63[c]	-	-	4.42[c]		
CR8071	Head	-	-	2.04[c]	-	-	-	broad B	
CR8071 Fab	Head	-	-	-	-	-	-		
CH65[g]	Head	0.44 [d]	-	-	0.88 [d]	-	-	broad H1	[8]
CH65 Fab	Head	4.20 [d]	-	-	17.7[d]	-	-		
2D1[g]	Head	0.08 [e]	-	-	0.22 [e]	-	-	narrow H1	[9]
CR9020	Head	<0.01 [d]	-	-	0.22 [d]	-	-	narrow H1	[i]
CR8057	Head	-	<0.01 [f]	-	-	0.03 [f]	-	narrow H3	[6]
CR8057 Fab	Head	-	<0.02 [f]	-	-	0.03 [f]	-		

[a] A/Puerto Rico/8/34
[b] A/Aichi/2/68-X31
[c] B/Florida/04/06
[d] A/New Caledonia/20/99
[e] NYMC X-181 (6:2 reassortant of PR8 with the HA and NA segments of A/California/07/09)
[f] A/Wisconsin/67/2005
[g] The variable heavy and light chains of CH65 and 2D1 were cloned into Crucell's human IgG backbone. The resulting IgGs (CR11055 and CR11054, respectively) have identical specificity as the published antibodies.
[h] A = Influenza A virus, G1 = influenza A virus group 1 (comprises the H1, H2, H5, H6, H8, H9, H11, H12, H13, H16 and H17 subtypes), G2 = influenza A virus group 2 (comprises the H3, H4, H7, H10, H14 and H15 subtypes) B = influenza B virus
[i] Chapter 2 and Appendix 1 data
– No activity

Table A1-2 – Co-localization of virus-antibody complexes in infected MDCK cells

Virus	Strain	bnAb	# cells counted	# particles counted	% colocalization virus + bnAb	Stdev
H1N1	A/PR/8/34	CR6261	175	605	93.5	1.9
		CR8020	142	582	0.2	0.5
H3N2	A/Aichi/68-X31	CR8020	159	1257	92.0	5.6
		CR6261	153	1158	0.14	0.3

A1.4 Supplementary movies descriptions

Movie M1-1 – Stem-binding bnAb CR8020 is internalized into live cells in complex with H3N2 virus particles. R18-labeled A/Aichi/2/68-X31 (H3N2) virus particles pre-incubated with AF647-labeled CR8020 are internalized into live MDCK cells (nucleus, blue). Movie (~27 min past incubation, mpi) shows the directed motion of virus particles (red) together with mAbs (green) along *TubulinTracker*-stained microtubules (white).

Movie M1-2 – Stem-binding bnAb CR6261 is internalized into live cells in complex with H1N1 virus particles. R18-labeled A/Puerto Rico/8/34 (H1N1) virus particles pre-incubated with AF647-labeled CR6261 are internalized into live MDCK cells (nucleus, blue). Movie (~40 mpi) shows the directed motion of virus particles (red) together with mAbs (green) along *TubulinTracker*-stained microtubules (white).

Movie M1-3 – Stem-binding bnAb CR8020 is not internalized after incubation with H1N1 virus particles. After incubation of R18-labeled A/Puerto Rico/8/34 (H1N1) virus particles (red) with AF647-labeled non-binding control antibody CR8020, only virus particles are internalized ~33 mpi into live MDCK cells (nucleus, blue).

Movie M1-4 – Stem-binding bnAb CR6261 is not internalized after incubation with H3N2 virus particles. After incubation of R18-labeled A/Aichi/2/68-X31 (H3N2) virus particles (red) with AF647-labeled non-binding control antibody CR6261, only virus particles are internalized ~41 mpi into live MDCK cells (nucleus, blue).

Movie M1-5 – H1N1 virus incubated with only 15nM CR6261-AF488 can undergo fusion. Representative portions of dual-color fluorescence viral fusion recordings obtained with 200 ms exposure times; scale bar equals 2 μm. R18-labeled A/Puerto Rico/8/34 (H1N1) virus (false colored magenta, center column) incubated for 30 min with 15 nM AF488-labeled CR6261 (green, right column). Co-localization between the virus and bound bnAb (white) is shown in the left column (merge). Time t = 0 indicates drop of pH from 7.4 to 5.0. Fusion events are observed as the rapid increase in fluorescence signal (dequenching) at the site of a virus, followed by quick, outward diffusion of the lipophilic R18 dye away from the fusion site. Both movies (M1-5 and M1-6) were recorded under identical illumination conditions. Contrast settings of the 15 nM bnAb incubation has been enhanced 25% relative to the 1500 nM incubation (Movie S6). All images were scaled 4-fold larger using bicubic interpolation. For assay details see experimental procedures.

Movie M1-6 – H1N1 virus incubated with 1500nM CR6261-AF488 is fusion incompetent. As in (M1-5) except, R18-A/Puerto Rico/8/34 (H1N1, magenta) was incubated with 1500nM AF488-labeled CR6261 (green). The higher bnAb concentration inhibited HA-mediated fusion and no dequenching or R18 diffusion is observed. Both movies (M1-5 and M1-6) were recorded under identical illumination conditions.

A1.5 Supplementary references

1. Floyd DL, Ragains JR, Skehel JJ, Harrison SC, van Oijen AM (2008) Single-particle kinetics of influenza virus membrane fusion. Proc Natl Acad Sci U S A 105: 15382-15387.

2. Floyd DL, Harrison SC, van Oijen AM (2009) Method for measurement of viral fusion kinetics at the single particle level. J Vis Exp 31: e1484.

3. Qin D, Xia Y, Whitesides GM (2010) Soft lithography for micro- and nanoscale patterning. Nat Protoc 5: 491-502.

4. Tokunaga M, Imamoto N, Sakata-Sogawa K (2008) Highly inclined thin illumination enables clear single-molecule imaging in cells. Nat Methods 5: 159-161.

5. Throsby M, van den Brink E, Jongeneelen M, Poon LL, Alard P, et al. (2008) Heterosubtypic neutralizing monoclonal antibodies cross-protective against H5N1 and H1N1 recovered fro m human IgM+ memory B cells. PLoS One 3: e3942.

6. Ekiert DC, Friesen RH, Bhabha G, Kwaks T, Jongeneelen M, et al. (2011) A highly conserved neutralizing epitope on group 2 influenza A viruses. Science 333: 843-850.

7. Dreyfus C, Laursen NS, Kwaks T, Zuijdgeest D, Khayat R, et al. (2012) Highly conserved protective epitopes on influenza B viruses. Science 337: 1343-1348.

8. Whittle JR, Zhang R, Khurana S, King LR, Manischewitz J, et al. (2011) Broadly neutralizing human antibody that recognizes the receptor-binding pocket of influenza virus hemagglutini n. Proc Natl Acad Sci U S A 108: 14216-14221.

9. Yu X, Tsibane T, McGraw PA, House FS, Keefer CJ, et al. (2008) Neutralizing antibodies derived from the B cells of 1918 influenza pandemic survivors. Nature 455: 532-536.

Appendix 2 – Supplementary information for Chapter 3

This appendix contains the following supplementary information:

A2.1 Supplementary methods

A2.2 Supplementary figures and movie

A2.3 Supplementary tables

A2.4 Supplemental references

A2.1 Supplementary methods

A2.1.1 Microfluidic Flow Cell and Glass Cleaning

Experiments were performed in microfluidic channels formed using either double-sided tape sandwiched between quartz top and cover slips bottom as described previously [1], or multi-channel PDMS chips. PDMS (polydimethylsiloxane; Dow Corning, Slygard 184) based multichannel microfluidic chips were formed by standard PDMS cast molding techniques [2,3]. Each chip housed five microfluidic channels having inner dimensions 0.5(w) x 0.2 (h) x 10(l) mm^3 and separated by 0.5 mm. PDMS chips were non-permanently adhered to the surface of the cleaned glass microscope cover slips (No. 1, VWR, USA) and housed in a home-built microscope adapter. Inlet and outlet polyethylene tubing (PE20 and PE60, respectively; Intramedic)) was coupled to each microfluidic channel to allow for rapid buffer exchange via connection to a syringe pump (New Era Pump Systems Inc., NE-1000). All chips and flow channels were used only once.

A2.1.2 Virus and IgG/Fab Labeling

Influenza A strains PR/8/34 (H1N1) and A/Aichi/2/68 (X-31, H3N2) propagated in SPF eggs were purchased from Charles River (North Franklin, Connecticut, USA) and used without

further purification. Stock samples were certified by the manufacturer to have 2 mg of total viral protein per milliliter. Electron microscopy confirmed that the viruses used were mono-disperse, spherical particles of uniform size, the latter being due to the method of virus propagation. Labeling was performed by diluting virus stocks 1:3 into HNE buffer (5.0 mM Hepes, 140 mM NaCl, 0.2 mM EDTA, pH 7.4), then adding 0.5 % volume equivalent of octadecyl rhodamine B lipophilic dye (R18, Invitrogen Inc.) in DMSO to a final dye concentration of 1 μM. The virus-dye mixture was placed on a rotating micro-tube mixer (Cole-Parmer) for three hours. Unincorporated dye was removed using a PD-10 desalting column (GE Healthcare). Fractions of 200 μl were collected and checked for labeled virus using the microscope setup. The three to four fractions with highest particle count were pooled into a single volume, aliquoted, frozen using liquid nitrogen and stored at -80ºC until use. Labeled viruses were previously confirmed to be infectious [4].

A2.1.3 IgG and Fab production

Human IgG1 antibodies CR6261 and CR8020, were constructed by cloning the heavy (VH) and light (VL) chain variable regions into a single expression vector containing the IgG1 constant regions. HEK293-F cells were transfected with the IgG expression constructs and the expressed antibodies were purified from serum-free culture supernatants using protein A chromatography (HiTrap, GE healthcare) followed by a desalting step (HiPrep 26/10, GE healthcare). The Fab fragments were obtained by IdeS digestion of the purified IgG, followed by protein G purification (GE Healthcare), cation exchange (MonoS, GE Healthcare), and gel filtration (Superdex200, GE Healthcare).

A2.1.4 IgG/Fab labeling and degree of labeling determination

HA-specific antibodies CR6261 and CR8020 were fluorescently labeled with Alexa Fluor 488 (AF488, Molecular Probes) according to manufacturers' guidance. In brief, IgG/Fab fragments were added to AF488 dye in sodium bicarbonate buffer. The solutions were mixed at moderate speed on a Ferris wheel mixer for 2h and protected from light. Free dye was removed from the sample using a PD10 desalting column (GE Healthcare). The AF488-labeled IgG/Fab were eluted into 20mM sodium acetate, 75mM NaCl, 5% sucrose, pH 5.5.

The number of Alexa-488 molecules bound to the IgG/Fab molecules was determined using photobleaching analysis and MALDI mass spectrometry. The degree of labeling was taken as an average of these two results and the percentage of labeled IgG/Fab molecules visualized was estimated from a Poisson calculation (Table A2-1).

Photobleaching measurements were performed by adsorbing labeled IgG/Fab molecules to a clean glass surface and illuminating with ~5 W/cm^2 488 nm laser power to observe individual photobleaching steps. Distributions of the final bleaching height were extracted and well-fit by Gaussian distributions. The initial fluorescence intensity of visualized molecules was divided by the mean intensity identified by Gaussian fitting to obtain the distributions for the number of fluorophores bound to each IgG/Fab (Figure A2-2.i). These distributions for IgG were well fit by Poisson distributions to determine the expected number of covalently linked Alexa-488 molecules. The distributions for Fab were reasonably well fit by Poisson distributions, but showed higher than expected population densities at lower number of linked Alexa-488 molecules, indicating that not all available N-terminal amino groups are equally accessible for labeling.

MALDI mass spectra at mass-to-charge ratios of one (m/z=1) and two (m/z=2) were obtained for unlabeled and Alexa-488 labeled IgG/Fab using sinapinic acid as the matrix. The peak value in the mass spectra of the unlabeled IgG/Fab was subtracted from the mass spectra of the labeled molecules. The shifted mass spectra of the labeled molecules was then divided

by the mass of individual Alexa-488 molecules, determined to be 515 Da using molecular structures provided by the manufacturer, to scale the mass values in terms of numbers of covalently linked Alexa-488 molecules (Figure A2-2). The resulting spectra were well fit by Poisson distributions to identify the expected number of Alexa-488 per IgG/Fab (Figure A2-2.ii).

A2.1.5 Proteoliposome Preparation

Proteoliposomes were composed of a 0.8:0.2:2.5x10-5 ratio of molar fractions of DOPC:CH:biotin-DHPE (respectively: 1,2-dioleoyl-sn-glycero-3-phosphocholine and Cholesterol, Avanti Polar Lipids, Alabama, USA; N-((6-(biotinoyl)amino)hexanoyl)-1,2-dihexadecanoyl-sn-glycero-3-phosphoethanolamine triethylammonium salt, Invitrogen) mixed in chloroform solutions, dried under argon, then desiccated for two hours. Dried lipids were suspended in HNE buffer at 5 mg/ml, freeze/thawed five times, then extruded using 0.2 μm-pore size polycarbonate filters (mini-extruder, Avanti). Liposomes were solubilized by Triton X-100 (molecular biology grade, VWR International) to a final concentration of 0.5% (w/v) and incubated at 37°C for 15 minutes then on ice for 15 minutes. The sialoglycoprotein glycophorin A (GYPA; Abnova, Taipei City, Taiwan; full-length recombinant protein with a GST tag) was added to solubilized lipids at lipid:protein molar ratio of approximately 1:40,000 and mixed at 4°C for 30 minutes. Bio-Beads (SM-2 absorbent, Bio-Rad Laboratories, Inc.) removed the Triton-X detergent by two subsequent two-hour incubations at 4°C with constant rocking, using 200 mg Bio-Beads per 300 μl of solution. Proteoliposome preparations were stored at 4°C under an argon atmosphere for up to 48 hours prior to use with no further treatment.

Glycophorin A membrane protein was used in lieu of membrane-bound gangliosides, such as GD1a [1], because we found that the H1N1 virus strain did not become immobilized upon planar bilayers when sialic acid was presented in this fashion (including use of ganglioside mixtures (Calbiochem, USA, cat# 345717) and S-Sialyl-a(2,6)-lactosylceramide (Wako Pure

Chemical Industries, Japan)). Previous bulk fusion studies had shown a difference in fusion kinetics for H1N1 in fusing with ganglioside-containing liposomes versus GYPA-containing proteoliposomes (Alford et al., 1994). Both the H1N1 and H3N2 virus strains used bound readily to planar bilayers comprising the GYPA membrane protein.

A2.1.6 Microscope Specifications

Measurements were conducted on an inverted fluorescence microscope (Olympus IX-71) equipped with a custom-ordered microscope filter cube (Chroma Ltd. filters zet488/561m and zt488/561rpc) and either a 60x NA 1.49 objective (Olympus APON60OTIRF) or a 60x NA 1.45 objective (Olympus PLANAPON60TIRF). The NA 1.45 objective was found to exhibit less chromatic aberration at the edge of the images, improving the co-localization between virus and IgG/Fab signal. Virus particles and labeled IgG/Fab were illuminated, respectively, with ~0.25 W/cm^2 561 nm and ~0.2 W/cm^2 488 nm continuous-wave solid state lasers (Sapphire models, Coherent Inc.) focused onto the back-focal plane of the microscope objective and aligned in objective-based total internal reflection (TIR) mode. The configuration was optimized to homogeneously illuminate the entire virus particle and the fluorescence intensity of labeled IgG/Fab bound to viruses was found to be independent at TIR incidence angles less than 57° (Figure A2-4), while still suppressing background fluorescence. Emitted green and red fluorescence was separated by a home-built dual view with Thorlabs DMLP567 long-pass filter or by a commercial Dual-View system (Photometrics, Tucson, AZ, USA)) with Chroma T560LPXR long-pass filter. Signals were filtered to remove stray laser light and background from Raman scattering (Chroma ET525-50m and ET605-70m, green and red respectively), then focused onto either half of an electron multiplying CCD camera (Hamamatsu Photonics K.K., Image-EM model C9100-13). False-color representative images resulting from this setup are depicted in Figure 3-1.

A.2.1.7 Fusion Experiment

Glass-supported planar bilayers were formed by adding the proteoliposome solution to a HNE-hydrated microfluidic flow cell mounted upon the microscope and incubated with the glass surface for a minimum of 45 minutes at room temperature. R18-labeled viruses were diluted 10-fold into a solution of 100% Alexa-488 labeled IgG/Fab, bringing the IgG/Fab to the desired final concentration. Virus and IgG/Fab were incubated for 45-60 minutes at room temperature, and then added to the microfluidic flow cell at 5 μl/min wherein the viruses immobilized on the planar bilayer through specific HA-GYPA interactions. Fluorescein-labeled streptavidin (Invitrogen) was subsequently added at 0.2 μg/ml using a flow rate of 10 μl/min for 5 minutes; therein the labeled IgG/Fab not bound to viruses washed away to leave a low background. A 2-minute wash with clean HNE buffer at a high (100 μl/min) rate removed unbound viruses, IgG and streptavidin-fluorescein. Finally, viral fusion was initiated by rapid injection of a citric acid buffer (10.0 mM citric acid, 140 mM NaCl, 0.2 mM EDTA, pH 5.0) at 200 μl/min and recorded using Metavue imaging software (Life Science Imaging Ltd., Marlow, Buckinghamshire, England) at an acquisition rate of 5 Hz for 240 seconds and maximal EM gain. Laser illumination during the first 5-6 seconds and before the pH drop was with 561 nm only, then the 488 nm illumination was initiated. This alternation allowed for identification of viruses in the red channel, then co-localization in the green channel. Total laser illumination was approximately 400 mW/cm^2 and was set such that at high neutralizing molecule concentration there were very few saturated pixels together with a large range of pixel intensity values. Following immobilization of the virus on the bilayer surface, the fusion experiments required 10 to 20 minutes total experimental time.

A2.1.8 Data Extraction and Analysis

The laser illumination profile in each channel was identified after the pH drop by smearing out fluorescent peaks with a 40-pixel radius median filter, which allowed for fitting of

the underlying beam profile with a two-dimensional Gaussian. The fitted profile was set to have a maximal value of one at its peak. Each image extracted from the recording was corrected for the illumination profile (flattened) by first removing dark-counts and then dividing by the fitted profile.

Individual viral particles were identified and their fluorescent trajectories extracted using custom MATLAB code similar to that described previously [1]. The arrival of the low-pH buffer was detected, as previously described [1], as a sudden loss of fluorescein signal in the green channel. Red-channel fluorescence peaks were identified by averaging ten frames under 561 nm illumination only, flattening and removing global fluorescence background (next paragraph), and then applying a discoidal averaging filter [5]. Peaks were identified by thresholding using a $\mu+2*\sigma$ criterion, where μ and σ are the average intensity and intensity standard deviation, respectively, of the filtered red channel. Green-channel peaks were similarly identified by averaging ten frames after the pH drop. Co-localization was achieved by translating the locations found in the red channel onto the green channel and grouping the nearest neighbor pairs of peaks.

Peaks in the green channel were fit with a two-dimensional Gaussian profile and all pixels within 3σ of the peak center were identified for signal integration; red channel peaks were surrounded with a 4x4 pixel square box for fluorescence signal integration. Fluorescence background in the green channel was identified on a per-particle basis as the baseline offset resulting from Gaussian fitting, while the red channel background was found globally by taking the peak of the distribution of the pixel intensities from the flattened image used for particle co-localization.

Red-channel fluorescent trajectories were plotted and manually selected as exhibiting hemifusion similar to previous description [1]. Those showing clear dequenching spikes followed by dissipative signal loss, as shown in the Figure 3-1B, were directly classified as fusing virions.

Trajectories showing characteristics of dequenching and/or dissipative signal loss, but that were not as overtly similar to the trajectory of Figure 3-1B, were subjected to further manual inspection. In these cases, a virus particle in question is observed in the recorded fusion movie and those showing a rapid, outward movement of R18 molecules away from the virus identifiable by eye were also classified as fusing virions. Absolute hemifusion efficiency in each experiment was calculated as the number of particles in a field of view determined to undergo hemifusion divided by the total number of particles initially detected in the same field of view. Hemifusion efficiency data was fit using a four-parameter logistic model using the transform both sides approach for variance stabilization [6] utilizing a *logit* transformation (Equation 1, Table A2-2). For fitting, conditions with no fusion events were set to 1 event.

The integrated green-channel fluorescence corresponding to the virus-bound labeled IgG/Fab was averaged over 15 frames (three seconds), starting five frames (one second) after the pH drop (dark green square, Figure 3-1C). Separately, the average integrated intensity of individual labeled IgG or Fab molecules was obtained by non-specifically adsorbing them to a clean glass surface within a microfluidic channel and measuring their fluorescence intensity under identical illumination conditions as used in the fusion experiments (Figure A2-4). Laser power was varied to ensure fluorophore excitation occurred within the linear response regime (Figure A2-4) and to obtain photobleaching data (Figure A2-2).

The number of molecules bound to HA on the surface of each virus was calculated by dividing the average integrated fluorescence intensity measured from the fusion experiments by the average integrated intensity measured for the individual antibodies. The value for the number of IgG/Fab bound to each virus was corrected for the presence of unlabeled IgG/Fab using the visualized fraction measured by MALDI and photobleaching (Table A2-1). For each experimental run, the distribution for the numbers IgG/Fab bound to all virions (both fusing and non-fusing) was determined and its median value calculated (Figure 3-2). The median values for the numbers of IgG/Fab bound were fit with a hyperbola using the transform both sides

approach for variance stabilization [6] utilizing a square root transformation (Equation 2, Table A2-2).

Numbers of IgG/Fab were related to hemifusion efficiency by combining both models into one analysis (proc NLMIXED, SAS v9.2). In this combined method, the number of bound IgG/Fab at each point along the fit line was used to back-calculate the corresponding IgG/Fab concentration. From this estimated concentration, the hemifusion efficiency and 95% confidence interval were calculated using the delta method [7] and the lowest degrees of freedom from the two models.

Hemifusion time-to-event for each particle was determined as the elapsed time between the pH-drop frame and the frame when hemifusion occurs, defined as the time-point with the maximal rate of fluorescence increase. The time-to-hemifusion distribution for each experimental run was determined and its geometric mean time and geometric standard deviation (error) determined. The geometric mean was utilized to preserve the semi-log distribution, often used to analyze waiting time distributions [8]. The times resulting from each experiment were $\log_{10}$ transformed fitted by a hyperbola with a constant offset (Equation 3, Table A2-2). The geometric means in the absence of IgG/Fab reported in Chapter 3 (46 seconds for H1N1, 30 seconds for H3N2) are comparable to estimates obtained from data fitting (Table A2-2), indicating our models were properly anchored.

A2.1.9 Monte Carlo Simulation

To simulate protein packing on the viral surface we used a simple 2D hard sphere model. Each protein was approximated with a number of spheres (Figure A2-7) such that their final dimensions were in agreement with appropriate crystal structures. Model viral membranes were comprised of the envelope embedded proteins hemagglutinin (HA), neuraminidase (NA) and M2 proton pump. Binding geometry of IgG/Fab to the HA proteins was constrained to be in agreement with the CR8020-HA co-crystal structure (PDB code 3SDY [9]).

IgG molecules (14 nm in total length) containing two paratopes were modeled with the Fc domain pointing vertically from the *in silico* viral surface and were allowed to have flexibility about their midpoint. They were constructed from five spheres - two for each fab, one representing the variable and the other, the constant region, and one sphere corresponding to the Fc tail. Fab fragments (7 nm in length), were not flexible, had a single paratope and were constructed from two spheres. HA was approximated with four spheres: one larger for the stem, and three for the HA1 heads. The diameter of the HA stem was measured around the epitope area of the CR8020 antibody in order to assure correct binding geometry. The approximate size of the extracellular domain of the M2 ion-channel was estimated from its the molecular mass, accounting for the protein's tetrameric quaternary structure. Neuraminidase was modeled as a single sphere.

The spike protein (HA and NA) density was set at 8000 spikes per μm^2 and an HA:NA ratio of 7:1 in agreement with previous studies of similar influenza virus samples [10,11]. From this density, a surface representing our average 125 nm virus particles contained 392 spike proteins, 341 of which were HA.

Simulations were performed by placing viral proteins randomly within a 2D periodic simulation surface. The surfaces were minimized with a Monte Carlo-like algorithm in order to remove protein overlap from a randomly generated surface. The overlap energy was modeled as a square well potential with additional term proportional to the overlap surface. Increasing IgG/Fab concentrations were added and their final structure and position determined using the Monte Carlo sampling. The paratope-epitope interaction energy was modeled using the patchy spheres approach [12] so as to impose appropriate distances and angles between the epitope and paratope as dictated by their co-crystal structure [9]. We found that employing a smooth potential instead of a square-well interaction energy allowed Monte-Carlo minimization to converge faster due to the longer range interactions. For the minimization we use the following moves: single protein rotation and perturbation, two proteins swapping, IgG/Fab jumping to

another binding site, randomizing Fab-Fab angle of the IgG (only). The concentration at which we were not able to get rid of the protein overlap was taken as the steric packing limit.

Previous studies have argued that groups of HA in close proximity could represent fusogenic clusters that cause nucleation of membrane fusion events [13]. Simulation data was analyzed to identify HA clusters defined to be groups of HA trimers free from IgG/Fab that were in close proximity to each other without any additional surface proteins between them; cluster disruption was defined to occur when these conditions were not met. Unfortunately defining clusters of fixed sizes from 3–6 neighboring HA trimers did not result in replication of trends observed in the experimental data of hemifusion efficiency, namely a need for more Fab than IgG to achieve equal cluster disruption, and the results of these analyses are not included.

A2.2 Supplemental figures and movie

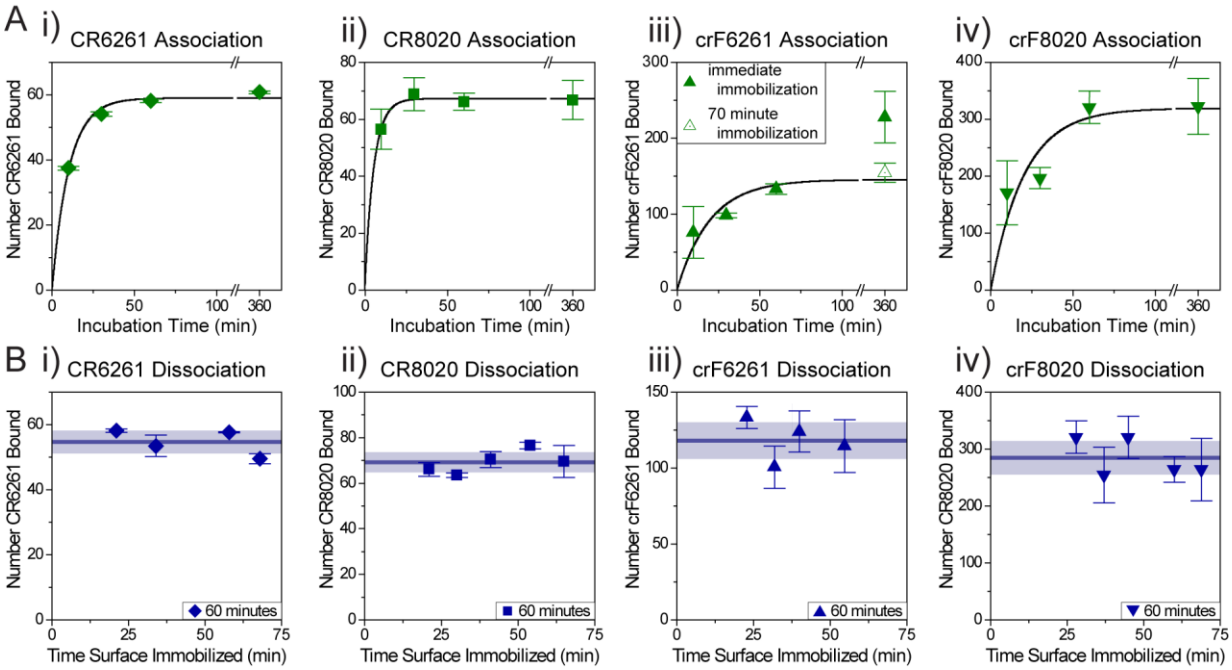

Figure A2-1 – *Association (A) and dissociation (B) of CR6261 (i) and CR8020 IgG (ii), and of crF6261 (iii) and crF8020 Fab (iv).* ***A****) For IgG/Fab association plots, H1N1 (i,iii) or H3N2 (ii,iv) viruses were incubated with 130 nM IgG or Fab for the time indicated on the horizontal axis, then added to flow channels to become immobilized on the supported lipid bilayer (SLB). Flow-in time of the virus plus IgG/Fab solution was ~20 minutes. Two fields of view were imaged in rapid succession and the average IgG/Fab coverage ± SEM is reported.* ***B****) For dissociation after immobilization, IgG/Fab coverage on the same virus samples as in (A) were quantified at ~10-20 minute intervals without repeated imaging of the same fields of view. Typical experiment run time after flow-in of the virus-IgG/Fab solution was 10 minutes. For clarity, only dissociation measurements corresponding to 60 minute incubation (blue) from (A) are shown. Mean values of the number of bound IgG/Fab ± standard deviation over the times after immobilization are indicated by the horizontal line and shaded regions. Fluorescence intensity fluctuated between fields of view, as indicated in the scatter of the data points, but did not systematically decrease as would be expected if non-specific binding occurred or if the IgG/Fab otherwise dissociated from the virus. Non-specific binding occurred only for 360 minute incubation of crF6261 with H1N1 (A.iii, filled symbol at 360 minutes), which was observed to systematically decrease to coverage levels equivalent to 60 minute incubation (open-faced symbol at 360 minutes in A.iii) after 70 minutes of immobilization on the SLB surface.*

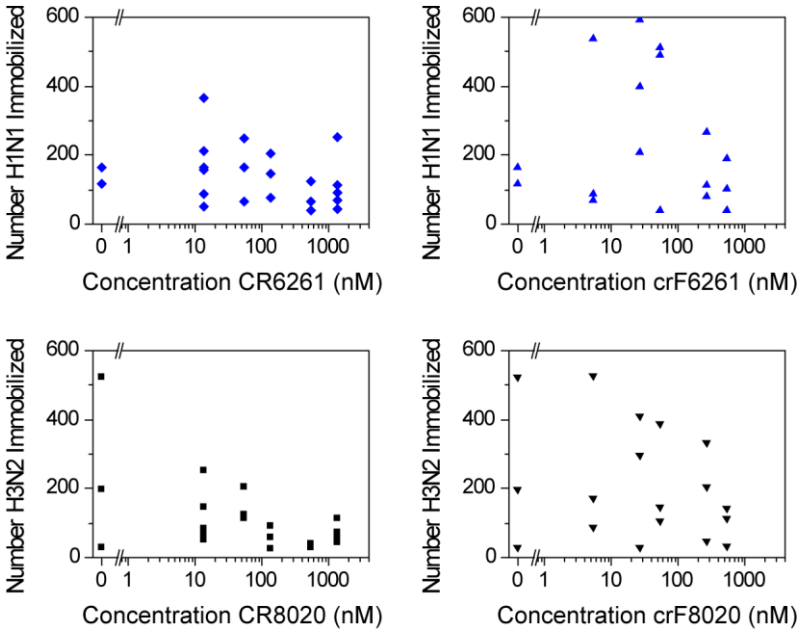

Figure A2-2 – *Immobilization of the virus to target bilayers through glycophorin A binding was largely unaffected by IgG/Fab binding to the viral surface. Each data point corresponds to a single fusion experiment and represents the total number of virions imaged in equal sized fields of view. While there is some decrease in binding at the highest concentrations, many virions are still imaged at the highest IgG/Fab concentrations indicating that binding does not prevent HA-receptor recognition.*

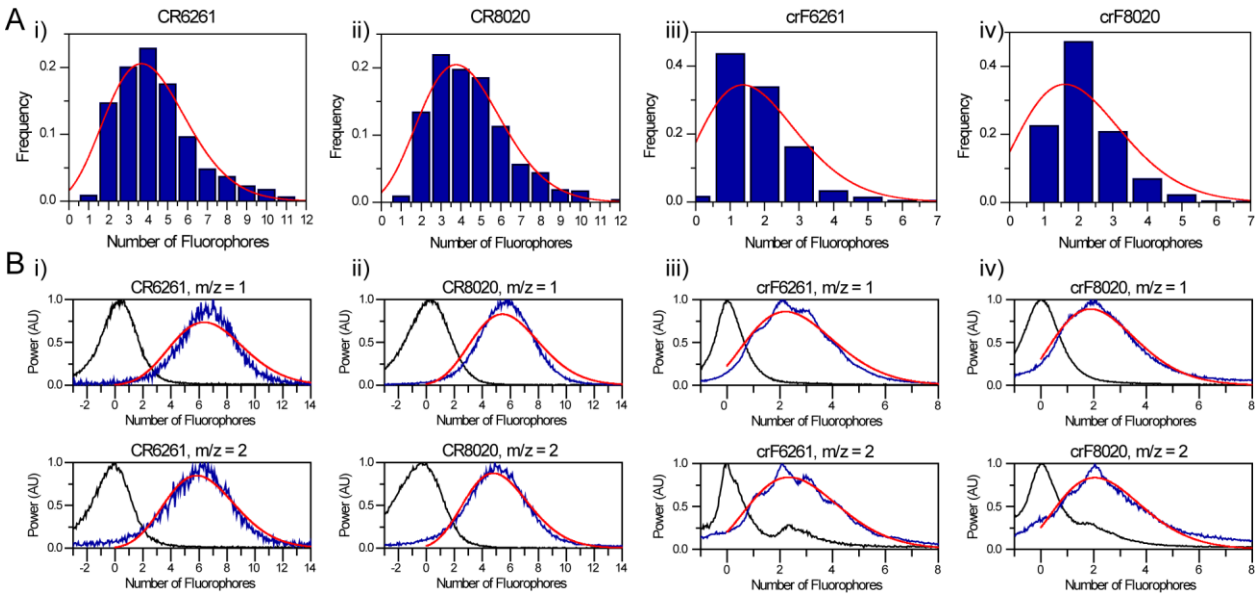

Figure A2-3 – *Degree of Alexa-488 labeling for 6261 IgG (i) and Fab (ii), and for 8020 IgG (iii) and Fab (iv) as measured by photobleaching analysis (A) and MALDI mass spectrometry (B).* ***A****) Photobleaching measurements resolved the distribution of number of Alexa-488 molecules bound to each molecule as described in SI Methods. These distributions were fit with a Poisson distribution (red lines) to identify the expected number of fluorophores bound to each IgG/Fab.* ***B****) Mass spectra at mass:charge ratios of 1 and 2 were determined for the unlabeled IgG/Fab mass spectra (black) and the Alexa-488 labeled IgG/Fab mass spectra (blue). The peak value from the unlabeled spectra was subtracted from each labeled spectra and divided by the molecular mass of Alexa-488. The labeled mass spectra was fit with a Poisson distribution (red) to identify the expected number of fluorophores linked to each IgG/Fab. Spectra for Fab molecules resolved identifiable peaks corresponding to molecules having one, two, three and four dye molecules (B.iii and B.iv). Results of fitting are summarized in Table A2-1.*

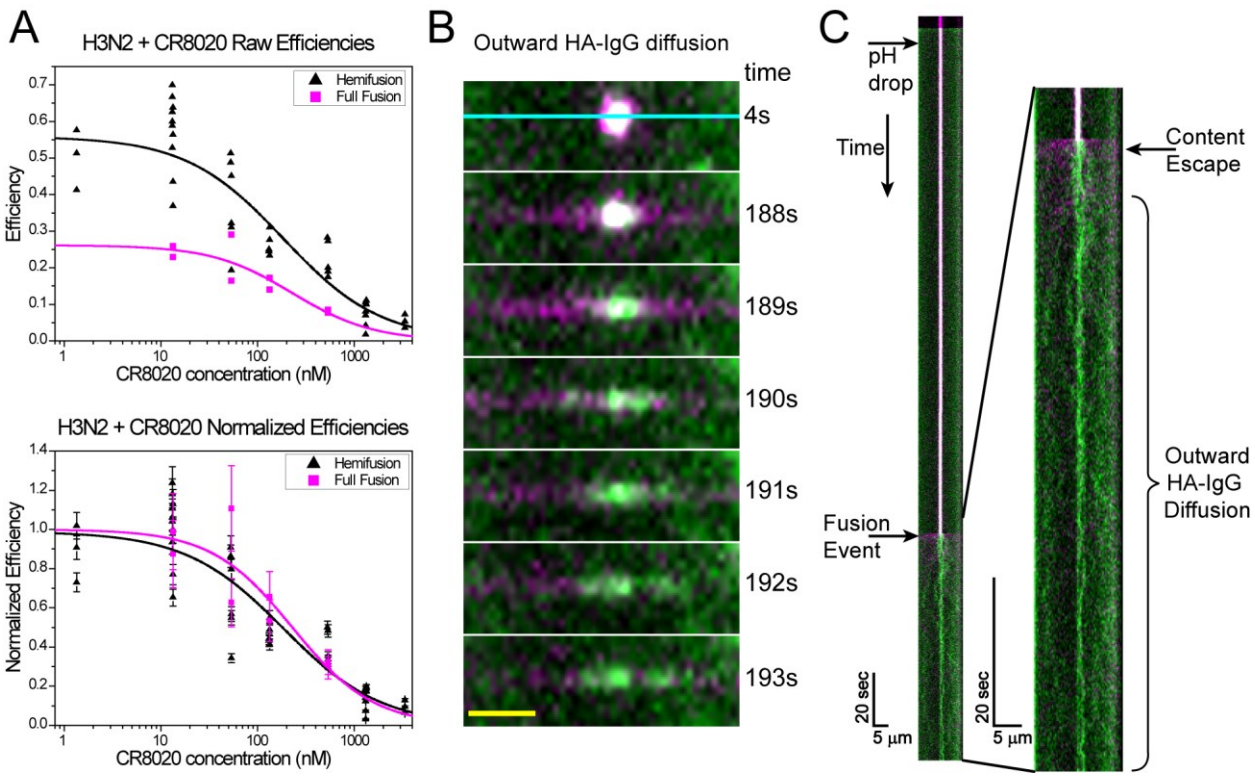

Figure A2-4 and Movie M2-1 – *Pore formation is inhibited by CR8020 in a similar fashion as hemifusion. IgG inhibits pore formation similarly to hemifusion inhibition. H3N2 viruses were content labeled with aqueous sulforhodamine B dye, as described previously [1], and incubated with Alexa 488-labeled CR8020 IgG (CR8020af488). Planar bilayers were formed in a microfluidic chamber upon dextran-functionalized glass cover slips [1] or upon polyethylene glycol (PEG) functionalized glass cover slips where 5% of the PEG used was covalently coupled to DSPE (3-(N-succinimidyloxyglutaryl)aminopropyl, polyethyleneglycol-carbamyl distearoylphosphatidyl-ethanolamine) [14,15]. Bilayer composition was supplemented with 1% molar fraction of the ganglioside Gd1a to allow virus immobilization. Upon pH drop, the viruses underwent membrane fusion as measured by the loss of content dye from the viral lumen [1].* ***A****, top) the efficiency of full fusion decreased as the concentration of CR8020af488 increased (magenta data). The raw hemifusion efficiency data (black) aggregated from the data shown in Figures 2-2F,G and 3-2A is shown for comparison; full fusion shows a lower overall efficiency compared to hemifusion.* ***A****, bottom) Full fusion and hemifusion data were normalized to their respective efficiencies in the absence of CR8020. Best fit lines using Equation 1 (Table A2-2) show good overlap between the two functional read outs and indicate that hemifusion inhibition is an appropriate read out for full fusion inhibition.* ***B****) Some viruses fusing to DSPE-PEG supported bilayers showed outward diffusion of HA-CR8020af488 complexes concomitant with content release. In the image montage of full fusion from Movie M2-1 depicted here, the SRB label (magenta) co-localizes with the CR8020af488 signal (green). The SRB content is observed to rapidly diffuse outward from the site of fusion in what appears to be 1D diffusion along a line (frames 188 and 189 sec). The one-dimensional nature is presumably the result of bilayer defects that arose during lipid hydration. Shortly after SRB release, the CR8020af488*

*(**Figure A2-4 Continued**) signal is seen to diffuse along the same one-dimensional area (frames 190-193 sec). This green diffusion signal indicates that the HA trimers diffuse outward from the viral envelope into the DSPE-PEG supported bilayer after full fusion has occurred, since HA is in a stable complex with CR8020af488 (Figure A2-1). Scale bar (yellow) is 2 μm. **C**) Kymograph over the cyan line in (B) shows co-localization of the virus and CR8020af488 signals (white) until the fusion event. At the point of fusion, the SRB content label rapidly diffuses as described in (B), followed by outward diffusion of the HA-CR8020af488 complexes.*

***Movie M2-1**) Content labeled H3N2 virus bound by a sub-inactivating number of CR8020af488 IgG molecules is immobilized upon a DSPE-PEG tethered bilayer. Content labeling is false-colored magenta, signal from the labeled antibodies bound to HA is false-colored green and the co-localization between them is white. As described in the caption to Figure A2-4, the SRB content is observed to rapidly diffuse outward from the site of fusion in what appears to be 1D diffusion along a line, which is likely a result of bilayer defects that arose during lipid hydration. Shortly after SRB release, the CR8020af488 signal is seen to diffuse along the same one-dimensional area, indicating that the HA trimers diffuse outward from the viral envelope into the target bilayer after fusion occurs. Two non-fusogenic viruses can also be seen on the left hand part of the movie. Scale bar is 2 μm.*

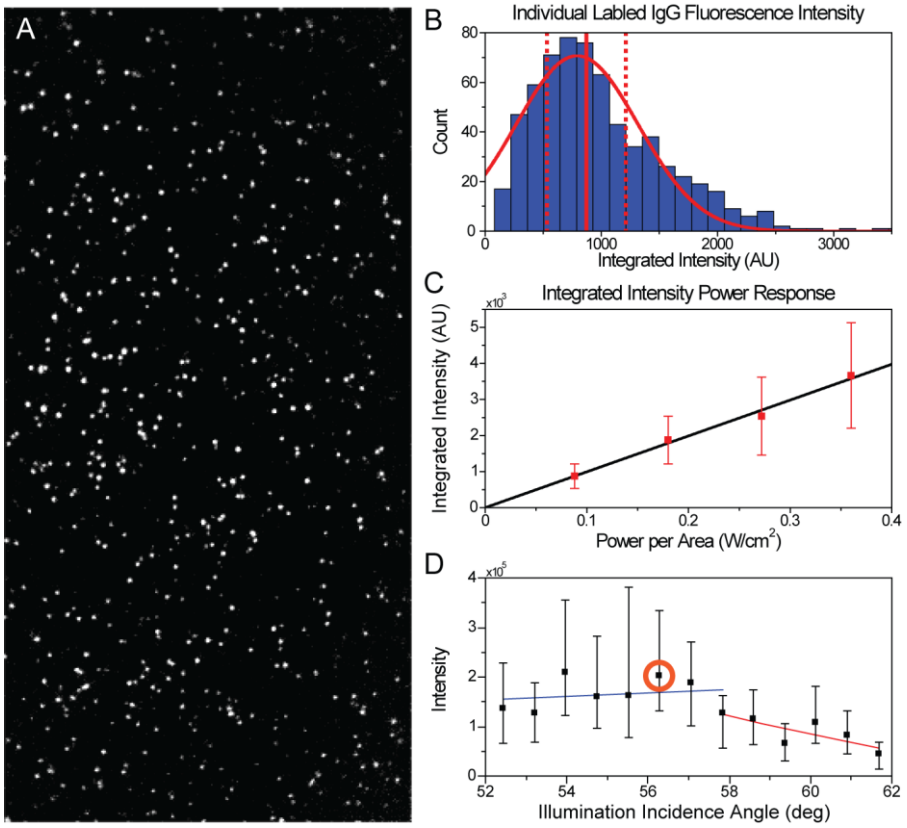

Figure A2-5 – *Imaging of individual, labeled IgG molecules.* ***A****) Representative image of CR8020af488 labeled IgG molecules adsorbed to a clean glass surface, visualized at ~0.1 W/cm^2 in pH 5.0 citric acid buffer, averaged over 100 frames acquired at 200 ms exposure time, and corrected for the Gaussian laser beam illumination profile. Image size is 512 x 256 pixels (140 x 70 μm).* ***B****) Distribution of integrated fluorescence intensities acquired from (A). The distribution is well fitted by a Gaussian distribution (red curve, R^2 = 0.932). The median value of this distribution (solid vertical line ± median absolute deviation, dashed lines) is taken as the integrated fluorescence intensity per IgG/Fab molecule used in calculating the number of bound IgG/Fab.* ***C****) Median values of the averaged integrated fluorescence intensities, as measured in (B), increases linearly with increasing laser illumination power, indicating that fluorescence read out of individual labeled IgG/Fab is linearly dependent on illumination input.* ***D****) The angle of incidence of the excitation lasers upon the glass-water interface (horizontal axis) was varied to measure the fluorescence intensity (vertical axis) of CR8020af488 IgG bound to H3N2 virus incubated with 130 nM IgG and immobilized upon a glass-supported bilayer. As expected, total internal reflection occurred near 61° relative to the axis perpendicular to the glass surface. Data points are median values ± interquartile range. For angles smaller than 57°, the fluorescence intensity varied only slightly (blue line), indicating a homogenous evanescent field over the length-scale of a virus. The effect of the evanescent wave was apparent for larger incidence angles (red line). The TIR angle was set to ~56° (orange circle) for all experiments to minimize the effect of the evanescent field, but still achieve high signal-to-background recordings ((A) and Figure 3-1A).*

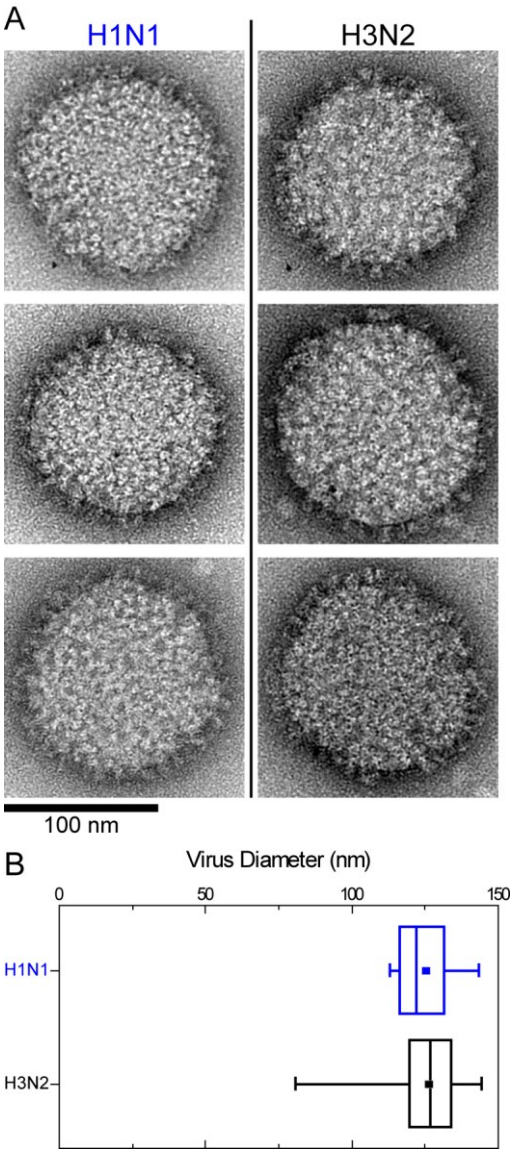

Figure A2-6 *– Electron microscopy of influenza strains H1N1 and H3N2.* ***A****) H1N1 and H3N2 viral strains were negatively stained with uranyl acetate upon a carbon-coated TEM grid and imaged at 45,000x magnification. Both virus strains were spherical in appearance and surface spike proteins were visible. Diameters of the virus particles were measured at the base of the spike proteins and the area of high contrast surrounding the virus, indicated by the yellow circle in the image.* ***B****) Box plot of the diameters of the H1N1 (n = 19 particles, blue) and H3N2 (n = 23 particles, black). The square data point and vertical line inside the box represent the mean and median diameters, respectively. Left and right edges of the box are the 25th and 75th percentiles, respectively, and similarly the left and right whiskers are the 1st and 99th percentiles, respectively.*

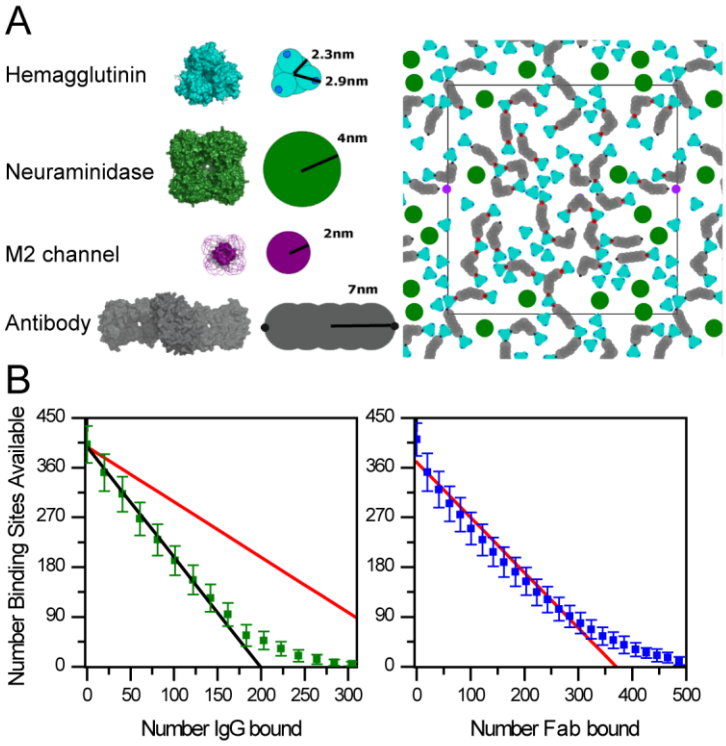

Figure A2-7 *– Monte Carlo simulations of protein packing on a viral surface.* ***A****) Simulations represented relevant proteins as spheres of crystallographic dimensions (left) – HA in cyan, NA in green, M2 proton pump in violet and IgG (or Fab) in gray. The spike protein (HA or NA) density shown corresponds to 8000 spikes/μm^2 (right) with a 7:1 ratio of HA:NA. Epitopes on the HA and paratopes on the antibodies are depicted as dark blue and black circles, respectively. Binding of an epitope by an antibody is indicated with a red circle.* ***B****) The number of sterically available epitopes (vertical axis) diminished as the number of IgG (left, green points) or Fab (right, blue data points) molecules on the viral surface increased. We see that no epitopes are sterically available when ~250-300 IgG or ~500 Fab molecules are bound. Lines having slopes of -2 (black) and -1 (red) are included for visual comparison of the rate of epitope loss upon IgG/Fab binding. For IgG, the data nicely follows the black line until ~175 IgG are bound, suggesting that each IgG binds with both paratopes to remove two binding sites up to this point. Beyond this region the slope is more similar to the red line, suggesting that steric interactions primarily allow single paratope binding by the IgG. A majority of the Fab data is roughly parallel to the red line, as would be expected for single paratope binding and low amounts of steric interactions until high coverage regimes.*

A2.3 Supplementary tables

Table A2-1 – Degree of IgG/Fab labeling and Percent Visualized

Fusion Inhibiting Molecule	Photobleaching		MALDI Mass Spectroscopy					Dyes per Molecule ± SEM	Percent Visualized **
	λ^*	R^2	λ^* (m/z = 1)	R^2	λ^* (m/z = 2)	R^2	$<\lambda>$ ± SEM		
CR6261	4.2 ± 0.1	0.950	6.87 ± 0.03	0.934	6.34 ± 0.03	0.959	6.6 ± 0.2	5.4 ± 0.8	99.5 ± 0.4
CR8020	4.3 ± 0.1	0.958	5.94 ± 0.02	0.955	5.29 ± 0.02	0.978	5.6 ± 0.2	5.0 ± 0.5	99.3 ± 0.3
crF6261	1.9 ± 0.2	0.850	2.73 ± 0.01	0.974	2.86 ± 0.02	0.941	2.80 ± 0.05	2.4 ± 0.3	91 ± 3
crF8020	2.1 ± 0.2	0.881	2.39 ± 0.01	0.964	2.56 ± 0.03	0.853	2.48 ± 0.06	2.3 ± 0.1	90 ± 1

* Results for Poisson distribution ($p(k,\lambda) = A*(\lambda^k)*exp(-\lambda)/\Gamma(k+1)$) fits from Figure A2-3, where *A* was unconstrained to allow for various amplitudes; parameter errors are those reported by Originlab plotting software during chi-squared minimization using mean residual variance and the parameter covariance matrix.

** Percent visualized corresponds to the percentage of labeled IgG/Fab molecules bound with at least one fluorophore. Error is calculated by error propagation for a Poisson distribution.

Table A2-2 – Fit lines and corresponding estimated parameters determined by fitting data points from all experimental runs.

Data & Fit Model	Param	H1N1 CR6261	H1N1 crF6261	H3N2 CR8020	H3N2 crF8020
Hemifusion Efficiency [$E(c)$] Equation 1 * $logit[E(c)] = logit\left[D + \frac{A-D}{1+\left({}^{C}/_{10^{C_0}}\right)^{p}}\right]$	***A***	0 (Constrained)	0.011 (-0.001, 0.023)	0.031 (-0.043, 0.104)	0.033 (0.017, 0.049)
	C_o	1.812 (1.324, 2.299)	2.151 (1.906, 2.397)	2.115 (1.819, 2.412)	1.894 (1.726, 2.063)
	D	0.469 (0.309, 0.628)	0.454 (0.326, 0.582)	0.591 (0.500, 0.682)	0.603 (0.490, 0.716)
	p	-1.048 (-1.424,-0.672)	-2.232 (-3.755, -0.708)	-1.299 (-2.077, -0.521)	-2.245 (-3.460, -1.030)
Number Molecules Bound [$N(c)$] Equation 2 $N(c) = \sqrt{\frac{M \times c}{10^{Z} + c}}$	***M***	154.7 (107.1, 202.2)	248.1 (158.1, 338.1)	130.2 (111.5, 148.9)	492.5 (393.5, 591.6)
	z	2.411 (2.086, 2.736)	2.525 (2.162, 2.887)	1.871 (1.691, 2.050)	1.843 (1.576, 2.111)
Time to Hemifusion [$t(c)$] Equation 3 ** $t(c) = t_0 + \frac{B \times c}{10^{c_1} + c}$	t_o	1.660 (1.546, 1.773)	1.704 (1.531, 1.877)	1.421 (1.318, 1.524)	1.466 (1.416, 1.515)
	B	0.339 (0.207, 0.470)	0.433 (0.212, 0.655)	0.326 (0.184, 0.468)	0.414 (0.353, 0.478)
	C_1	1.461 (0.861, 2.060)	1.937 (0.985, 2.889)	1.982 (1.229, 2.736)	1.657 (1.415, 1.898)

Values in parenthesis represent 95% confidence bounds (lower, upper).

* Confidence intervals for 50% hemifusion efficiency reduction reported in Chapter 3 was calculated using the delta method [7] and the lowest degrees of freedom from the two models.

** Parameters B, C_1, and t_0 were modeled on a $\log_{10}$ scale.

Parameters:

Equation 1 – E represents the proportion fusion events over total events, D and A represent respectively the upper and lower asymptote, p represents a slope factor, C represents the IgG/Fab concentration (in nM) and C_0 represents the inflection point. Equation 2 – N represents the number of bound IgG/Fab defined as (median intensity)/(labeling correction * intensity per molecule), C is the concentration of IgG/Fab (in nM), M is the maximum number of IgG/Fab that can bind and Z is the IgG/Fab concentration where the half-maximum number of molecules is binding.

Equation 3 – t represents the time to hemifusion, t_0 the time to hemifusion without IgG/Fab, B the interval between t_0 and the upper asymptote, C represents the IgG/Fab concentration (in nM) and C_1 represents the IgG/Fab concentration corresponding to the geometric mean of t_0 and B being modeled on a $\log_{10}$ scale.

For stabilization of all models, the hemifusion data without IgG were placed at an infinite low IgG concentration. All statistical analysis for fitting was performed using proc NLMIXED (SAS v9.2). Where necessary (Equation 1, Table A2-2), fitting involved a restriction that the lower asymptote was ≥ 0. Standard errors and 95% confidence limits were estimated using the delta method [7,16].

A2.4 Supplementary references

1. Floyd DL, Ragains JR, Skehel JJ, Harrison SC, van Oijen AM. (2008) Single-particle kinetics of influenza virus membrane fusion. Proc Natl Acad Sci U S A 105: 15382-15387.

2. Delamarche E, Bernard A, Schmid H, Michel B, Biebuyck H. (1997) Patterned delivery of immunoglobulins to surfaces using microfluidic networks. Science 276: 779-781.

3. Xia Y, Whitesides G. (1998) Soft lithography. Annu Rev Mater Sci 28: 153-184.

4. Brandenburg B, Koudstaal W, Goudsmit J, Klaren V, Tang C, et al. (2013) Mechanisms of hemagglutinin targeted influenza virus neutralization. PLoS One In Press.

5. Hedde PN, Fuchs J, Oswald F, Wiedenmann J, Nienhaus GU. (2009) Online image analysis software for photoactivation localization microscopy. Nat Methods 6: 689-690.

6. Findlay JW, Dillard RF. (2007) Appropriate calibration curve fitting in ligand binding assays. AAPS J 9: E260-7.

7. Billingsley P. (1986) Probability and measure. New York: John Wiley & Sons, Inc.

8. Limpert E, Stahel W, Abbt M. (2001) Log-normal distributions across the sciences: Keys and clues. Bioscience 51: 341-352.

9. Ekiert DC, Friesen RHE, Bhabha G, Kwaks T, Jongeneelen M, et al. (2011) A highly conserved neutralizing epitope on group 2 influenza A viruses. Science 333: 843-850.

10. Harris AK, Meyerson JR, Matsuoka Y, Kuybeda O, Moran A, et al. (2013) Structure and accessibility of HA trimers on intact 2009 H1N1 pandemic influenza virus to stem region-specific neutralizing antibodies. Proc Natl Acad Sci U S A 110: 4592-4597.

11. Harris A, Cardone G, Winkler DC, Heymann JB, Brecher M, et al. (2006) Influenza virus pleiomorphy characterized by cryoelectron tomography. Proc Natl Acad Sci U S A 103: 19123-19127.

12. Huisman BA, Bolhuis PG, Fasolino A. (2008) Phase transition to bundles of flexible supramolecular polymers. Phys Rev Lett 100: 188301.

13. Bentz J. (2000) Minimal aggregate size and minimal fusion unit for the first fusion pore of influenza hemagglutinin-mediated membrane fusion. Biophys J 78: 227-245.

14. Reich C, Andruzzi L. (2010) Preparation of fluid tethered lipid bilayers on poly(ethylene glycol) by spin-coating. Soft Matter 6: 493-500.

15. Mashaghi S, van Oijen AM. (2013) A versatile approach to the generation of fluid supported lipid bilayers and its applications. J Mater Chem Submitted.

16. Cox C. (1998) Delta method. In: Armitage P, Colton T, editors. Encyclopedia of Biostatistics. New York: John Wiley. pp. 1125-1127.

Appendix 3 – Fusion Tracker User's Guide

This appendix contains the following information:

A3.1 Getting started with the Fusion Tracker program

A3.2 Input data and user-defined parameters

A3.3 Output data

A3.4 Rejection reason explanations

A3.5 Supplementary references

A3.1 Getting started with the Fusion Tracker program

Information contained in this appendix describes the **Fusion_Tracker** automated data analysis software described in Chapter 4. Inputs required for running the program are described in Section A3.2. Outputs obtained from successful completion of the program are described in Section A3.3. Reasons for rejection of a particle's fluorescence trajectory or any fits performed upon it are described in Section A3.4. It is assumed that readers have a basic understanding of the various MATLAB variable types, such as structures, structure arrays, cells, character strings and arrays. To use the program, the '`Fusion_Tracker`' folder should be saved into a user's main MATLAB folder with all subfolders and files. A recommended directory would be the following: `D:\MATLAB\Fusion_Tracker`. Saved within this main folder are a number of scripts meant to be altered by a user:

- `Files2Analyze.m` – script defining files to be analyzed in batch (see Section A3.2.2).
- `SetImageAnalysisParam.m` – script defining parameters for image analysis and particle detection(see Section A3.2.2.1).
- `SetTrajectoryAnalysisParam.m` – script defining parameters for trajectory selection (see Section A3.2.2.2).

- `Detection_Tracking_Analysis.m` – main analysis script handling data calling and handling.

A3.1.1 Program initialization

Program Initialization is performed by navitating first the current MATLAB folder to the '`Fusion_Tracker`' folder and running the `setup_Fusion_Tracker.m` script from the command line. Execution of this script will open the MATLAB pool of workers that enables parallel processing using the default '*`local`*' cluster profile. It also establishes working directories needed by Fusion_Tracker and adds relevant folders to the MATLAB path.

Once setup has been completed, users should appropriately define the *`Files2An`*, *`imgParam`* and *`anParam`* variables described in Section A3.2. Analysis of all files included in *`Files2An`* can be analyzed by initiating the script `Detection_Tracking_Analysis.m` either from the command line or by running the script from the *Editor* window. FIRST TIME USE: prior to first use of `Detection_Tracking_Analysis.m`, users should ensure that the path specified on approximately line 30 of the code is correct. This path should describe the location of the `.tif` data files that will be subsequently analyzed. Files should be named according to the format described in Section A.3.2.2. Processing time on a single CPU running with a 3.4 GHz clock speed is approximately 400 trajectories analyzed per hour, when extracting only fluorescence information at the locations of particles and not surrounding them.

In sections below describing a number of field names present in structure variables, a short hand forward-slash `/` is utilized to indicate similar field names present in the structure. The forward-slash itself does not constitute part of the field name. For instance, the *`Trajectory`* structure variable has the fields *`ch1analysis`* and the field *`ch2analysis`*; the short hand notation preceding their description is: *`Trajectory.ch1/2analysis`*.

A3.2 Input data and user-defined parameters

A3.2.1 File type and recording orientation

Input files tested thus far are multi-stack `.tif` images containing 16-bit greyscale information recorded with split-field imaging. The tested images were recorded at 60x magnification using an Andor iXon 887-BI EMCCD camera controlled by the Andor imaging software identical to [1]. This camera has 16 μm pixel size, such that one pixel in the image corresponds to 0.267 μm in real space. Time stamp information is automatically extracted from the `.tif` images via the `getandortiffinfo2.m` script written by Milos Popovic. The output of this script is an column vector containing the time stamp in milliseconds for each frame of the `.tif` image. For images recorded using a Hamamatsu C9100-13 EMCCD camera controlled by the MetaVue imaging software, a script is included in the **Fusion_Tracker** package titled `getmetavuetime.m` that can extract time stamp information into a column vector containing the time stamp in seconds for each frame of the `.tif` image. Automatic detection of which script is used to extract time stamp information is not incorporated and instead requires manual selection.

Fluorescence recordings tested thus far having a top-bottom split-field orientation. Channel 1 on the top half-image corresponds to red/orange fluorescence emission for recording of the virion's sulforhodamine B content label. Channel 2 on the bottom half-image corresponds to green fluorescence emission for recording of the virions octadecyl rhodamine 110 lipid label and the pH-detecting fluorescein dye bound to the surface of the glass-supported bilayer.

A3.2.2 User defined parameters

This section lists and describes the parameters **Fusion_Tracker** requires a user to define before analyzing a fusion movie. All user-defined parameters and input data are called by the main program script `Detection_Tracking_Analysis.m` (DTA). Multi-stack image

files in `.tif` format can be processed in batch once the *`Files2An`* variable is defined in `Files2Analyze.m`. Essential to batch mode operation is the definition of all files to be analyzed as well as relevant frame numbers. The *`Files2An`* cell array has one row dedicated to each movie to be analyzed and the following format for its columns:

Column 1	Column 2	Column 3	Column 4	Column 5
File name (include *.tif* extension)	pH drop frame	Number of frames to be analyzed	Type of principal bilayer lipid	Molar percent of cholesterol in bilayer

The file name of column 1 must have the format: *YYMMDD_pH#*, where *YYMMDD* is a six-digit string representing the year (*YY*), month (*MM*) and day (*DD*) the recording was made, *pH* is a two-digit string indicating the pH used to induce fusion and # is the iteration of the given experimental conditions. For instance, the file name 100115_501 indicates the movie was recorded on January 15, 2010 using pH 5.0 fusion inducing buffer and is the first iteration of this experiment type of the day. The pH drop frame from column 2 is an integer value used in defining parts of the image analysis and must be identified before running the **Fusion_Tracker** analysis algorithm. A script is included in the **Fusion_Tracker** package titled `phFind.m` that will read in a defined number of frames from a given recording having the above described file name format and via user interaction will determine the pH drop frame. Column 4 and 5 are character strings representing meta-data about the experiment that is saved into the *`description`* variable (see Section A3.3).

A3.2.2.1 Image analysis parameters

Image analysis parameters are saved in the *`imgParam`* variable defined by the user in the script named `SetImageAnalysisParam.m`. This structure variable has a number of parameters, some optional and others required, that determine how images are handled and corrected, and how particles detected. It is relevant to the image analysis portion of the

programmatic outline of Figure 4-2. The list here describes the field names indicating parameters to be defined in `SetImageAnalysisParam.m`.

`AnalyzeAround`: REQUIRED. Binary value determining if the integrated fluorescence from the pixels surrounding virus particles is extracted.
- A value of '0' indicates the intensity surrounding a particle will not be extracted.
- A value of '1' indicates the intensity surrounding a particle will be extracted.
- If *`BkCorr`* is set to '*`local`*' then it is obligatory for *`AnalyzeAround`* = 1.

`aroundPeak`: REQUIRED. Single value multiplication factor used to determine the radius of the circle centered at each particle that identify which pixels are used for fluorescence signal integration. The radius of the circle is defined by its 2D Gaussian width as: σ_w.

`BkCorr`: REQUIRED. String array having one of the two permitted values below. It determines how fluorescence background will be measured and removed from the integrated fluorescence signals extracted from each frame of a movie. It is used in `ExtractIntensity.m`.
- '*`global`*' indicates that after an image is corrected for electronic offset and the illumination profile, the peak value of the distribution of pixel intensities in the flattened image is set as the global fluorescence background. This global background is subtracted from the entire flattened image such that the peak of the pixel intensity distribution is located at zero. Once this operation is carried out, fluorescence signals comprising the fluorescence trajectories are extracted.
- '*`local`*' indicates that for each particle being analyzed, the average value of the pixels identified inside the doughnut ring surrounding a particle is subtracted from the each pixel lying within the doughnut center. The pixels corrected for average local background lying within the center of the doughnut are then used for extraction of the integrated fluorescence signal comprising the fluorescence trajectories. This option is particularly useful if the intensity extraction scripts are adapted to obtain photobleaching traces.

`edge`: REQUIRED. Two-element array defining the number of pixels away from the edges of the half-images for each channel wherein particles are not identified.
- Format: *[x_edge, y_edge]* where x = columns, y = rows.

`dxdy`: OPTIONAL. Two-element array that defines the rigid 'x' and 'y' ('column' and 'row') translations necessary for moving from channel 1 to channel 2. It is set as channel_2 = channel_1 – dxdy. Design intent: *`dxdy`* should be first correctly identified by the program automatically before a user attempts to initialize its value. Its definition serves as a programmatic override and is intended to be used only when the automated detection of *`dxdy`* fails.
- If defined, it must be a two-element array of values in the order: [column_translation, row_translation].
- If undefined, then it should be an empty array and will be determined by the script `ChannelRegistration.m`.

`frames`: REQUIRED. Three-element array containing information about the frames to be used for particle tracking.
- Format is *[start_frame end_1 end_2]*.

From *start_frame* to *end_1*, the particles are tracked in frames separated by *step_1* defined below. From *end_1* to *end_2* particles at tracked in frames separated by *step_2* defined below.
- The second element *end_1* can be defined as the pH drop frame plus a value.

frames_id_particles: REQUIRED. Two-element array that will define the frames to be used for localizing the final, fixed positions of the virus particles after pH drop. The values of the array are the number of frames post-pH drop and pre-fusion that localization should occur.

margins: OPTIONAL. Two-element array that defines the number of pixels at the edges of the half-images for each channel that lie outside the co-registered image. Design intent: *margins* should be first correctly identified by the program automatically before a user attempts to initialize its value. Its definition serves as a programmatic override and is intended to be used only when the automated detection of *margins* fails.
- If defined, it must be a two-element array of values in the order:
  [column_margin, row_margin]
- If undefined, then it should be an empty array and will be determined by the script `ChannelRegistration.m`.

minTrackLength: REQUIRED. Two-element vector whose values are in units of frames. These are the minimum number of frames that a particle tracking trajectory must be followed over if it is to be accepted and assigned to one of the particles identified in *centroid_fix*.
- Format: *[length_step_1 length_step_2]*. Suggestion: *length_step_1* > *length_step_2*
  The first value is the tracking trajectory length during high temporal resolution tracking at the beginning of a movie between *start_frame* and *end_1* of *frames*. The second value is the track length required when following particles between *end_1* and *end_2* of *frames* to correct for microscope drift.

movethresh: REQUIRED. Single value threshold value in units of pixels that is the minimum number of pixels a particle must move while rolling between *frames* *start_frame* and *end_1* if it is to be counted as rolling. Particles surpassing this minimum displacement have their distance trajectories subjected to MLE-based fitting for determination of the frame when they stop rolling.

multfact: REQUIRED. Two-element vector defining the multiplication factor used when setting the threshold for particle detection after discoidal image filtering. The threshold is calculated as $\mu+m*\sigma$ where μ and σ are the average and standard deviation of the pixel intensities following discoidal filtering, respectively, and *m* is the channel-appropriate multiplication factor.
- Format: *[multfact_channel_1 multfact_channel_2]*

orientation: REQUIRED. Field defining a character string that sets the recording orientation of the movie.
- Two values are permitted:
  '*TopBottom*' where channel 1 is on the top half-image channel 2 is on the bottom half-image.
  '*LeftRight*' where channel 1 is on the left half-image and channel 2 is on the right half-image.

`outsidePeak`: REQUIRED. Single value additive factor that is added to the `aroundPeak` field when determining the outer radius of the doughnut used to extract fluorescence intensity surrounding a particle. For example, if the `aroundPeak` field is set to 2 and `outsidePeak` is set to 1, then the doughnut used for signal integration to set `TrajectoryAround` would have an inner radius 2*σ_w and an outer radius 3*σ_w.

`pixelAccuracy`: OPTIONAL. Single value used by `dftregistration.m` [2]. Default value is 0.1.

`radius_link`: REQUIRED. Single value distance in pixels that is the maximum distance allowed for assigning a tracking trajectory to the location of a particle's fixed position, as determined in the frames `imgParam.frames_id_particles` and save in the `centroid_fix` variable.

`radius_track`: REQUIRED. Single value distance in pixels that is the maximum distance between a particle in frame *f* and in frame *f+step* allowed for linking the two localization positions together into a trajectory during particle tracking. The same value is used both when linking localizations to follow rolling viruses (*step_1*) or to correct for drift (*step_2*).

`sigmult_rej`: REQUIRED. Single value multiplication factor, *m*, used to remove particles having a fitted 2D Gaussian width that is too large or too small. The mean, μ, and standard deviation, σ_w, of the distribution of 2D Gaussian widths are calculated in both the 'x' columns and 'y' rows directions. Particles having their width in either 'x' or 'y' larger than μ+*m**σ_w are removed.

`step`: REQUIRED two-element array defining the inter-frame step size used in particle tracking. This variable determines the temporal resolution with which particles are tracked in the frames of the movie defined by `frames` above.
- Format: *[step_1 step_2]*, where *step_1* < *step_2*
  > From *start_frame* to *end_1* of `frames`, images separated by *step_1* frames are used, first for particle localization, then for linking of particle locations to create tracking trajectories of high temporal resolution and follow rolling viruses.
  > From *end_1* to *end_2* of `frames`, images separated by *step_2* frames are used, first for particle localization, then for linking particle of locations to create tracking trajectories that compensate for microscope drift.

A3.2.2.2 Trajectory analysis parameters

Trajectory analysis parameters are saved in the `anParam` variable defined by the user in the script named `SetTrajectoryAnalysisParam.m`. This structure variable has a number of parameters, some optional and others required, that determine how extracted fluorescence trajectories are handled and smoothed. It also serves to define aspects critical to the Boolean decision function outlined in Figure 4-2B. It contains two nested substructures that determine

how the trajectories from the two channels are handled and selected for either depicting fusion events or not. The list here describes, first, the field names indicating parameters used on trajectories from both channels, then the channel-specific substructures *ch1* and *ch2* are described in detail. All parameters are defined in the script:

`SetTrajectoryAnalysisParam.m`.

A3.2.2.2.a – parameters common to trajectory analysis of both channels:

alphaval: REQUIRED. Single value between 0 and 1 that sets the confidence/significance level, α, used during maximum likelihood estimator calculation during trajectory fitting. This value also specifies the theoretical false-positive limit when determining the statistical significance of a fit over the null, linear fit.

bleedThruFrac: REQUIRED. Single value between 0 and 1 that represents the fraction of the short wavelength fluorescence emission intensity that bleeds through into the long wavelength detection channel.

maxiter: REQUIRED. Single value determining the maximal number of fitting iterations to be performed when searching for maximal Q_S values during the MLE-based trajectory selection. This parameter greatly determines the processing time required to determine optimal fitting parameters that are statistically significant. During testing, a value of 10 worked well to identify good fitting domains.

niter: REQUIRED. Single value determining the maximal number of iterations to be performed when changing sliding window sizes while searching for intensity up- or down-shots using the SGolay and sliding window difference filters (see Chapter 4).

noiseExlFr: REQUIRED. Single value indicating how many frames to use when defining the sampling frequency for Fourier filtering of trajectories to smooth them. For instance, *noiseExlFr* = 3 will define a cutoff frequency of 1/3 frames. See `fftf.m` for more information [3].

numfrq: OPTIONAL. Single value indicating how many frequencies to use when reconstructing a trajectory after Fourier filtering. Define an empty array if no value is desired. See `fftf.m` for more information [3].

numcores: REQUIRED. Character string containing the number of processing cores (CPU's) present on the computer being used for analysis.

paramconf: REQUIRED. Single value between 0 and 1 that determines the percent confidence intervals for the MLE-determined fitting parameters. For instance, a value of 0.9 determines the 90% confidence intervals for all fit parameters calculated by the program.

pthresh: REQUIRED. Single value between 0 and 1 that determines the *p*-value required for passing the *t*-test testing for the "Normalcy" of the signal noise distribution. Rejection of

the *t*-test null hypothesis with a *p*-value less than `1-pthresh` results in particle rejection for not having a sufficiently Normal noise profile.

`shortWavelength`: REQUIRED. Character array of strings having one of two values that dictates which of the two emission channels corresponds to the shorter wavelength emission that will bleed thru into the long wavelength channel.
- Permitted values: '`ch1`' or '`ch2`'.

`SNsite`: OPTIONAL. Single value dictating the signal-to-noise that a particle fluorescence trajectory is required to have in the period starting with the pH drop and ending of particle identification, *i.e.* in the frames determined by: [`pHdrop imgParams.frames_id_particles(2)`]. If a value is not set, then the user will be prompted during analysis by the script `SignalIntensitySelection.m` to determine a value by selecting it from the distribution of signal-to-noise values measured from trajectories of the two channels.

`stepsz`: REQUIRED. Single value determining the step size increases in the smoothing windows between iterations when finding potential up- and down-shots using the SGolay and sliding window difference filters. Together with the `winfilt_st` value set for each channel, the maximal smoothing window size that will be tested for intensity up- or down-shots is: `winfilt_st` + `stepsz` * `niter`.

Channel-specific parameters contained in the `ch1` and `ch2` substructures are used when compiling the results of the MLE-based fitting. With the exception of `winfilt_st`, these values can be altered to allow for re-analysis of trajectories without having to pass through a second round of MLE-based fitting.

A3.2.2.2.b – parameters varying between the channels during trajectory analysis:

`deqlim`: OPTIONAL. Two-valued array placing absolute limits on the permitted values of the dequenching time, p_4, found for dequenching fits of Equation 4-1.
- Format: *[minimum maximum]*

`dissiplim`: OPTIONAL. Two-valued array placing absolute limits on the permitted values of the diffusion constant, p_4, found for dequenching fits of Equation 4-2.
- Format: *[minimum maximum]*

`mtfc`: REQUIRED. Two-element array setting the multiplication factors used when determining large intensity up- and down-shots during sliding window filtering by the SGolay and sliding window difference filters.
- Format: *[up-shot_multiplication_factor, down-shot_multiplication_factor]*

`

ndeqfr: OPTIONAL. Two-valued array setting the maximum and minimum number of frames a dequenching event is allowed to occur over. It is an alternative method for placing upper and lower limits on the dequenching time, p_4. Values set here are converted into limits by multiplying their values by the elapsed time between frames: dequench limit = *ndeqfr**time_between_frames.
- Format: *[minmum maximum]*.

ndissipfr: OPTIONAL. Two-valued array setting the maximum and minimum number of frames a dissipation event is allowed to occur over. It is an alternative method for placing upper and lower limits on the diffusion constant, p_4. Values set here are converted into limits by first calculating the average radius used for intensity signal integration: *avg_r = imgParam.aroundPeak*mean(Sigma(:))*0.267*, with units resulting in μm. The diffusion constant limits = *avg_r*^2/(4*time_between_frames).
- Format: *[minmum maximum]*.

readout: REQUIRED. Character array containing one of two values describing the interpretation of the signal in each channel.
- '*Hemifusion*' indicates the ascribed channel depicts the lipid signal of the dual labeled virus.
- '*Pore Formation*' indicates the ascribed channel depicts the content signal of the dual labeled virus.

signalType: REQUIRED. Character array containing one of four values indicating the type of events that will be detected in the trajectories of the ascribed channel:
- '*dequench_dissipation*' indicates the trajectories will be scanned for both intensity up-shots corresponding to dequenching and intensity down-shots corresponding to dissipation.
- '*dissipation*' indicates the trajectories will be scanned for both intensity up-shots corresponding to dissipation only.
- '*dequenching*' indicates the trajectories will be scanned for both intensity up-shots corresponding to dequenching only.
- '*no_analysis*' indicates the trajectories will not be analyzed to detect membrane fusion signals

SNthresh: REQUIRED. Two-element array setting the required signal-to-noise thresholds that must be surpassed by fits of dequenching with Equation 4-1 and from fits of dissipation from Equation 4-2. Signal-to-noise calculations are described for the *SN* field of the *Trajectory* variable in Section 3.3.
- Format: *[up-shot_S/N_threshold, down-shot_S/N_threshold]*.

winfilt_st: REQUIRED. Single value setting the starting window size for SGolay and sliding difference window filtering when identifying intensity up- and down-shots. Smaller values are needed for detecting short-lived events, larger values will smooth over short-lived events to detect only longer-lived events.

A3.3 Output data

Upon completion of the DTA script running the entire **Fusion_Tracker** algorithm, a MATLAB file is saved titled *filename*_automated_analysis.mat located in the folder containing the .tif file analyzed. This file contains all of the variables saved during analysis. The list below describes the variables saved in the .mat file along with their format. If a user wishes to re-compile the results of an analysis using different trajectory analysis parameters (see Section A3.2.2.2), then this .mat file must first be loaded into the MATLAB working memory. Once loaded, the trajectory analysis parameters can be changed and the results compiled using the Compile_fit_parameters script, which can be found on in the 'goto == 4' section in the DTA script. Running this command will alter the *Trajectory* variable in a reversible fashion; specifically the reasons some fits are rejected is updated in accord with the trajectory analysis parameters, but no fits are removed or overwritten. The shorthand '*nchannel*' is used in the list that follows to indicate the number of channels analyzed.

A3.3.1 List of variables saved by the **Fusion_Tracker** algorithm:

anParam:
- Contains parameters used during trajectory selection
- 1x1 Structure array; fields described in *User Defined Parameters* section

centroid_fix
- Contains locations of the final (fixed) particle positions determined in the *frames_id_particles* field of *imgParam*. It is used to link movement trajectories with particles to be used for fusion detection.
- Double array containing location for each particle each row. Format:
  column 1 = channel 1 'x' position; column 2 = channel 1 'y' position;
  column 3 = channel 2 'x' position; column 4 = channel 2 'x' position.

Centroid
- Contains information about particle tracking ONLY during the initial part of the recording when tracking is performed with HIGH temporal resolution
- Structure array *npart* x *nchannel* in dimensions with each row corresponding to a particle and each column corresponding to a channel analyzed. Fields present in the structure for each particle in each channel are:
  > *xyCoord*: contains the (x,y) or (column, row) positions of the virus during tracking. Column 1 = frame; column 2 = x/column position, column 3 = y/row position

> movement: binary information, 1 = particle moved and was tracked, 0 = particle did not move.
> *RfrmInit*: data of distance from a particle's initial position during tracking; only present for particles having movement = 1 and whose stop frame was recorded.
This field is a structure containing the fields:
>> *fr_data_fit*: Array containing data used to determine stop frame. Column 1 = frames, column 2 = distance of particle from its initial position, column 3 = sigmoidal fit to the data of column 2.
>> *param*: Sigmoidal fit parameters (Equation 4-1). Array having row 1 = fit parameters p_1, p_2, p_3, p_4; row 2 = fit parameter lower bound estimates; row 3 = fit parameter upper bound estimates
> *R2final*: data of distance from a particle's final position during tracking; only present for particles having movement = 1 and whose stop frame was recorded.
This field is a structure containing the fields:
>> *fr_data_fit*: Array containing data used to determine stop frame. Column 1 = frames, column 2 = distance of particle from its final position, column 3 = sigmoidal fit to the data of column 2.
>> *param*: Sigmoidal fit parameters (Equation 4-1). Array having row 1 = fit parameters p_1, p_2, p_3, p_4; row 2 = fit parameter lower bound estimates; row 3 = fit parameter upper bound estimates

CentroidDrift
- Contains information about particle tracking ONLY during the last part of the recording when tracking is performed with LOW temporal resolution
- Structure array *npart* x *nchannel* in dimensions with each row corresponding to a particle and each column corresponding to a channel analyzed. Fields present in the structure for each particle in each channel are:
> *xyCoord*: contains the (x,y) or (column, row) positions of the virus during tracking. Column 1 = frame; column 2 = x/column position, column 3 = y/row position
> *movement*: binary information, 1 = particle moved and was tracked, 0 = particle did not move.

CentroidTracked
- Contains information about particle tracking throughout the recording and is an aggregation of the *xyCoord* and movement data stored in the *Centroid* and *CentroidDrift* variables. As well, it stores information about the number of pixels used during intensity integration, which allows for calculation of average pixel intensity in the script SignalIntensitySelection.m.
- Structure array *npart* x *nchannel* in dimensions with each row corresponding to a particle and each column corresponding to a channel analyzed. Fields present in the structure for each particle in each channel are:
> *xyCoord*: contains the (x,y) or (column, row) positions of the virus during tracking. Column 1 = frame; column 2 = x/column position, column 3 = y/row position
> *numPixIntIn*: number of pixels lying within the circle defined for a particle during intensity integration. The circle is centered at the particle and having a radius defined by the particle's Gaussian width: *imgParam.aroundPeak*$*\sigma_w$. Data used in SignalIntensitySelection.m
> *numPixIntOut*: if *imgParam.AnalyzeAround* is set to '1', then this field appears and records the number of pixels used for integration of the *TrajectoryAround* signal intensity. The pixels here are those lying within a doughnut centered at the particle and

having an inner radius defined as for numPixIntIn and an outer radius defined by: *imgParam.outsidePeak*σ_w. Pixels used for signal integration within the circle are excluded here. Data used in `SignalIntensitySelection.m`.

description
- Structure array containing meta-data about the fusion recording.
- Current field names are:
  > `name`: includes the file name of the recording
  > `lipid`: type of lipid comprising the target bilayer, set in `Files2Analyze.m`.
  > `pH`: acidity of the fusion buffer used to initiate fusion, extracted from the filename.
  > `ch`: molar percent of cholesterol in the target bilayer, set in `Files2Analyze.m`.

elecoff
- Pixel value electronic offset specific to the camera and EM gain settings. Its value is set either by the user or determined as the minimum value present in the initial frames used to determine *centroid_fix*.

filename
- Character string describing the full name of the file to be analyzed including file type extension.

illumProf
- Gaussian-approximated illumination profile of the excitation beam. The maximum value at its peak is one and the profile is used to flatten the images by dividing it into each frame used for trajectory intensity extraction.

image
- Image of the fusion movie averaged over the frames dictated by the user-defined, post-pH drop frames set by the input variable *imgParam.frames_id_particles*.

imgParam
- Structure containing all the user-defined input parameters relevant for image analysis.

mergedDiscMask
- Binary mask resulting from discoidal filtering [4] and thresholding of the *image* variable. Pixels in the filtered image lying above the threshold are ones, those below are zeros.

mergedImage
- Overlay of channel 1 and channel 2 from image after registration using the offset found by `dftregistration.m`

mergedRGB
- Three color RGB image of the two color *mergedImage* variable where channel 1 is in blue and red (thus magenta) and channel 2 is in green.

nframes
- Number of frames in the file specified by *filename* to be included for fluorescence trajectory extraction and tracking.

npart

- Number of particles detected and used in the fusion analysis.

pHdrop

- Frame of the fusion recording where the fluorescein signal is set to have disappeared. Set by the user in `Files2Analyze.m`.

Results

- Structure variable produced by `Compile_fit_parameters.m` that contains the results of compiling all the kinetic information resulting from fitting and trajectory selection. Structure field names are the following:
  - > *rejectPart*: *npart* x *nchannels* array, column 1 for channel 1, column 2 for channel 2. A zero value indicates the particle was not rejected in the given channel. Other values indicate the fits for the particle in the given channel were rejected.
  - > *rejectPartReason*: *npart* x *nchannels* cell array containing a brief description why a particle was rejected. See Section A3.4 for explanations.
  - > *rejectDeq*: *npart* x *nchannels* array, 0 indicates the dequenching fit was not rejected, Other values indicate the dequenching fits were rejected
  - > *rejectDeqReason*: *npart* x *nchannels* cell array containing a brief description why a dequenching signal for a particle was rejected. See Section A3.4 for explanations
  - > *rejectDissip*: *npart* x *nchannels* array, 0 indicates the dissipation fit was not rejected, Other values indicate the dissipation fits were rejected
  - > *rejectDissipReason*: *npart* x *nchannels* cell array containing a brief description why a dissipation signal for a particle was rejected. See Section A3.4 for explanations
  - > *kinetics*: Structure containing kinetic data in the following structure fields
    - >> *DeqWidths*: *nchannels* x 3 cell array containing the time, in seconds, for the width of the dequenching events as measured by the p_4 parameter of Equation 4-1. Column 1 contains all p_4 values, Column 2 contains the p_4 values for the selected particles and Column 3 the p_4 values for the rejected particles. Each cell contains an array with two columns. Column 1 is the dequenching width values and column 2 is the particle number corresponding to the dequenching width value in column 1.
    - >> *DiffConst*: *nchannels* x 3 cell array containing the two-dimensional diffusion constant, in μm^2/second, for the signal dissipation events as measured by the p_4 parameter of Equation 4-1. Column 1 contains all p_4 values, Column 2 contains the p_4 values for the selected particles and Column 3 the p_4 values for the rejected particles. Each cell contains an array with two columns. Column 1 is the dequenching width values and column 2 is the particle number corresponding to the dequenching width value in column 1.
    - >> *deqtime*: *npart* x *nchannels* array containing the recorded dequenching times. A *NaN* value is present for rejected dequenching fits.
    - >> *dissiptime*: *npart* x *nchannels* array containing the recorded dissipation times (p_3 of Equation 4-2). A *NaN* value is present for rejected dissipation fits.
    - >> *deq2dissiptime*: *npart* x *nchannels* array containing the elapsed time between a dequenching and dissipation event within a trajectory in a single channel. NaN value indicates no time was detected.
    - >> *HPdeq2deqtime*: *npart* x 1 array containing the elapsed time between a hemifusion dequenching event and pore formation dequenching event in the two channels corresponding to a particle. *NaN* value indicates no time was detected. Field not present if dequenching was not an option for both channels. Negative values indicate the pore formation event occurred first.

>> *HPdissip2dissiptime*: *npart* x 1 array containing the elapsed time between a hemifusion dissipation event and pore formation dissipation event in the two channels corresponding to a particle. *NaN* value indicates no time was detected. Field not present if dissipation was not an option for both channels.

>> *HPdeq2dissiptime*: *npart* x 1 array containing the elapsed time between a hemifusion dequenching event and pore formation dissipation event in the two channels corresponding to a particle. *NaN* value indicates no time was detected. Field not present if dequenching was not an option for the hemifusion channel and dissipation was not an option for the pore formation channel. Negative values indicate the pore formation event occurred first.

>> *HPdissip2deqtime*: : *npart* x 1 array containing the elapsed time between a hemifusion dissipation event and pore formation dequenching event in the two channels corresponding to a particle. *NaN* value indicates no time was detected. Field not present if dissipation was not an option for the hemifusion channel and dequenching was not an option for the pore formation channel. Negative values indicate the pore formation event occurred first.

>> *stopframes*: array containing the frames detected for viruses to stop rolling.

> *plotdata*: cell array containing information for plotting the data contained in the aforementioned *kinetics* field. Each row constitutes one of the field names listed, in order, above in *kinetics*. Column 1 is the data corresponding to each field in *kinetics*, separated into channels where appropriate, Column 2, 3 and 4 indicated the title, 'x' label and 'y' label of a plot showing the data in Column 1, Column 5 indicates any user-defined limits on the p_4 fit parameters, absence of limits is indicated as *[0, Inf]*.

Sigma

- Width, σ_w, in pixels for each particle as determined by fitting the intensity peak with a two-dimensional Gaussian function
- Format is a double array, each row corresponding to a particle, column 1 being the width along the 'x' direction and column 2 being the width along the 'y' direction.

stopframes

- Cell array containing information about the detected frames where individual virus particles stopped rolling as a result of buffer drag. The first row indicates the information contained in each column: channel of detection, particle number, stop frame detected for the distance trajectory relative to start (column 3) or end (column 4) position, and the average of the detected stop frames.

time

- *nframes* x 1 array containing the time stamp, in seconds, corresponding to each frame analyzed in the fusion recording. Currently, this is detected with the script `getandortiffinfo2.m` but can also be determined with the included script `getmetavuetime.m`.

trackmask

- Image created during particle tracking that is a summation of all binary masks used for particle tracking during the first round of particle tracking at high temporal resolution. Tracking consists of discoidally filtering and thresholding each frame to obtain a binary 0/1 mask and identifying particles. *trackmask* image is the sum of all masks generated, so each pixel value will range from 0 to *imgParam.frames(2)*. It can be used as the base

image for plotting the trajectories determined for the particles and was used to create Figure 4-4.

`Trajectory`

- Structure created by the `ExtractIntensity.m` script and modified by both the `Analyze_Trajectories.m` and the `Compile_fit_parameters.m` scripts. It contains the following field names:
  - > *`ch1`* or *`ch2`*: *`nframes`* x *`npart`* array containing the raw, integrated fluorescence trajectories acquired from particle locations in either channel 1 or channel 2. Pixels used for signal integration are those lying within a circle centered at the particle having a radius defined by the particle's Gaussian width: *`imgParam.aroundPeak`*$*\sigma_w$. These values are corrected for electronic offset, illumination profile and fluorescence background. The channel designated to contain fluorescence emission of the lower wavelength is also corrected for inter-channel cross-talk/bleed-thru.
  - > *`readout`*: Structure containing meta-information about what the signals in channel 1 and channel 2 are interpreted as. Valid values are 'Pore Formation' or 'Hemifusion'.
  - > *`signalType`*: Structure containing the type of signal present in channel 1 and channel 2. Valid values are 'dissipation', 'dequenching', 'dequench_dissipation' or 'no_analysis'.
  - > *`ch1analysis`* or *`ch2analysis`*: *`npart`* x 1 structure array where information about trajectory selection and fitting results are saved for each particle (rows). Contents vary depending on input parameters and determined analysis type. Data stored in the following field names:
    - >> *`trajectory`*: *`nframes`* x 2 array containing the trajectory for the particle in question. Column 1 is the trajectory after intensity normalization and Column 2 is the result of Fourier filtering the raw trajectory.
    - >> *`deqch`*: Structure containing information about <u>each</u> dequenching peak that was fit using the following field names:
      - >>> *`param`*: 3 x 4 array containing the fit parameter values (row 1) for each of the four parameters (columns 1-4) in Equation 4-1. Row 2 is the lower bound for each parameter and Row 3 is the upper bound for each parameter.
      - >>> *`conf`*: Residuals from the dequenching model fit to the raw data are fitted with a Normal distribution. The R^2 value calculated for this fit is calculated here. It is obsolete and not used when compiling kinetic results.
      - >>> *`R2val`*: R^2 value resulting from the fit of the dequenching model to the raw data. It is obsolete and not used when compiling kinetic results.
      - >>> *`fit`*: array containing the fitting domain used during MLE-based fit testing and can be used for plotting the determined fit. Column 1 is the time, column 2 is the fitted intensity values.
      - >>> *`initGuessFrame`*: column vector containing the frame number (column 1) used to obtain the initial guesses for MLE-based fitting. Column 2 and 3 are the lower and upper estimates for the guess frame. Column 4 is the signal-to-noise measured at the initial guess point.
      - >>> *`rejectReason`*: character string explaining why the particular dequenching fit was rejected. See Section 3.4 for further details.
      - >>> *`slope`*: dequenching fit p_4 parameter with lower and upper confidence bounds, extracted from the *`param`* field.
      - >>> *`Delta`*: Test to ensure the fitted parameters correspond to dequenching. Row 1 is $p_2 - p_1$, Row 2 is $p_{2\_lower\_bound} - p_{1\_upper\_bound}$, Row 3 is $p_{2\_upper\_bound} - p_{1\_lower\_bound}$. If Row 2 is negative, then the fit is

determined to be not dequenching.

>>> *SN*: signal-to-noise for the fit, determined as *Delta* row 1 divided by *noise*.

>> *dissip*: Structure containing information about each intensity down-shot that was fit as a dissipation signal using Equation 4-2. Saved data is identical to the *deqch* field, with the exception that the *slope* field is absent and these fields are defined:

>>> *Diffusion*: dissipation fit p_4 parameter with lower and upper confidence bounds, extracted from the *param* field.

>>> *Delta*: Test to ensure the fitted parameters correspond to signal dissipation. Row 1 is $p_1 - p_2$, Row 2 is $p_{1\_lower\_bound} - p_{2\_upper\_bound}$, Row 3 is $p_{1\_upper\_bound} - p_{2\_lower\_bound}$. If $p_{1\_lower\_bound}$ is less than Delta Row 3, then the fit is determined to be not dissipating.

>>> *SN*: signal-to-noise for the fit, determined as p_2 divided by *noise*.

>> *noise*: Signal noise determined for the normalized data contained in column 1 of the *trajectory* field. Its value is set by `getSignalNoise.m` and results from a two-step process. A domain of the normalized data domain is selected starting with *imgParam.frames_id_particles(1)* and ending with either: a) the first initial guess point or b) 30 frames after the *frames_id_particles(1)* field, whichever is larger. This domain is fit to a straight line, which is subsequently subtracted from the normalized intensity data to obtain the corresponding residuals. These residuals are binned and fit by a normal distribution. The width of residuals' distribution is set as the signal noise for the particle. A minimum of 30 frames are utilized to ensure a minimum of 5 bins are available in the distribution.

>> *reject*: binary entry with 0 = not rejected, 1 = rejected particle.

>> *rejectPartReason*: Character string describing why the particle in question was rejected. See Section 3.4 for further details.

`TrajectoryAround`

- Intensity here is optionally recorded if *imgParam.AnalyzeAround* is set to '1' or if the background fluorescence correct method is set to '*local*.' Otherwise it is an empty array.
- Structure containing the integrated fluorescence intensity information from the doughnut region immediately surrounding each virus particle. The pixels used for integration are those lying with in a doughnut ring circle centered at the particle and whose radii are defined by the particle's Gaussian width. The inner radius is: *imgParam.aroundPeak*$*\sigma_w$ and the outer radius is *imgParam.outsidePeak*$*\sigma_w$.
- Fluorescence data is saved in field names: *ch1* or *ch2*, each being arrays of dimension *nframes* x *npart*.
- Data saved in this variable is used only in the scripts `ExtractIntensity.m` and `SignalIntensitySelection.m`. It is also corrected for inter-channel signal bleed-thru from the shorter wavelength channel to the longer wavelength channel. It is not normalized.

`TrajectoryAroundOrig`

- This variable is the raw data saved in *TrajectoryAround* prior to correction of inter-channel bleed thru.
- Intensity here is optionally recorded if *imgParam.AnalyzeAround* is set to '1' or if the background fluorescence correct method is set to '*local*.' Otherwise it is an empty array.

`TrajectoryOrig`

- This variable is the raw integrated fluorescence information saved in Trajectory prior to

correction of inter-channel bleed thru and only contains fields ch1 and/or ch2. No analysis is performed using this variable.

A3.4 Rejection reason explanations

The Boolean decision function of Figure 4-2B describes the process of separating fluorescence trajectories showing behavior consistent with fusion from those trajectories that do not meet this criteria. Selection of trajectories involves the rejection of the entire trajectory for a particle, or the rejection of some fits to portions of a trajectory and acceptance of others. When a particle trajectory or a fit within a trajectory is rejected, the program reports a reason justifying the rejection. These reasons are saved in the *rejectPartReason* field of *Trajectory* or in the *rejectReason* field of the *deqch* and *dissip* substructures of *Trajectory*, respectively, as described in section A3.3. Included below are lists describing these reasons, the script within the program where rejection occurred and what parameter governs that rejection step. When describing the script responsible for rejecting a trajectory or fit, the abbreviation AT is used for scripts called by `Analyze_Trajectories.m`. Within AT are three main analysis scripts that call a number of the of analysis subroutines responsible for trajectory fitting and rejection: `analyze_deq_dissip.m`, `analyze_deq.m` and `analyze_dissip.m`. These three trajectories look for dequenching and dissipation, or dequenching or dissipation only, respectively. If a script is not overtly included in AT, it will be included in one of these three scripts.

A3.4.1 List of reasons why a particle's entire trajectory can be rejected:

"*Dissip b/4 Deqch*"

- Originating script: `Compile_fit_parameters.m`
- Relevant Parameters:
  Not under direct parameter control. Given the model of fusion that is presumed to occur, namely that hemifusion precedes full fusion (pore formation), it is not allowed that a dissipation signal precedes a dequenching event within a single trajectory in a

single channel. It is allowed for a dissipation event in one channel to precede a dequenching/dissipation event in the second channel.

"*Fitted up/down-shots rejected*"

- Originating script (AT): `analyze_deq_dissip.m`, `analyze_deq.m` or `analyze_dissip.m`
- Relevant Parameters:
  Not under direct parameter control. This message indicates that all MLE-based fittings of possible event points were rejected. See *`rejectReason`* under the *`deqch`* and *`dissip`* fields in *`Trajectory`* for the particles in question.

"*found no up/down-shots*"

- Originating script (AT): `getIncDecIdx.m`
- Relevant Parameters:
  1) *`anParam.ch1/2.mtfc`* – larger values raise the threshold that the rate of intensity change must surpass if a point in a trajectory is to be considered a possible intensity up- or down-shot. See Figure 4-5 for reference of how these events points are detected by the sliding window filters.
  2) *`anParam.alphaval`* – a *t*-test is performed on the distribution of intensities immediately before and after a possible intensity up- or down-shot to test for statistical significance of the difference between them. If the null hypothesis is rejected with a *p*-value less than *`anParam.alphaval`*, then the event point is rejected and not used for MLE-based fitting. During testing, it was found that more spurious event points were rejected at this point of the decision function if the value of *`alphaval`* was used instead
  of the pthresh value, which is typically lower.
  > Future expansion suggestion: include an additional parameter to define this threshold separately from *`alphaval`*.
  3) *`anParam.ch1/2.winfilt_st`* – if too large a value is set as the first sliding window filter size, then short-lived events may be washed out.

"*Lims Dqch$_w$*" or "*Lims D$_{2D}$*" or "*Lims Dqch$_w$ Lims D$_{2D}$*"

- Originating script: `Compile_fit_parameters.m`
- Relevant Parameters:
  `anParam.ch1/2.ndeqfr/ndissipfr/deqlim/dissiplim` – These parameters set permitted values for the p_4 parameter of Equations 4-1 or 4-2, whichever is relevant for the type of signal being fit. See description of these parameters in Section A3.2 for more information.

"*Multiple good fits*"

- Originating script: `Compile_fit_parameters.m`
- Relevant Parameters:
  Not under direct parameter control. Only a single dequenching event and a single dissipation event is permitted per trajectory. If more than one type of event is detected, then all fits of that event type are rejected. If more than one dequenching and more than one dissipation events are detected, then the trajectory itself is rejected.

"*non-Gaussian signal noise*"

- Originating script (AT): `getSignalNoise.m`
- Relevant Parameters:

anParam.pthresh – as described in the definition of this parameter value and the description of the *Trajectory.ch1/2analysis.noise* output, a portion of the normalized trajectory data up to the first possible event frame is taken, fit with a line and the residuals of the linear fit modeled by a Normal distribution. If a *t*-test performed on the residuals from the Normal distribution modeling rejects the null hypothesis with a *p*-value lower than *1-anParam.pthresh*, then the particle trajectory is rejected.

"*Poor Dqch & Dssp S/N*"

- Originating script: `Compile_fit_parameters.m`
- Relevant Parameters:
  anParam.ch1/2.SNthresh – This parameter describes the signal-to-noise limit that must be surpassed by the fit parameters obtained from MLE-based fits of Equations 4-1 or 4-2. Larger thresholds will exclude more fits. See the *SN* field of the *Trajectory.ch1/2analysis.deqch/dissip* variable for details on *SN* calculation. If all fits for a trajectory are rejected due to poor S/N, then the particle's whole trajectory will be rejected with this output as evidence.

"*weak/noisy signal*"

- Originating script (AT): `SignalIntensitySelection.m`
- Relevant Parameters:
  anParam.SNsite – larger values reject more particles. NOTE: this input value plays a role prior to MLE-based dequenching and dissipation fitting. As such, altering its value will require additional trajectory analysis by the `Analyze_Trajectories.m` script.

A3.4.2 List of reasons why a particular dequenching or dissipation fit within a trajectory can be rejected:

"*All Deq slope outside limits*" or "*All D_{2D} outside limits*" or "*Deq duration outside limits*" or "*D_2D const outside limits*"

- Originating script: `Compile_fit_parameters.m`
- Relevant Parameters:
  anParam.ch1/2.ndeqfr/ndissipfr/deqlim/dissiplim – These parameters set permitted values for the p_4 parameter of Equations 4-1 or 4-2, whichever is relevant for the type of signal being fit. See description of these parameters in Section A3.2 for more information.

"*Bad deqch params: p2<p1*" or "*Bad dissip params*"

- Originating script (AT): `analyze_deq_dissip.m`, `analyze_deq.m` or `analyze_dissip.m`
- Relevant Parameters:
  Not under direct parameter control. The fit parameters p_1 and p_2 are tested to ensure that dequenching events correspond to signal increases and dissipation events to signal decreases. See the description of the *Delta* field saved under the variable *Trajectory.ch1/2analysis.deqch/dissip* for more information.

"*Failed 1st round Likelihood test – no acceptable fitting range*"

- Originating script: `findDequench.m` or `findDissipation.m`
- Relevant Parameters:
  `anParam.alphaval` – this parameter value establishes the $C_{S,1-\alpha}$ value that a Q_S value must surpass if a fit is to be accepted. This first round only looks at the maximal Q_S value found, the second round looks at the start/end fitting frame corresponding to maximal Q_S value relative to the fit R^2 value.

"*Failed 2nd round Likelihood test – no useful Jacobian identified*"

- Originating script: `findDequench.m` or `findDissipation.m`
- Relevant Parameters:
  Not under direct parameter control. This rejection reason arises because the Jacobian matrix used for parameter determination during least squares fitting was not properly defined and confidence intervals for the resulting parameters cannot be determined.

"*Failed 2nd round Likelihood test – Z-statistic too small*"

- Originating script: `findDequench.m` or `findDissipation.m`
- Relevant Parameters:
  Not under direct parameter control. The first round MLE-based fitting resulted in a maximal Q_S (or Z) test statistic that was not near the maximal R^2 value. In the second round of testing, the maximal Q_S obtained near the average frame taken between maximum Q_S and maximum R^2 failed to be larger than the $C_{S,1-\alpha}$ value (Figure 4-6).

"*Failed 2nd round Likelihood test - max(R^2) not near max(LogLikelihood_val)*"

- Originating script: `findDequench.m` or `findDissipation.m`
- Relevant Parameters:
  Not under direct parameter control. The first round MLE-based fitting resulted in a maximal Q_S (or Z) test statistic that was not near the maximal R^2 value. In the second round of testing, the maximal Q_S obtained near the average frame taken between maximum Q_S and maximum R^2 failed to be larger than the $C_{S,1-\alpha}$ value (Figure 4-6).

"*Failed to have Normally distributed fit residuals*"

- Originating script: `findDequench.m` or `findDissipation.m`
- Relevant Parameters:
  `anParam.alphaval` – a *t*-test is performed on the residuals resulting from fitting dequenching or dissipation Equations 4-1 or 4-2 to the normalized intensity data. If *t*-test rejects the null hypothesis with a *p*-value less than `1-anParam.alphaval`, then the fit is rejected.
  > Future expansion suggestion: include an additional parameter to define this threshold separately from `alphaval`.

"*Multiple good fits*"

- Originating script: `Compile_fit_parameters.m`
- Relevant Parameters:
  Not under direct parameter control. Only a single dequenching event and a single dissipation event is permitted per trajectory. If more than one type of event is detected, then all fits of that event type are rejected. A particle having a single dequenching event and multiple dissipation events will not be rejected, and vice versa.

"*No Dequenching Signal*" or "No *Dissipation Signal*"

- Originating script: `Compile_fit_parameters.m`
- Relevant Parameters:

  1) *`anParam.ch1/2.SNthresh`* – This output is saved to the *`rejectDeqReason`* or *`rejectDissipReason`* fields when the signal-to-noise threshold of a fit is not surpassed. Larger threshold values will reject more fits.

  2) *`imgParam.winfilt_st`* – Setting this parameter value too high when searching for initial guess points can wash out short-lived signals, such as dequenching.

  3) *`imgParam.frames_id_particles`* – this is a problem for missing rapid fusion events if the first value of this two-element array is set too far from the pH drop. If fusion events occur between pHdrop and *`imgParam.frames_id_particles(1)`* then they will likely be skipped over because there is not enough signal in the data between *`imgParam.frames_id_particles(1)`* and the event point for detection of a statistical difference in intensity before and after the event point.

"*Poor deqch fit S/N*" or "*Poor dissip fit S/N*"

- Originating script: `Compile_fit_parameters.m`
- Relevant Parameters:

  `anParam.ch1/2.SNthresh` – This parameter describes the signal-to-noise limit that must be surpassed by the fit parameters obtained from MLE-based fits of Equations 4-1 or 4-2. Larger thresholds will exclude more fits. See the *`SN`* field of the *`Trajectory.ch1/2analysis.deqch/dissip`* variable for details on *`SN`* calculation.

A3.5 Supplementary references

1. Floyd DL, Ragains JR, Skehel JJ, Harrison SC, van Oijen AM. (2008) Single-particle kinetics of influenza virus membrane fusion. Proc Natl Acad Sci U S A 105: 15382-15387.

2. Guizar M. (2008) Efficient subpixel image registration by cross-correlation (http://www.mathworks.nl/matlabcentral/fileexchange/18401-efficient-subpixel-image-registration-by-cross-correlation), MATLAB central file exchange. Retrieved June 13, 2013.

3. Ben-Ezra S. (2009) FFT filter - clean your signals and display results! (http://www.mathworks.nl/matlabcentral/fileexchange/25017-fft-filter-clean-your-signals-and-display-results), MATLAB central file exchange. Retrieved July 19, 2013.

4. Hedde PN, Fuchs J, Oswald F, Wiedenmann J, Nienhaus GU. (2009) Online image analysis software for photoactivation localization microscopy. Nat Methods 6: 689-690.

Appendix 4 – Supplementary information for Chapter 5

This appendix contains the following supplementary information:

A4.1 Supplementary figures

A4.2 Supplementary movie description

A4.3 Supplementary tables

A4.1 Supplementary figures

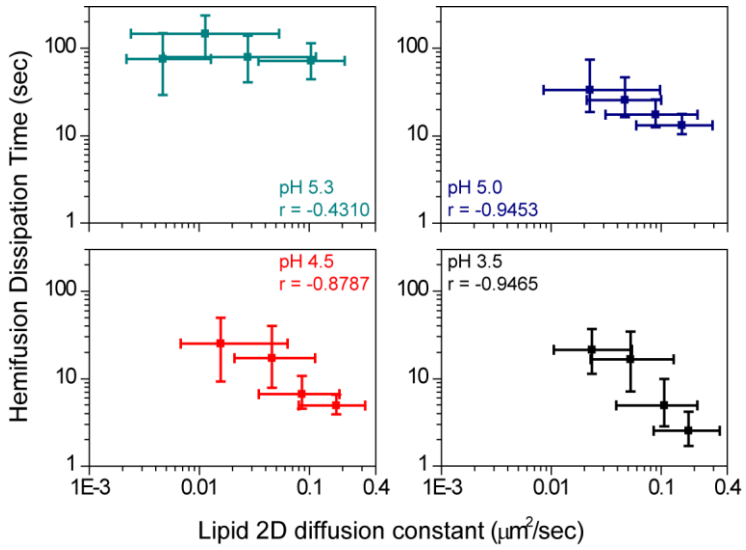

Figure A4-1 – *Correlation between lipid 2D diffusion constant and the time to lipid dissipation. Values for T_{LP} and Lipid D_{2D} reported in Figure 5-3A and Figure 5-3B, respectively, are plotted against each other here to visualize the correlation between these values for pH 5.0, 4.5 and 3.5. Correlation r values are indicated in the figure and show a weak correlation between T_{LP} and Lipid D_{2D} for fusion induced at pH 5.3, with significant correlation at lower pH values. Data points are median values ± interquartile range, as in Figure 5-3.*

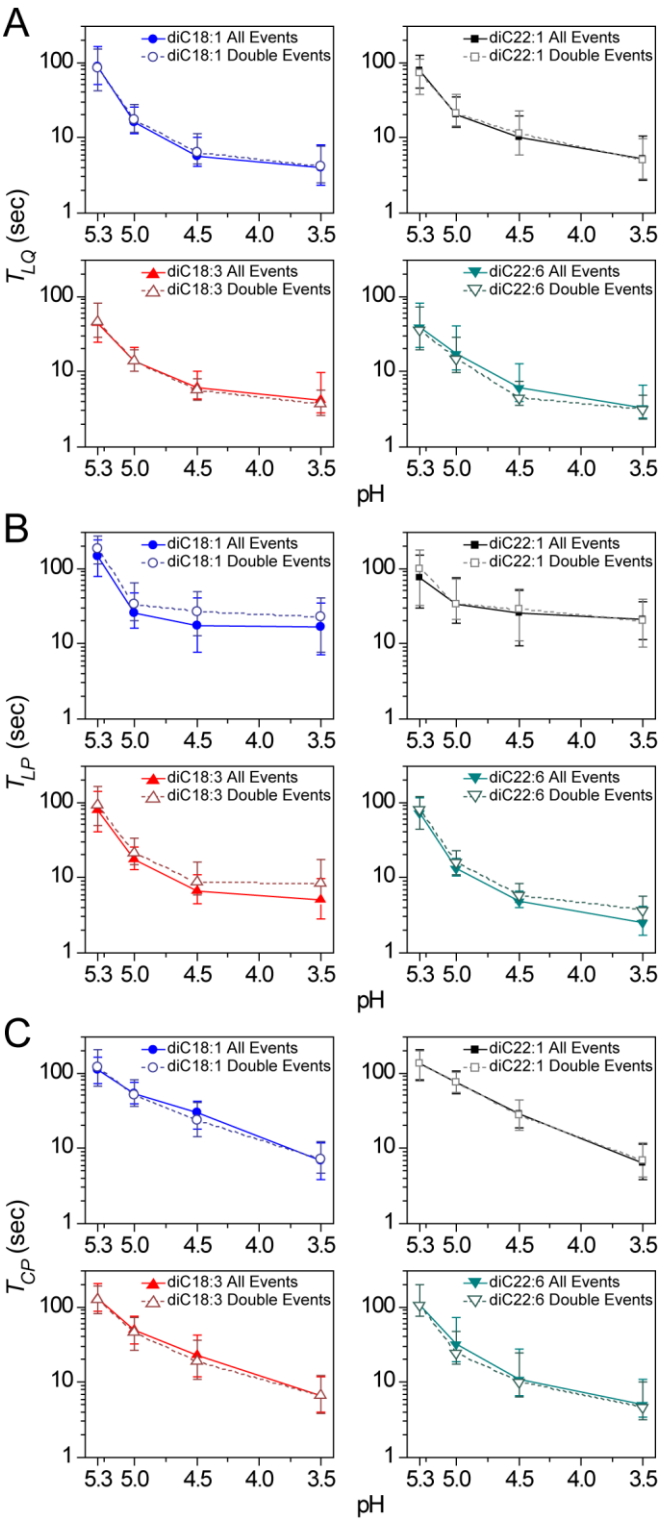

Figure A4-2 *– Correspondence of kinetics for particles showing two fusion events with the population of all viruses. A) The lipid dequenching kinetics for double event particles, which show lipid dequenching along with lipid dissipation and/or content dissipation, agree well with the lipid dequenching kinetics for all particles analyzed. B) The lipid dissipation kinetics for double event particles, which show lipid dissipation along with lipid dequenching and/or content dissipation, agree well with the lipid dissipation kinetics for all particles analyzed. C) The content dissipation kinetics for double event particles, which show content dissipation along with lipid dequenching and/or lipid dissipation, agree well with the content dissipation kinetics for all particles analyzed.*

A4.2 Supplementary movie description

Movie M4-1 – Dual colored influenza virus fusing to a dextran-supported planar bilayer at pH 3.5 that shows content release before exit from a restricted hemifusion state. The fluorescence trajectory from this particle is shown in Figure 5-1D of Chapter 5. Content SRB label is false-colored magenta, lipid label Rh110 is false-colored green, co-localization between the channels is shown in white. The same field of view is shown in triplicate with the red and green emission channels merged (left), the red content channel alone (middle), and the green lipid channel alone (right). In this instance, the content release occurs very shortly after the lipid dequenching signal. The increase in fluorescence intensity persists for several seconds before giving way to a lipid dissipation signal. Scale bar is 1 μm.

A4.3 Supplementary table

Table A4-1 – Number of events visualized*

	Number T_{LQ}	Number T_{LP}	Number T_{CP}	Number T_{LQ} & T_{LP} (confinement lifetime)	Number T_{LQ} & T_{CP} (hemifusion lifetime)	Number T_{LP} & T_{CP} (inter-dissipation time)	Total viruses visualized
pH 3.5							
diC18:1	301	272	253	48	76	24	1403
diC18:3	201	811	236	100	44	46	1805
diC22:1	427	238	398	65	169	30	1701
diC22:6	97	1075	346	56	43	164	1660
pH 4.5							
diC18:1	356	364	197	85	32	26	1238
diC18:3	231	1212	163	140	32	61	1818
diC22:1	571	299	282	93	94	50	1654
diC22:6	105	1052	234	63	34	154	1333
pH 5.0							
diC18:1	591	715	132	212	37	31	1562
diC18:3	300	1182	186	185	29	62	1930
diC22:1	582	322	180	137	68	37	1330
diC22:6	128	1219	248	82	30	151	1673
pH 5.3							
diC18:1	442	297	136	105	41	19	1095
diC18:3	123	929	120	64	19	44	1717
diC22:1	207	477	225	81	54	66	1284
diC22:6	87	504	111	37	21	64	904

* Values reported in Chapter 5 Figure 5-3C and Figure 5-3F are the mean values across all experiments, not the fraction of total numbers reported here.